Dual Dye-Enhanced FIT^2 Probes for Sequence-Specific Detection of RNA

Dissertation

zur Erlangung des akademischen Grades

doctor rerum naturalium
(Dr. rer. nat.)

im Fach Chemie

eingereicht an der

Mathematisch-Naturwissenschaftlichen Fakultät
der Humboldt-Universität zu Berlin

von

M. Sc. Sophie Schöllkopf

Präsidentin der Humboldt-Universität zu Berlin
Prof. Dr. Julia von Blumenthal

Dekanin der Mathematisch-Naturwissenschaftlichen Fakultät
Prof. Dr. Caren Tischendorf

Gutachter:
1. Prof. Dr. Oliver Seitz
2. Prof. Dr. Christian Hackenberger
3. Prof. Dr. Hans-Achim Wagenknecht

Tag der mündlichen Prüfung: 20. Februar 2023

The experimental work presented in this dissertation was carried out between February 2016 and August 2020 in the research group of Prof. Dr. Oliver Seitz at the Institute of Chemistry of the Humboldt University of Berlin.

1 Abstract

The ability to detect and visualize nucleic acids in living organisms is crucial for understanding cellular processes. For this purpose, the research group of Prof. Dr. Oliver Seitz has introduced fluorogenic *forced intercalation* (FIT) hybridization probes, which exploit the unique property of the cyanine dyes thiazole orange and quinoline blue to exhibit increased fluorescence when placed in the constrained environment of a nucleic acid duplex formed between probe and specific target sequence. Although FIT probes demonstrate solid fluorescence enhancement and specificity, further improvement of their absolute brightness and signal-to-background ratio would be desirable.

To achieve this, the present thesis investigated an approach that equips FIT probes with two identical fluorophores (FIT^2 strategy). This should on the one hand increase probe brightness, while simultaneously reducing fluorescence in the single strand and when hybridized to mismatched RNA, through a combination of contact-mediated quenching and non-radiant energy transfer. Various probe lengths, dye-dye distances and positions were screened, and it could be confirmed that FIT^2 probes have higher extinction coefficients, greater fluorescence enhancement and better selectivity than their mono-dye counterparts. Moreover, they better retain their ability to discriminate match and mismatch targets in viscous cell lysate.

Finally, it was demonstrated that the FIT^2 concept can be extended by adding a hybridization-insensitive Cyanine 7 dye to the probes, allowing ratiometric detection of hybridized probe and correction of brightness differences due to local fluctuations in probe concentration during live-cell imaging. Using these $qFIT^2$ probes, Jurkat and CCRF-CEM T-cells could be distinguished in a microscopy-based experiment.

Keywords: RNA detection, hybridization probes, forced intercalation, thiazole orange, quinoline blue, self-quenching

Die Fähigkeit Nukleinsäuren in lebenden Organismen nachzuweisen und zu visualisieren, ist entscheidend für das Verständnis zellulärer Prozesse. Die Forschungsgruppe von Prof. Dr. Oliver Seitz hat zu diesem Zweck fluorogene FIT-Hybridisierungssonden entwickelt, die die besondere Eigenschaft der Cyaninfarbstoffe Thiazolorange und Chinolinblau nutzen, stärker zu fluoreszieren, wenn sie in die beengte Umgebung eines Nukleinsäureduplex aus Sonde und spezifischer Zielsequenz eingebracht werden. Obwohl FIT-Sonden eine gute Fluoreszenzverstärkung und Spezifität aufweisen, wäre eine weitere Verbesserung ihrer Helligkeit und des Signal-Hintergrund-Verhältnisses wünschenswert.

Um dies zu erreichen, wurde in dieser Arbeit ein Ansatz untersucht, bei dem FIT-Sonden mit zwei Fluorophoren desselben Typs ausgestattet werden (FIT^2-Strategie). Dies sollte sowohl die Helligkeit der Sonde erhöhen, als auch die Fluoreszenz im Einzelstrang und bei Hybridisierung mit fehlgepaarter RNA durch eine Mischung aus kontaktvermittelter Fluoreszenzlöschung und strahlungsfreiem Energietransfer verringern. Verschiedene Sondenlängen, Farbstoffabstände und -positionen wurden untersucht und es konnte bestätigt werden, dass FIT^2-Sonden eine höhere Extinktionskoeffizienten, größere Fluoreszenzverstärkung und eine bessere Selektivität aufweisen als einfach markierte Sonden. Außerdem behalten sie ihre Fähigkeit zur Unterscheidung von Match- und Mismatch-Zielen in viskosem Zelllysat besser bei.

Zudem konnte gezeigt werden, dass das FIT^2-Konzept durch Hinzufügen eines hybridisierungsunempfindlichen Cyanin 7 Farbstoffs zu den Sonden dahingehend erweitert werden kann, dass eine ratiometrische Detektion der hybridisierten Sonde möglich ist und Helligkeitsunterschiede aufgrund von lokalen Schwankungen der Sondenkonzentration bei der Bildgebung lebender Zellen korrigiert werden können. Mit diesen qFIT^2-Sonden konnten Jurkat und CCRF-CEM T-Zellen in einem Mikroskopie-basierten Experiment unterschieden werden.

Stichworte: RNA Detektion, Hybridisierungssonden, erzwungene Interkalation, Thiazol-Orange, Quinolin-Blau, Selbst-Löschung

2 Table of Contents

3 Theoretical Background

3.1 RNA and Posttranscriptional Sequence Alterations

RNA is an essential biopolymer, which is structurally very similar to DNA, but contains a ribose instead of deoxyribose unit as part of its backbone (**Figure 1A**). This relatively small change leads to a drastically different stability, as the additional hydroxyl group makes RNA more prone to hydrolysis. It also causes the helical structure to adopt an A-type geometry, as opposed to the B-type helix formed by DNA. Like DNA, the function of RNA is governed by the genetic code, which comprises the purines adenine (A) and guanine (G) and the pyrimidines cytosine (C) and uracil (U). These four nucleobases interact by forming hydrogen bridges according to the rules discovered by James Watson, Francis Crick and Rosalind Franklin (adenine-uracil and guanine-cytosine).[1]

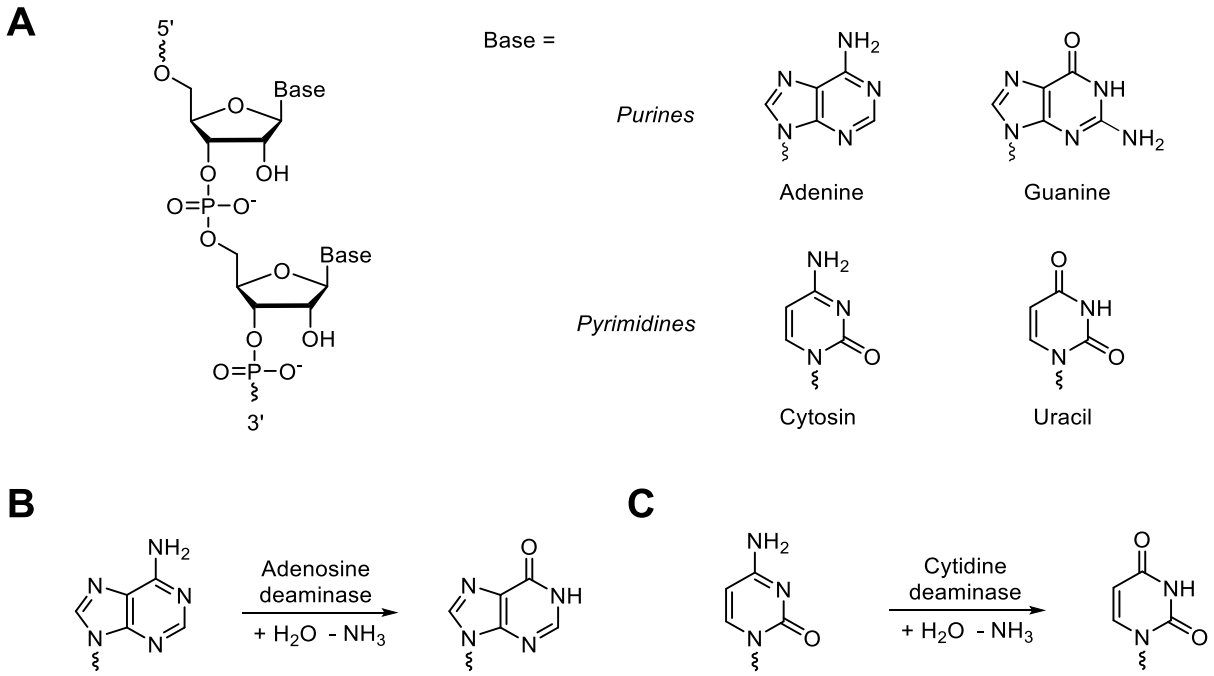

Figure 1: (**A**) Chemical structure of RNA and its four nucleobases. (**B**) Adenosine-to-inosine and (**C**) cytidine-to-uracil editing by specialised deaminases.

RNA is most well-known for its role in the central dogma of biology, wherein it serves as working copy of the genetic information that instructs the synthesis of new proteins. However, RNA is a much more versatile molecule than DNA, able to form complex secondary and tertiary structures, allowing it to also exert other functions beyond the transfer of genetic information.[2] In addition to the three major RNA types involved in translation, messenger RNA (mRNA), transfer RNA (tRNA) and ribosomal RNA (rRNA), today a large variety of non-coding RNAs (ncRNAs) are known that act as regulatory elements or can have enzyme-like function,

such as small interfering RNA (siRNA), microRNA (miRNA), small nuclear RNA (snRNA), small nucleolar RNA (snoRNA), long non-coding RNA (lncRNA) and many others.[3-5] The structural and functional diversity of RNA is further enhanced by a number of chemical alterations that are often performed co- or post-transcriptionally.[6] The most well-studied amongst them is mRNA processing, during which a 7-methylguanosine (m^7G) cap and a poly(A) tail are enzymatically appended to the 5'- and 3'-end, respectively.[7] It is also possible that single nucleotides within the sequence are modified, e.g. by methylation, the nucleobase is attached via an alternative linkage or bulky residues are added. Particularly tRNAs often contain a large number of such non-canonical nucleotides, which serve to enhance anticodon specificity, help to maintain tRNA structure, or promote tRNA-enzyme interactions.[8, 9] Another important processing mechanism is RNA splicing. Here, the sequence of the native RNA transcript (pre-mRNA) is altered by removing certain non-coding parts (introns) and reconnecting the coding sections (exons) to create mature mRNA.[7] This process is catalysed by the spliceosome, a large ribonucleoprotein complex assembled from numerous proteins and snRNA.[10] Based on which exons are included or excluded in the process, different combinations for the final, mature mRNA are possible. This so-called alternative splicing allows multiple protein variants to be encoded by a single gene, increasing proteomic diversity. But when splicing occurs in the wrong position it may also lead to a loss of function.[11] Mis-splicing is the cause of a number of human diseases, such as Duchenne muscular dystrophy or the Prader-Willi syndrome. Moreover, splicing may be exploited by certain pathogens. For example, the influenza A virus hijacks the cellular splicing machinery during its replication cycle, to generate multiple different proteins from a relatively small genome.[12, 13]

In addition to the large-scale re-arrangements caused by RNA splicing, the sequence information of an RNA molecule can be site-specifically altered on the single nucleotide level. In so-called RNA-editing, individual nucleotides of a transcript are added, removed, or replaced post-transcriptionally, resulting in a sequence differing from the one originally encoded by the genome.[14] This phenomenon was first observed in kinetoid plastozoa, where uridine residues were found to be inserted into and deleted from mitochondrial RNA to create new open reading frames.[15] Since then, RNA editing has been confirmed to occur in all living organisms and can significantly influence the function, stability and localization of RNA molecules or the proteins encoded by them.[14, 16] In higher eukaryotes, the most prevalent type of editing is the conversion of adenosine into inosine (A-to-I editing; **Figure 1B**) and cytidine into uracil (C-to-

U editing; **Figure 1C**). Both of these modifications are catalysed by special deaminases and occur in a tissue-specific manner.[17, 18] Although the exact role of RNA editing is still under investigation, several studies have indicated that it may be associated with disease.[18-20] For example, C-to-U editing of the glycine receptor (GlyR) in the brain has been shown to be involved in temporal lobe epilepsy (TLE) disease progression.[21]

Due to its multifaceted involvement in cell homoeostasis, RNA has gained considerable interest as both agent and target for the prevention and treatment of diseases.[22] Over the years, several strategies for RNA-based therapies have been developed, ranging from techniques such as antisense oligonucleotides[23] and RNA interference (RNAi)[24] to more recent developments like mRNA vaccines.[25] However, in order to utilize the full potential of these methods, a detailed understanding of the occurrence, and spatio-temporal distribution of ribonucleic acid molecules inside living cells is required. For this, it is important to have tools that allow detection and visualization of specific sequences, ideally with single nucleotide resolution.

3.2 Fluorescence and Quenching Mechanisms

Most modern techniques to probe cellular dynamics and visualize nucleic acids rely on fluorescence.[26, 27] This photochemical phenomenon is the ability of certain molecules, so-called fluorophores, to absorb and re-emit electromagnetic radiation. Fluorophores are typically polyaromatic hydrocarbons, heterocyclic compounds or otherwise unsaturated compounds with an extended system of conjugated π-electrons that can transition into higher energy excited states.[28] Labelling of biological molecules with these dyes allows a highly sensitive detection, even if the target is otherwise too small to be resolved by conventional light microscopy.

Fluorescence occurs via a three-step process illustrated in the so-called Jablonski diagram (**Figure 2A**):[29] (**1**) Absorption of a photon causes an electron to be lifted from the ground state S_0 into an excited electronic state (S_n). Depending on the wavelength of the absorbed photon, different vibronically excited levels can be attained. (**2**) These higher energy states are short-lived (10^{-15} to 10^{-9} s) and quickly relax to the semi-stable, vibrationally relaxed, lowest level electronically excited state (S_1) through non-radiative processes that dissipate some of the absorbed energy as heat (e.g. through conformational changes of or interaction with its environment). (**3**) From the S_1, fluorescence can occur: On a ns timescale, the remaining energy is released as a photon, causing the molecule to relax back to the ground state S_0.[30]

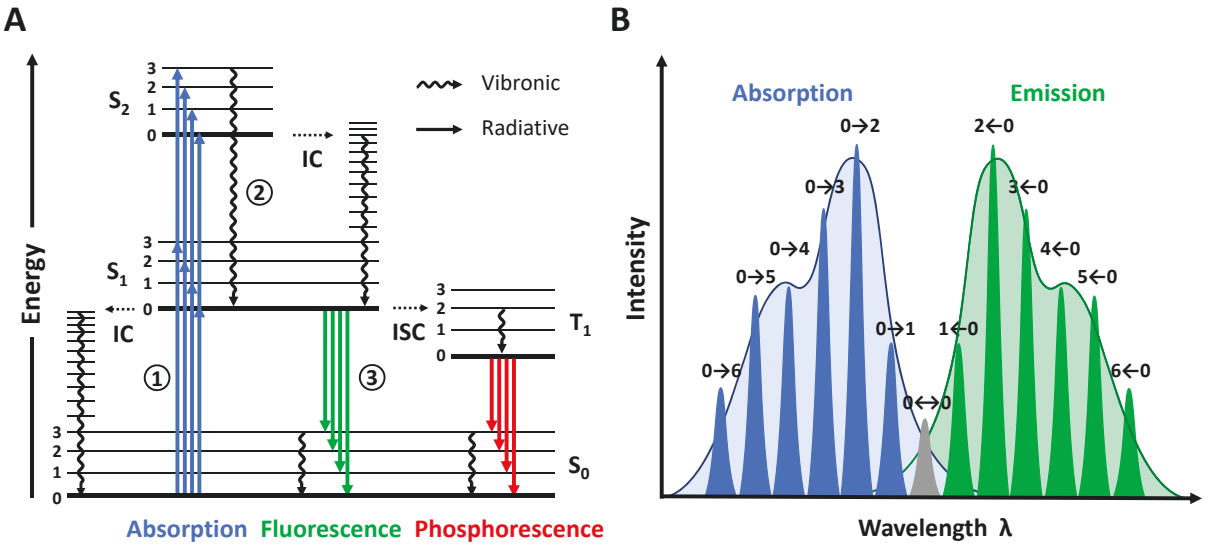

Figure 2: Spectroscopy of fluorophores. (**A**) Jablonski diagram illustrating the different electronic states of a molecule and the radiative and non-radiative transitions between them. Fluorescence follows a three-stage process: ① absorption of a photon, ② vibronic relaxation, ③ emission of a longer wavelength photon. ISC = inter system crossing; IC = internal conversion. (**B**) Symmetry of absorption and emission spectra, with the underlying vibronic transitions.

Excitation and fluorescence emission both occur only in discrete energy steps, which correspond to the different vibronic transitions between S_0 and S_n. Together, they produce a characteristic absorption and emission spectrum, in which preferred transitions manifest as local maxima (**Figure 2B**). How strongly a specific wavelength is absorbed, can be described by the Beer-Lambert law:[31]

$$\varepsilon = \frac{\log(I_0 / I_1)}{c \cdot l} \qquad (1)$$

Here, ε is the molar extinction coefficient, I_0 and I_1 are the intensities of the light received by and passed through the sample, c is the concentration of the fluorophore, and l is the path length of the light beam. As the distance between nuclei can be approximated as constant on the timescale of electronic transitions (Franck-Condon principle), the potential curves of the ground and excited state have similar shapes and thus similar transitions. As a result, the absorption and emission spectra are almost mirror images of each other. However, due to the partial dissipation of the absorbed energy as heat during the lifetime of the exited state, the emission spectrum is shifted to longer wavelengths. This is referred to as *Stokes shift*.[28]

Importantly, fluorescence is not the only mechanism by which the S_1 can be depopulated. It is also possible that an excited state electron undergoes singlet-to-triplet conversion ($S_1 \rightarrow T_1$), in a process called intersystem crossing (ISC). The radiative decay from the resulting excited triplet state T_1 is called phosphorescence. Because it requires another change of the electron's spin multiplicity to comply with the Pauli exclusion principle, it occurs at a much slower rate

(10^3 to 10^0 s^{-1}) than fluorescence. As a result, phosphorescence can often still be observed seconds to minutes after irradiation has stopped.[28] A second major deexcitation mechanism is internal conversion (IC). Here, the vibrational ground state of an electronically excited state (e.g. S_1) non-radiatively transitions into a high level vibronically excited state of a lower electronic state (e.g. S_0). The energy is then given off as heat.

Besides ISC and IC, there are other important non-radiative deactivation (quenching) processes (**Figure 3A**):[28] In *static quenching* (also known as contact quenching), the ground state fluorophore and a quencher molecule form a non-fluorescent complex with different absorption properties that returns to the ground state without emission of a photon upon excitation. High temperatures destabilize the complex and thus reduce the efficiency of this mechanism. In *dynamic quenching*, the excited state is passed from the fluorophore onto a colliding molecule. This occurs via *Dexter electron transfer* (**Figure 3B**), when the wave functions of the donor and acceptor overlap at very short distances, typically ≤ 10 Å.[32]

In contrast to static quenching, the efficiency of this mechanism grows with temperature, as higher kinetic energies increase the probability for collisions. Another type of dynamic quenching is *Förster resonance energy transfer* (FRET). Here, the energy of the electronically excited fluorophore is transferred onto an acceptor molecule via non-radiative dipole-dipole

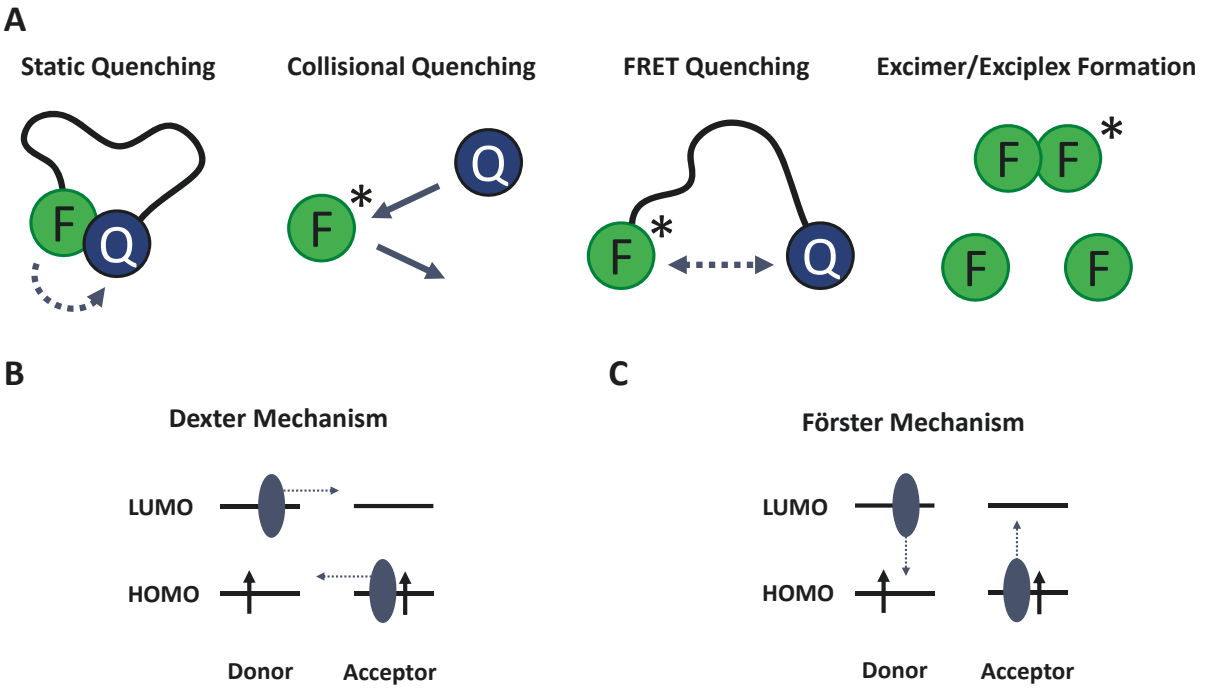

Figure 3: Fluorescence quenching mechanisms. (**A**) Overview of different types of deexcitation pathways involving a fluorophore (F) and a quencher (Q). Two fundamental types of energy transfer involved are (**B**) electron exchange (Dexter mechanism) and (**C**) dipole-dipole coupling (Förster mechanism). HOMO = highest occupied molecular orbital; LUMO = lowest unoccupied molecular orbital.

coupling (**Figure 3C**).[33] A prerequisite for this mechanism is an overlap of the donor's emission and the acceptor's absorption spectrum. Importantly, the acceptor does not have to be fluorescent itself. The FRET efficiency E is highly dependent on the distance between the two molecules r. It can be calculated by the Förster equation:

$$E = \frac{R_0^6}{R_0^6 + r^6} \tag{2}$$

Here, R_0 is the distance at which the FRET efficiency is 50 %. It results from the quantum yield of the donor in absence of FRET ϕ_D, the dipole orientation factor κ, the refractive index of the medium n and the integral of the spectral overlap J(λ):

$$R_0^6 = \frac{8.8 \cdot 10^{-28} \cdot \phi_D \cdot \kappa^2 \cdot J(\lambda)}{n^4} \tag{3}$$

The inverse sixth-order dependence of FRET efficiency on r makes it a highly sensitive tool for molecular biology. Using fluorophore-labelled probes, FRET can be applied as a "spectroscopic ruler" to map distances, detect specific molecules or interactions, or gain information about conformational changes.[34-37] An important sub-type of FRET is homo-FRET. Because of its spectral requirements, FRET typically takes place between two different chromophores. However, if a dye has sufficient overlap between its own excitation and emission spectrum, homo-FRET can occur, and energy can be transferred from one molecule to another of the same type. This mechanism is of particular interest when different chemical microenvironments alter the fluorescent properties of either the acceptor or donor.

A fourth quenching mechanism is *excimer formation*. Excimers (from "*exci*ted state di*mer*") are homodimeric aggregates of normally monomeric molecules that only form and exist in an excited state.[38, 39] Mechanistically, excimer formation occurs, when an valence shell electron of one of the binding partners is excited and occupies a higher energy, binding molecular orbital. As a result, a short-lived covalent bond forms between the molecules, which is broken up again as soon as the excited state ends. Excimers have different emission properties than their corresponding monomers. Due the expended association enthalpy (ΔH_A), their excited state is energetically lower than the monomer S_1. In addition, they relax into an energetically higher, unstable ground state, which dissociates under further expenditure of repulsion energy (ΔE_R) and possesses no defined vibrational levels.[40] The involvement of these additional processes causes excimer emission to be broad and red-shifted.

A related photophysical phenomenon is J- or H-aggregate formation.[41, 42] When two or more fluorophores of the same type come into close contact, e.g. due to hydrophobic interactions or π-stacking, their excited states can interact and become delocalized. This effect is well-documented for cyanine dyes but may also be observed in other chromophores, such as porphyrins, chlorins, carotenoids and perylene bisimides.[43-48] Excitonic coupling splits the degenerate excited states of each dye pair into two discrete energy levels (**Figure 4**), one in which the transition dipole moments align and one where they point in opposite directions.[49-51] Which of these two states is populated upon excitation depends on geometry: In head-to-tail aggregates (J-aggregates) the transition to the higher state (E_+) is optically forbidden, as the two dipole moments cancel each other out.[52-54]

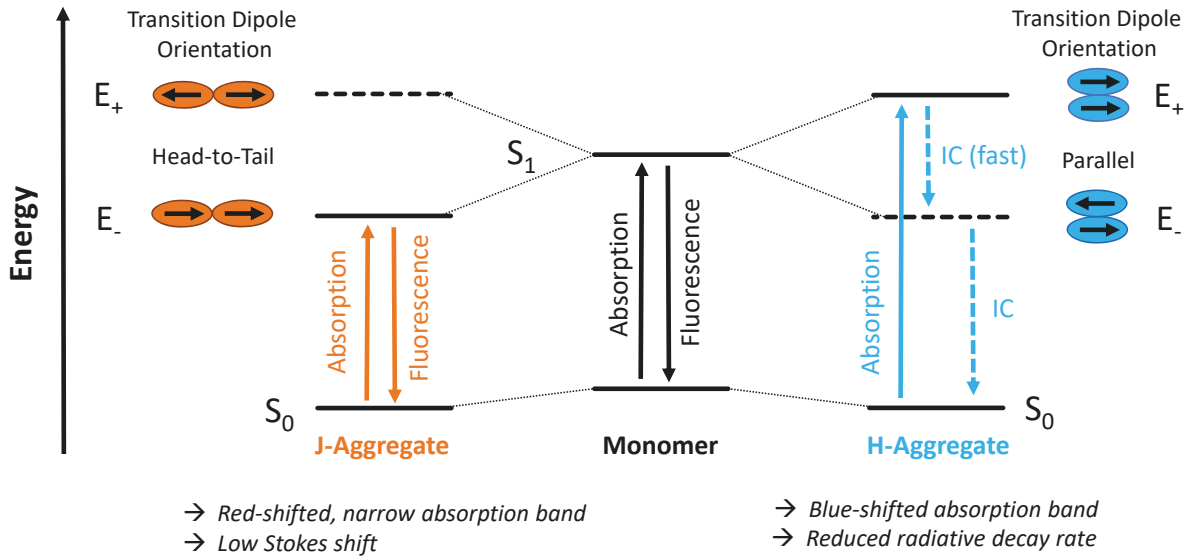

Figure 4: Energy diagram for J- and H-type aggregates and the associated changes in absorption and emission. Forbidden states, in which the transition dipole moments cancel each other out, are represented as dashed lines.

As a result, they have a narrow, red-shifted absorption band (bathochromic shift). Moreover, because the excitation of J-aggregates directly populates the lowest level excited state (E_-), their emission has almost no Stokes shift. Parallel molecule stacks (H-aggregates), behave in the opposite way. Here, the transition to the lower energy state (E_-) is forbidden. This shifts their absorption spectrum to shorter wavelengths (hypsochromic shift) but also results in a drastically different emission behaviour: Following excitation, a rapid internal conversion process relaxes the excited state to the favoured lower energy level (E_-). However, as this state has no net transition dipole moment, its radiative decay rate is very small. As a result, H-aggregates typically display greatly diminished fluorescence.[41]

It must be noted that the presented deexcitation pathways are not mutually exclusive and several mechanisms may occur simultaneously. The efficiency of a molecule as a fluorophore depends on the relative proportion of fluorescence and the sum of all non-radiative processes. This ratio is known as fluorescence quantum yield (ϕ_F).[28] The higher ϕ_F at a given wavelength, the more photons are re-emitted as fluorescence after absorption. It can be calculated as:

$$\phi_F = \frac{\text{photons}_{em}}{\text{photons}_{abs}} = \frac{k_f}{k_f + \sum k_{nr}} \quad (4)$$

Here, k_f and k_{nr} represent the rate constants for fluorescence and the non-radiative relaxation processes, respectively. For unknown fluorophores, ϕ_F can be determined experimentally by comparing it to a reference compound with known absorption and emission properties, using the same experimental setup and entering the measured values into the following formula:

$$\phi_F = \phi_R \cdot \frac{I_F \cdot A_R}{I_R \cdot A_F} \quad (5)$$

Here, ϕ_R is the quantum yield of the reference, I_F and I_R are the integrated fluorescence intensities of fluorophore and reference and A_F and A_R are their respective absorbances for a specific wavelength. Finally, using the fluorescence quantum yield ϕ_F and the molar extinction coefficient ε of a fluorophore, its brightness (Br) can be calculated as:

$$Br = \phi_F \cdot \varepsilon \quad (6)$$

For the comparison of different fluorophores, this parameter is often more practical than the quantum yield, as it also considers the respective absorption behaviour.

3.3 The Thiazole Orange Fluorophore Family

Some molecules only fluoresce under certain conditions. So-called intercalator dyes are planar aromatic molecules that are normally non- or weakly fluorescent but display drastically increased emission in the presence of nucleic acids. A well-known example is ethidium bromide, which is commonly used in molecular biology to stain DNA or RNA bands following gel electrophoresis.[55] Another important group is the thiazole orange (TO) family. Its archetypical compound, TO, is an asymmetric cyanine-type dye that consist of a 3-methylbenzothiazol and a 1-methylquinolinium subunit, linked by a methine bridge (**Figure 5A**).[56] It was first characterized by Lee *et al.* who screened a series of thioflavin T-based compounds in search for brighter, RNA-responsive dye for flow cytometric detection of reticulocytes.[57, 58]

Thiazole orange gave the best results, being virtually dark on its own but exhibiting a more than 1000-fold higher fluorescence ($\phi = 0.2$) upon addition of double stranded nucleic acids.[57, 59, 60] In complex with RNA, TOs absorbance maximum lies at 508 nm, with a small shoulder at 485 nm. Its emission is strongest at 535 nm (**Figure 5B**). Viscosimetric and NMR spectroscopic experiments revealed several binding modes, the two most important ones being stacking between the nucleobases ($K_d = 3.03 \cdot 10^{-6}$ M)[59] and minor groove binding.[61-63]

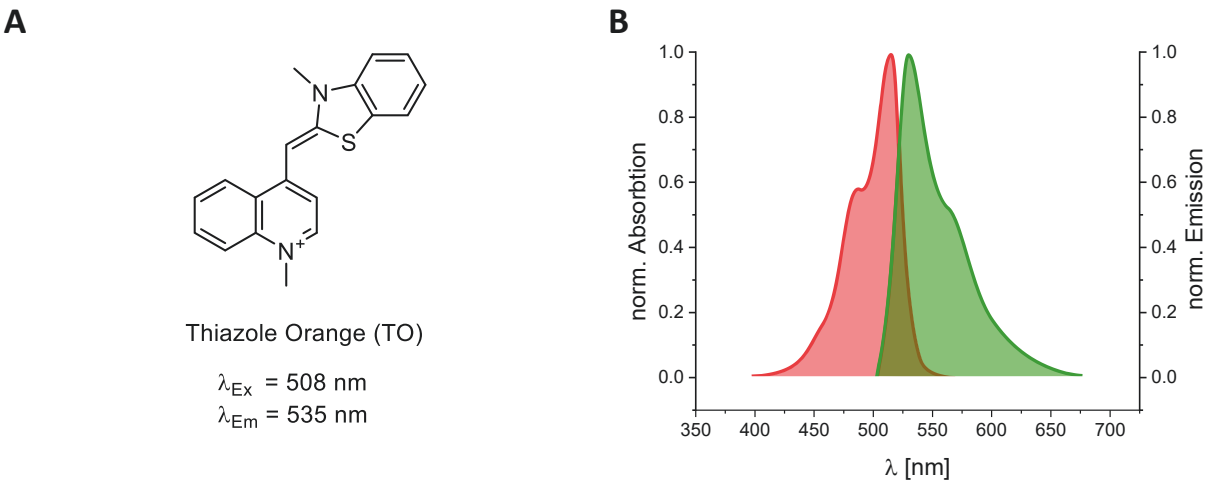

Figure 5: The intercalator dye thiazole orange. (**A**) Chemical structure and (**B**) absorption (red) and emission (green) spectra as base surrogate in an RNA-FIT probe.

The enhanced fluorescence of TO and related cyanine dyes upon insertion into the base stack results from the closure of a competing deexcitation pathway: In the ground state, rotation around the central methylene bridge is restricted by an energy barrier (**Figure 6**).[64] Excitation to the S_1 removes that barrier and causes the molecule to re-equilibrate through a very fast (sub-picosecond) bond twisting (photoisomerization). This causes the molecule to leave the Frank-Condon region and changes its electronic energy levels. At a torsion angle of about 90°, the potential energy surfaces of S_0 and S_1 cross and form a so-called *conical intersection*.[65] Here, a highly efficient, ultrafast internal conversion process can occur. In low viscosity environments, this constitutes the preferred deexcitation mechanism and therefore fluorescence quantum yield is very low. In higher viscosity solvents, the rotation is slower, which causes fluorescence to increase. For example, in 90 % glycerol, the fluorescence of TO is about 135-times higher than in water. Similarly, intercalation into the base stack conformationally locks the molecule in a planar geometry and closes the non-radiative decay channel.[66-68]

The dependence of TO emission enhancement on the degree of torsional restriction renders it sensitive to the nucleic acid composition and the space available at the intercalation site. It was shown that TO reacts more strongly to poly-dG sequences than to polypyrimidines.[60, 69]

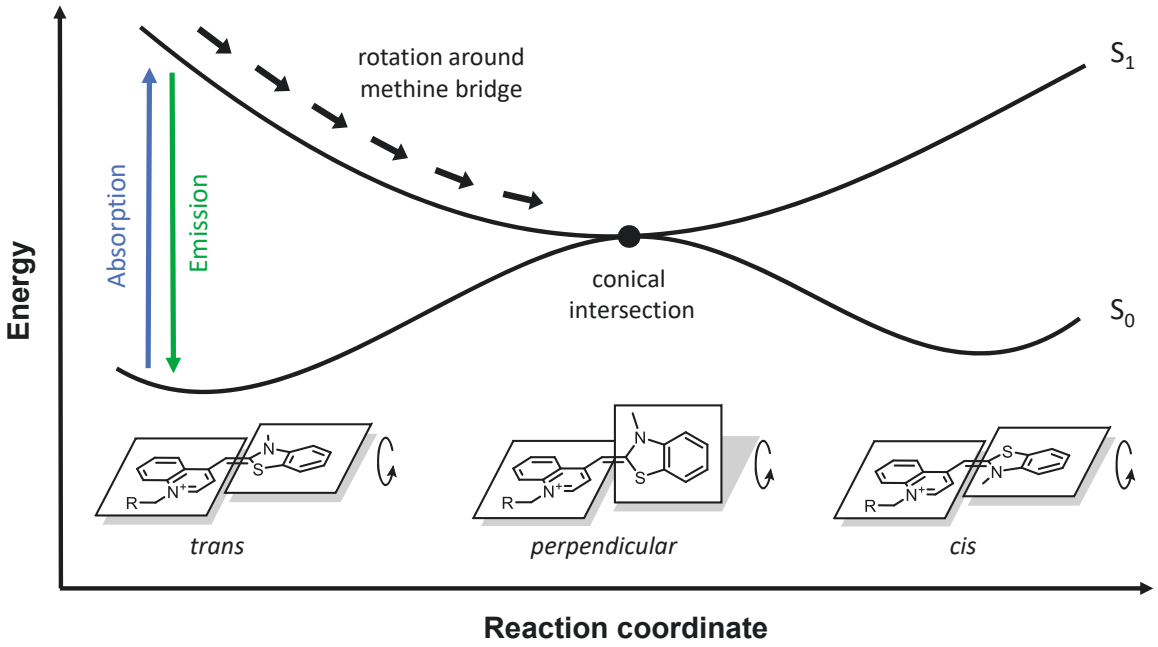

Figure 6: Schematic 2D potential energy diagram illustrating the TO deexcitation pathway favoured in non-viscous solutions. In the ground state S_0, rotation around the central methylene bridge is restricted by an energy barrier. In the S_1, the molecule rotates freely to re-equilibrate. Upon reaching a 90° angle, conical intersection of the S_0 and S_1 potential energy surfaces causes the absorbed energy to be rapidly dissipated by internal conversion.

Notably, the achievable quantum yield also depends on temperature and decreases about three-fold between 5 °C and 50 °C. This is due to the greater thermal motion of the nucleic acid facilitating rotation of the intercalated dye.[60, 69]

Although originally proposed for cell staining, TOs high signal-to-noise ratio has prompted researchers to utilize the dye for biomolecule sensing and quantification.[70] For example, it has been used as DNA/RNA staining in gel electrophoresis and fluorometric assays.[71, 72] In contrast to the classical UV fluorophores used for this purpose, e.g. ethidium bromide, DAPI or Höchst 33342, TO has the advantage of being relatively non-toxic and can be excited by visible light, which reduces the autofluorescence of biological samples. Naturally occurring fluorophores such as flavins and NADPH are also excited by UV light, which leads to high background fluorescence.[73] Moreover, the use of visible light minimizes radiation-induced damage of the DNA and RNA analytes. A drawback that TO shares with the other dyes used for nucleic acid staining, is its lack of sequence specificity. To overcome this limitation, TO has been attached to short synthetic oligonucleotides complementary to the sequence of interest.[70] These probes are able to detect specific DNA or RNA molecules, often with single mismatch resolution. Different strategies to achieve this are discussed in more detail in **Chapter 3.5**.

3.4 Chemical Synthesis of Modified DNA and RNA Oligonucleotides

Synthetic oligonucleotides are essential for many modern molecular biology techniques, such as DNA sequencing or PCR, but their ability to recognize a specific sequence of interest also makes them a powerful tool for analytical applications. Thanks to the pioneering works of Bruce Merrifield,[74] Har Gobind Khorana[75, 76] and Robert Letsinger,[77-80] today custom ribo- and deoxyribo oligonucleotides with a range of chemical modifications, such as fluorophores, can be efficiently and inexpensively prepared by automated solid-phase synthesis. In this process, the product is assembled in a step-by-step fashion on a solid support, typically silica-based controlled pore glass (CPG) or microporous polystyrene (MPPS).[81] As reagents are washed away after each step, they can be used in excess to drive each coupling to completion without requiring intermediate purification. This greatly accelerates synthetic speed and efficiency.

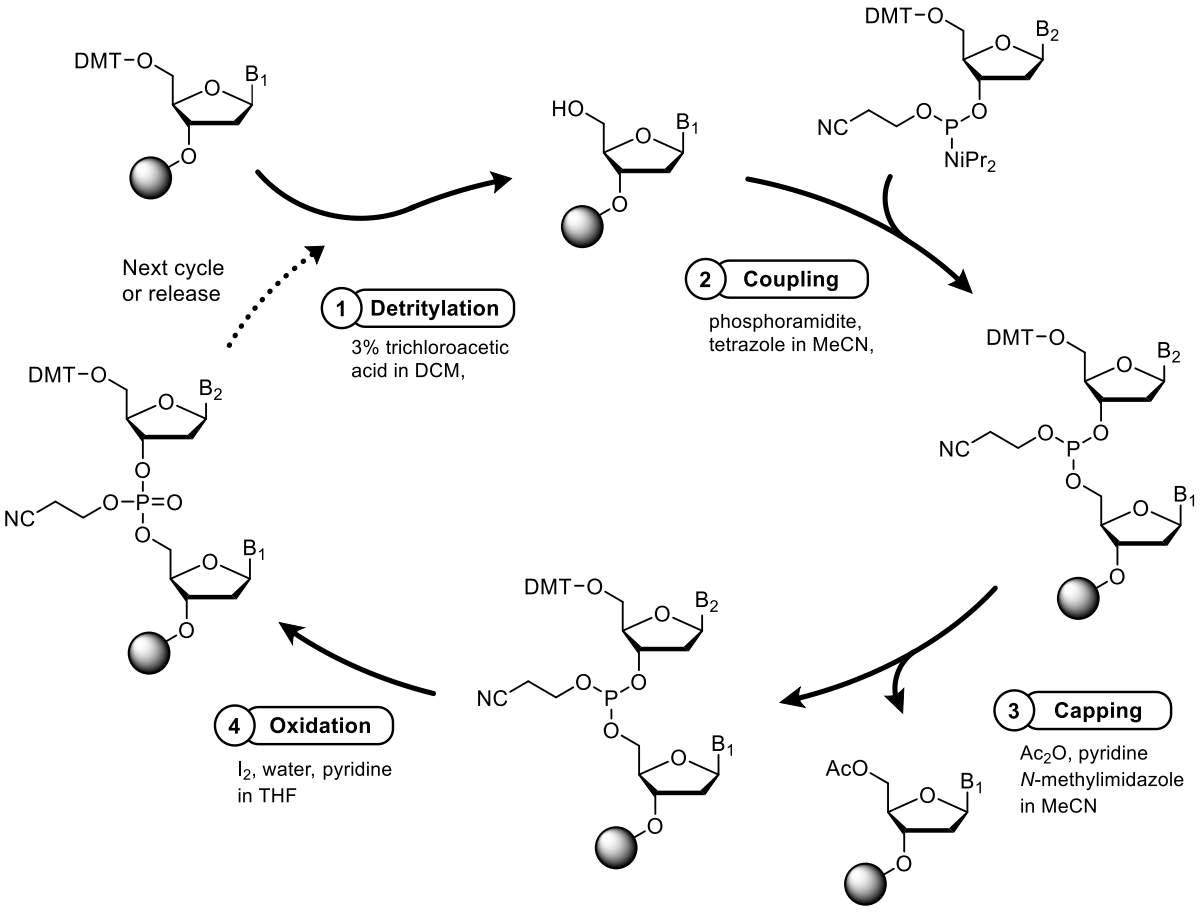

Figure 7: Synthetic cycle for the preparation of oligonucleotides by the phosphoramidite method. The synthesis starts with the de-blocking of the first nucleoside (1), which is anchored to the solid support via its 3'-hydroxyl group. The 4,4'-dimethoxytrityl (DMT) group on the 5'-oxygen is removed by treatment with acid, then the phosphoramidite of the next nucleoside is coupled using a tetrazole catalyst (2).[82, 83] Unreacted hydroxyl groups are capped using a mixture of Ac_2O, pyridine and *N*-methylimidazole (3). Finally, the resulting phosphite triester is oxidized by treatment with I_2 in the presence of water and pyridine to create a phosphate (4), before the cycle can start anew. Alternatively, the oligonucleotide chain can be released from the solid support by treatment with aqueous ammonia, methylamine or a mixture of both.[84]

Most contemporary nucleic acid synthesizers utilize the phosphite triester strategy (**Figure 7**), conceived by Marvin Caruthers and his group in the 1980s.[85-87] Unlike its predecessors, the H-phosphonate,[88, 89] phosphodiester[75] or -triester[77, 90] synthesis, this elegant technique introduces the nucleosides as highly reactive, yet relatively shelf-stable phosphoramidite derivatives. A particular advantage of this chemistry is its high speed: a typical coupling cycle only takes about 5-10 min.[91] The method is also very robust, allowing a wide range of fluorescent labels, modified linkages, and non-canonical bases to be introduced. A variety of such chemical modifications have been developed, with the aim of improving the physicochemical properties and/or enzymatic stability of synthetic DNA or RNA molecules.[92-94] So-called nucleic acid analogues can have altered ribose, nucleobase, or phosphate moieties but may also comprise completely different, non-natural backbone structures. As a large and constantly evolving area of research, new derivatives are reported every year, but several key modifications can be considered well-established and are routinely incorporated into synthetic oligonucleotides (**Figure 8**).[93, 95]

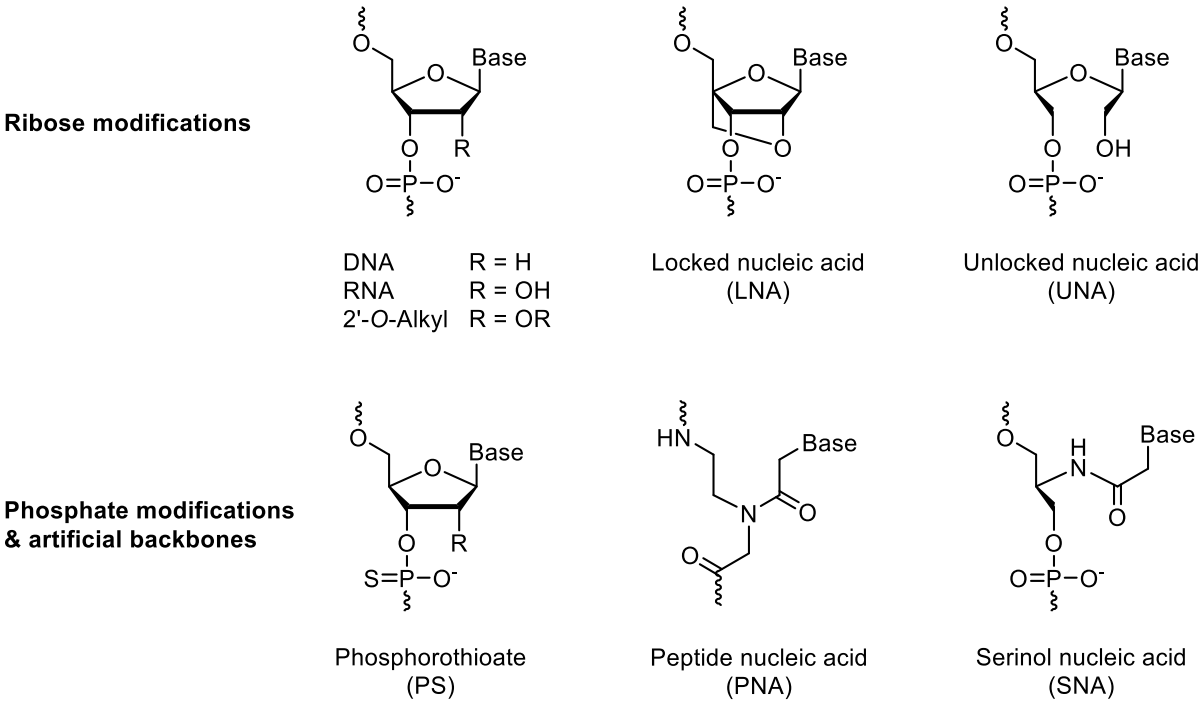

Figure 8: The chemical structure of DNA, RNA and a selection of different, chemically modified nucleic acid analogues.

One of the most common nucleic acid analogues is 2'-*O*-alkylated RNA. The substitution of the reactive 2'-hydroxy group greatly improves the hydrolytic stability of oligonucleotides and renders them more resistant against nucleases. It also slightly increases the binding affinity to complementary RNA strands by stabilizing the resulting A-type duplex.[96] This allows probes

against a specific oligonucleotide sequence to be shorter in length, improving their ability to discriminate between match and mismatch targets.[97] The most widely used 2'-modification is 2'-methoxy (2'-OMe) RNA, but variants with longer alkyl chains, such as 2'-methoxyethyl (MOE) RNA also exist. Oligonucleotides containing 2'-*O*-alkyl nucleotides can be either fully substituted or bear the modification only at certain key positions.[98]

A similar, more recent development is locked nucleic acid (LNA).[99-101] In this bicyclic RNA derivative, the ribose ring is constrained by connecting the 2'-oxygen and the 4'-carbon via a methylene bridge. This locks the molecule in the 3'-*endo* ribose conformation typical for A-type RNA duplexes, resulting in a local pre-organization of the phosphate backbone and a remarkable affinity increase. A single LNA modification can raise the melting temperature of an LNA/RNA heteroduplex by 2-10 °C.[100, 102, 103] Its strong binding is accompanied by an excellent sequence specificity: A single mismatch decreases the T_m of the heteroduplex by 17-22 °C for short LNA probes.[100, 104]. An acyclic counterpart to LNA is unlocked nucleic acid (UNA). Here, instead of increasing rigidity, the ribose ring is opened between C2' and C3', resulting in a much more flexible molecule. Depending on its position, incorporation of UNA into a sequence lowers its T_m by several degrees. Strategically placed, UNA can either increase binding specificity by reducing the thermal stability of mismatch duplexes or achieve the opposite and promote universal base behaviour.[105] LNA and UNA may be used in tandem to fine-tune the recognition properties and duplex characteristics of chimeric oligonucleotides.[106]

Modifications have not only been introduced in the ribose or nucleobase moieties, but also in the backbone of oligonucleotides. One of the first such nucleic acid analogues was phosphorothioate (PS) oligonucleotides.[107] Here, an oxygen atom of the phosphodiester internucleotide linkage is replaced with sulfur, creating a thiophosphate analogue. This can be achieved by replacing the oxidizer in the phosphoramidite synthetic cycle with a sulfurization agent, such as 3-(dimethylaminomethylidene)amino-3*H*-1,2,4-dithiazole-3-thione[108] (DDTT) or the Beaucage reagent.[109] PSOs have found particular application in the field of antisense oligonucleotides, as they possess increased resistance against endo- and exonucleases, while still being able to induce RNAse H-mediated cleavage of their target sequence. For fluorescent probes, PSOs are less suitable because they have somewhat lower duplex stability and tend to non-specifically bind to proteins.

As mentioned above, artificial, oligonucleotide-like molecules have been constructed using completely different, non-phosphodiester backbone structures. For example, Nielsen *et al.* developed a peptide-based analogue consisting of repeating, amide-linked *N*-(2-aminoethyl)-glycine units, to which the nucleobases are attached via methylene carbonyl linkers.[110, 111] Due to the considerable structural differences to regular nucleic acids, this so-called peptide nucleic acid (PNA) is no substrate for cellular enzymes and possesses excellent metabolic stability.[112] However, it is still able to strongly bind to complementary DNA or RNA sequences according to Watson-Crick base pairing.[113, 114] The lack of a negatively charged phosphate and thus electrostatic repulsion between the backbones greatly enhances duplex stability, but also brings about solubility issues and complicates cellular delivery. Enhanced uptake has been reported for PNA conjugated to cell-penetrating peptides,[115-117] complexed with a partially complementary carrier DNA[118] or modified with positively charged side chains,[119] but so far, no universal solution for this problem exists.[120]

A particular advantage of PNA over regular nucleic acids is its facile modification with artificial bases or fluorophores. Using coupling agents, carboxylic acid-bearing molecules can be attached to the secondary amine instead of a nucleobase, eliminating the need for a synthetically demanding modification of the ribose.[121-123] To realize the same level of synthetic flexibility in oligonucleotides with a phosphodiester backbone, serinol nucleic acid (SNA) was developed.[124] Structurally related to both DNA and PNA, this amino-alcohol-based nucleic acid analogue is created by linking the hydroxy groups of repeating L-2-amino-1,3-propanediol units with a phosphate, while the nucleobases (or suitable surrogates) are coupled to the primary amine via amide bond. Unlike PNA, SNA monomers can be incorporated into DNA or RNA sequences by phosphoramidite chemistry, allowing the preparation of chimeric oligonucleotides. Despite its increased flexibility, SNA forms heteroduplexes with RNA that are of higher stability than DNA/RNA ones and due to its negatively charged backbone, cell delivery by lipofection is possible.[125] The combination of these properties makes SNA a useful tool for the synthesis of internally modified oligonucleotide probes.[126, 127]

3.5 Fluorescence-Based Tools for RNA-Detection

3.5.1 Biological Methods

Qualitative and quantitative analysis of specific RNA sequences in cellular extracts can be performed by polymerase chain reaction (PCR), northern blot, or DNA microarrays, established techniques that offer high efficiency and low to very low detection thresholds.[128] Unfortunately, these methods require defined reaction conditions, which precludes a use in living cells and they can only provide a "snapshot" of the examined system with limited temporal resolution. Moreover, they are typically performed on bulk material obtained from the lysis of many cells, so no information about individual cells or cell-to-cell heterogeneity can be inferred.[129] Although techniques for single-cell real-time PCR exist, they typically involve complex experimental procedures and are prone to errors.[130, 131]

In order to study the subcellular localization of RNA and the spatio-temporal dynamics of its expression, processing, or transport, dedicated visualization tools had to be developed.[132-134] A majority of them are fluorescence-based, as this readout offers a highly sensitive, yet non-invasive detection, with a resolution down to the single molecule level.[135, 136] In general, RNA imaging methods can be classified into those that are able to detect endogenous, unmodified sequences and those that require a modification of their target.[134] The latter are often biological methods, which are based on the introduction of a sequence tag that acts as recognition site for RNA-binding proteins (RBP) or other reporters.[137] A popular example is the so-called MS2 system.[138] MS2 is a hairpin-forming sequence, originally discovered in the genome of the eponymous bacteriophage.[139] It specifically binds to the MS2 coat protein (MCP).[140] This interaction can be utilized for RNA detection: When an MS2 tag is genetically engineered into the 3'-untranslated region of an RNA sequence of interest, a fusion of MCP and an optical reporter, such as the green fluorescent protein (GFP), can be used for detection (**Figure 9A**).[141] Typically, multiple copies of the MS2 sequence are introduced to produce a local accumulation of GFP and create a signal above background. Another way to increase contrast is the use of a so-called bimolecular fluorescence complementation (BiFC) system (**Figure 9B)**.[142] Here, the reporter protein is split into two inactive halves, which are linked to different RBPs, such as MCP, the PP7 bacteriophage coat protein (PCP)[143], or two halves of the eukaryotic initiation factor 4A (eIF4A).[144] The target RNA is then modified with both binding sequences. Interaction of the probes with the target brings the two halves of the reporter together and they spontaneously fuse to form the active fluorophore.[145]

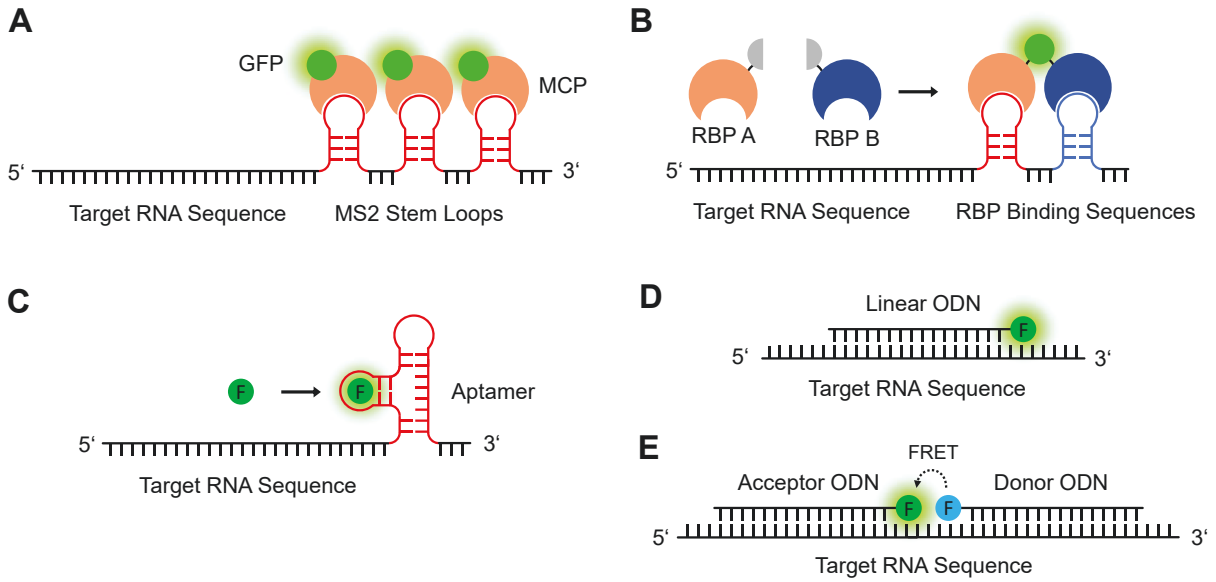

Figure 9: Fluorescence-based methods for RNA visualization. Genetically encoded reporter systems, such as (**A**) the hairpin forming MS2 tags, which can be detected by probes based on the MS2 coat protein (MCP) fused to a green fluorescent protein (GFP), or (**B**) light-up aptamers that bind and activate fluorogenic dyes, can be directly expressed together with the RNA of interest but require a prior genetic modification of the cell. (**C**) Detection of endogenous RNA sequences is possible with oligonucleotide-based hybridization probes, which are labelled with a fluorescent dye. (**D**) FRET probes are a more advanced version that uses a set of two probes labelled with dyes that create a FRET pair. As a signal is only generated upon hybridization, they have reduced background.

More recently, light-up aptamers have emerged as a powerful alternative for generating fluorescent RNA (**Figure 9C**).[146-148] The most prominent example is the *spinach* aptamer, a synthetically derived, 84 nt long RNA sequence designed to mimic GFP.[149] It was created by systematic evolution of ligands by exponential enrichment (SELEX)[150] and binds the fluorogenic dye 3,5-difluoro-4-hydroxybenzylidene imidazolinone (DFHBI),[151] a close relative of the GFP fluorophore.[152] The interaction with the aptamer increases the fluorescence emission of the dye by more than 1000-fold, creating a system with very high contrast.[147] Like MS2 tags, RNA aptamers can be genetically encoded in an RNA sequence of interest. In the past few years, several analogues of *spinach* with different emission characteristics have been developed, such as the green fluorescent *brokkoli*[153], the orange *mango*[154] and the yellow *corn*[155] aptamer. Another variant is the miniaturized *baby spinach*, which possesses the same fluorescence properties as the original *spinach* sequence, but is only half its size.[151] Very recently, Jäschke and co-workers reported a colour-shifting aptamer-dye complex based on benzopyrylium-coumarin hybrid fluorophores. These molecules exist in an equilibrium between a cyan fluorescent spirocyclic and a near-infrared fluorescent zwitterionic form. Their 38 nt aptamer selectively binds the latter, allowing the system to change its emission wavelength upon binding.[156]

Although biological RNA labelling methods are very effective, they typically require a genetic modification of their target (the exception being recently developed CRISPR/Cas9-based systems[157, 158]), which precludes a use in wildtype cells. Moreover, insertion of additional nucleotides into the sequence of interest or interaction with large, bulky proteins can influence RNA expression, transport, or function, which is often particularly problematic for short sequences.[159] To avoid these shortcomings, it is advantageous to use alternative methods that can detect endogenous, tag-free RNA. So-called hybridization probes, which are based on short, artificial oligonucleotides, meet this requirement. Due to their programmable nature, straight-forward synthesis, and amenability to chemical modifications, nucleic acids represent an ideal platform for the construction of molecular sensors.[129] One of the simplest oligonucleotide-based techniques for RNA visualization is fluorescence *in situ* hybridization (FISH).[160] Developed in the 1980s as a simpler and less hazardous alternative to radioactive *in situ* hybridization,[161] FISH utilizes fluorescently-tagged, linear oligonucleotides complementary to the RNA sequence of interest (**Figure 9D**).[162] The method is typically performed on fixed cells, which, following incubation with the probes, have to be washed several times in order to remove unbound molecules and reduce background. To increase sensitivity, sets of multiple probes can be used that all bind to the same target. For RNAs that are long enough (e.g. mRNA) this can be done with probes that cover the whole length of the sequence of interest, while for shorter ones, branched DNA scaffolds to which the probes can hybridize may be used together with a specific, interchangeable adaptor sequence for target recognition.[163-166] Singer and colleagues demonstrated that a set of ten FISH probes, each equipped with multiple Cy3 fluorophores, was sensitive enough to detect individual mRNA transcripts.[163] This strategy was later named single molecule FISH (smFISH). Raj *et al.* and many others have since improved the method, i.e. by introducing larger pools of up to 48 short, single labelled probes, computational image analysis and combinatorial labelling, allowing the multiplexed analysis of hundreds of RNA species.[167-172] Today, smFISH is considered a benchmark technique for the visualization of single RNA molecules and probe sets are commercially available under the brand names Stellaris™ probes[173] and RNAScope™.[174] Other important extensions of the FISH methodology include the pairing with immunohistochemistry (immunoFISH)[175-177] to detect interactions between nucleic acids and proteins or the combination with signal amplification methods such as hybridization chain reaction,[178] rolling circle amplification[179, 180] and enzyme-mediated reactions.[181, 182]

Although FISH has greatly contributed to our understanding of RNA, it suffers from a major drawback: To create a detectable signal, it relies on washing steps that separate probe-target complexes from excess probe. This makes the method time-consuming and restricts its application to fixed cells, which can only provide limited information about the real-time dynamics of intracellular RNA. Strategies to use FISH for live-cell imaging have been developed (using large probe sets to increase local signal intensity[183] or targeting RNAs that accumulate in specific compartments) but they usually suffer from high background.[184]

To successfully use oligonucleotide-based hybridization probes in living cells, it is crucial to improve contrast. A more advanced version of FISH uses linear FRET probes, which consist of a set of two oligonucleotides, one labelled with a donor fluorophore on its 3'-end, the other with a FRET acceptor on its 5'-end, or vice versa. (**Figure 9E**).[185] The probes hybridize to adjacent regions on the target sequence, bringing both dyes together to generate a FRET signal. FRET-based systems achieve higher signal-to-background ratios than regular FISH probes (up to 1:20), which allows them to be used in live-cell experiments.[133, 186] For example, Tsuji *et al.* demonstrated how a FRET-based probe could be used to detect the subcellular localization of mRNA expressed from a plasmid,[187] while Siuox *et al*. used a similar method to detect nucleic acid sequences that had been injected into a cell.[188] An additional benefit of FRET probes is their higher selectivity. Because two probes must hybridize to the target to generate a signal instead of only one, the probability for false-positive signals is reduced. Conversely, this also means that a longer stretch of secondary structure-free RNA is required as target.

FRET probes were an important improvement over simple, fluorescently tagged oligonucleotides, but they still have relatively high background due to unwanted direct excitation of the acceptor fluorophore or spectral bleed-through of the donor emission. This can interfere with measurements, particularly if the dye pairs are not carefully selected. To provide the highest sensitivity in live-cell RNA imaging, oligonucleotide probes should ideally be completely non-fluorescent in the unhybridized state and only light up when bound to their specific target. Multiple strategies to develop such hybridization-sensitive, fluorogenic probes have been pursued, the most important of which are presented below. A defining parameter that can be used to compare them is their fluorescence enhancement. It is calculated as the ratio of the fluorescence intensity of the bound (I) and unbound (I_0) state and describes how responsive a particular probe is.

3.5.2 Molecular Beacons

One of the most popular and widely used types of fluorogenic hybridization probes are *molecular beacons* (MBs). Developed by Tyagi and Kramer[189] in 1996, MBs are 20-30 nt long oligonucleotides that comprise a 15-25 nt long targeting sequence flanked by two 4-6 nt long, self-complementary regions. The 5' and 3' end are modified with a fluorescent dye and a quencher, respectively. In the absence of target RNA, MBs form a stem-loop structure (**Figure 10A**). In this inactive state, very little fluorescence is emitted due to the proximity (ca. 7-10 nm) of dye and quencher.[190] Upon hybridization, a conformational change is triggered that opens the structure and separates both labels, restoring fluorescence. This unique light-up mechanism provides MBs with high sensitivity and specificity: Well-designed probes can achieve fluorescence enhancements of up to 200-fold and are able to discriminate between sequences that differ in only one base.[191-193] Recent works have demonstrated that under certain circumstances, single-molecule detection is possible.[194] Because of their simple design and high efficacy, molecular beacons have found extensive application in live-cell RNA imaging[195-197] and real-time PCR,[192, 198, 199] and are today readily available from commercial suppliers with a wide range of quencher and dye choices.[200, 201]

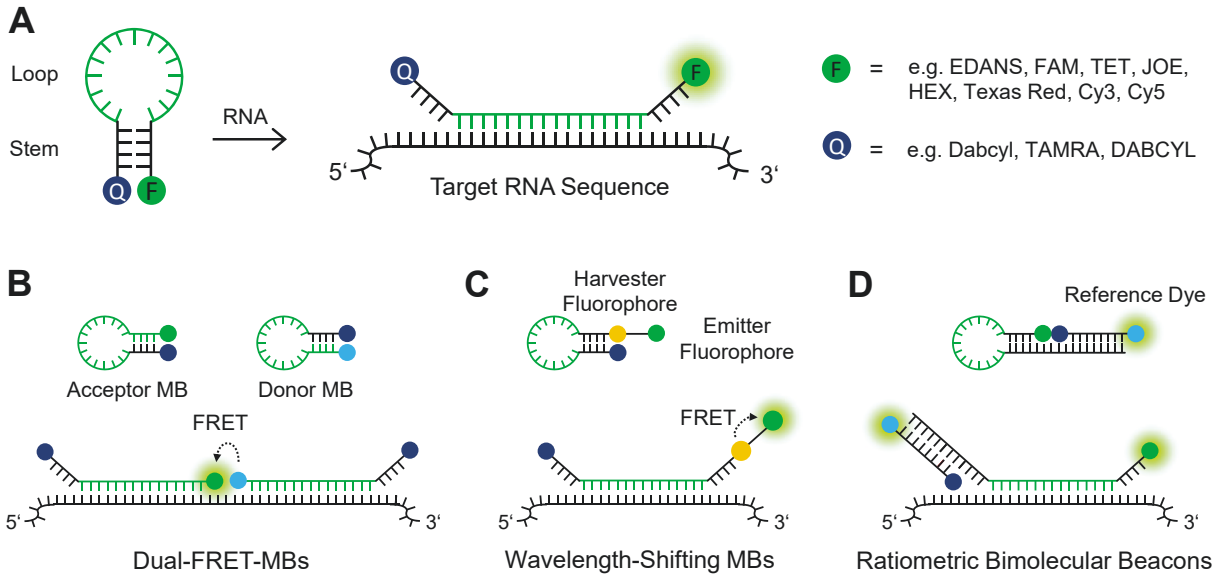

Figure 10: Structure and light-up mechanism of molecular beacons. (**A**) In the absence of target RNA, the molecular beacon forms a hairpin, which juxtaposes fluorophore (F) and quencher (Q). Hybridization of the loop to a target sequence, separates the two labels and fluorescence is restored. Extensions of the original concept include (**B**) FRET-based systems, (**C**) wavelength-shifting MBs and (**D**) ratiometric bimolecular beacons.

MBs are generally tolerant to modifications and researchers have exploited this to further improve their performance; not only with more effective fluorophores[189, 202] and additional quenchers,[191, 203, 204] but also with unnatural nucleic acid analogues and various other

extensions of the original concept. For example, it was quickly realized that the non-specific opening of the hairpin by cellular nucleases constitutes one of the major sources of high background in live-cell imaging.[205] To reduce such false-positive signals, metabolically stable MBs have been constructed from nuclease-resistant 2'-OMe-RNA,[206] PS-DNA,[207, 208] LNA,[209-211] SNA[126] or PNA.[212] Especially LNA-based probes proved highly resistant to enzymatic degradation, allowing a detection of target mRNA more than 24 hours after their introduction into a cell.[210] Other research groups have prepared fluorescent nucleotide analogues to create in-stem molecular beacons with increased fluorescence sensitivity.[213-215]

Enhanced specificity has been achieved with additional adaptor molecules that comprise an analyte and a beacon-binding portion (binary DNA probes)[216] or FRET-dependant systems. In so-called dual-FRET-MBs, two molecular beacons equipped with different fluorophores bind side-by-side to a complementary target sequence, generating a FRET signal upon hybridization (**Figure 10B**).[217] As the readout is not based on the emission of single MBs, this can drastically reduce non-specific signals, however it also requires a target sequence long enough to accommodate hybridization of both probes as well as a careful selection of suitable fluorophore pairs. Multiplexed measurements are possible with wavelength-shifting molecular beacons (**Figure 10C**).[218] Developed by Tyagi and co-workers, these probes fluoresce in different colours but can be excited by a single, monochromatic light source. To achieve this, they are equipped with a universal "harvester fluorophore" that absorbs the light and transfers the energy to different "emitter fluorophores" via FRET. Another, recent development are caged MBs, whose activity can be controlled by light[219] or application of a magnetic field.[220, 221]

Although MBs have proven to be a powerful tool for RNA detection, they suffer from several issues that may complicate their application in certain contexts. For example, there have been reports that upon introduction into a cell, MBs are rapidly sequestered into the nucleus.[222] This limits their ability to hybridize to target sequences that predominantly reside in the cytoplasm and reduces overall sensitivity. To mitigate this effect, MBs have been linked to transfer RNA (tRNA) transcripts[223] or double stranded siRNA mimics,[224] which are naturally exported from nucleus to cytosol or macromolecules too large to traverse the nuclear pores (e.g. streptavidin or nanoparticles).[205, 225] Although these strategies can improve cytoplasmic retention, they are not always practical, as the increased size may negatively affect MB delivery or activity. A second drawback is that MBs often require extensive optimization of their melting temperature, stem and loop size, as well as the distance between fluorophore and quencher to

provide an optimal response. Finally, even fully nuclease-resistant probes often still exhibit a relatively high degree of background fluorescence, due to insufficient quenching. This limits the sensitivity that can be achieved. One method that has been used to overcome non-specific background is ratiometric imaging.[226] By incorporating a second, optically distinct dye into the probe design (**Figure 10D**), the signal generated upon hybridization can be calibrated against this internal reference. Since relative instead of absolute fluorescence intensities are measured, the system is insensitive to concentration fluctuations and has a higher signal-to-background ratio. Using so-called ratiometric bimolecular beacons (RBMBs), Tsourkas and co-workers demonstrated visualization of the directed transport of individual mRNA transcripts in real-time.[205, 224, 227]

3.5.3 Light-Up Probes

As described in **Chapter 3.3**, asymmetric cyanine dyes of the thiazole orange family are extremely sensitive to restrictions of their torsional degrees of freedom and demonstrate markedly increased fluorescence quantum yields upon intercalation into double stranded DNA or RNA. In solution, these molecules are essentially non-fluorescent, but in complex with nucleic acids their brightness is increased by several orders of magnitude. This very good signal-to-noise ratio has prompted researches to use TO and its congeners to construct fluorogenic hybridization probes that do not rely on conformational changes of the oligonucleotide part.[70]

Early attempts by Svanvik *et al.* used PNA oligomers that were *N*-terminally modified with TO (**Figure 11**).[60, 228] A long, flexible linker allowed the dye to insert itself into the base stack of the duplex upon hybridization to the target sequence, leading to a detectable fluorescence increase of up to 50-fold. Owing to their good enhancement, these *Light-Up probes* have been successfully applied in PCR[229] and real-time PCR, as well as in a FRET-based approach for the analysis of RNA splicing.[230] Komiyama and co-workers used derivatives based on pseudo-complementary PNA (in which the nucleobases A and T were replaced with 2,6-diaminopurine and 2-thiouracil), to detect specific DNA sequences and induce site-specific photo-damage by generating singlet oxygen.[231]

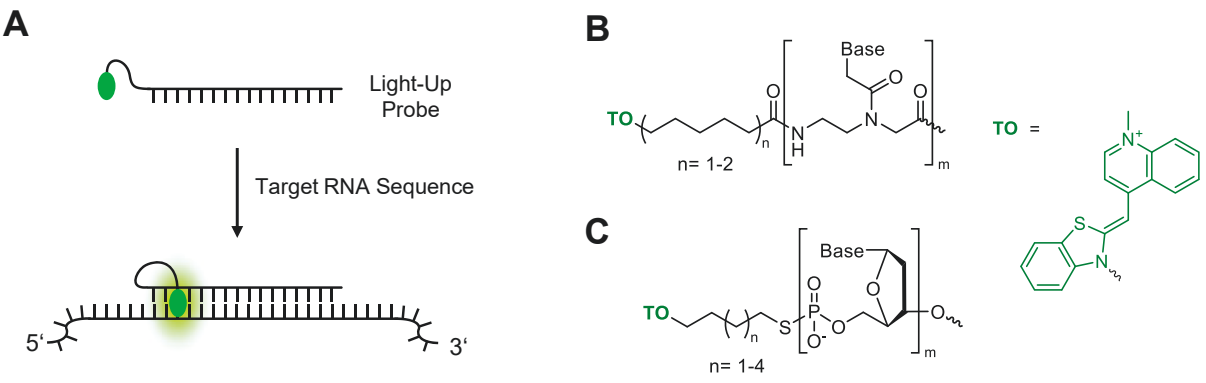

Figure 11: Schematic drawing of the Light-Up probe concept (**A**) Light up probes operate by intercalating thiazole orange (TO, green oval) into the duplex formed with the target sequence. (**B**) The chemical structure of the probes originally reported by Svanvik *et al.* and (**C**) Asseline *et al.*'s DNA analogue.

Like in their PNA-based congeners, the dye was appended to the probe via a flexible alkyl linker on their 3'-end or an internucleonic thiophosphate group (**Figure 11C**). Although Komiyamas group reported good discrimination between sequences that differed in only one base, they also observed that the fluorescence enhancement was strongly dependant on probe length, sequence context and the type of linker used, and careful optimization was required to obtain good results. They also tested different other cyanine dyes, but found their responsiveness to be inferior to TO.[232]

Despite these promising application examples, the background emission of Light-Up probes remained relatively high, as the fluorophore can also interact intramolecularly with the nucleobases of the PNA oligomer.[233] This explains why the observed enhancements were much lower than for unconjugated TO. Notably, there have been efforts to use alternative backbone structures to mitigate this problem. The group of Peter Dervan developed pyrrole-imidazole polyamide-based Light-Up probes that form triplex structures with specific sequences of dsDNA, despite lacking nucleobases.[234] Their system demonstrated a better signal-to-noise ratio and brightness enhancements close to the value of the free dye (>1000-fold).

3.5.4 Traffic Lights

Traffic light probes are a hybrid form of molecular beacons and TO-based probes, developed by Wagenknecht and co-workers.[235-237] For their creation, they incorporated two asymmetric cyanine dye base surrogates, a green-emitting thiazole orange and a red-emitting thiazole red (TR) into the stem of a hairpin-forming probe[238] (**Figure 13**) or an siRNA-like duplex[239]. Attachment of the fluorophores was achieved via an acyclic (*S*)-3-amino-1,2-propanediol linker,[238, 240, 241] or by "clicking" them to 2'-*O*-propargylated uridine derivatives.[242, 243]

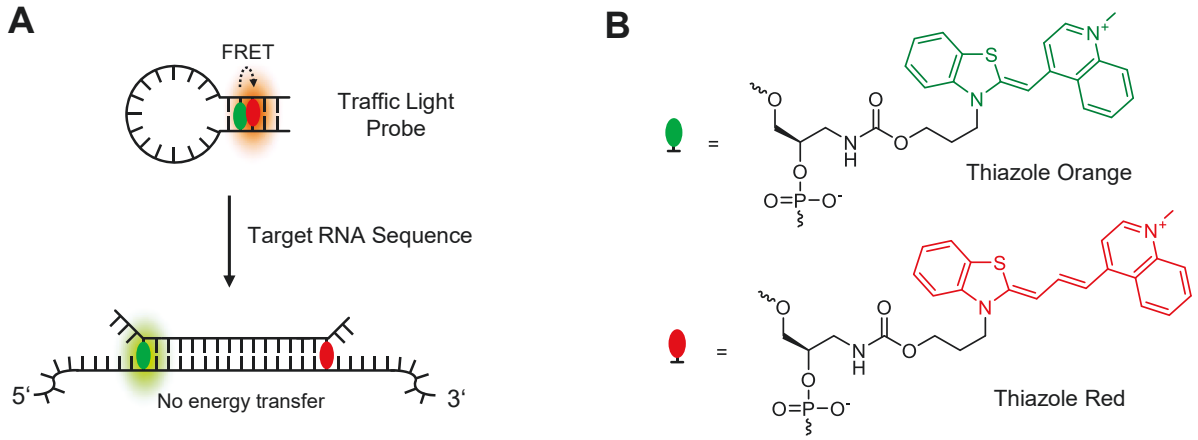

Figure 12: Schematic drawing of the Traffic Light probe concept. (**A**) Traffic lights change their emission wavelength upon binding to their target by separating a TO/TR FRET pair. (**B**) Chemical structure of the 3-amino-1,2-propanediol and 2'O-propargyl uridine base surrogates used to incorporate the dyes into the sequence.

Traffic lights function by switching their fluorescence emission wavelength from red (660 nm) to green (530 nm). In the unhybridized state, both fluorophores are situated diagonally opposite of each other and exitonic, excimer and energy transfer interactions between them shift the emission maximum of the probe to the longer wavelength (**Figure 13A**).[239] Upon recognition of the target sequence, the dye pair is separated and the green emission of TO is restored, while the intensity of the TR emission drops. This distinct colour change produces contrast ratios of up to 1:20 and can be detected in cuvettes as well as living cells.[239, 244] In comparison to single-wavelength readouts, this two-dye strategy offers the advantage of being more easily detectable against cellular background autofluorescence.

DNA traffic lights have been successfully used to monitor the uptake and integrity of siRNA, while still permitting knockdown of the target mRNA.[239, 245] More recently, the group of Wagenknecht has constructed a remarkable split aptamer traffic light, which, in addition to producing a fluorescence colour change, switches an attached nanomechanical DNA origami construct from an open to a closed state.[246] This topology change can be detected by atomic force or electron microscopy, adding an additional readout mode to the system.

3.5.5 ECHO Probes

As discussed earlier, the aggregation of multiple cyanine molecules can significantly alter their emissive properties due to excitonic coupling between the individual fluorophores.[50, 247] This was exploited by Okamoto and co-workers to improve the TO signal-to-noise ratio of their so-called *exciton-controlled hybridization-sensitive fluorescent oligonucleotide* (ECHO) probes.[248-250] Okamotos group modified a linear deoxy oligonucleotide sequence with a central uridine or cytidine residue, to which two TO molecules were attached via a long flexible linker (**Figure 13B**).[251-254] In the unhybridized state, the fluorophores interact with each other and form an H-aggregate, which leads to a blue-shifted absorption and a strongly attenuated emission. When the probe binds to a complementary target sequence, the dyes intercalate into the duplex, which disrupts the excitonic interaction and produces a significant increase of the TO fluorescence (**Figure 13A**). Using a 13-mer poly-dT probe, an emission intensity up to 160-fold higher than in the single strand was measured, although the obtainable enhancement proved strongly dependent on nucleotide composition and was typically much lower in mixed-base sequences.[255]

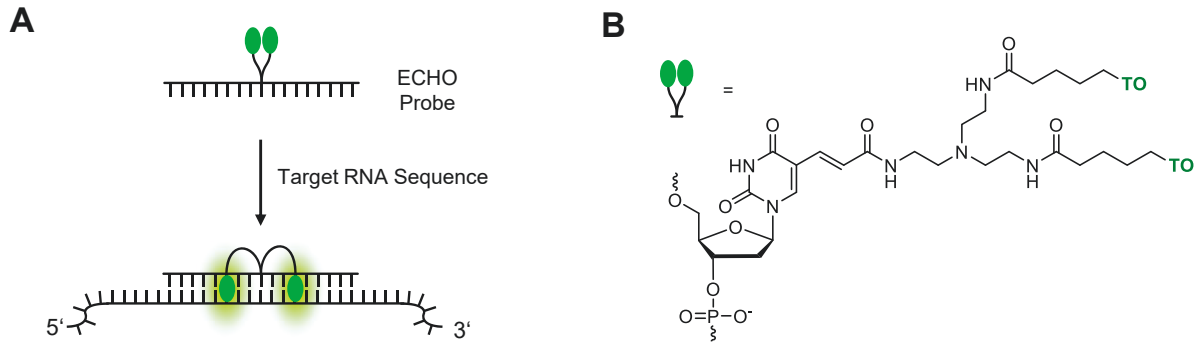

Figure 13: Schematic drawing of the ECHO probe concept. (**A**) ECHO probes reduce background fluorescence by promoting non-emissive H-aggregate formation between two TO molecules in the unhybridized state. Upon target recognition, the dyes intercalate separately into the duplex and fluorescence is restored. (**B**) Chemical structure of the central, fluorescently labelled nucleotide.

Since their conception, ECHO probes have been tested in a range of different applications.[250] Early live-cell studies targeting the polyA tail of mRNA showed that following microinjection into HeLa cells, fluorescence emission of hybridized ECHO probes could be detected in the cytoplasm and nucleus.[256] As DNA-based probes were rapidly digested by cellular enzymes, Kubota *et al.* designed 2'-OMe-RNA-based variants, which remained stable in the presence of an endonuclease for more than 12 h and could be successfully applied in a long-term imaging experiment with dividing HeLa cells.[255] In addition to providing improved stability, the 2'-OMe-modification positively influenced the fluorescence enhancement of the probes, mainly due

to a lower fluorescence in the single strand. To allow multiplexed measurements, Ikeda *et al.* developed ECHO probes modified with other fluorophores. By substituting TO with cyanine dyes based on different heterocycles, they created probes with emission maxima ranging from 455 to 677 nm.[257] A later publication added a dye that emits in the near-infrared (NIR) region (727 nm).[258] Using these new probes, the authors successfully demonstrated multicolour labelling of three different cellular microRNAs in microinjected HeLa cells. In another study, ECHO probes were applied in an *in vivo* experiment with live mice and chicks.[259] Following delivery by electroporation, lipofection or microinjection, three different types of RNA, 28*S* rRNA, small nucleolar RNA (snoRNA) U3 and poly(A) RNA could be independently visualized in nucleoli und nuclear speckles.

Numerous other applications and extensions of the original concept have been reported, such as pH-sensitive ECHO probes based on desmethyl thiazole orange,[260] photo-caged probes,[261] or a variant that contains an additional Cy5 fluorophore for a combined use with FRET.[262] Recent developments include the sensing of telomerase activity in live HeLa cells[263] and the transfer of the ECHO system into an aptamer format, which allowed quantification of bacterial rRNA.[264] Despite this long list of examples, ECHO probes have several shortcomings that have so far limited universal applicability: Aside from the aforementioned dependence of the quenching efficiency on sequence composition, they tend to non-specifically bind to dsDNA, due to the high affinity of dimeric TO for nucleic acids.[248] Moreover, to avoid high background arising from self-dimerization, careful optimization is required.[265] Another issue is that, by their design, ECHO probes do not discriminate well between matched and singly mismatched sequences, as even a partial hybridization can promote intercalation of the fluorophores.[252] This has been somewhat remedied by the introduction of LNA residues at select positions, but the overall selectivity remains low.[266]

3.5.6 FIT Probes

The research group of Oliver Seitz developed so-called *forced intercalation* (FIT) probes. Here, a single TO fluorophore is introduced into the sequence of a PNA oligomer to act as a base surrogate.[267-270] When the probe hybridizes to its target sequence, the dye is forced into the duplex, which restricts its rotation around the methylene bridge and turns on fluorescence (**Figure 14A**).[68] In contrast to Light-Up probes, the intercalation occurs at a predetermined location, providing a higher level of control. As the strength of the emission directly depends on the level of constraint provided by the immediate environment of the dye, the system is highly sensitive to mismatches near the intercalation site. Local misalignments provide the fluorophore with more torsional space, thereby increasing its quantum yield. For fully complementary sequences, enhancement factors of 20- to 30-fold have been reported, while the fluorescence increase was up to five times weaker when a local mismatch was present.[271] Köhler *et al.* found that the ability of FIT probes to discriminate between single nucleotide variants strongly depends on the type of linkage between fluorophore and aminoethyl glycine backbone: Attachment via a short carboxymethyl linker tethered to the quinoline nitrogen (**Figure 14B**) provided much better responsiveness than the use of longer linkers or a connection through the benzothiazole ring.[272]

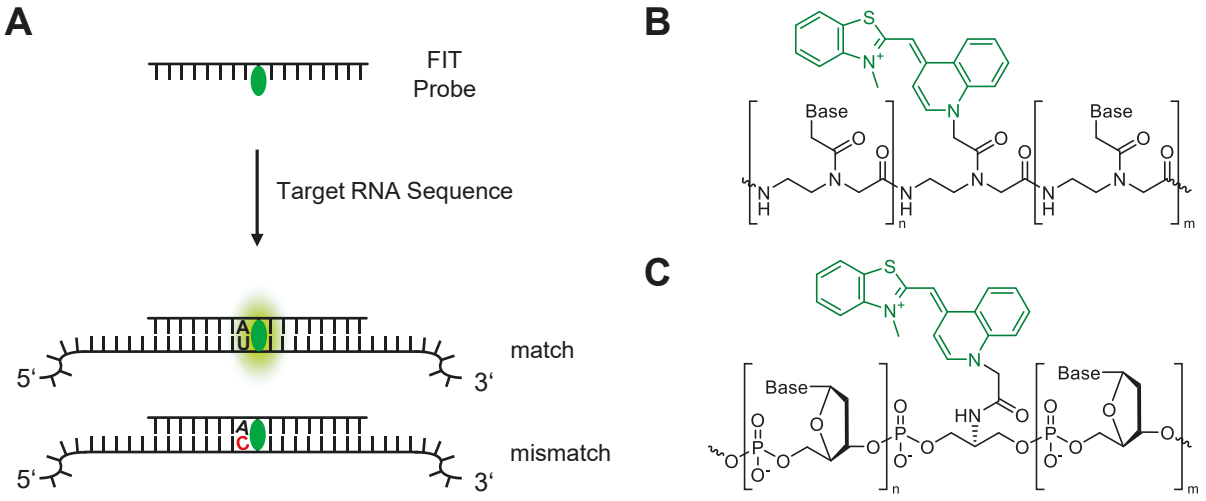

Figure 14: Schematic drawing of the FIT probe concept. (**A**) FIT probes turn on fluorescence by forcing TO into the duplex formed with the target probe. As the dye is sensitive to the level of constraint provided by its immediate surroundings, these probes are highly sensitive to local misalignments. Chemical structure of (**B**) PNA- and (**C**) DNA-based TO FIT probes.

Owing to their high sequence specificity, PNA FIT probes have been successfully used in single-nucleotide-specific genotyping by real-time and quantitative PCR.[273-276] However, excellent biological stability also makes them suitable for live-cell imaging. Kummer *et al.* were the first to show that FIT probes can be used to detect viral RNA inside living, H1N1-infected cells.[277]

Delivery was achieved by reversible permeabilization with the pore-forming exotoxin Streptolysin O.[278] To improve solubility, the probes were *N*-terminally modified with a PEGylated lysine. Infected cells that were treated with FIT probe fluoresced up to 4.5-times more strongly than non-infected ones, a signal-to noise ratio superior to that of a molecular beacon included in the experiment for comparison. In a later publication, the concept was extended with an additional benzothiazole orange (BO)-labelled probe to allow simultaneous multicolour imaging of two different viral targets.[276] Since these original works by Seitz and co-workers, other researchers have adopted the FIT concept and applied it to the detection of various targets, including mRNA,[279-282] dsRNA,[283, 284] miRNA[285, 286] and lncRNA, [282, 287] in solution and in cells.[288] Notably, Kam *et al.* were the first to successfully demonstrate the ability of PNA FIT probes to discriminate between two variants of a KRAS mRNA inside living cells, with single nucleotide resolution.[279] Like in the study by Kummer *et al.*, delivery proved to be a key issue. To transport their probes into cells, Kam *et al.* annealed them to a partially complementary DNA sequence and complexed the resulting duplex with the transfection agent polyethyleneimine. The resulting lipid nanoparticles could then be used for lipofection. Wickstrom and co-workers employed a different strategy: To achieve cell-type specific delivery, they linked FIT probes to an insulin-like growth factor (IGF-1) tetrapeptide.[280] These conjugates were actively taken up by IGF1 receptor-overexpressing lung cancer cells through receptor-mediated endocytosis and allowed mismatch-specific detection of KRAS mRNA. Finally, the groups of Gait and Yavin modified PNA FIT probes with positively charged amino acids and cell penetrating peptides, respectively, to detect mRNA and non-coding RNAs in living cells and tissues.[281, 282, 285, 287]

Despite their high biological stability and simple chemical modification, PNA-based suffer from several potential drawbacks. Because their backbone is relatively hydrophobic, they are less water-soluble than phosphate-based oligonucleotides and have a tendency for self-aggregation.[110] Moreover, PNAs lack of charge renders them incompatible with established transfection methods such as lipofection. Instead, PNA-based probes require other techniques that often have to be extensively optimized.[120] Finally, the preparation of PNA is more expensive and time-consuming than conventional phosphoramidite oligonucleotide synthesis. These issues have prompted Seitz and co-workers to develop DNA-based FIT probes.[289] An important consideration was how backbone and fluorophore are connected to provide high responsiveness and cause minimal distortion of the nucleotide structure. Due to the high lability of TO-*N* glycosides, a direct, isosteric attachment was not feasible. Instead, several backbones based

on carbocyclic and open-chain ribose analogues were screened and it was found that the highest enhancement (up to 12-fold) is achieved with TO linked to L-serinol via a short carboxymethyl spacer (**Figure 14C**).[289, 290] This attachment proved rigid enough to reduce background fluorescence from unwanted intramolecular interactions in the single strand, while still allowing the dye to intercalate into the duplex formed with the target RNA. Using DNA FIT probes modified with L-serinol-linked TO or BO, Hövelmann *et al.* demonstrated the detection of viral mRNA in cell culture medium as well as in a qPCR-based analysis.[290] Nuclease-resistant DNA FIT probes based on 2'-OMe-RNA or LNA have also been used for live-cell imaging.[291-296] Chamiolo *et al.* directly compared CPP-conjugated PNA and DNA FIT probes for multicolour imaging of three different mRNAs expressed by a genetically engineered HEK293 cell line and found the latter to provide higher fluorescence intensity and responsiveness.[297] Recently, alternative attachment modes for TO via the sugar or nucleobase moieties of a modified thymine nucleotide have been proposed by the Brown group that have also resulted in highly responsive probes.[298]

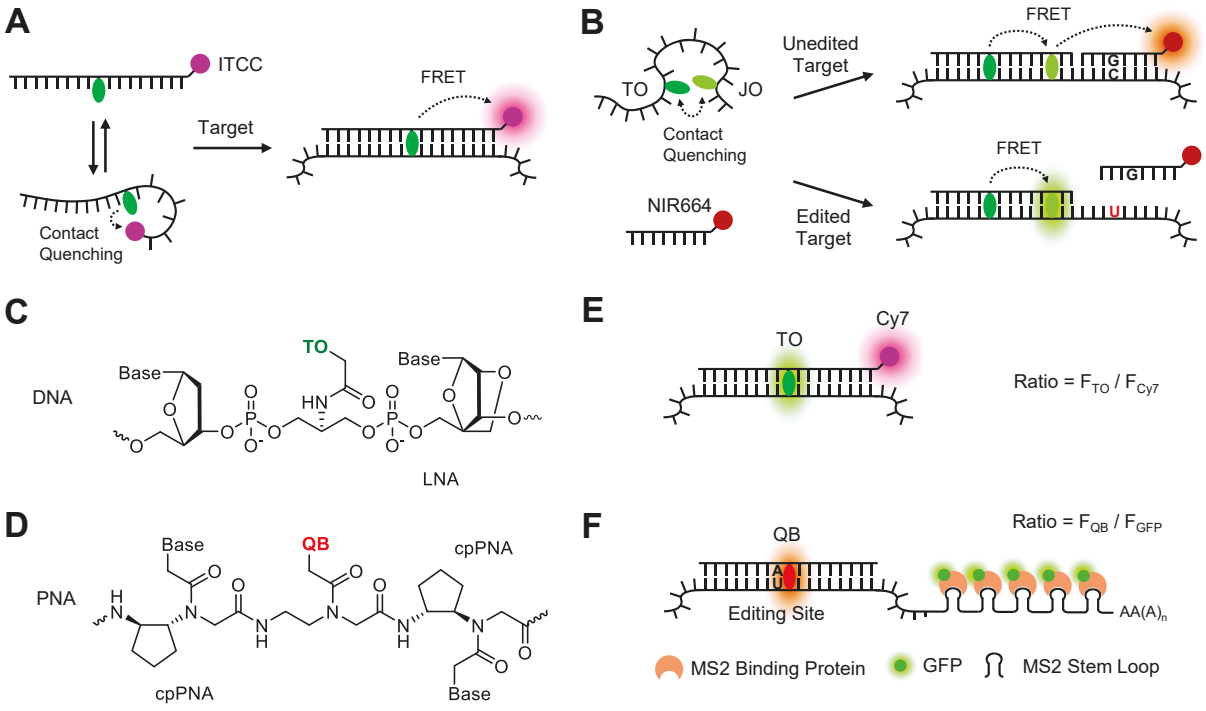

Figure 15: Extensions of the original FIT probe concept. (**A**) Addition of a FRET acceptor to the C-terminus of PNA FIT probes reduces single strand emission via collisional quenching and creates a FRET signal upon hybridization. (**B**) TO can also be combined with the highly emissive, but less responsive cyanine dye JO to create bright probes with good enhancement. Fang *et al.* combined this concept with a second, single nucleotide-specific NIR664 probe to study GlyR mRNA editing. Probe brightness can also be enhanced by introducing high affinity (**C**) LNA (DNA-FIT probes) or (**D**) cpPNA (PNA FIT probes) units next to the dye, which rigidify the duplex at the intercalation site and increase TO emission. In cell experiments where probe distribution is not homogenous, ratiometric approaches can help to map FIT probe fluorescence intensity to its hybridization state. A suitable reference signal can be generated by (**E**) an additional hybridization-insensitive reporter like Cy7, linked to the FIT probe, or (**F**) a biological reporter like the MS2-GFP system.

In addition to the examples presented above, several extensions of the FIT probe concept have been developed with the aim of further improving the signal-to-noise-ratio. For so-called stemless molecular beacons, Socher *et al*. appended a second reporter dye to the C-terminal end of a PNA FIT probe (**Figure 15A**).[274] This design drastically reduced background emission in the single strand by promoting collisional quenching between the two fluorophores. Hybridization to the target sequence disrupts the direct dye-dye interaction and activates TO fluorescence or alternatively switches the energy transfer mechanism to FRET. A screening of different acceptor dyes revealed that hydrophobic and polarizable acceptor dyes that possess little spectral overlap with TO provide greater responsiveness, with the heptamethine cyanine dye ITCC resulting in a remarkable enhancement of up to 450-fold.[299] However, it has to be mentioned that the responsiveness of these probes was largely dependent on the sequence context. A similar use of FRET to enhance DNA FIT probe performance was reported by Hövelmann *et al*.[291] They constructed dual-labelled probes equipped with TO and the spectrally overlapping oxazolopyridine analogue JO. Owing to a large extinction coefficient and high quantum yield ($\varepsilon_{max} \approx 110\,000\ L \cdot mol^{-1} \cdot cm^{-1}$; $\phi_{max} \approx 0.8$), JO is much brighter than TO, but less responsive.[122] In the single strand these probes are dark, due to contact-mediated quenching between TO and JO. Upon target recognition, the fluorophores are separated, and a FRET signal is generated. Hereby, TO acts as a light collector that transfers its excitation energy to JO. The combination of a highly responsive (TO) and a highly emissive (JO) cyanine dye resulted in very bright probes (up to 43 $mol^{-1} \cdot cm^{-1}$ at λ_{ex}= 516 nm) with increased enhancement (E>12) compared to mono TO-labelled sequences.

Recently, Fang *et al.* presented a modification of this concept for the detection of C-to-U edited glycine receptor (GlyR) mRNA.[300] In an approach that resembles dual-FRET-molecular beacons, they constructed a binary system consisting of two PNA sequences; one dual-labelled with TO/JO, the other equipped with the near-infrared FRET acceptor NIR664. Both probes were designed to bind to adjacent sites on GlyR mRNA, with the NIR acceptor probe being specific for the unedited target (**Figure 15B**). FRET transfer to NIR664 can only occur when both probes are bound, potentially allowing the system to distinguish between three states: absence of target (low overall emission) and presence of unedited (high JO emission) or edited target (high NIR664 emission). For TO/JO probes with an optimal distance of 4 to 5 nucleotides between the fluorophores, an enhancement factor of 30 was reported. Interestingly, when an abasic *N*-(2-aminoethyl)glycine (aeg) building block was placed next to JO, the value could be

further increased to 38-fold. This was explained with a facilitated interaction between the dyes in the single strand, allowing more effective quenching. In the NIR664 channel, a maximum FRET efficiency increase of 14 was determined. The authors used this system to image GlyR mRNA in fixed and live HEK293T cells.

Although the responsiveness of a probe is crucial for its good signal-to-noise ratio, its absolute brightness can be a limiting factor when low-abundance RNAs are targeted or cellular autofluorescence is high. A simple, yet effective strategy to increase the emission of DNA FIT probes was developed by Hövelmann *et al*.[292] They hypothesized that the rigidifying effect LNA monomers on DNA:RNA duplexes could decrease the helical rise per base pair and thus increase the local constraint experienced by the fluorophore.[102, 301-304] Indeed, incorporation of a single LNA unit next to the dye significantly improved FIT probe quantum yield, depending on the position by 30-187 %. It also increased TO absorbance (up to ε = 98 000 $M^{-1} \cdot cm^{-1}$), which was rationalized with the hypothesis that the enforced stacking may promote ground-state interactions between the fluorophore and neighbouring nucleobases. Together, both effects caused an increase in overall brightness by up to 107 %. Although the "LNA effect" affects both single and double strand, the responsiveness of the probes remained the same, given that only one LNA unit was present. In his bachelor's thesis, Simon Bartsch tried to transfer the same principle to PNA-based FIT probes.[305, 306] Instead of LNA, he used cyclopentane-modified PNA (cpPNA) monomers, which were placed next to the fluorophore. Originally developed by Appella and co-workers,[307-310] these constrained building blocks have extremely high affinity for DNA or RNA and can increase the T_m of a corresponding duplex by 5-10 °C per unit. Although this modification did improve the brightness of his probes, it also reduced their overall responsiveness, as the intensity gain in the single strand was greater than in the double strand. Very recently, however, Tepper *et al.* reported PNA FIT probes bearing the same cpPNA modification that exhibited both increased brightness and responsiveness and could discriminate between certain pyrimidine–pyrimidine mismatches.[311]

Early after the conception of the FIT probe concept, there have been attempts to expand it with other fluorophores (**Figure 16**), including the asymmetric cyanine dyes oxazole yellow (YO), thiazolopyridine (MO), and oxazolopyridine (JO).[122, 276] Although some of these molecules are very bright (e.g. JO), none of them reached the responsiveness of TO. Recently, Seitz and co-workers identified a 4,4'-linked bisquinoline derivative, with a large extinction coefficient (ε = 129 000 $L \cdot mol^{-1} \cdot cm^{-1}$) and high fluorescence quantum yield (ϕ = 0.47).[293]

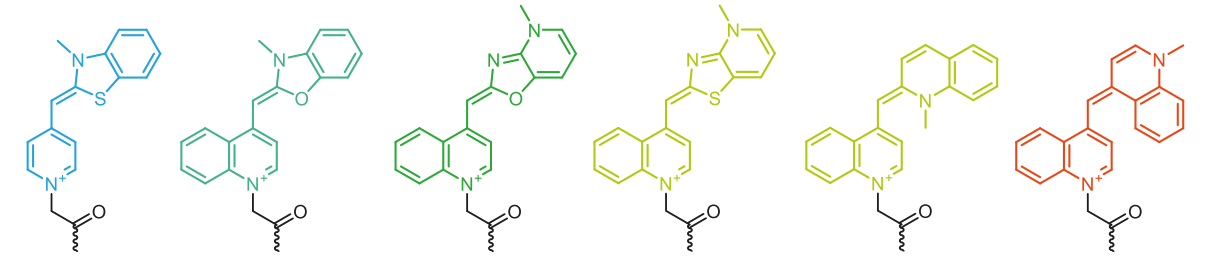

Benzothiazole Orange (BO)	Oxazole Yellow (YO)	Oxazolopyridine (JO)	Thiazolopyridine (MO)	Quinoline Violet (QV)	Quinoline Blue (QB)
λ_{Ex} = 440 nm	λ_{Ex} = 491 nm	λ_{Ex} = 494 nm	λ_{Ex} = 517 nm	λ_{Ex} = 530 nm	λ_{Ex} = 560 nm
λ_{Em} = 485 nm	λ_{Em} = 509 nm	λ_{Em} = 521 nm	λ_{Em} = 570 nm	λ_{Em} = 570 nm	λ_{Em} = 610 nm

Figure 16: Alternative FIT probe dyes of the thiazole orange family with their excitation and emission maxima.

This dye, which was named quinoline blue (QB), proved exceptionally responsive, providing enhancement factors of up to 195-fold when incorporated into DNA FIT probes. Its red emission (λ_{Em} = 605 nm) is orthogonal to TO's, which allowed Hövelmann *et al.* to use this new derivative for a simultaneous visualization of two different mRNAs in developing *D. melanogaster* oocytes.[281, 282, 293] Shortly after, Yavin and co-workers introduced the same dye into PNA FIT probes.[281, 282, 312] Building up on these works, Loibl *et al.* demonstrated how two orthogonally labelled TO and QB PNA FIT probes can be used to monitor miRNA-21 processing by DICER and loading of the mature miRNA fragments into the RNA-induced silencing complex (RISC).[286] Like TO, QB benefits greatly form an adjacent LNA residues, which can improve its brightness by or 3-4 (from 13-16 to 55-58 $L \cdot mmol^{-1} \cdot cm^{-1}$).[293] Using LNA-enhanced QB DNA FIT probes, Haralampiev *et al.* demonstrated selective and sensitive detection of influenza virus A infection in different host cells.[294]

A remaining challenge for the application of FIT probes in biological systems is to correlate signal intensity and hybridization state. Differences in delivery efficiency and subcellular localization can result in an uneven distribution of the probes within cells and greatly affect the background signal. Using intensity-based signalling only, it is not possible to distinguish between high local concentrations of unbound probe and low concentrations of bound probe. To address this issue, two strategies have been proposed by the Seitz group. Inspired by ratiometric bimolecular beacons (RBMBs) and a recently reported FISH-based approach for the detection of A-to-I editing,[313] Gaspar *et al.* devised quantitative FIT (qFIT) probes that combine a regular FIT probe with a non-responsive fluorophore that serves as concentration reporter (**Figure 15E**).[295] This enables the system to convey information about both the hybridization state and the local probe concentration. The ratio between the emission of both dyes can be used to determine a background-corrected enhancement of the probe at any given location.

An important prerequisite for this approach is a concentration reporter that is both non-responsive and does not quench TO emission by energy transfer or ground state interactions. The authors selected the near-infrared dye cyanine 7 (Cy7), which has very little spectral overlap with TO and is positively charged, a feature that was thought to help reduce dye-dye contacts with the likewise charged TO. Cy7 was appended to the 5'-end via a short azide-alkyne linker to minimize possible interactions. To their surprise, weak FRET still occurred between the dyes in the single strand, but this effect did in fact help to lower background emission. When the distance between both fluorophores was sufficiently large (≥18 nt) in the double strand, TO brightness remained unaffected. Most importantly, the Cy7 channel showed independent emission. Using a combination of three qFIT probes with enhancement factors of up to 16.5, the authors localized and quantified *oskar* mRNA in Drosophila oocytes with a detection limit of about nine copies within 0.075 μm^{-3} (ca. 200 nM).

Another second possibility for ratiometric signal quantification is use of FIT probes in combination with a biological reporter. For a recent study of GlyR mRNA C-to-U editing, Knoll *et al.* introduced two different MS2-tagged GlyR mRNAs into HEK cells and used QB DNA FIT probes to distinguish their editing states (**Figure 15F**).[296] The GFP emission generated by the tagged RNA served as a guide signal to direct the analysis to target-containing areas within the cells. The local ratio of TO and GFP fluorescence was used to determine if edited or unedited target was present. For their system, Knoll *et al.* screened three different FIT probes and found that the most specific one produced an up to 12-fold higher signal ratio in cells expressing the edited versus the unedited mRNA. Despite this high selectivity, the absolute brightness of the probe was rather low (4.3 $L \cdot mol^{-1} \cdot cm^{-1}$) and it was difficult to distinguish the match and mismatch case visually. Instead, the respective fluorescence intensities of QB and GFP were determined pixel-wise, using line scan measurements through target-containing areas of the cell. The obtained ratio distributions were then compared between cell populations.

With the qFIT probes and the chemo-biological FIT-MS2 approach, Seitz and co-workers introduced two strategies to better correlate FIT probe signal intensity and hybridization state. Although these methods have been successfully applied in two studies, the absolute brightness of the respective probes remains a limiting factor. To achieve a stronger signal and lower limit of detection, probes that combine high brightness and specificity would be highly desirable.

4 Aims of the Thesis

FIT probes have proven a powerful tool for RNA detection *in vitro* and in living cells. Nevertheless, their performance could be further improved by increasing brightness and reducing background emission, lowering their limit of detection. Previously, it was tried to achieve this by incorporating quencher molecules into the probe design or combining dyes with different fluorescence properties to create FRET pairs. Although these efforts were largely successful, adding another dye molecule complicates the synthesis of such probes and makes it considerably more time-consuming, as an additional custom-made base surrogate is required. Moreover, optimization of such probes is complex, as different dyes might have different requirements regarding their optimal microenvironment. Most importantly, these approaches often only offer a partial solution: Quenchers can only improve the signal-to-background ratio, not the absolute fluorescence output of a probe. And although FRET-pairs can somewhat improve brightness (for example by exploiting the increased emission properties of dyes like JO), this approach is ultimately limited by the maximum efficiency of the required resonance energy transfer, which reduces the effective quantum yield of these probes.

In this work it should be investigated whether an increase in probe performance could instead be achieved by combining two fluorophores of the same type (hereinafter referred to as the FIT^2 approach). Due to a partial overlap of their respective absorption and emission spectra, thiazole orange and quinoline blue are capable of homo-FRET, allowing them to transfer excitation energy between two dye molecules. If one is in an environment where rotation around the methine bridge is possible, for example when a mismatch is present near the intercalation site, energy transfer may also quench the fluorescence of the other. At the same time both dyes will experience a fluorescence increase when the probe is hybridized to a matched target, as the rotation of both fluorophores is equally restricted by the duplex (**Figure 17**). It was thought that together, both effects could increase brightness and specificity of the probes. Additionally, the background fluorescence in the single strand may be decreased due to contact-mediated quenching, as observed in previous approaches with two different dyes. This would improve the signal-to-background ratio.

In order to find the optimal probe design for the FIT^2 approach, different dye-dye distances and 5'-extension lengths should be evaluated. For this, TO and QB probes specific for unedited (UE) or C-to-U edited (ED) glycine receptor (GlyR) mRNA should be synthesized. As in previous

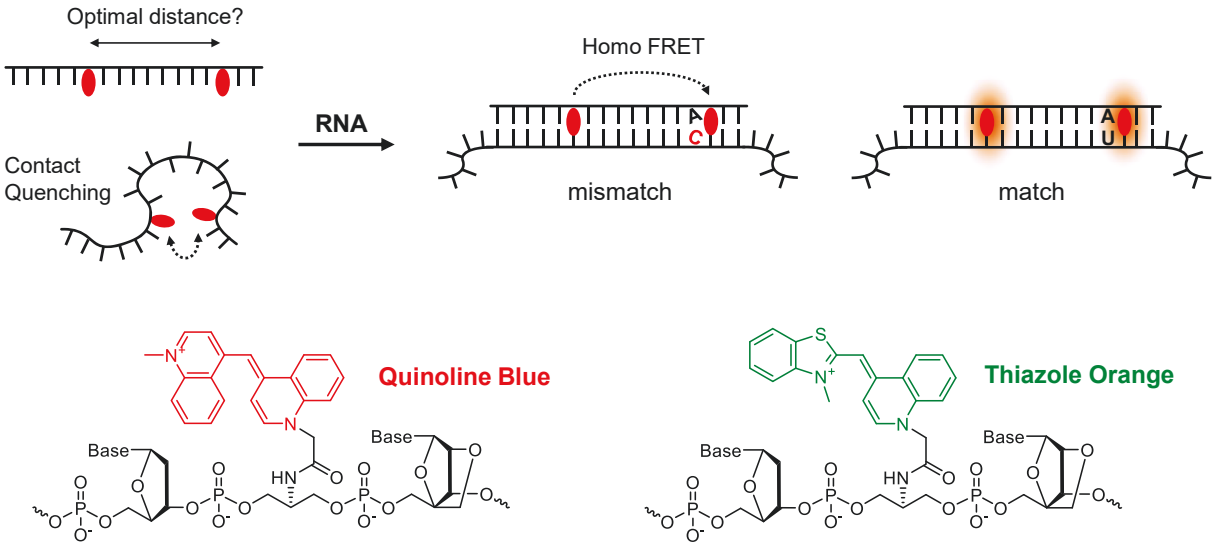

Figure 17: Concept for dual dye FIT^2 probes with increased brightness and reduced background emission. Probes are equipped with either two thiazole orange or two quinoline blue dyes. At an optimal dye-dye spacing, homo-FRET may lower emission in the duplex with mismatched target, whereas increased fluorescence output is achieved in the match state. In the single strand, contact-mediated quenching reduces background fluorescence.

reports, LNA monomers should be placed adjacent to the dyes to increase local constraint and improve fluorescence output in the duplex. The probes should be compared to mono-dye controls, to detect potential differences in their emission and specificity for matched or mismatched RNA target. Ultimately a system should be created that combines two suitable UE- and ED-FIT^2 probes equipped with different dyes for a simultaneous detection of edited and unedited GlyR mRNA in two separate channels. In preparation for biological experiments, the FIT^2 design should also be transferred to nuclease-resistant 2'OMe-based probes.

As the duplex stability of 2'-modified nucleic acids is higher than that of regular DNA (a property known to negatively influence probe performance), the screening should be repeated, and the results compared with the previous experiments. The best probe designs should be tested in a biological environment represented by buffer containing different concentrations of cell lysate. Finally, the FIT^2 concept should also be combined with a system for a ratiometric quantification of fluorescence emission. For this "qFIT^2" approach, a Cy7 fluorophore should be appended to the 3'-end of TO^2 probes (**Figure 18**) to allow calculation of a TO/Cy7 ratio, which may help to improve discrimination between target-bound and single strand probes. Building up on previous work by Jasmine Chamiolo,[305] qFIT^2 probes complementary to T-cell receptor mRNA of two different cell lines should be prepared, allowing a potential later application in FACS-based sorting of different T-cell populations. Again, different TO-TO, as well as TO-Cy7 distances should be evaluated. Finally, the influence on different LNA monomer positions should be assessed.

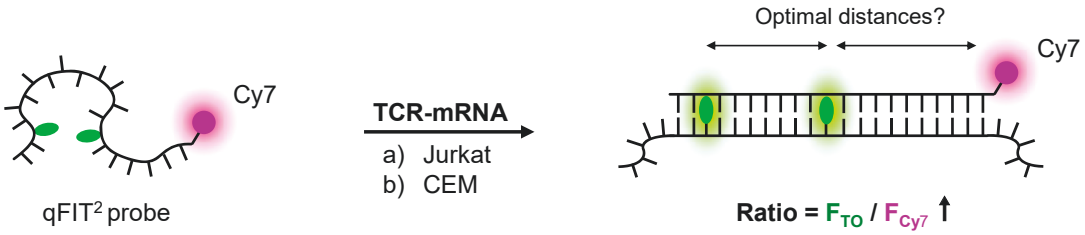

Figure 18: Combination of the dual dye FIT^2 approach with the qFIT concept. Appending an additional, hybridization-insensitive Cy7 dye to the 3'-end of the probes should allow background correction through ratiometric signal quantification.

To apply the concept to live-cell experiments, a transfection method, capable of delivering the qFIT^2 probes to two different T-lymphocyte cell lines should be searched and optimised. After successful development of a transfection protocol, both cell lines should be transfected with the same qFIT^2 probe and analysed via fluorescence microscopy. Thereafter, the ratiometric data of the experiment should be analysed with a suitable method to determine if a discrimination between the two cell lines is possible.

5 Result and Discussion

In previous works, the research group of Oliver Seitz developed FIT probes for the visualisation of biological mRNA targets and demonstrated their versatile application in test tube as well as in live-cell experiments.[122, 258, 276, 292, 293, 314-321] However, despite good fluorescence enhancement, FIT probe performance is limited by the maximum achievable brightness, target specificity and signal-to-background ratio. To improve upon the existing design, this work aimed to explore a new concept in which FIT probes are equipped with a second fluorophore of the same type. These so-called FIT^2 probes were evaluated in two different application scenarios: the detection of GlyR mRNA C-to-U editing (**Chapter 5.1**) and recognition of the CDR3 (complementarity determining region) of two different T-cell receptor mRNAs (**Chapter 5.2**).

5.1 RNA FIT Probes for Visualization of mRNA C- to U-Editing

In mammals, two types of RNA single nucleotide sequence-alterations are known to exist: A-to-I and C-to-U editing. These post-transcriptional modifications can have significant impact on the final gene product and are often associated with disease. For example, C-to-U-editing has been linked to the progression of temporal lobe epilepsy (TLE). So far methods that allow a direct tracking of the spatiotemporal occurrence and immediate consequences of this process are still lacking. The visualisation of mRNA editing is no trivial task because it asks for probes that allow a simultaneous detection of the edited and unedited state of the target and single nucleotide alterations must be resolved. Recently, the research group of Oliver Seitz introduced DNA-based FIT probes that generate a fluorescence signal upon hybridization to GlyR mRNA (**Figure 14**).[322, 323] Early DNA FIT probe experiments were conducted by Felix Hövelmann.[324] In his dissertation, he presented a short study on the optimal positioning of the dye adjacent to the editing site. His screening gave valuable insight into how FIT probes should be designed to create bright, yet responsive and specific tools. Two types of fluorophores proved especially suitable, the asymmetric cyanine thiazole orange and the symmetric quinoline blue (**Figure 19**). Both dyes are spectroscopically independent and may be excited individually in the presence of the other. A system that combines both fluorophores might therefore allow the simultaneous detection of edited and unedited GlyR mRNA in two separate channels. For this purpose, probe sets based on both dyes were prepared in this work and screened with regards to their fluorescence properties and melting characteristics. As a set of nuclease-resistant QB-based 2'OMe-RNA FIT probes had recently been created by Andrea Knoll *et al.*,[316]

a matching TO-based was prepared first. These mono-dye FIT probes should be evaluated and later compared to dual-dye FIT[2] probes specific for the same target.

All probes were synthesized by solid phase oligonucleotide synthesis (see **Chapter 3.4**) on CPG solid support. The fluorophores were introduced as custom made serinol phosphoramidites, which were prepared according to a procedure previously described by Hövelmann *et al.* (see **Figure 19**).[293, 323] For this, *N*-methyl-4-chlorquinoline **1a** or 2-methylbenzothiazole **1b** were methylated with methyl iodide and subsequently reacted with *N*-carboxymethyl-4-methquinolinium bromide in the presence of triethylamine, to form the corresponding cyanines **2a** and **2b**. The carboxymethyl-modified dyes were then coupled to a DMT- and TBDS-protected serinol linker **3** (prepared from L-serine, according to a procedure described by Bethge *et al.*)[289, 325] using PyBOP and pyridinium *p*-toluene sulfonate as activators in the presence of *N*-methylmorpholine. The resulting compounds were deprotected with tetrabutylammonium fluoride and converted into the phosphoamidite by mixing them with 2-cyanoethyl chloro *N*,*N*-diisopropyl phosphoramidite and DIPEA in dry DCM. The building blocks were co-evaporated with benzene and dried under high vacuum before being used in oligonucleotide synthesis.

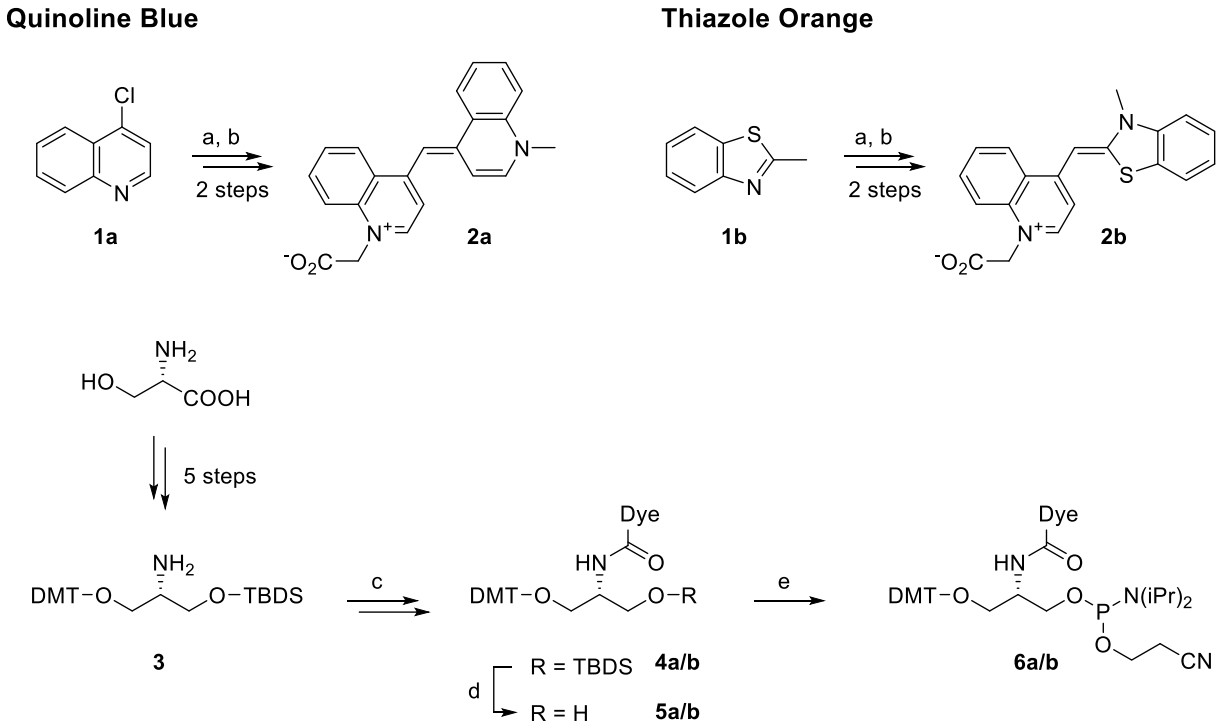

Figure 19: Synthesis of QB and TO 2-cyanoethyl-*N*,*N*-diisopropylchloro phosphoramidite for use in solid phase oligonucleotide synthesis according to Hövelmann *et al.* and Bethge *et al.*[289, 293] a) MeI, reflux, b) *N*-carboxymethyl-4-methquinolinium bromide, NEt_3, DCM, c) **2a** or **2b**, PyBOP, pyridinium *p*-toluene sulfonate, NMM, DMF, d) TBAF, aq. $NaHCO_3$, THF, e) 2-cyanoethyl chloro *N*,*N*-diisopropyl phosphoramidite, DIPEA, dry DCM.

5.1.1 Mono-Dye Approach

For the general design of the single nucleotide responsive FIT probes, the fluorophore was placed adjacent to the editing site. To enhance responsiveness, it was flanked by an LNA nucleoside, and to increase nuclease resistance, a gapmer strategy with 2'OMe-modified ribose nucleosides was applied. (**Figure 20B** and **C**).[292, 293] In the experiment, it should be determined how different nucleotide microenvironments alter the fluorescence behaviour of the probes. To that end, different placements of dye and LNA unit were compared. With probe design **TO-OMe-1** to **-4**, the influence of the LNA position relative to the fluorophore and editing site were explored. In addition, two different 3'-extension sizes (2 or 3 nt) were studied (**TO-OMe-1** vs. **-2** and **TO-OMe-3** vs. **-4**). This was thought to allow unconstrained flexibility of the dye in the single strand and mismatch conditions, while still providing adequately increased local constraint by the double helix in the matched hybridisation state. Finally, in **TO-OMe-5** and **-6**, the fluorophore was placed 5' of the editing site, again, with an adjacent LNA monomer.

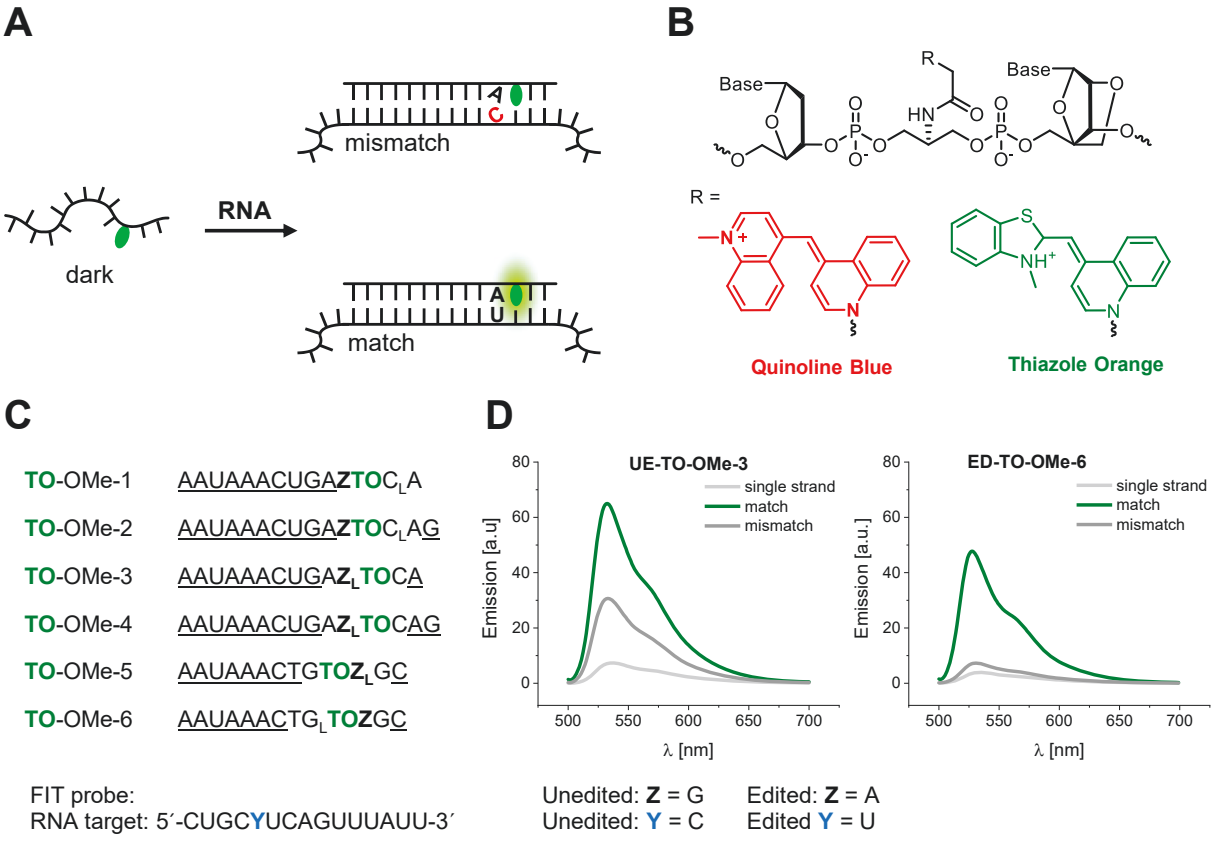

Figure 20: Mono-dye GlyR mRNA FIT probes. (**A**) In the single strand, the excitation energy is dissipated via unconstrained rotation around the methine bridge. Hybridisation to a mismatch target does not provide sufficient constraint and rotation can still occur. Hybridisation with a match target locks thiazole orange or quinoline blue in the base stack and closes the non-radiative relaxation pathway, causing the probe to light up. (**B**) The two dyes used in the oligonucleotide sequence are flanked by an LNA (right) and deoxy (left) nucleotide. (**C**) Name and the sequence design of the probes used in the mono dye approach. Underscored letters represent 2'OMe-modified ribose nucleosides, while the subscript L represents a Locked Nucleic Acid (LNA) building block. The editing site is indicated as bold **Z**. (**D**) Exemplary fluorescence emission spectra for **UE-TO-OMe-3** and **ED-TO-OMe-6**. λ_{Ex} = 485 nm, λ_{Em} = 500-700 nm, $slit_{ex/em}$ = 5 nm.

Table 1: Spectroscopic properties of single nucleotide-specific UE-TO-OMe and ED-QB-OMe FIT probes.

	Sequence 5' – 3'	RNA target	E	S	ϕ	Br	T_m
UE-TO-OMe							
1	AATAAACTGA**G**TOC_LA	m mm	17.5 9.4	1.9	0.44 0.31	21.7 14.6	55.5 42.5
2	AATAAACTGA**G**TOC_LAG	m mm	3.1 2.1	1.5	0.49 0.38	22.9 18.4	57.1 46.7
3	AATAAACTGA**G$_L$**TOCA	m mm	8.7 4.0	2.5	0.31 0.22	14.1 10.8	52.3 40.2
4	AATAAACTGA**G$_L$**TOCAG	m mm	14.3 8.9	1.6	0.30 0.25	13.9 11.2	53.3 41.8
5	AATAAACTG**TOG$_L$**GC	m mm	10.5 5.1	2.0	0.44 0.30	17.5 13.6	51.9 47.6
6	AATAAACTG$_L$**TOG**GC	m mm	13.7 6.8	2.2	0.23 0.14	9.8 6.1	52.7 49.8
ED-QB-OMe							
1	AATAAACTGA**AQB**C_LA	m mm	41.2 5.8	7.1	0.29 0.10	10.0 2.8	48.8 40.8
2	AATAAACTGA**AQB**C_LAG	m mm	15.0 2.4	6.3	0.31 0.11	15.0 4.6	50.4 42.1
3	AATAAACTGAA**A$_L$QB**CA	m mm	63.3 2.4	26.4	0.11 0.02	4.3 0.6	45.1 37.0
4	AATAAACTGAA**A$_L$QB**CAG	m mm	12.8 1.4	9.1	0.24 0.03	6.2 1.0	46.7 37.0

Conditions: 0.5 µM probe and 4 eq. RNA target (5'-CUGC**Y**UCAGUUUAUU-3', UE: Y = C; ED: Y = U) were measured in buffer (100 mM NaCl, 10 mM Na_2HPO_4, pH 7.0) at 37 °C to determine fluorescence enhancement $E = I / I_0$ and specificity $S = E_m / E_{mm}$. Quantum yield ϕ and brightness $Br = \varepsilon_{\lambda ex} \cdot \phi / 1000$ in $M^{-1} \cdot cm^{-1}$ were measured at 25 °C. QB: λ_{ex} = 560 nm, λ_{em} = 605 nm; TO: λ_{ex} = 485 nm, λ_{em} = 535 nm; $slit_{ex/em}$ = 5 nm. Melting temperature T_m in °C was measured with 1 µM probe and 1 eq. (1 µM) RNA target. Underscored letters = 2'OMe-RNA; subscript L = LNA, bold letters = editing site (black) and dyes (colour). Match and mismatch target are indicated with m and mm.

All six probe designs were prepared as two versions: one complementary to the unedited target (UE) and one to the edited target (ED). The fluorescent properties of all twelve probes were then compared with the QB-probe set previously prepared by Knoll *et al*. [316] (**Table 1** and **Table 2**). For this, their fluorescence emission spectra were recorded in the single strand and in the presence of a match or mismatch RNA target (**Figure 20**). It should be noted that high fluorescence intensity is not the only criterion by which FIT probes should be evaluated. For example, **UE-TO-OMe-3** (**Figure 20D**, left) has a stronger absolute fluorescence emission than **UE-TO-OMe-6** (right). However, the difference between match duplex and single strand or mismatch duplex is significantly smaller for this probe. Evidently, for a low background and unambiguous detection of single base alterations, probes must exhibit a fluorescence increase only upon hybridization (enhancement: $E = I_{ds} / I_{ss}$) and possess a good ability to discriminate the correct target from other sequences (selectivity: $S = E_m / E_{mm}$).

Table 2: Spectroscopic properties of single nucleotide specific ED-TO-OMe and UE-QB-OMe FIT probes.

	Sequence 5' – 3'	RNA target	E	S	ϕ	Br	T_m
ED-TO-OMe							
1	AATAAACTGA**G**TOC_LA	m mm	18.2 3.6	5.0	0.43 0.19	25.0 8.8	46.4 39.2
2	AATAAACTGA**G**TOC_LAG	m mm	2.4 0.6	4.0	0.67 0.26	32.3 12.7	49.0 43.0
3	AATAAACTGA**G$_L$**TOCA	m mm	14.7 5.5	2.6	0.24 0.17	14.8 8.1	45.7 38.2
4	AATAAACTGA**G$_L$**TOCAG	m mm	12.5 2.4	5.3	0.28 0.18	12.5 8.4	46.8 38.7
5	AATAAACTGTO**G$_L$**GC	m mm	10.8 2.4	4.6	0.52 0.16	18.6 5.8	47.5 40.5
6	AATAAACTG$_L$TO**G**GC	m mm	10.9 1.8	6.0	0.38 0.11	16.0 5.6	44.3 36.8
UE-QB-OMe							
1	AATAAACTGA**A**QBC_LA	m mm	87.5 28.4	3.1	0.45 0.35	16.8 14.6	56.3 43.9
2	AATAAACTGA**A**QBC_LAG	m mm	12.8 8.1	1.5	0.48 0.47	24.5 26.0	60.5 47.0
3	AATAAACTGAA**A$_L$**QBCA	m mm	15.3 8.0	1.9	0.18 0.27	6.1 8.3	47.3 39.0
4	AATAAACTGAA**A$_L$**QBCAG	m mm	37.4 21.2	1.7	0.22 0.32	7.5 11.5	52.9 41.8

Conditions: 0.5 µM probe and 4 eq. RNA target (5'-CUGC**Y**UCAGUUUAUU-3', UE: Y = C; ED: Y = U) were measured in buffer (100 mM NaCl, 10 mM Na_2HPO_4, pH 7.0) at 37 °C to determine fluorescence enhancement $E = I / I_0$ and specificity $S = E_m / E_{mm}$. Quantum yield ϕ and brightness $Br = \varepsilon_{\lambda ex} \cdot \phi / 1000$ in $M^{-1} \cdot cm^{-1}$ were measured at 25 °C. QB: λ_{ex} = 560 nm, λ_{em} = 605 nm; TO: λ_{ex} = 485 nm, λ_{em} = 535 nm; $slit_{ex/em}$ = 5 nm. Melting temperature T_m in °C was measured with 1 µM probe and 1 eq. (1 µM) RNA target. Underscored letters = 2'OMe-RNA; subscript L = LNA, bold letters = editing site (black) and dyes (colour). Match and mismatch target are indicated with m and mm.

The recorded and calculated properties of the probes are summarized in **Table 1** and **Table 2**. In the experiment, each FIT probe was placed in a cuvette and the fluorescence characteristics of the single strand (I_0) were determined. This measurement was performed as duplicate, once each for the cuvette of the later match and mismatch readings. As the deviation between both values was typically very low (<1 AU, see **Chapter 8.2**) and the RNA target was later added in excess (saturating the FIT probe to be measured), the following duplex readings were considered reliable without performing additional replicates. After addition of 4 eq. of either unedited or edited target, the duplex fluorescence was measured (I). Generally, TO-based FIT probes had higher fluorescence intensities in a match hybridization scenario than the QB ones (Br = 9.8–32.3 vs. 4.3 – 24.5). However, this was also true for the mismatch case, resulting in a lower overall selectivity (S = 1.5–6.0). In contrast, QB-based probes remained darker in the

mismatch duplex, resulting in higher selectivity. Surprisingly, this was only true for the **ED-QB-OMe** set, (S = 6.3–26.4), whereas the **UE-QB-OMe** probes were much less discriminatory (S = 1.5–3.1). This might be due to differences in the base composition, with the UE set binding more strongly to the target, a fact also reflected in their higher mismatch T_m values.

For a better comparison with other fluorescent dyes, quantum yields (ϕ) were calculated for each sample (see **Chapter 3.2**). Then probe brightness (Br) was calculated as the product of quantum yield and extinction coefficient at the excitation wavelength (TO: 485 nm; QB: 560 nm). This allowed a more concise description of the optical properties of the synthesised probes. In general, probe brightness mirrored previous results, with TO probes being significantly brighter than QB ones, mostly due to their higher fluorescence quantum yield per photon absorbed. It is important to bear in mind that brightness values can also be raised by increasing the extinction coefficient at a given excitation wavelength. An unexpected observation was the very high quantum yield of **ED-TO-OMe-2** (ϕ = 67 %). The validity of this result was confirmed in multiple experiments. Interestingly, **ED-TO-OMe-2** also showed a significantly higher fluorescence emission in the single strand than in the mismatch duplex, with otherwise near identical emission spectra shapes. It can be speculated that intra- or intermolecular interaction of this particular probe restricts TO rotation in the single strand, leading to higher background emission.

To test whether the differences in fluorescence were due to different hybridisation states of the probe-target complex, the melting temperatures (T_m) of the match and mismatch duplexes were determined. This was done spectroscopically, based on the hyperchromic properties of nucleic acid duplexes: When heated, they show a sigmoidal increase of their absorbance at 260 nm. From the maximum of the first derivative of this curve, the T_m can be obtained as the inflection point of the increase. This value represents the temperature at which 50 % of the probe resides in a duplex, while the other 50 % remain in a non-hybridised state.[326, 327]

The data obtained shows that the melting points of the measured FIT probes lie around 47 °C for the ED probes and 54 °C for the UE probes (though values for individual probes varied by as much as 10 °C). As mentioned above, this difference can be explained with the different nucleotide compositions of the sequences. The extra guanine present in the ED target offers an additional hydrogen bridge for Watson-Crick base pairing.[328, 329] As expected, hybridization to the mismatch target lowered the melting temperature for both sets (by about 7–8 °C for

the ED probes and 10–13 °C for the UE probes). Some probes (such as **ED-QB-OMe-3** and **-4**) exhibited melting temperatures as low as 37 °C in the mismatch duplex. This means that under the conditions of the experiment, only half of these probes is actually bound to the RNA target. This results in a lower fluorescence output than expected and might explain their comparatively high specificity values. Consequently, it is questionable, whether a probe length of 14–15 nt is sufficient to ensure complete hybridisation under conditions that are not saturating the FIT probe, e.g. when the target concentration is limited.

A major requirement for FIT probe pairs is that they allow discrimination between match and mismatch RNA when exposed to the target together. To test the ability of the synthesized probes to do so, a competitive experiment was performed, in which two FIT probes were placed in a cuvette at a 1:1 ratio. The presence of equimolar concentrations was verified by determining the absorbance of the sample at 260 nm after addition of each probe. Single strand fluorescence was then measured in both the thiazole orange and quinoline blue channel. After addition of one equivalent of either match or mismatch target the fluorescence of the double strand was determined. To ensure correct hybridisation, the cuvette was heated to 90 °C prior to the fluorescence measurements and slowly cooled back down to 37 °C. From the obtained fluorescence intensities, specificity values were calculated and compared to the previous experiment (**Figure 21A** and **B**), in which the target RNA was used in excess (4 eq.).

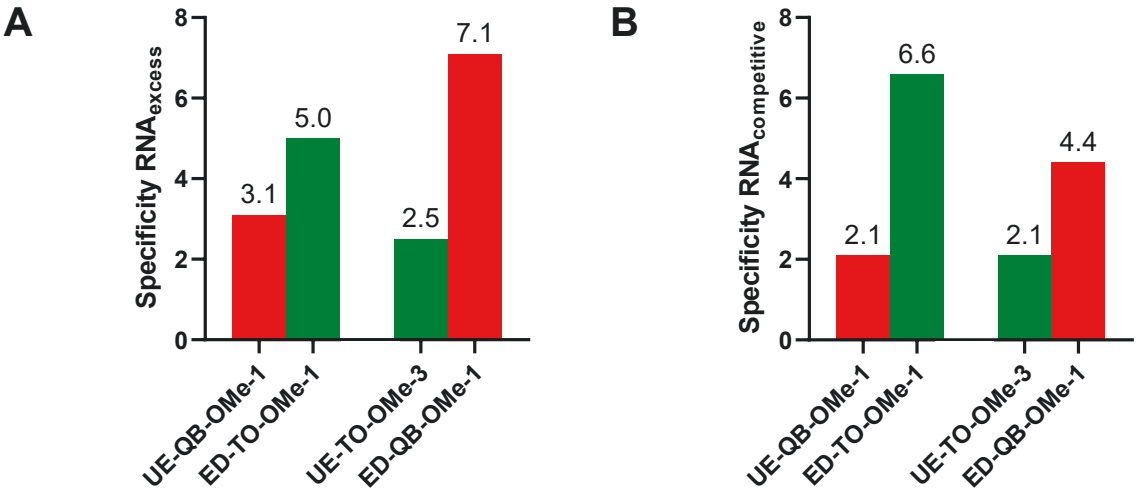

Figure 21: Comparison of probe specificity in the presence of excess and stoichiometric amounts of probe. (**A**) Specificity values ($S = E_m / E_{mm}$) for selected FIT probes (0.2 µM) obtained in the previously described experiments (**Table 1** and **2**) with 4 eq. of target RNA. (**B**) Specificity of the same probes in a competitive setup on stoichiometric amounts of target RNA (0.2 µM). Samples were measured in buffer (100 mM NaCl, 10 mM Na_2HPO_4, pH 7.0) at 37 °C.

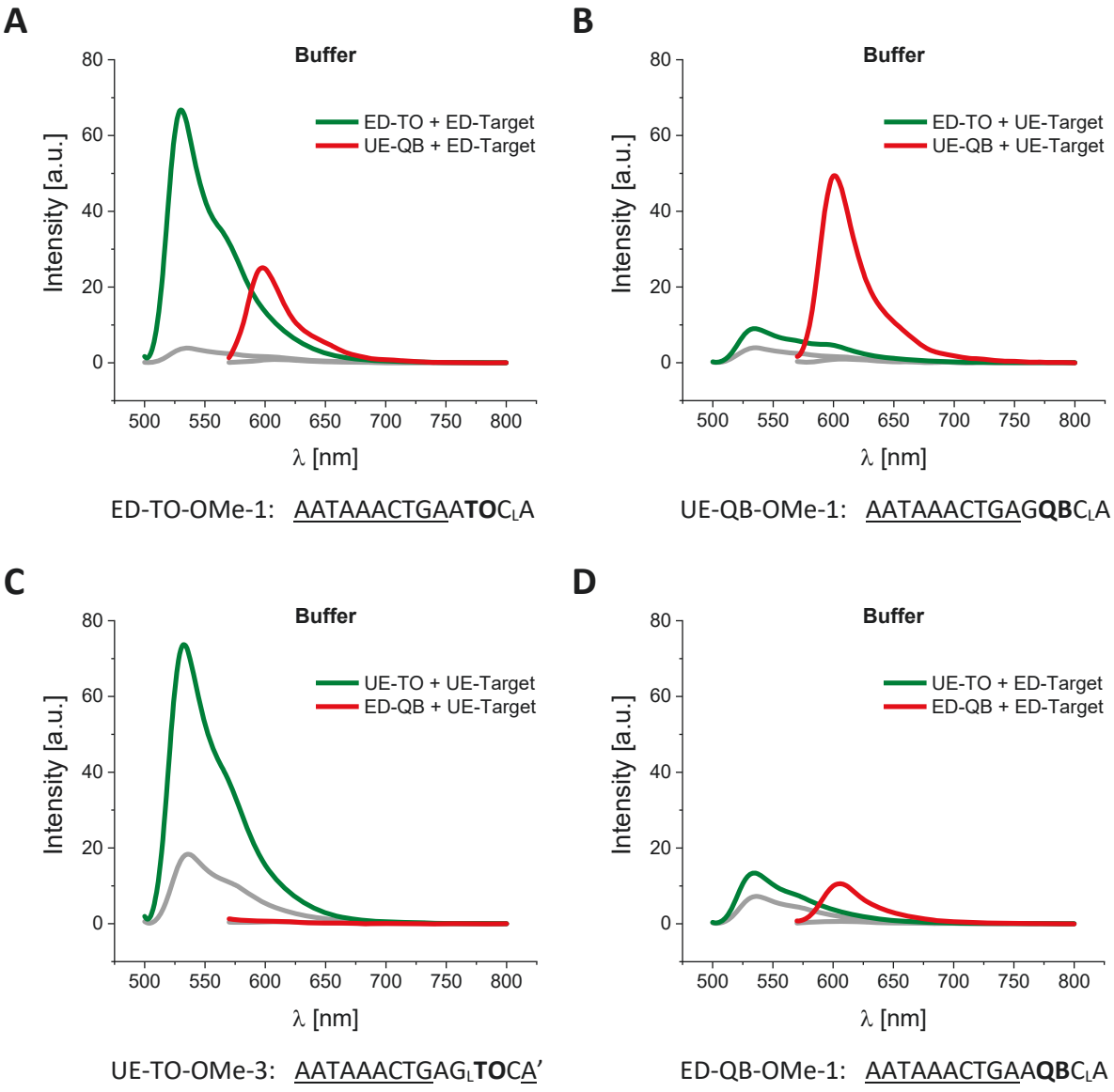

Figure 22: : Fluorescence emission of competitive setup at 37°C. Probes were measured in the absence (grey) or presence of either edited or unedited RNA-target. Conditions: (**A**) & (**B**) 0.2 µM **ED-TO-OMe-1**, 0.2 µM **UE-QB-OMe-1** and (**C**) & (**D**) **UE-TO-OMe-3**, 0.2 µM **ED-QB-OMe-1** and 0.2 µM target-RNA (5'-CUGAAGGACUCACCCUGC**Y**UCAGUUUA-UUUUGA-3'; UE: Y = C, ED: Y = U). Experiments were conducted in buffer (100 mM NaCl, 10 mM Na_2HPO_4 pH 7.0). QB: λ_{ex} = 560 nm, λ_{em} = 605 nm; TO: λ_{ex} = 485 nm, λ_{em} = 535 nm, $slit_{ex/em}$ = 5 nm.

The probes used for the experiment were selected based on their previously determined properties. Due to their comparatively high enhancement, specificity and brightness values, pairings of **UE-QB-OMe-1** (S = 3.1) and **ED-TO-OMe-1** (S = 5.0), as well as **UE-TO-OMe-3** (S = 2.5) and **ED-QB-OMe-1** (S = 7.1) were tested. Comparing the specificity values determined in the previous experiment on excess RNA and the competitive setup on equimolar amounts of target, it appears that the QB FIT probes are affected more strongly by the presence of a competing TO probe than vice versa. **UE-QB-OMe-1** had slightly decreased specificity when hybridised to RNA in the presence of **ED-TO-OMe-1** (S = 2.1 vs 3.1). In contrast, the specificity of **ED-TO-OMe-1** actually increased (S = 5.0 vs. 6.6). The reason for this observation is that the

background fluorescence of single stranded **ED-TO-OMe-1** seems to have been suppressed – down to the same level as in the QB probe (see **Figure 22A** and **B**).

This suggests the influence of a quenching mechanism, possibly by dye-dye contact, that effectively increases the relative fluorescence gain upon hybridization. The specificity of **UE-QB-OMe-1** was not increased, as its single strand fluorescence was already very low without another probe being present. For the second probe set, originally **ED-QB-OMe-3** had been considered, which previously demonstrated a remarkable specificity of 26.4 (see **Table 1**) but had also a rather low brightness value of only 4.3. In addition, its thermal stability (T_m = 37 °C) was deemed too low for applications at 37 °C. It is likely that the high specificity observed for this probe was due to incomplete hybridization to the target RNA. Therefore, the second-best candidate, **ED-QB-OMe-1**, was paired up with **UE-TO-OMe-3** in the second set instead (**Figure 22C** and **D**). For **UE-TO-OMe-3** there was nearly no change in specificity in the competitive setup. It appears that this FIT probe is less impacted by the presence of competing **ED-QB-OMe-1**, possibly due to its higher melting temperature. In contrast, the specificity of **ED-QB-OMe-1** was significantly decreased (from 7.1 to 4.4). This stems from reduced fluorescence output in the double strand.

Taken together, the competitive experiments demonstrated that quinoline blue and thiazole orange FIT probes can be used together in the same setup. It should be noted that the specificity of FIT probes obtained in individual measurements on excess RNA does not directly translate to a competitive setting. However, a generally high specificity likely also means better discrimination in the presence of competing sequences. To achieve higher probe specificity, the length of future FIT probes may be extended to increase the proportion of probe that is bound to the target. Nonetheless, care must be taken not to promote non-specific interactions. Instead, it might be better to address the specificity of the probe by increasing fluorescence enhancement upon interaction with matched RNA target while simultaneously suppressing the emission of mismatch duplexes. As outlined in the aims of the thesis, this may be done by introducing additional dyes or quenchers to the probe. It is known that cyanine dyes are able to quench themselves not only via collisional quenching, when in close local contact, but also through homo-FRET, when at least one dye molecule is in an environment where it can dissipate its excitation energy by rotation around the methine bridge (see **Chapter 3.3**).[43, 330] FIT probes carrying two dyes of the same type may thus benefit from both reduced emission in the non-hybridized and mismatch state, as well as increased fluorescence when both

dyes are embedded in a duplex formed with the correct target. The following chapters will explore the possibilities and limitations of such dual-dye FIT^2 probes, which are modified with an additional thiazole orange or quinoline blue fluorophore, 5' of the editing site.

5.1.2 Dual-Dye Approach

5.1.2.1 DNA-Based FIT^2 Probes

Standard FIT probe designs are limited by their maximum brightness and achievable fluorescence gain. To improve performance, different secondary fluorophores have been introduced that act as quenchers and/or interact with the primary dye via FRET.[241, 252, 331] While this strategy has resulted in probes with high enhancement factors, it requires careful optimization of the dye pair and generally improves contrast by lowering single strand/mismatch emission, not by actually increasing probe brightness. However, it is equally conceivable that two fluorophores of the same type are used, whose combined emission can be detected in the same channel. The second dye should not only enhance overall brightness but may also quench background fluorescence via dye-dye contact-mediated quenching in the single strand, to improve the signal-to-noise ratio. Additionally, when placed at the correct distance, it could also allow non-radiant energy transfer between an intercalated and a non-intercalated dye to occur during mismatch hybridisation, resulting in increased specificity.

This concept is applicable to fluorophores of the thiazole orange family, like TO itself, as well as QB. The challenge is to find the optimal dye-dye distance that provides high homo-FRET efficiency in mismatch hybridisation, but is also large enough to allow independent, simultaneous fluorescence in the match duplex. In order to screen for suitable distances, the previously employed FIT probes (see **Table 1** and **Table 2**) were taken as basis and a second dye was introduced seven or nine base pairs upstream of the editing site. These distances were previously reported as optimal for FRET-based FIT probes bearing two different fluorophores and should theoretically also provide efficient homo-FRET energy transfer during mismatch hybridisation. [323] Given that RNA:RNA duplexes form A-type helices with a rise of 2.46 nm per 11-bp turn,[332, 333] we can assume a distance of 1.8 to 2.3 nm between the dyes. It is known that FRET occurs efficiently (E > 95 %) at a distance of up to 3 nm.[331, 334] The probe design agrees with this requirement. Nonetheless, it remained to be tested, whether the distances would be large enough to allow both dyes to fluoresce efficiently in the match state, e.g. by increasing r or changing the orientation factor κ of the fluorophores (see equation (2) and (3)).

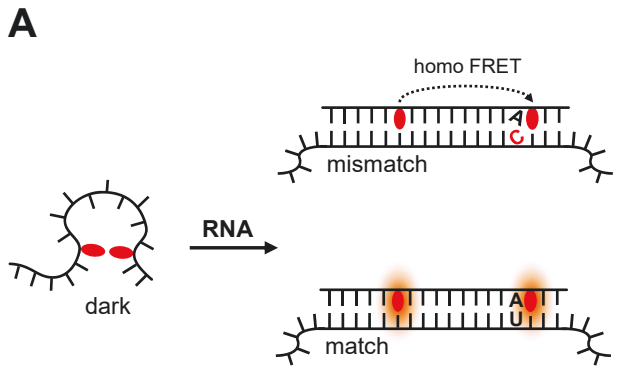

Figure 23: Principle of the dual dye FIT^2-approach. (**A**) In the single strand dye-dye contact mediated quenching renders the probes dark. During partial or single mismatched hybridization fluorescence also stays low, due to homo-FRET to the non-intercalated fluorophore. Recognition of a perfectly matched target locks both dyes in the helical base stack and closes the homo-FRET quenching channel and the probe lights up (**B**) Probe design of the FIT^2 approach with two dye-dye distances of 7 or 9 nt and three different 5' extension lengths (3, 4 and 5 nt). Subscript L = LNA.

The synthesis of dual-dye FIT-probes was conducted as described for the mono-dye probes (**Chapter 5.1.1**). A total length of 16–18 nt was chosen to ensure genome-wide uniqueness, but also provide enough room for sequence variations. Other reasons for the extension were the previous observation that shorter probes are often only partially hybridized (particularly in the mismatch duplex), possibly leading to an overestimation of their specificity, as well as compensation of decreased probe thermostability due to the additional base surrogate. It should be noted that sequences that are too long will also have higher affinity for the mismatch target, again decreasing selectivity. Against this backdrop, a length of 16-18 nt was seen as a good compromise. Two dye distances (7 or 9 nt) and three 5'-extension lengths (3, 4 and 5 nt), resulting in a total of six candidate sequences, were tested for their suitability as dual-dye FIT^2 probes (**Figure 23B**). As before, the LNA effect was utilized and one LNA monomer was placed next (on the 3' side) to each dye. The design around the editing site was based on **TO-OMe-1** and **QB-OMe-1**, which previously resulted in the best combination of enhancement, specificity and brightness.[316] To allow a focus on the effects of the placement of second dye, it was kept constant for all probes. Of note, the two different dye-dye distances result in two different dye microenvironments. While the 9 nt distance places an A and a T-LNA monomer adjacent to the second dye, the 7 nt distance has a T and an A-LNA monomer as direct neighbours. Whether and how this impacts probe performance should also be evaluated in the following experiments.

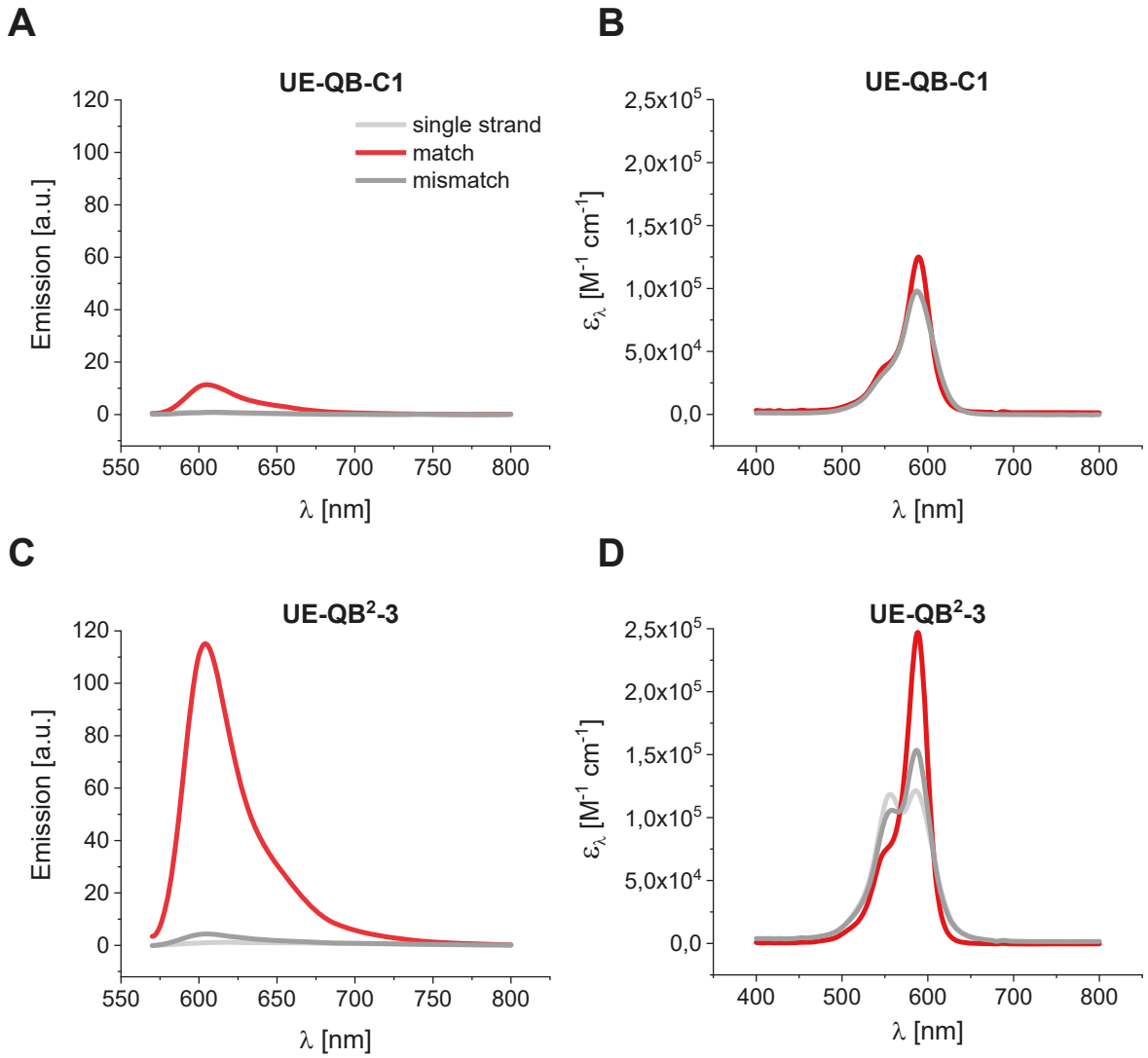

Figure 24: Exemplary fluorescence (left; 37 °C) and extinction coefficient ε_λ (right; 25 °C) spectra. Probes were measured in the absence (light grey) or presence of match (red) and mismatch (dark grey) target. Conditions: 0.5 µM **UE-QB-C1** or **UE-QB^2-3** FIT probe, 5 eq. target RNA (5'-CUGAAGGACUCACCCUGC**Y**UCAGUUUAUUUUGA-3'; UE: Y = C, ED: Y = U) in buffer (100 mM NaCl, 10 mM Na_2HPO_4 pH 7.0). QB λ_{Ex} = 560 nm, λ_{Em} = 570-800 nm, $slit_{ex/em}$ = 5 nm.

As before, the spectroscopic properties of the dual dye probes **UE-QB^2-1** to **-6**, including their quantum yields, brightness and thermal stability were determined. The results of these experiments are summarized below (**Table 3**). They suggest that the initial hypothesis is true: Introduction of a second dye of the same type can increase match-state fluorescence, while keeping single strand and mismatch state emission low (**Figure 24**). As an example, the emission spectra of **UE-QB^2-3** and the corresponding mono-dye control probe **UE-QB-C1** are depicted in **Figure 24A-D**. Strikingly, the FIT^2 probe shows little very difference between mismatch target-hybridized and single strand background fluorescence. The respective absorption spectrum reveals that the reason for this is likely the appearance of a secondary absorption band, blue-shifted compared to the original peak (**Figure 24D**).

This so-called H-band ("H" for hypsochromic shift) can be a consequence of cyanine dyes forming local polymers (also referred to as H-aggregates; see **Chapter 3.2**). In these complexes, excitation energy is not released by fluorescence, but instead vibrational relaxation through internal conversion.[50, 334, 335] Presumably, these aggregates are broken up upon hybridisation to the target RNA and fluorescence can occur again.

The screening should also explore the influence of the distance between both dyes. The results revealed that the shorter dye-dye distance of 7 nt is favourable in terms of specificity. The enhancement factor in the match duplex increased with probe length, while it remained almost constant in the mismatch case. Furthermore, when comparing probe quantum yields (**Table 3**), it became apparent that in mismatch environments they are dependent on the dye-dye distance. All three 9 nt spaced FIT^2 probes had quantum yields of 3 % in the mismatch duplex, while the values for the 7 nt spaced FIT^2 probes were 1 %. Conceivably, the shorter distance results in higher homo-FRET efficiency than the larger one. Considering the data obtained, it can be speculated that the dye spacing has a larger impact on homo-FRET efficiency in mismatch hybridisation, while the 5' overhang governs quantum yield and brightness in the match state. The previously raised concern that shorter distances might impair individual fluorescence of the dyes can be dismissed, as the brightness for both distances was comparable (albeit slightly lower for the 7 nt probes). The data also reveals that while specificity was high for both distances tested, the shorter 7 nt spacing produced remarkably high values of up to 78.8. At the same time, the quantum yields fell within the same range as for the mono-dye FIT probes presented in **Table 1** and **Table 2** (**Chapter 5.1.1**). All probes were also tested against a partial match target with only 14 complementary (out of 35) nucleotides (see **Appendix 8.2.2**). Here, the probes exhibited only negligible enhancement (E = 1.0–1.5), which again indicates their high specificity.

As a more appropriate control, the FIT^2 probes were compared to mono-dye probes of the same length. The longest design **UE-QB^2-3** / **UE-QB^2-6** was chosen as basis and the fluorophore was placed either adjacent to the editing site (**UE-QB-C1**) or in 7 nt (**UE-QB-C2**) and 9 nt (**UE-QB-C3**) upstream to it, respectively. Surprisingly, the specificity of **UE-QB-C1** was only slightly lower than that of the best dual-dye FIT^2 probes. This was due to an exceptionally low enhancement in the mismatch state, which have been a result of the use of weaker affinity deoxynucleotides in combination with the positioning very close to the 3'-end.

Table 3: Spectroscopic properties of dual-dye QB FIT^2 probes specific for UE GlyR mRNA and mono-dye controls.

	Sequence 5' – 3'	RNA target	E	S	ϕ	Br	T_m
UE-QB^2							
1	AAAQBT$_L$AAACTGAGQBC$_L$A	m mm	66.1 2.6	22.0	0.18 0.03	13.5 3.2	49.9 50.9
2	CAAAQBT$_L$AAACTGAGQBC$_L$A	m mm	106.7 3.8	26.5	0.15 0.03	13.1 2.8	51.2 48.5
3	TCAAAQBT$_L$AAACTGAGQBC$_L$A	m mm	131.7 4.4	32.7	0.15 0.03	12.3 2.7	52.0 48.7
4	AAAATQBA$_L$ACTGAGQBC$_L$A	m mm	82.2 1.3	63.1	0.11 0.01	8.9 0.7	49.6 50.9
5	CAAAATQBA$_L$ACTGAGQBC$_L$A	m mm	110.0 2.6	36.6	0.12 0.01	10.3 1.4	48.3 50.6
6	TCAAAATQBA$_L$ACTGAGQBC$_L$A	m mm	121.3 2.4	78.8	0.13 0.01	11.0 1.0	49.2 51.1
UE-QB							
C1	TCAAAATAAACTGAGQBC$_L$A	m mm	69.6 1.2	56.7	0.32 0.03	12.7 1.0	48.4 53.3
C2	TCAAAQBT$_L$AAACTGAGGCA	m mm	26.1 3.0	8.7	0.19 0.07	7.4 2.8	49.8 49.0
C3	TCAAAATQBA$_L$ACTGAGGCA	m mm	47.1 2.5	18.9	0.30 0.08	10.3 3.2	49.2 51.1

Conditions: 0.5 µM probe and 5 eq. RNA target (5'-CUGAAGGACUCACCCUGC**Y**UCAGUUUAUUUUGA-3', UE: Y = C; ED: Y = U) were measured in buffer (100 mM NaCl, 10 mM Na_2HPO_4, pH 7.0) at 37 °C to determine fluorescence enhancement $E = I / I_0$ and specificity $S = E_m / E_{mm}$. Quantum yield ϕ and brightness $Br = \varepsilon_{\lambda ex} \cdot \phi / 1000$ in $M^{-1} \cdot cm^{-1}$ were measured at 25 °C. QB: λ_{ex} = 560 nm, λ_{em} = 605 nm; TO: λ_{ex} = 485 nm, λ_{em} = 535 nm, $slit_{ex/em}$ = 5 nm. Melting temperature T_m in °C was measured with 1 µM probe and 1 eq. (1 µM) target. Subscript L = LNA, bold letters = editing site (black) and QB base surrogates (red). Match and mismatch target are indicated with m and mm.

Interestingly, the specificity values for controls **UE-QB-C2** and **UE-QB-C3** were relatively high, which is puzzling considering that the dye is not located near the editing site in those sequences and the melting temperatures for their match and mismatch duplexes are comparable. This suggests that under certain circumstances quinoline blue may be able to respond to sequence misalignments, even when they are several nucleotides away.

Although the quantum yield of control probe **UE-QB-C1** was almost twice that of the dual dye congeners, the brightness values of most **UE-QB^2** probes were still higher. From the absorption spectra it can be inferred, that in the non-hybridised state, their absorption capability is comparable to that of the mono-dye control (see **Figure 24A-D**) but upon hybridization with the match target they reach twice its value. This indicates that the QB FIT^2 probes absorb light more efficiently, increasing their brightness. As mentioned above, the introduction of a second fluorophore causes a new, blue-shifted maximum to appear in the absorption spectra of

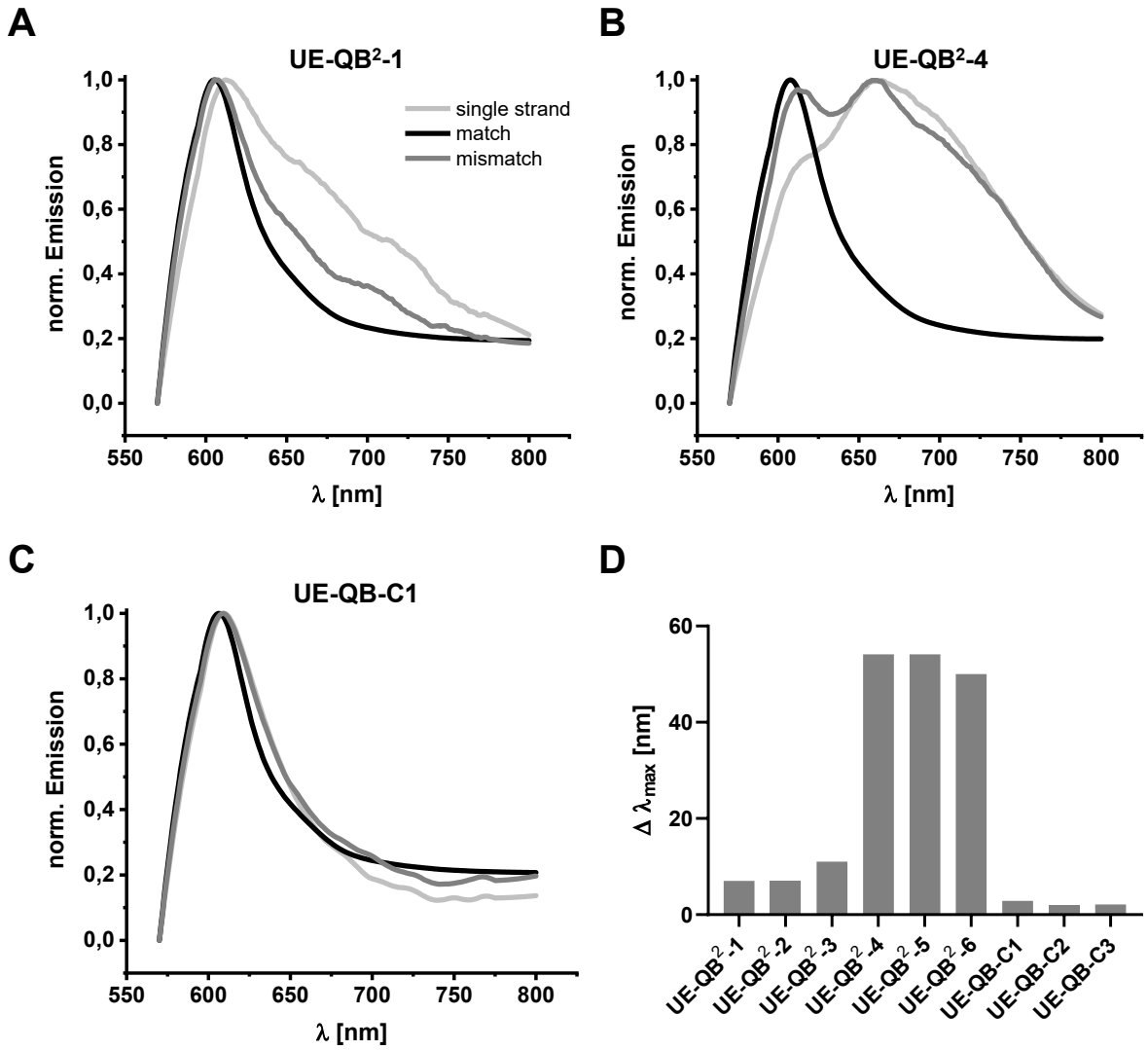

Figure 25: Normalised fluorescence emission spectra of selected dual-dye QB FIT^2 probes. Depicted are the spectra of (**A**) the 9 nt spaced probe **UE-QB^2-1**, (**B**) the 7 nt spaced probe **UE-QB^2-4** and (**C**) the mono-dye control **UE-QB-C1**. (**D**) Wavelength shifts of the fluorescence maxima of different probes upon hybridization to the match target.

the single stranded QB^2 probes. Conversely, their emission spectra display a new, red-shifted maximum. Such H-bands are indicative of the formation of local cyanine dye aggregates, which can efficiently depopulate excited states by internal conversion instead of fluorescence (see **Chapter 3.2**).[334] This observation becomes more evident when the emission graphs are normalised (**Figure 25**).

This transformation of the data reveals that the two dye-dye distances tested exhibit particular differences in how strongly the fluorescence maximum of the single strand is shifted compared to the double strand. In the 9 nt spaced probe **UE-QB^2-1**, hardly any shift is visible (**Figure 25A**), whereas the 7 nt spaced **UE-QB^2-4** experiences a shift of up to 50 nm between its single strand and double strand fluorescence maximum (**Figure 25B**). Additionally, its mismatch trace shows two local maxima, which implies that collisional quenching cannot be the

only quenching mechanism involved. Instead it hints at the presence of other quenching mechanisms, possibly H-aggregate formation and/or homo-FRET. Importantly, the corresponding mono-dye control probe **UE-QB-C1** (**Figure 25C**) displays no such shift of its fluorescence maximum. An overview of the absolute wavelength shift for each probe is given in **Figure 25D**. It clearly shows that the shorter dye-dye distance produces more strongly red-shifted fluorescence peak maxima.

As described before, the thermal stability of this probe set was examined. Interestingly, in the whole set of DNA-based FIT^2 probes, the first derivative of the sigmoidal curve fit displays a relatively broad peak, indicating a wide melting range of the duplex (**Figure 26**). This means that the calculated melting temperature is likely less precise and subject to a certain error. Notably, the nuclease-resistant mono-dye FIT probes discussed in **Chapter 5.1.1** had much narrower first derivatives than the dual-dye congeners discussed in this chapter (**Figure 26**). This may be ascribed to the generally higher RNA affinity and possibly different hybridization behaviour of the 2'OMe-building blocks. It must be noted that T_m calculations based on UV melting curves are firstly a measure of the global base stacking of the duplex and secondly assume a two-state dissociation model. However, duplex dissociation is heavily dependent on base succession. Thermodynamic measurements using IR spectroscopy have demonstrated that A/T-rich ends are more prone to fraying.[336] The general probe sequence used in this work has multiple A's on either of its ends. In addition to the two fluorophores, the mismatch probes have an extra, non-pairing A in their sequence. It is possible that at 37 °C local dissociation processes at the duplex ends enable single strand like behaviour, even though the overall T_m values (around 50 °C) indicate complete hybridization. This could contribute to the low fluorescence of the FIT^2 probes in the mismatch state. The broader peak shape of the first deviation of the mismatch melting curves compared to the match ones (**Figure 26**) supports this hypothesis.

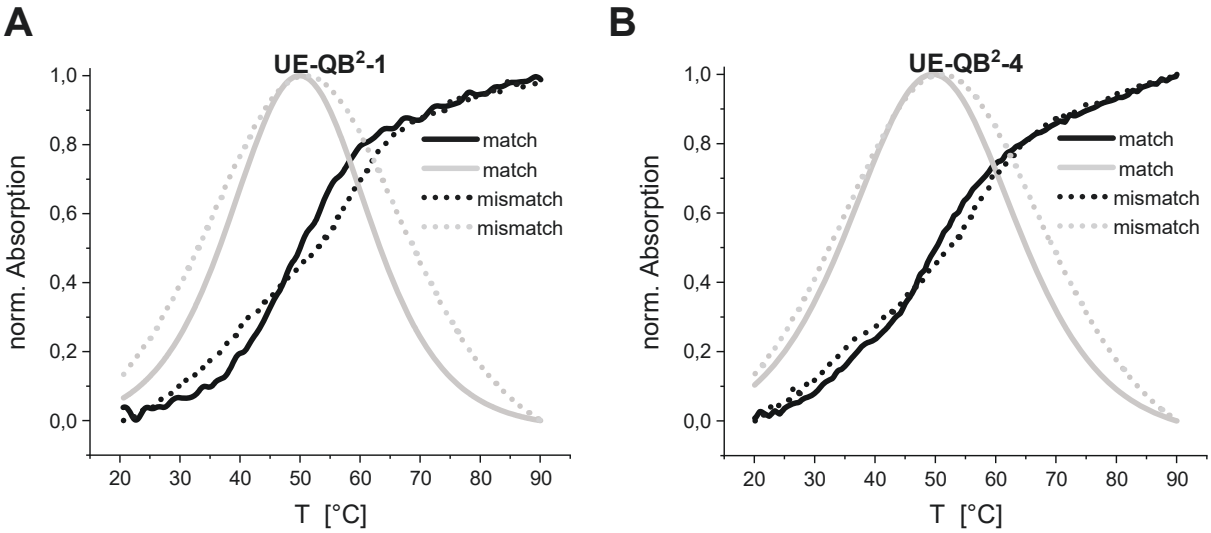

Figure 26: Melting curves of two DNA-based FIT^2 probes. Normalized absorbance of (**A**) **UE-QB^2-1** or (**B**) **UE-QB^2-4** in a duplex with match (solid black) or mismatch (dotted black) RNA and the first derivative of a sigmoidal curve fit (grey).

Regarding enhancement, specificity and brightness, **UE-QB^2-3** to **-6** exhibited the most suitable properties for a visualization of mRNA C-to-U editing. Especially **UE-QB^2-4** had pronounced H-bands (see **Appendix 8.2.3.2**) and consequently very low mismatch emission (**Table 3**).

5.1.2.2 Nuclease-Resistant 2'OMe-RNA FIT^2 Probes

In preparation for biological experiments, the FIT^2 probe design was modified to offer increased enzymatic stability. For the synthesis of nuclease-resistant probes, 2'OMe-RNA building blocks were incorporated into the sequence (**Table 4** and **Table 5**). It is known that 2'OMe-oligonucleotides have higher affinity for RNA and can thus increase the level of constraint experienced by TO family dyes, but this may also lead to higher mismatch and background emission.[293] To counteract this effect, a gapmer design was applied in which the dyes are flanked by unmodified deoxynucleotides. This was thought to allow the probes to benefit from the higher RNA affinity of 2'-OMe RNA, while simultaneously loosening up the structure with unmodified DNA monomers just enough to allow efficient non-radiant energy release via methine bridge rotation in the single strand and in mismatch hybridization. To provide a high level of local constraint upon formation of the correct duplex, again an LNA monomer was placed next to both dyes. By combining different nucleic acid modifications, it may be possible to overcome potential adverse effects on the system, while benefitting from their individual strengths. In addition, 2'OMe-containing probes appear to have sharper, more defined melting curves (see **Figure 26** and **Appendix 8.2.4**), making it easier to estimate the percentage of hybridised FIT^2 probe at 37 °C, which is important for life-cell experiments.

Because the design of **UE-QB^2-3** to **-6** was previously the most favourable, it was adopted for the nuclease-resistant FIT^2 approach. Two sets of orthogonal probes were prepared, one based on thiazole orange, the other on quinoline blue. Each set contained four QB^2 and TO^2 probes, specific for either the UE- or ED-target, for a total of 16 FIT^2 probes. As before, three mono-dye control sequences (**X-OMe-C1-C3**) were synthesized for each fluorophore. The spectroscopic properties of all probes were determined as described in previous chapters.

All three **UE-QB^2-OMe** probes demonstrated remarkable enhancement (E > 100), particularly **UE-QB^2-OMe-1**, which had an E value of almost 125. At the same time, their extinction coefficients were more than twice that of the mono-dye control probes. However, compared to the non-nuclease resistant probes presented in **Chapter 5.1.2.1** (**Table 3**), the set had lower specificity. This is probably due to the more sterically hindered duplex formed by the 2'OMe-RNA nucleosides, as mentioned earlier.

Table 4: Spectroscopic properties of nuclease-resistant QB and TO dual-dye FIT^2 and mono-dye control probes.

	Sequence 5' – 3'	RNA target	E	S	ϕ	Br	T_m
UE-QB^2-OMe							
1	UCAAA**QB**T$_L$AAACUGA**G****QB**C$_L$A	m	124.8	14.8	0.38	29.4	49.6
		mm	8.5		0.03	7.0	49.6
2	AAAAT**QB**A$_L$ACUGA**G****QB**C$_L$A	m	109.0	6.2	0.23	16.2	49.8
		mm	17.6		0.10	7.3	49.3
3	CAAAAT**QB**A$_L$ACUGA**G****QB**C$_L$A	m	119.0	2.9	0.24	16.8	48.3
		mm	41.0		0.15	11.2	48.6
4	UCAAAAT**QB**A$_L$ACUGA**G****QB**C$_L$A	m	108.2	4.1	0.25	17.1	48.6
		mm	26.4		0.13	9.0	48.2
UE-QB-OMe							
C1	UCAAAAUAAACUGA**G****QB**C$_L$A	m	91.2	1.2	0.58	23.1	62.1
		mm	75.1		0.53	21.2	53.2
C2	UCAAA**QB**T$_L$AAACUGA**G**GCA	m	28.4	0.9	0.30	9.9	66.5
		mm	32.8		0.26	9.2	59.6
C3	UCAAAAT**QB**A$_L$ACUGA**G**GCA	m	36.0	0.9	0.19	7.6	65.3
		mm	42.2		0.17	6.4	58.2
ED-TO^2-OMe							
1	UCAAA**TO**T$_L$AAACUGA**A****TO**C$_L$A	m	6.5	3.0	0.44	46.6	52.3
		mm	2.1		0.25	27.4	45.1
2	AAAAT**TO**A$_L$ACUGA**A****TO**C$_L$A	m	8.2	5.7	0.19	18.7	50.5
		mm	1.4		0.09	9.3	45.6
3	CAAAAT**TO**A$_L$ACUGA**A****TO**C$_L$A	m	7.0	2.9	0.19	19.5	50.3
		mm	2.5		0.10	7.5	42.4
4	UCAAAAT**TO**A$_L$ACUGA**A****TO**C$_L$A	m	7.6	3.3	0.19	19.3	50.0
		mm	2.3		0.08	6.3	42.3
ED-TO-OMe							
C1	UCAAAAUAAACUGA**A****TO**C$_L$A	m	13.2	3.3	0.38	18.2	56.1
		mm	4.0		0.17	7.8	49.5
C2	UCAAA**TO**T$_L$AAACUGA**A**GCA	m	10.3	1.0	0.54	27.5	60.4
		mm	9.9		0.46	23.0	53.4
C3	UCAAAAT**TO**A$_L$ACUGA**A**GCA	m	7.7	0.5	0.28	12.8	52.4
		mm	14.8		0.43	20.1	61.8

Conditions: 0.5 µM probe and 5 eq. RNA target (5'-CUGAAGGACUCACCCUGC**Y**UCAGUUUAUUUUGA-3', UE: Y = C; ED: Y = U) were measured PBS buffer (100 mM NaCl, 10 mM Na_2HPO_4, pH 7.0) at 37 °C to determine fluorescence enhancement $E = I / I_0$ and specificity $S = E_m / E_{mm}$. Quantum yield ϕ and brightness $Br = \varepsilon_{\lambda ex} \cdot \phi / 1000$ in $M^{-1} \cdot cm^{-1}$ were measured at 25 °C. QB: λ_{ex} = 560 nm, λ_{em} = 605 nm; TO: λ_{ex} = 485 nm, λ_{em} = 535 nm, $slit_{ex/em}$ = 5 nm. Melting temperature T_m in °C was measured with 1 µM probe and 1 eq. (1 µM) target. Underscored letters = 2'OMe-RNA; subscript L = LNA; bold letters = editing site (black) and base surrogates (colour). Match and mismatch RNA target are indicated with m and mm.

Nevertheless, specificity and enhancement were higher compared to the mono-dye controls (**QB-OMe-C1 to -C3**). Also, the 2'OMe-RNA-based probes generally provided higher brightness than their non-nuclease resistant congeners, an important benefit for cell experiments on limited amounts of target.

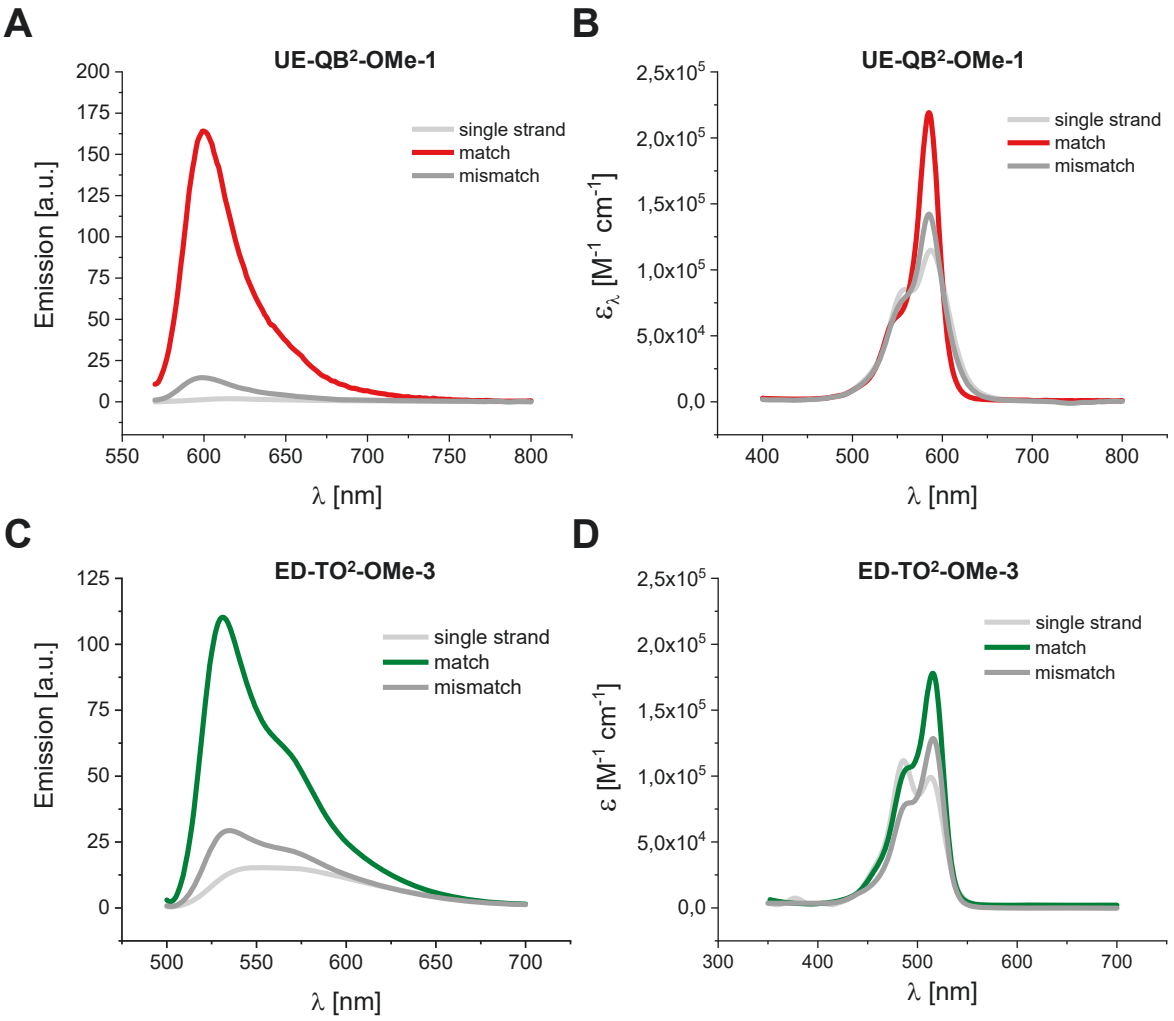

Figure 27: Emission and absorption spectra for selected QB and TO FIT[2] probes. Fluorescence emission of 0.5 µM (**A**) **UE-QB²-OMe-1** or (**C**) **ED-TO²-OMe-3** recorded at 37 °C in presence or absence of 5 eq. RNA target. Molar extinction coefficient as a function of absorption wavelength for (**B**) **UE-QB²-OMe-1** or (**D**) **ED-TO²-OMe-3**, recorded at 25 °C.

To create an orthogonal probe set, nuclease resistant TO FIT[2] probes were prepared as well. Amongst them, **ED-TO²-OMe-1** and **ED-TO²-OMe-2** stood out the most, the former due to its extraordinary brightness (E = 46.6), the latter because of its high specificity (S = 5.7). Still, the TO probes proved much less responsive than the QB-based ones (E = 7–15 vs. 26–125). This matches the observations made previously for the mono dye FIT probes. As for the QB probes, three control probes where synthesised for comparison (**ED-TO-OMe-C1** to **-C3**). **ED-TO-OMe-C1**, for which the dye is located next to the editing site, had about half the specificity (S = 3.3) of the best TO[2] probe, **ED-TO²-OMe-2** (S = 5.7). As expected, **ED-TO-OMe-C2** and **ED-TO-OMe-C3**, like **UE-QB-OMe-C2** and **UE-QB-OMe-C3**, exhibited much lower specificity values (S = 0.5-1), as in these probes the local microenvironment of the dye does not differ between match and mismatch duplexes. This contrasts the results of **Chapter 5.1.2.1**, where DNA-based QB FIT[2] probes were able to sense a mismatch even when the base surrogate was placed 7 to 9 nt away from the editing site (**UE-QB-C2** and **UE-QB-C3**). It is possible that the stronger binding

of the 2'OMe nucleotides fixes the dye more firmly in the duplex and thus reduces the impact of less proximal misalignments. This is favourable, as such probes will be generally more specific towards their intended target and respond less strongly to sequence patterns that might be present further away from the editing site.

Examining the emission and absorption spectra of the nuclease-resistant QB^2 probes (**Figure 27A** and **B**) more closely, it is noticeable that the pronounced H-bands previously observed in the non-nuclease resistant probes (**Figure 24**) almost disappeared. It must be assumed, that the introduction of 2'OMe building blocks somehow suppresses H-aggregation formation of QB. Despite this obvious drawback, **UE-QB^2-OMe-1** exhibited only very limited single strand fluorescence (**Figure 27A**). Conceivably, homo-FRET and/or collisional quenching is sufficient to suppress fluorescence in the absence of target in these probes. In contrast, the TO^2 probes (e.g. **ED-TO^2-OMe-3**; **Figure 27C**) showed significant single strand fluorescence. In addition, their absorption and emission peak shapes in the non-hybridized state differed strongly from that of the match (**Figure 27C and D**, green line) and mismatch (dark grey line) duplexes, while this was not the case for the QB^2 probes (in the emission spectrum, differences could not be determined due to the low single strand intensity close to baseline level). Finally, mismatch duplex fluorescence of the TO^2 probes was higher than that of the QB^2 probes. Together, these observations again confirm the high sensitivity of quinoline blue. Despite this, hybridisation of TO^2 probes with a matching target RNA caused enhancements well above single strand and/or mismatch level.

In the absorption spectrum of **ED-TO^2-OMe-3** (**Figure 27D**), one finds the characteristic second H-aggregate absorption band previously observed in the non-nuclease resistant QB^2 probes (**Figure 24**). It appears that the H-aggregate formation of TO-based FIT^2 probes is influenced less strongly by the presence of 2'OMe-RNA building blocks than that of the QB-based ones. As before, the effect becomes more obvious when the emission spectra are normalised (**Figure 28**). The single strand emission maximum of **UE-QB^2-OMe-3** (**Figure 28A**; light grey line) is still somewhat red-shifted compared to the duplex emission, but the extent of this effect is much smaller than in the non-nuclease resistant probes (**Figure 25A** and **Figure 28C**). Also, the peak shape is more similar to that of the duplex. In contrast, the single strand emission spectrum of **ED-TO^2-OMe-3** (light grey; **Figure 28B**) displays a somewhat more diffuse and broad peak shape, indicative of H-aggregate formation. This also results in a larger absolute wavelength shift (up to 20 nm) compared to the QB^2 probes (**Figure 28C**).

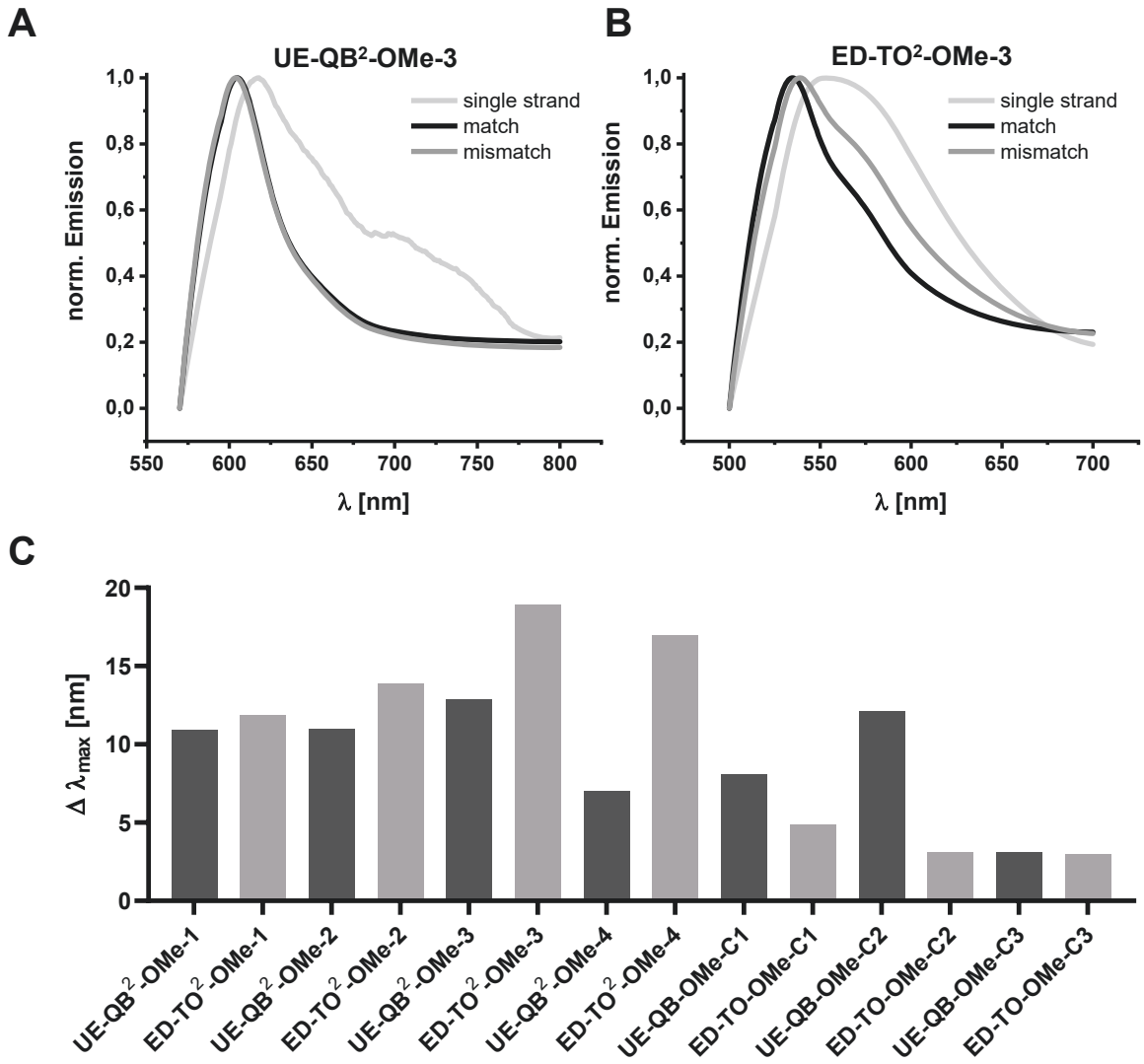

Figure 28: Normalised fluorescence emission spectra illustrating the wavelength shift of λ_{max} upon hybridization for select nuclease-resistant QB/TO FIT^2 probes. Emission spectra of (**A**) **UE-QB^2-OMe-3** or (**B**) **ED-TO^2-OMe-3**. (**C**) Wavelength shifts of single strand and match duplex emission for all probes of the set.

An outlier to this effect was **ED-TO-OMe-C2**. Here, the shift was much greater than for the other mono-dye control probes. It can be hypothesized that this probe's relatively short 5' extension leads to a broader fluorescence maximum. Furthermore, the nucleobase composition of the extension, comprising mostly adenine and uracil, may contribute to a locally weaker hybridisation, giving the cyanine dye more space to release energy by rotation instead of fluorescence.

To study the spectroscopic properties of probes with reversed specificity, another FIT^2 probe set was prepared, in which the probes targeting unedited mRNA carried thiazole orange, while those recognizing edited mRNA were equipped with quinoline blue (**Table 5**). In the same manner as before, control probes were designed and synthesised. To ensure complete hybridization, they were based on the sequence with the longest 5' extension.

Table 5: Spectroscopic properties of nuclease-resistant FIT[2] and mono-dye control probes with reversed specificity.

	Sequence 5' – 3'	RNA target	E	S	ϕ	Br	T_m
UE-TO[2]-OMe							
1	UCAAATOTLAAACUGAGTOCLA	m	16.1	2.8	0.37	37.1	56.9
		mm	5.8		0.25	25.2	50.2
2	AAAATTOALACUGAGTOCLA	m	10.2	4.2	0.22	22.2	52.5
		mm	2.4		0.11	11.8	51.3
3	CAAAATTOALACUGAGTOCLA	m	10.2	2.7	0.24	23.8	54.4
		mm	3.8		0.16	15.9	50.2
4	UCAAAATTOALACUGAGTOCLA	m	9.9	2.6	0.23	22.3	47.6
		mm	3.8		0.14	13.8	42.1
UE-TO-OMe							
C1	UCAAAATAAACUGAGTOCLA	m	15.2	2.0	0.59	4.5	58.4
		mm	7.7		0.32	2.8	48.2
C2	UCAAATOTLAAACUGAGGCA	m	11.0	1.1	0.43	7.5	63.5
		mm	10.3		0.44	7.5	56.5
C3	UCAAAATTOALACUGAGGCA	m	5.0	1.0	0.16	6.9	61.7
		mm	4.8		0.15	6.8	55.9
ED-QB[2]-OMe							
1	UCAAAQBTLAAACUGAAQBCLA	m	59.0	4.4	0.24	20.5	50.7
		mm	13.5		0.13	8.3	43.2
2	AAAATQBALACUGAAQBCLA	m	26.4	8.1	0.17	14.1	49.3
		mm	3.2		0.04	2.6	45.0
3	CAAAATQBALACUGAAQBCLA	m	63.8	5.7	0.22	18.2	48.8
		mm	11.2		0.10	6.1	41.9
4	UCAAAATQBALACUGAAQBCLA	m	49.7	3.0	0.22	17.8	48.6
		mm	16.8		0.10	6.2	43.6
ED-QB-OMe							
C1	UCAAAAUAAACUGAAQBCLA	m	61.7	4.0	0.36	13.9	56.3
		mm	15.5		0.13	4.7	49.1
C2	UCAAAQBTLAAACUGAAGCA	m	27.9	1.1	0.33	14.9	60.1
		mm	26.4		0.31	14.2	53.2
C3	UCAAAATQBALACUGAAGCA	m	11.3	1.4	0.17	6.2	54.7
		mm	8.3		0.13	5.3	49.1

Conditions: 0.5 µM probe and 5 eq. RNA target (5'-CUGAAGGACUCACCCUGC**Y**UCAGUUUAUUUUGA-3', UE: Y = C; ED: Y = U) were measured PBS buffer (100 mM NaCl, 10 mM Na_2HPO_4, pH 7.0) at 37 °C to determine fluorescence enhancement $E = I / I_0$ and specificity $S = E_m / E_{mm}$. Quantum yield ϕ and brightness $Br = \varepsilon_{\lambda ex} \cdot \phi / 1000$ in $M^{-1} \cdot cm^{-1}$ were measured at 25 °C. QB: λ_{ex} = 560 nm, λ_{em} = 605 nm; TO: λ_{ex} = 485 nm, λ_{em} = 535 nm, $slit_{ex/em}$ = 5 nm. Melting temperature T_m in °C was measured with 1 µM probe and 1 eq. (1 µM) target. Underscored letters = 2'OMe-RNA; subscript L = LNA; bold letters = editing site (black) and base surrogates (colour). Match and mismatch RNA target are indicated with m and mm.

The first of these probes, **UE-TO[2]-OMe-1**, had remarkably high quantum yield (ϕ = 37 %) and brightness (Br = 37.1). Unfortunately, its specificity was rather low (S = 2.8), especially compared to the mono-dye control **UE-TO-OMe-C1** (S = 2.0). A reason for this could be the long dye-dye distance of 9 nt, which might impair radiation-less energy transfer between the

fluorophores. This leads to an overall higher fluorescence output but also increases the emission in the mismatch duplex, which offsets the otherwise extraordinary probe characteristics. The other three TO sequences, **UE-TO^2-OMe-2** to **-4** had significantly lower brightness. They all fell within the same range of 22–24, which is still somewhat higher than the values obtained for the previous set. Amongst them, the sequence with the shortest 5' extension (**UE-TO^2-OMe-2**) proved the most specific (S = 4.2). This reinforces the previous hypothesis that the dye-dye distance defines quantum yield and brightness, while the size of the 5' extension has greater influence on probe specificity.

Comparing the **UE-QB^2-OMe** probes with the **ED-QB^2-OMe** set, the latter displayed higher specificity. Even though the excellent discrimination of **UE-QB^2-OMe-1** (S = 14.8; **Table 4**) could not be achieved with the **ED-QB^2-OMe** probes, their average specificity was higher. Likewise, it was higher than that of the corresponding TO probes (S = 8.1 for **ED-QB^2-OMe-2** vs. 5.7 for **ED-TO^2-OMe-2**). In line with previous observations, the probes with the shortest 5' extension had the highest specificity (except for **UE-QB^2-OMe-1**). Gratifyingly, the brightness values of some of the **ED-QB^2-OMe** probes came close to those of the **UE-TO^2-OMe** probes. It can thus be concluded that with the FIT^2 dual-dye probe design, it is possible to raise the brightness of QB-based probes towards TO-levels, while retaining their high specificity.

Looking at both sets, it is obvious that the specificity values calculated for the **ED-TO^2-OMe** probe set (**Table 4**) exceed those of the **UE-TO^2-OMe** set (**Table 5**). The former reached values of up to 5.7 (**ED-TO^2-OMe-2**), while the maximum of the latter was only 4.2 (**UE-TO^2-OMe-2**). Interestingly, the reverse was true for the QB FIT^2 probes. Here, the UE set was more specific (max. S = 14.8 for UE vs. 8.1 for ED). Based on these results, it seems reasonable to conclude that in a combined application, edited GlyRα mRNA would best be targeted with TO^2-OMe probes, while QB^2-based ones would be used for the unedited sequence.

In both sets, the shorter dye-dye distance produced probes with higher enhancement factors and better discrimination. Conversely, a longer distance appeared to favour brightness. This suggests that for the latter quenching is less efficient, resulting in increased fluorescence output – but also in the mismatch state. To better assess the efficiency of quenching by H-aggregate formation, the wavelength shift of the fluorescence maxima was again compared by normalization of the emission spectra (**Figure 29**).

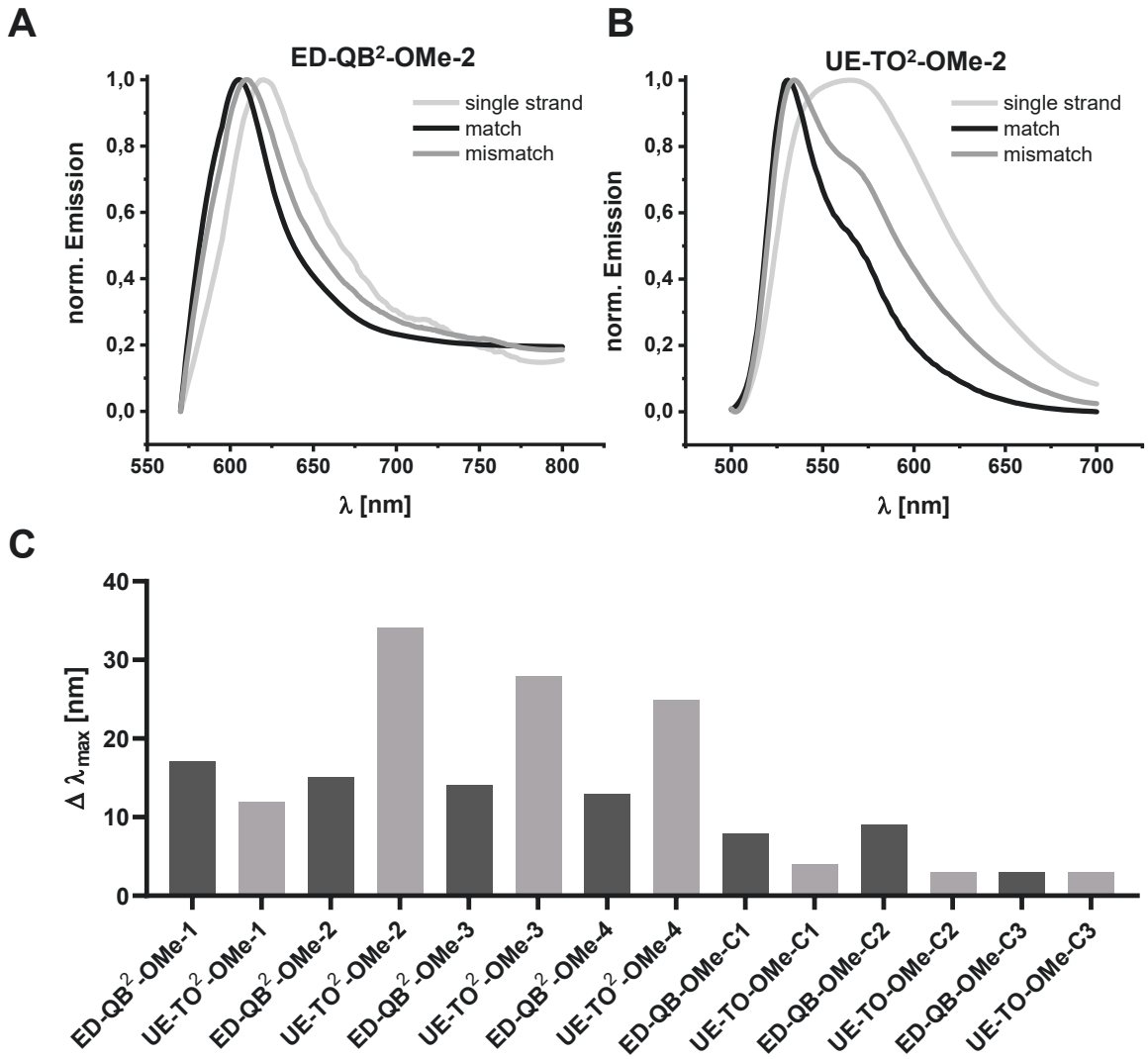

Figure 29: Normalised fluorescence emission spectra illustrating the wavelength shift of λ_{max} upon hybridization for select reversed specificity nuclease-resistant QB/TO FIT^2 probes. Emission spectra of (**A**) **ED-QB^2-OMe-3** or (**B**) **UE-TO^2-OMe-3**. (**C**) Wavelength shifts of single strand and match duplex emission for all probes of the set.

Consistent with previous results, the QB-based probes exhibited smaller $\Delta\lambda_{max}$ values and their peak shape remained narrower. Notably, the λ_{max} value for the 9 nt-spaced probe **UE-TO^2-OMe-1** did not differ significantly from the equivalent **ED-QB^2-OMe-1** probe. However, when the dye-dye distance was reduced to 7 nt, the shift almost tripled (**Figure 29C**). This suggests that homo-FRET processes and H-aggregate formation are more prevalent in probes with a shorter dye-dye distance, making them more suitable for the FIT^2 approach. Elongation of the 5'-end slightly decreased the $\Delta\lambda_{max}$ value, but even for the maximum probe length tested it remained above 25 nm. A common feature of all dual dye probes was that their $\Delta\lambda_{max}$, was significantly greater than that of the mono-dye controls, possibly due the absence of dye-dye interaction in the latter. It should be mentioned that, in contrast to the QB^2 FIT^2 probes, the TO^2 congeners had a much broader peak shape in the single strand. A possible explanation for this more diffuse emission could be partial excimer formation (see **Chapter 3.2**).

Regarding the thermal stability of the 2'OMe-RNA based probe sets, in most cases a larger difference between match and mismatch duplex was present than for the DNA-based probes. When comparing TO^2 and QB^2 probes of the same length and sequence, QB seems to have a more destabilizing effect than TO. Compared to their respective mono-dye control probes, the match duplex melting points of the dual dye probes were 2–4 °C lower for TO, while the introduction of an extra QB base surrogate resulted in a decrease of 6–13 °C. In **Figure 30** the melting curves of four probes of the **ED-QB²-OMe** probe set are shown. Notably, the hyperchromicity slope for **ED-QB²-OMe-2** and **ED-QB²-OMe-4** (**Figure 30A** and **B**) is nearly linear, resulting in a wider peak shape of the first derivative.

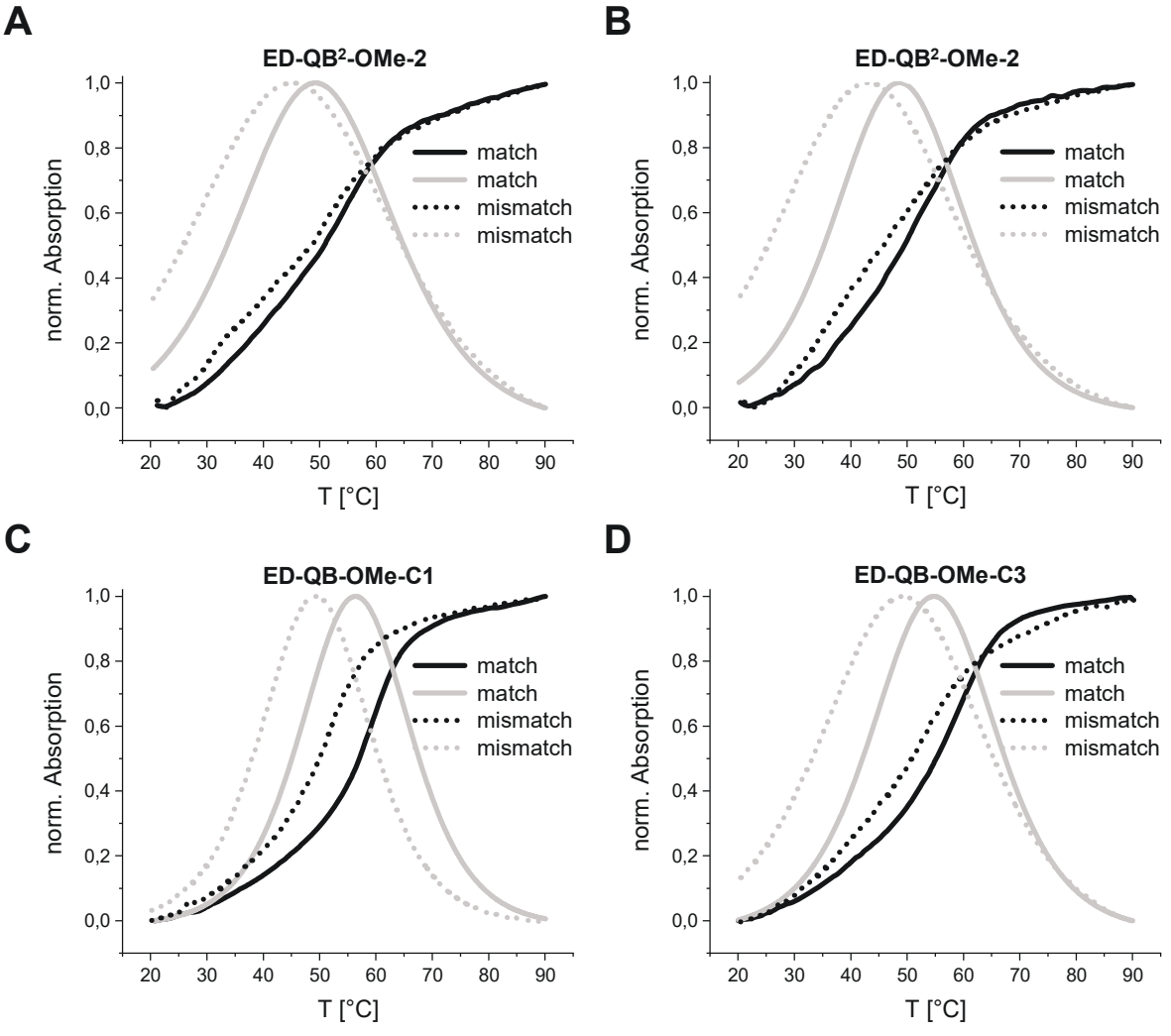

ED-QB²-OMe-2	AAAATQBA$_L$ACUGAAQBC$_L$A	ED-QB²-OMe-3	CAAAATQBA$_L$ACUGAAQBC$_L$A
ED-QB²-OMe-4	UCAAAATQBA$_L$ACUGAAQBC$_L$A	ED-QB-OMe-C1	UCAAAATQBA$_L$ACUGAAGCA

Figure 30: Exemplary melting curves for selected QB^2 probes. Melting temperature T_m in °C was measured with 1 µM probe and 1 eq. (1 µM) target RNA in PBS buffer (100 mM NaCl, 10 mM Na_2HPO_4, pH 7.0). (**A**-**D**) Thermal stability of match (solid black line) and mismatch (dotted black line) duplexes, as well as the respective first derivative (grey) of a sigmoidal Boltzmann fit.

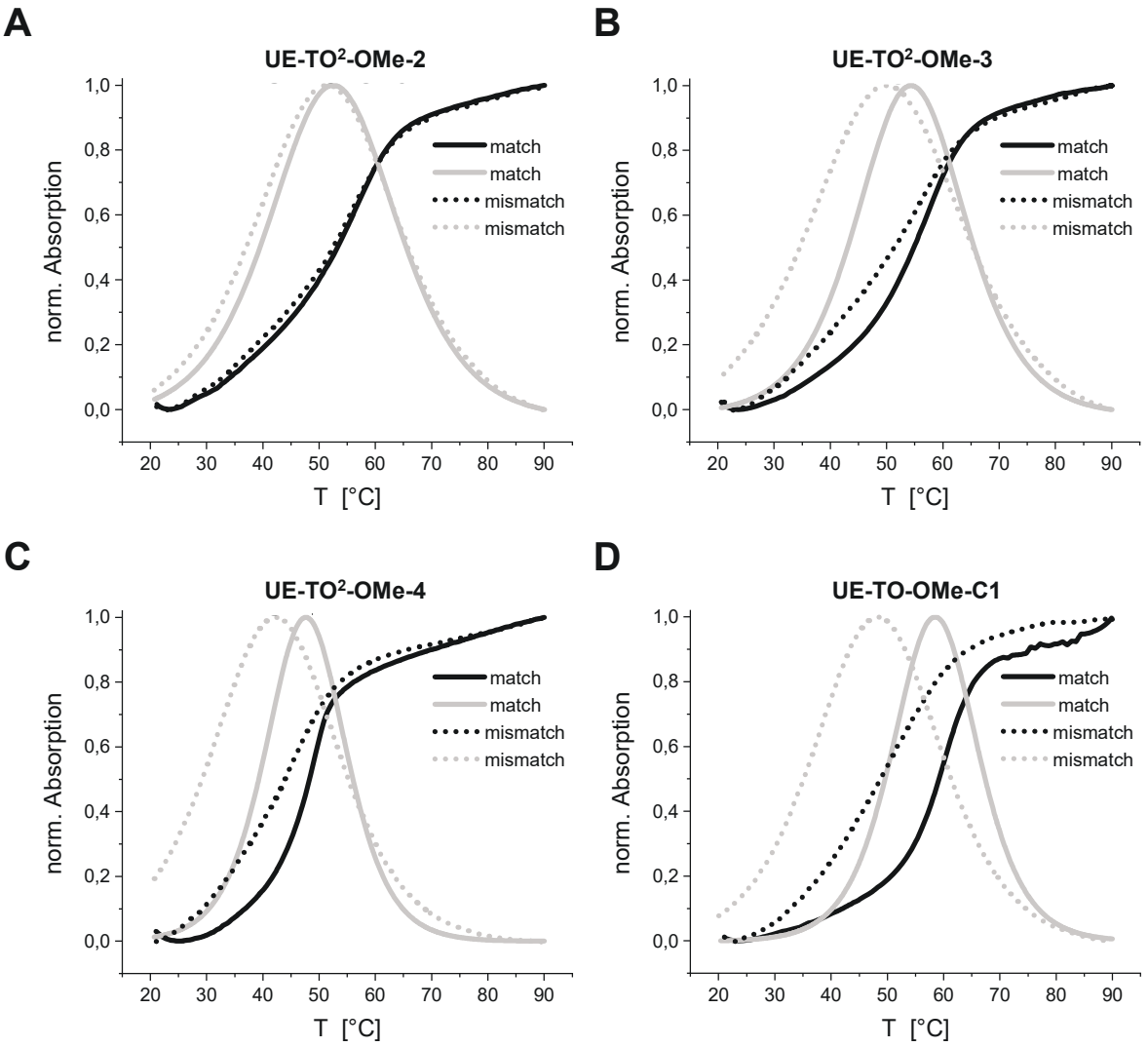

Figure 31: Exemplary melting curves for selected TO^2 probes. Melting temperature T_m in °C was measured with 1 µM probe and 1 eq. (1 µM) target RNA in PBS buffer (100 mM NaCl, 10 mM Na_2HPO_4, pH 7.0) **UE-TO²-OMe** and **UE-TO-OMe** control probes. (**A-D**) Thermal stability of match (solid black line) and mismatch (dotted black line) duplexes, as well as the first derivative (grey) of a sigmoidal Boltzmann fit.

In contrast, the melting curves of mono-dye control probes **ED-QB-OMe-C1** and **ED-QB-OMe-C1** more closely follow the expected sigmoidal shape. This illustrates the destabilising effect of an additional QB base surrogate, despite otherwise similar melting temperatures (ΔT_m = 4–5 °C). A comparison of the thermal stability curves of the **UE-TO²-OMe** probes reveals that with increasing length of the 5' extension, the discrimination between match and mismatch hybridisation becomes more pronounced (**Figure 31**) to better distinguish match and mismatch targets. The reason for this counter-intuitive behaviour may be due to the destabilizing effect of the additional base surrogate, which interferes with hybridization. This might also be reflected in the increasing asymmetry of the curves in the shorter probes.

In summary, this chapter described a new design principle for FIT probes that introduces two QB or TO fluorophores to gain increased specificity and brightness upon match hybridization while reducing background emission in the single strand and during mismatch hybridization. The optical properties of mono-labelled FIT and dual-labelled FIT^2 probes with different dye-dye distances and 5' extension lengths were compared in the presence of either excess or stoichiometric amounts of RNA target. These experiments demonstrated that a short inter-dye distance of 7 nt provides more efficient homo-FRET quenching during mismatch hybridisation than a wider spacing of 9 nt. Additionally, a shorter 5' extension often resulted in higher specificity, perhaps due to locally decreased thermal stability and thus reduced duplex rigidity.

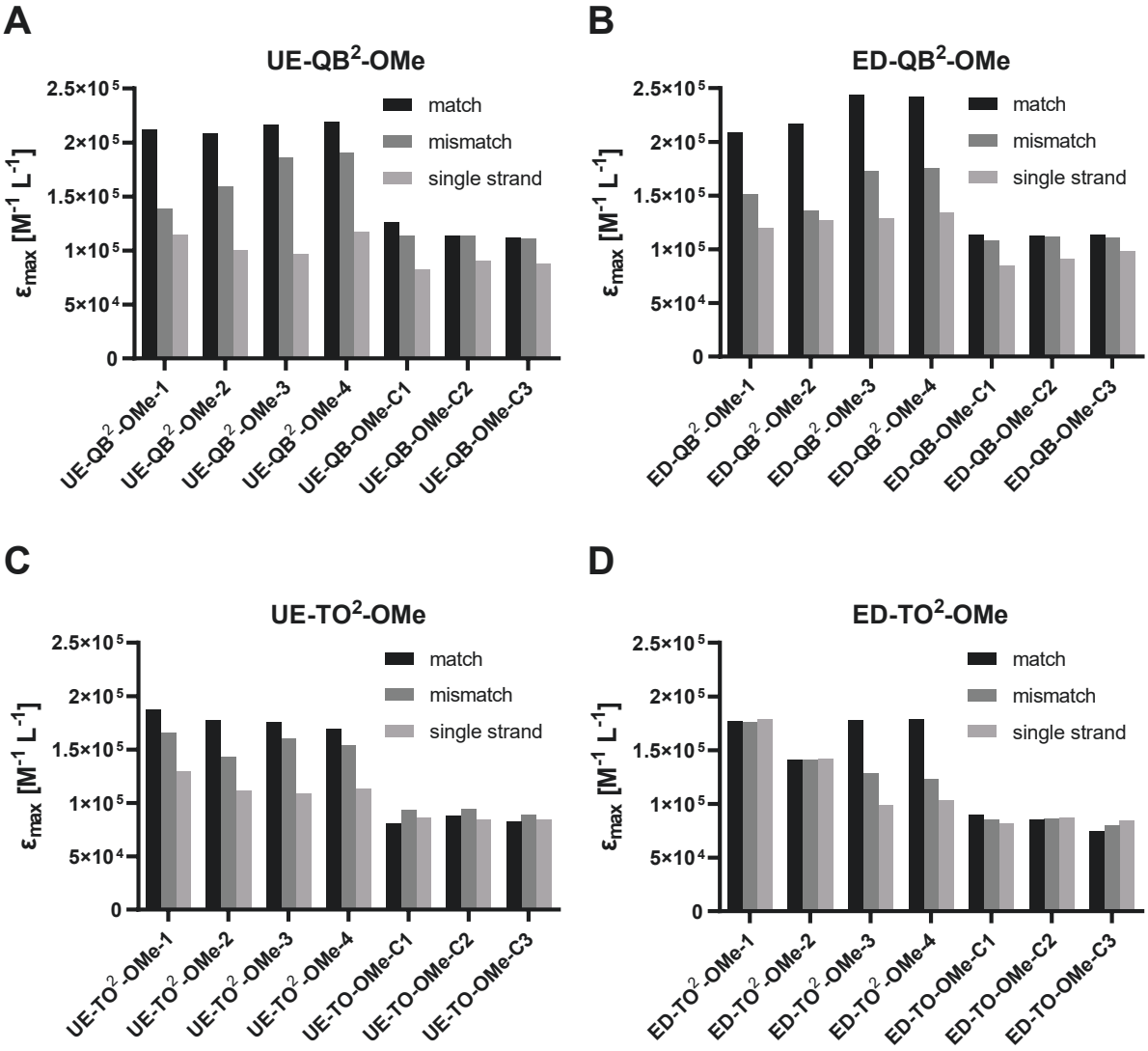

Figure 32: Maximum extinction coefficients of all synthesized nuclease-resistant dual dye probes and their respective mono-dye controls. Depicted are the values for probe sets (**A**) **UE-QB^2-OMe,** (**B**) **ED-QB^2-OMe**, (**C**) **UE-TO^2-OMe** and (**D**) **ED-TO^2-OMe**. Values for the QB probes were determined at λ_{ex} = 588 nm, values for the TO probes at λ_{ex} = 515 nm. All probes were measured at 25 °C.

A comparison of probes equipped with quinoline blue or thiazole orange revealed striking differences between the two dyes. In general, QB proved more responsive and gave higher enhancement factors than TO, but also suffered from lower brightness (in the mono-labelled probes). This was already known from previous works by Felix Hövelmann.[324] Gratifyingly, introduction of a second dye helped to overcome this limitation, increasing fluorescence brightness, while preserving the favourable high responsiveness of this fluorophore. This resulted in FIT^2 probes with extraordinary enhancement (E = 125 for **UE-QB^2-OMe-1** and 59 for **ED-QB^2-OMe-1**). In contrast, thiazole orange FIT probes, which are known to have decent quantum yield and brightness, but lack enhancement and specificity, did not benefit from introduction of a second dye molecule to the same extent as the QB-based ones did. Nevertheless, they demonstrated a remarkable further increase of their absolute brightness.

Irrespective of the dye used, all FIT^2 probes had comparable molar extinction coefficients at their respective absorption wavelength in the single strand, but hybridisation to their RNA target significantly increased that value (**Figure 32**). In case of the match duplex, the molar extinction coefficient nearly doubled for most sequences. In contrast, the ε_{max} value of most mono-dye control probes stayed more or less constant, regardless of their hybridization state. This is an indicator for the presence of the proposed dye-dye interaction mechanism of the dual-dye FIT^2 probes.

5.1.3 Competition Experiments in Phosphate Buffer and HEK295 Cell Lysate

To determine how FIT^2 probes would perform in a cell-like environment with many potentially interfering oligonucleotides and proteins present, a competion experiment in HEK 293 embryonic kidney cell lysate was set up. One equivalent (500 nM) each of both a UE- and ED FIT^2 probe were mixed with one equivalent of either UE- or ED-RNA target in PBS buffer supplemented with 0 %, 20 % or 100 % cell lysate. As a direct comparison, the same experiment was performed with the corresponding **C1** mono-dye control probe. As described before, the presence of equimolar amounts of the probes was verified by determining the UV absorption prior to each experiment. First, the fluorescence emission of both single stranded probes was measured in the presence of each other. Then, the RNA target was added and, after a 10 min incubation at room temperature for hybridization, the emission of the duplexes was measured.

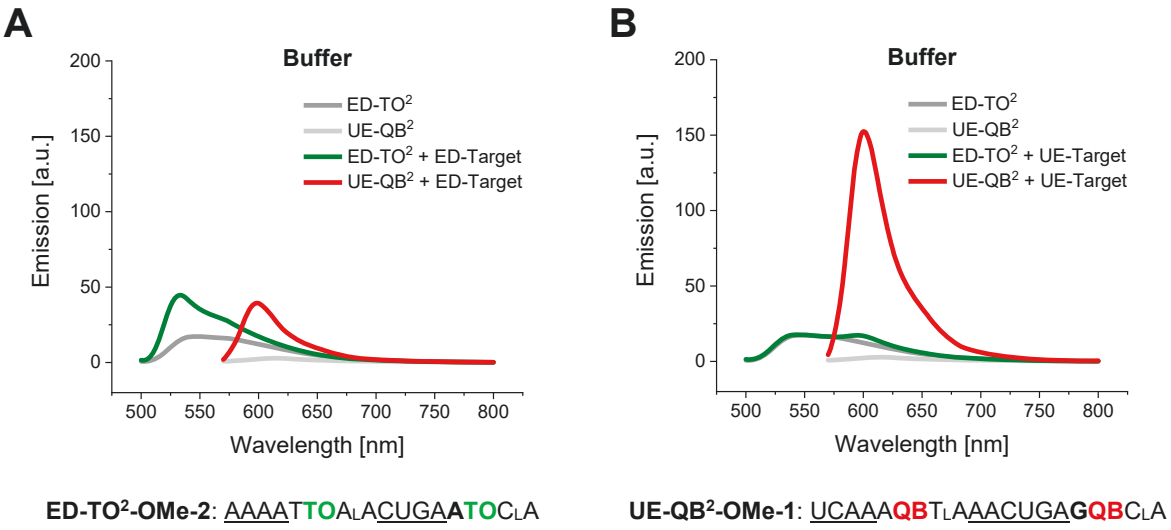

ED-TO^2-OMe-2: AAAATTOALACUGAATOCLA

UE-QB^2-OMe-1: UCAAAQBTLAAACUGAGQBCLA

Figure 33: Fluorescence emission of nuclease-resistant probes in a competitive setup in PBS buffer. Probes were measured in the absence (light and dark grey) or presence of either edited or unedited RNA-target. Conditions: 0.5 µM **ED-TO^2-OMe-2**, 0.5 µM **UE-QB^2-OMe-1** and 0.5 µM target-RNA (5'-CUGAAGGACUCACCCUGC**Y**UCAGUUUAUUUUGA-3'; UE: Y = C, ED: Y = U). Experiments were conducted at 37 °C in PBS buffer (100 mM NaCl, 10 mM Na_2HPO_4, pH 7.0). QB: λ_{ex} = 560 nm, λ_{em} = 605 nm; TO: λ_{ex} = 485 nm, λ_{em} = 535 nm, $slit_{ex/em}$ = 5 nm.

Surprisingly, the previously determined specificity values were not in all cases decisive for probe performance in this setup. **ED-TO^2-OMe-2** (S = 5.7; E = 8.2), the best candidate in previous experiments, failed to bind the target specifically enough in the presence of **UE-QB^2-OMe-1** (**Figure 33**). Conceivably, the short length of the **ED-X^2-OMe-2** design and presence of adenine at the editing site led to a weaker hybridisation when a longer UE competitor is present. As alternative, **ED-TO^2-OMe-4** was used, which is two nucleotides longer and previously exhibited the second highest selectivity (S = 3.3; E = 7.6). For a second reversed specificity probe set, **UE-TO^2-OMe-2** (S = 4.2; E = 10.2) and **ED-QB^2-OMe-1** (S = 4.4; E = 59.0) were selected. Both sets were compared with each other and the respective **C1** mono-dye control.

In **Figure 34** the enhancements of the probes in presence of match (**Figure 34A**) or mismatch (**Figure 34B**) RNA target are shown. It is evident that in lysate the enhancement factor of all probes was reduced – the higher the concentration, the greater the reduction. This is possibly a result of a non-specific interaction with proteins or non-target nucleic acid sequences in the lysate, which reduces the amount of probe available for hybridization with the target and thus limits the maximum achievable fluorescence gain. Interestingly, when measured in 100 % cell lysate, the enhancement factor of most probes seemed to plateau at a similar level (E = 5–10). Of note, the lysate concentration also had a considerable effect on single strand fluorescence intensity (**Figure 34C**-**F**). Probe background emission was higher when larger amounts of lysate were present. This is most likely a result of the increased viscosity of the lysate slowing down methine bridge rotation. The mono-dye probes, lacking the self-quenching abilities of the FIT² design, were affected by this to a greater extent. The introduction of a second fluorophore seemingly helps to reduce the impact of medium viscosity on probe performance, making the FIT^2 approach more suitable for cell experiments. Hybridization within cells takes place in the cytoplasm, where the presence of numerous biological macromolecules could potentially hinder rotational energy release, unfavourably increasing signal-to-noise ratio. Self-quenching FIT^2 probes may overcome this issue by providing alternative means of deexcitation.

To determine how well the two different probes sets discriminate match and mismatch target, their specificity values were calculated (**Figure 35A**). Although those were in some cases different from the previous, non-competitive experiments on excess target RNA (**Figure 35A**; see also **Table 4** and **Table 5**), the dual-dye probes generally retained a higher discrimination ability than their mono-dye counterparts (with the exception of **ED-TO^2-OMe-4**). Notably, the presence of lysate decreased the specificity of all probes tested. As described above, this may be connected to increased fluorescence emission in the single strand in a higher viscosity environment, but it is unclear why this should affect match and mismatch hybridization differently. Instead, it can be speculated that the Triton X-100 detergent present in the lysate somehow interferes with hybridization. This has a stronger effect on the match duplex, as here the fluorescence enhancement is greater than in the mismatch state and thus a destabilization might be more noticeable. Of note, in 100 % lysate all FIT² probes maintained higher specificity than their mono-labelled counterparts, including **ED-TO^2-OMe-4**.

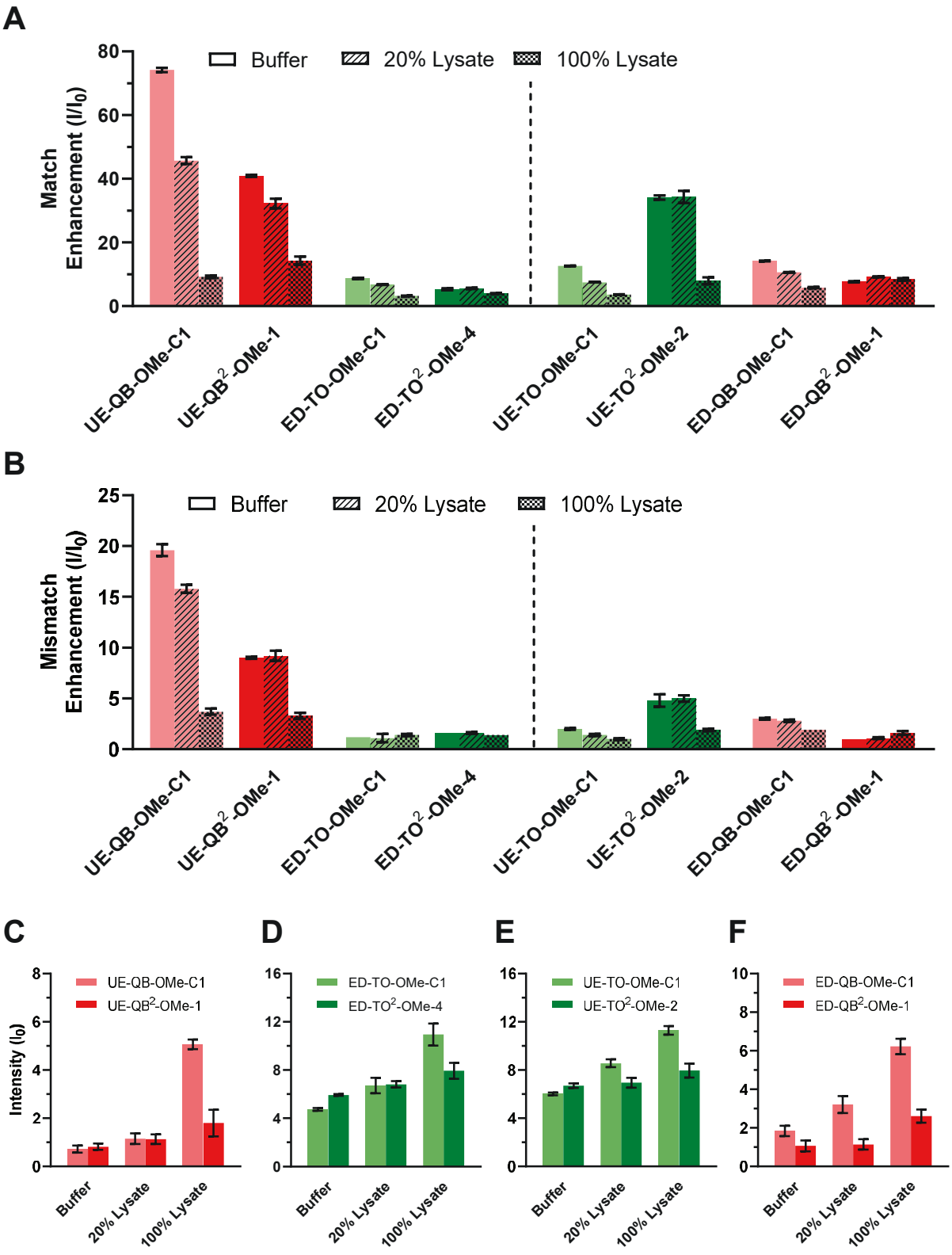

Figure 34: Competitive measurements of dual-dye FIT^2 and mono-dye control probe pairs in lysate. Enhancement factors of probe combinations (**UE-QB-OMe-C1** + **ED-TO-OMe-C1**; **UE-QB^2-OMe-1** + **ED-TO^2-OMe-4**; **UE-TO-OMe-C1** + **ED-QB-OMe-2**; **UE-TO^2-OMe-2** + **ED-QB^2-OMe1**) determined in the presence of (**A**) match or (**B**) mismatch RNA target. (**C–F**) Single strand emission intensity I_0 of the probes and their corresponding mono-dye control. Measurements were performed at 37 °C in phosphate buffer (100 mM NaCl, 10 mM Na_2HPO_4, pH = 7.0) supplemented with 0 %, 20 % or 100 % HEK 293 cell lysate. Probes were combined at a concentration of 500 nM each and 1 eq. (500 nM) RNA target was spiked into the mixture. Fluorescence emission was measured at QB: λ_{ex} = 560 nm, λ_{em} = 605 nm; TO: λ_{ex} = 485 nm, λ_{em} = 535 nm, $slit_{ex/em}$ = 5 nm. Data represents the mean of three independent measurements with SD.

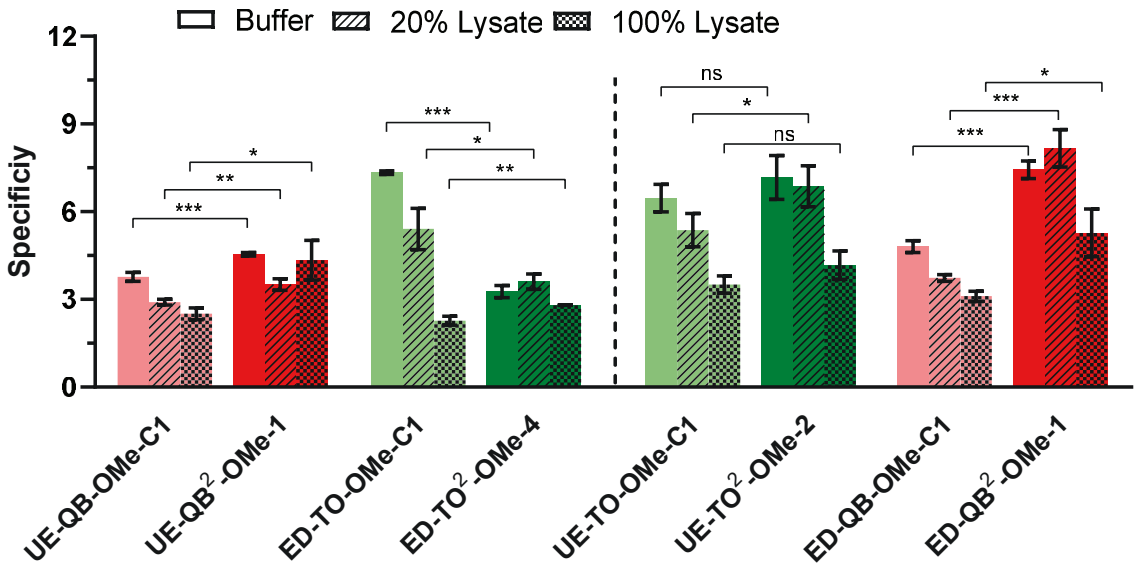

Figure 35: Comparison of the specificity of dual-dye FIT^2 and mono-dye control probes determined in competitive experiments in lysate. Measurements were performed at 37 °C in phosphate buffer (100 mM NaCl, 10 mM Na_2HPO_4, pH = 7.0) supplemented with 0 %, 20 % or 100 % HEK 293 cell lysate. Probes were combined at a concentration of 500 nM each and 1 eq. (500 nM) RNA target was spiked into the mixture. Fluorescence emission was measured at QB: λ_{ex} = 560 nm, λ_{em} = 605 nm; TO: λ_{ex} = 485 nm, λ_{em} = 535 nm, $slit_{ex/em}$ = 5 nm. Data represents the mean of three independent measurements with SD. Statistical analysis by two-tailed Student's t-test: ns = not significant, * $p \leq 0.05$, ** $p \leq 0.01$, *** $p \leq 0.001$.

Some sequences (such as **UE-QB²-OMe-1**) exhibited markedly reduced specificity in the presence of a competitor, while others (such as **UE-TO²-OMe-2**) had increased specificity values – the same effect could be observed for the mono-dye controls. In this context, it appears, that when introducing a second fluorophore, the 5' overhang must be long enough to provide sufficient rotational constraint to the fluorophore upon hybridization, so that specificity remains high in a competitive setup.

5.2 qFIT^2 Probes for T-Cell Receptor mRNA Recognition

The adaptive immune system consists of T- and B-lymphocytes, which both play a pivotal role in the recognition and elimination of foreign pathogens.[337] In addition, T-cells have been found to be able to detect cancer cells through proteins presented on their surface via the *T-cell receptor* (TCR).[338] This property is taken advantage of in so-called cancer immunotherapy.[339] In this approach, a patient's own immune system is exercised to eliminate malignant cells. Unfortunately, the body's capacity of cancer-recognising T-cells is often insufficient for an effective treatment. Moreover, the activation of a T-cell response upon recognition of cancer antigens is relatively weak. To improve therapeutic efficiency, T-cells from a patient are extracted and genetically modified *ex vivo* with a *chimeric antigen receptor* (CAR), which has high affinity for specific cancer antigens and induces a strong T-cell response upon their recognition. These modified T-cells are then cultivated and re-implanted into the patient.[340, 341] While this approach is highly efficient, there are considerable side effects. Administration of CAR T-cells can lead to a shock immune response, a so-called cytokine storm, which can be fatal to the patient. In addition, CAR T-cells often fail to distinguish cancer cells and B-lymphocytes, causing damage to the immune system.[342, 343] Finally, there is a practical disadvantage: genetic modification and cultivation of CAR T-cells requires a considerable amount of time and it is possible that patients succumb to their disease before the treatment can be administered.

In order to overcome these issues while still harnessing the potential of the immune system to fight cancer, it has been proposed to extract and enrich endogenous T-cells that recognise cancer cells, e.g. by fluorescence activated cell sorting (FACS).[305] As these cells are unmodified, side effects may be less severe. To pursue this strategy, however, a precise tool that allows specific tagging of endogenous T-cells that express the correct TCR is required. Typically, cells are sorted according to their surface proteins and antibodies are used for tagging.[344, 345] However, this requires a relatively high expression of the protein of interest and availability of suitable antibody. It is thus desirable to address the issue one step earlier, on the mRNA level.

In her PhD work, Jasmine Chamiolo developed a first generation of TO-based FIT probes that selectively stain a specific TCR-mRNA sequence upon hybridization.[305] Her probes were targeted against the CDR3 (complementarity determining region) of the TCR, the sequence that dictates antigen specificity. Using these FIT probes and quantitative analysis of fluorescence enhancement data, she was able to distinguish between Jurkat and MOLT-16 cells, which served as models for the natural diversity of the CD3 region.

In order to better discriminate between successfully hybridized FIT probes and false-positive signals generated by excess probe delivered into the cells during transfection, the qFIT system developed by Hövelmann *et al.* (see **Chapter 3.5.6**) was applied to the probes.[295] This allowed calculation of a ratio between the emission of thiazole orange and a Cyanine 7 (Cy7) reference dye, whose fluorescence is independent of hybridisation. A change in the ratio was interpreted as successful hybridization. Using these CDR3 qFIT probes, it was possible to positively tag 82% of Jurkat cells and 87 % of CCRF-CEM cells.[305] This demonstrated the principal applicability of the system for FACS-based sorting of mixed cell populations. Nevertheless, for an effective use, the probes would benefit from a higher signal intensity and a better signal-to-noise-ratio. The second part of this work should therefore evaluate whether this can be achieved with the FIT^2 concept.

5.2.1 qFIT^2 Probes for Jurkat Cell CDR3 Labelling

To improve upon the CDR3 labelling system developed by Jasmine Chamiolo, the FIT^2 concept was extended with a Cyanine 7 reference dye (**Figure 36**). The resulting qFIT^2 probes were targeted to the same CDR3 sequence as previously reported.[305] To find the optimal configuration, several distances, both between the two TO dyes as well as between TO and Cy7 should be screened. Experiments conducted by Jasmine Chamiolo suggested that a distance of nine nucleotides between TO and Cy7 (**Jurkat a-Cy7**) results in the greatest enhancement and thus the least amount of quenching between TO and Cy7 in the duplex.[305] For the qFIT^2 approach, the Jurkat-specific sequence chosen by Jasmine Chamiolo was extended to allow incorporation of a second TO base surrogate eight nucleotides upstream of the first. This distance was chosen deliberately, as pyrimidine bases are preferable to purines as direct neighbours of TO.[324] To find a suitable position for the reference dye Cy7, three different distances to TO (13, 15 and 17 nt or 3.38, 3.90 and 4.42 nm, respectively) were selected. As previously described, Cy7 was attached to the probe by copper-catalysed azide-alkyne cycloaddition (CuAAC).[346] For this, an alkyne-modified CPG solid support was used during phosphoramidite synthesis and azide-modified Cy7 was conjugated in solution after deprotection and cleavage (**Figure 36B**).[305, 347]

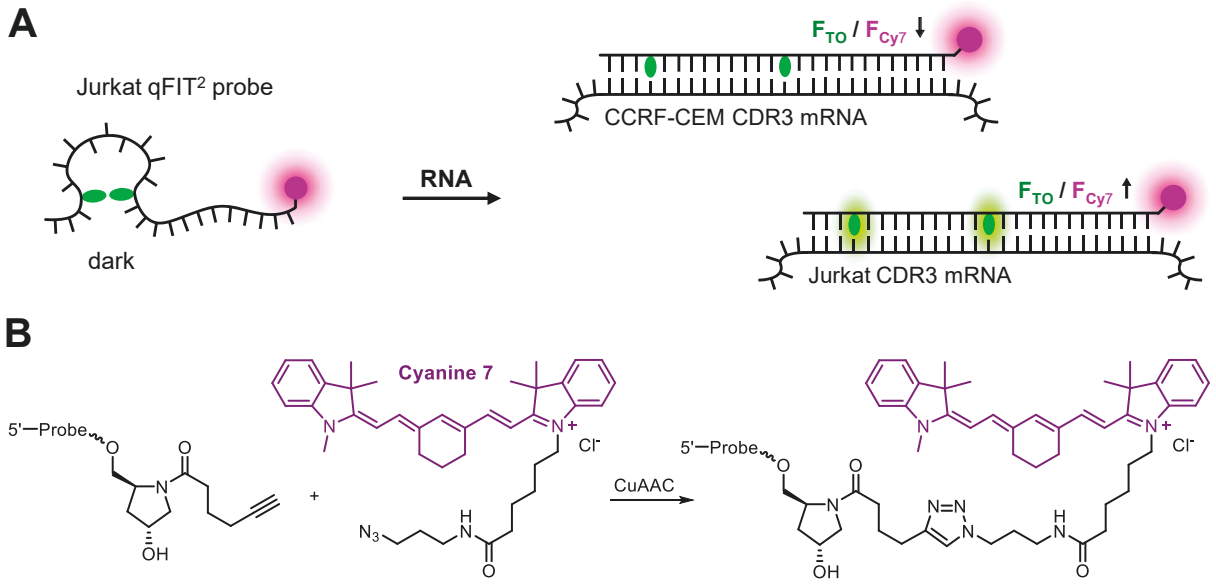

Figure 36: Principle of the qFIT²-approach. (**A**) FIT² probes equipped with an additional, non-hybridization sensitive Cyanine 7 reference dye allow calculation of a TO/Cy7 fluorescence ratio that can be used to account for local differences in probe concentration and to subtract background. Hybridization to the correct target sequence (e.g. binding of a Jurkat-specific probe to Jurkat CDR3 mRNA) is indicated by an increase in this ratio. (**B**) 3'-Modification of probes with Cy7 azide was achieved by copper-catalyzed azide-alkyne cycloaddition. The reaction was carried out in PUS buffer (100 mM Tris, 100 mM NaOAc, 1 mM $MgCl_2$, pH 8.0) supplemented with sodium ascorbate (100 eq.), tris-hydroxypropyltriazolylmethylamine (THPTA; 55 eq.) and $CuSO_4$ (11.25 eq.).

Following synthesis, the spectroscopic properties of the probes, including the TO/Cy7 ratio in the duplex, were determined (**Table 6**). The TO emission enhancement (E_{535}) of all probes ranged between 12.3 and 16.5. Interestingly, the shortest measured TO-Cy7 distance of 13 nt resulted in the highest enhancement. This contradicts an earlier hypothesis by Jasmine Chamiolo that any negative influence of reference dye on fluorescence enhancement (due to quenching), decreases with distance.[305] On the other hand, the assertion that Cy7 fluoresces independently of hybridization could be confirmed: The enhancement factors calculated for the Cy7 emission (E_{733}) remained close to 1.0 for all probes tested. To identify possible interactions between thiazole orange and Cy7, two additional parameters were included in the analysis: The ratios r_0 and r, which describe the relationship between thiazole orange and Cy7 emission in the single and double strand, respectively. The larger r, the higher the florescence emission of TO is compared to Cy7. In the single strand, the emission ratios of all probes fell within a narrow range of 0.2–0.6. In the double strand, however, greater values due to increased thiazole orange fluorescence could be detected. Here, the shortest TO–Cy7 distance (13 nt; **JK-TO²-Cy7-1**) gave the lowest ratio of 3.3, while this value more than doubled (to 7.2) when the distance was increased by two nucleotides (15 nt; **JK-TO²-Cy7-2**). When another two nucleotides were added (17 nt; **JK-TO²-Cy7-3**), the ratio decreased again to 4.7. It is likely that TO quenching is most effective at the medium distance for these probes.

Table 6 Spectroscopic properties of qFIT² probes specific for Jurkat CDR3 mRNA.

	Sequence 5' – 3'	E_{535}	E_{733}	r_0	r	ϕ_{535}	Br_{535}
JK-TO²-Cy7							
1	GGTTOT$_L$AGCCAUATOT$_L$TAGCCGAACAGG-CY7	16.5	1.1	0.2	3.3	0.41	38.7
2	GGTTOT$_L$AGCCAUATOT$_L$TAGCCGAACAGGUC-CY7	12.3	1.0	0.6	7.2	0.42	36.2
3	GGTTOT$_L$AGCCAUATOT$_L$TAGCCGAACAGGUCGA-CY7	14.8	1.2	0.4	4.7	0.41	36.0

Conditions: 0.5 µM probe and 5 eq. RNA target (5'-GGUGUAGCCAUAGUUAGCCGAACAGGUCGA-3') were measured to determine fluorescence enhancement $E = I / I_0$ for TO (E_{535}) and for Cy7 (E_{773}). Single strand ratio r_0 and double strand ratio r were calculated as I_{535} / I_{773}. Enhancement factors and ratios were measured at 37 °C, quantum yield ϕ_{535} and brightness $Br_{535} = \varepsilon_{535} \cdot \phi_{535} / 1000$ in $M^{-1} \cdot cm^{-1}$ at 25 °C. Cy7: λ_{ex} = 650 nm, λ_{em} = 773 nm; TO: λ_{ex} = 485 nm, λ_{em} = 535 nm; $slit_{ex/em}$ = 5 nm. All measurements were conducted in buffer (100 mM NaCl, 10 mM Na_2HPO_4, pH 7.0). Underscored letters = 2'OMe-RNA; subscript L = LNA.

For live-cell experiments, a high ratio is preferable, as this allows better discrimination between free and target-bound qFIT² probes. However, enhancement, absolute probe brightness, and quantum yield are important factors as well. As the microenvironment of TO was kept constant in this study, enhancement factors (E_{535}) and quantum yields (ϕ_{535}) did not show much variability – their values ranged between 12.3–16.5 and 41–42 %. Likewise, probe brightness was very similar (Br = 36.0–38.7). It can thus be assumed that the influence of extending the Cy7-bearing 3'-end on these properties is insignificant. Two exemplary fluorescence emission spectra of the Jurkat probe set are depicted in **Figure 37**.

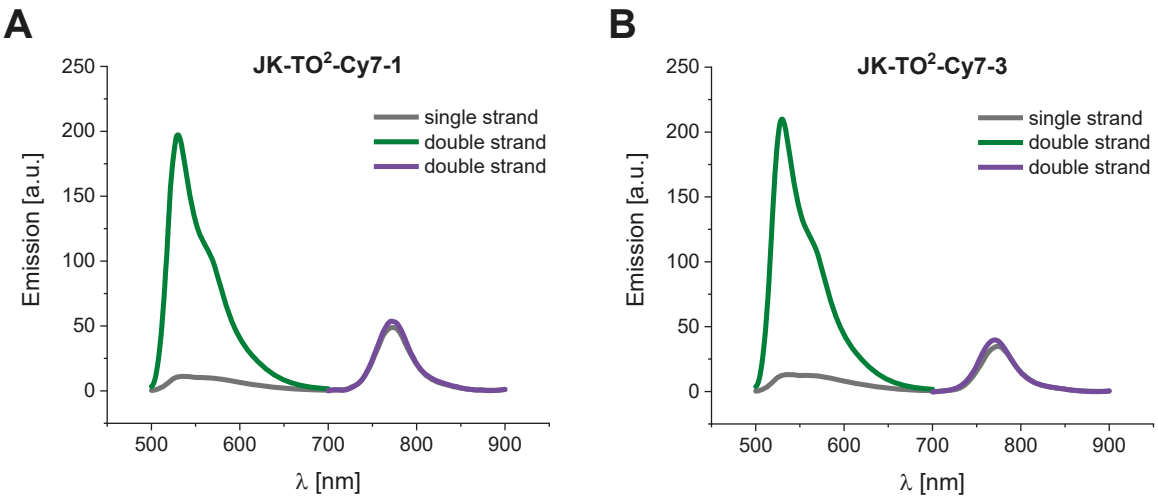

Figure 37: Fluorescence emission spectra of two different qFIT² probes specific for the Jurkat CDR3 region. Spectra of (**A**) **JK-TO²-Cy7-1** and (**B**) **JK-TO²-Cy7-3** recorded at 37° C in phosphate buffer (100 mM NaCl, 10 mM Na_2HPO_4, pH = 7.0). Depicted are the double strand fluorescence of TO (green) and Cy7 (purple), as well as the single strand emission (grey). Cy7: λ_{ex} = 650 nm, λ_{em} = 700–900 nm; TO: λ_{ex} = 485 nm, λ_{em} = 500–700 nm, $slit_{ex/em}$ = 5 nm.

5.2.2 qFIT^2 Probes for CCRF-CEM Cell CDR3 Labelling

To determine the influence of the TO-TO distance in the qFIT^2 design, different probes targeting the CDR3 region of CCRF-CEM cells were synthesised and evaluated (**Table 7**). For the first TO, a position between two thymidines in the middle of the sequence was selected. This position previously resulted in the best overall responsiveness and brightness.[305] As the chosen target sequence does not have a high pyridine content, options to also place the second TO in a pyrimidine-rich part were limited. Therefore, the second dye was placed 7-10 nt upstream.

For all probes the distance between TO and Cy7 was kept constant at 13 nt. A key finding from the previous experiment with the Jurkat qFIT^2 probe set was that the distance between TO and Cy7 does not have a significant impact on probe performance, given that a minimum distance of 13 nt is maintained. To reduce synthetic effort, the probe length was kept constant at 27 nt. Finally, in addition to the TO-TO distance, the effects of the microenvironment of the second dye should be assessed. As in previous experiments, a LNA building block was placed adjacent to both TO fluorophores to increase local constraint in the duplex. For the first TO moleculse, its position was fixed to the 3' side, while for the second one, it was varied.

Probes **CEM-TO^2-Cy7-1** and **-2** were designed with a distance of 9 nt between the two TO base surrogates. Assuming an A-type duplex with a rise of 2.6 Å/bp, this distance can be approximated as 2.3 nm, which still falls within the range where quenching via resonance energy transfer can occur effectively.[348] Both qFIT^2 probes demonstrated similar TO enhancement factors (E_{535} = 11.5 and 10.2; **Table 7**). Importantly, Cy7 emission remained almost constant (E_{773} = 1.1 and 1.2), confirming the independence of its fluorescence on the hybridization state. For both probes, an r_0 of 0.2 was determined. After hybridisation, that value increased 10-fold to 2.0 for **CEM-TO^2-Cy7-1**, and 7.5-fold to 1.5 for **CEM-TO^2-Cy7-2**, respectively. This difference was due to a higher TO fluorescence intensity for **CEM-TO^2-Cy7-1** in the duplex. This probe, with the LNA positioned 3' of TO, also had a higher TO quantum yield (ϕ_{535} = 25 %) and brightness (Br_{535} = 19) than **CEM-TO^2-Cy7-2** (ϕ_{535} = 20 %; Br_{535} = 15.8), for which the LNA was placed 5' of the fluorophore.

Table 7: Spectroscopic properties of qFIT^2 probes specific for CCRF-CEM CDR3 mRNA.

	Sequence 5' – 3'	E_{535}	E_{773}	r_0	r	ϕ_{535}	Br_{535}
CEM-TO^2-Cy7							
1	AUATOT_LGCGUAUCTTOT_LCCCAAGGCUGCU-CY7	11.5	1.1	0.2	2.0	0.25	19.0
2	ATA_LTOTGCGUAUCTTOT_LCCCAAGGCUGCU-CY7	10.2	1.2	0.2	1.5	0.20	15.8
3	AUACTTOC_LGUAUCTTOT_LCCCAAGGCUGCU-CY7	36.2	1.3	0.1	2.8	0.37	29.3
4	AUACT_LTOCGUAUCTTOT_LCCCAAGGCUGCU-CY7	33.7	1.3	0.1	1.9	0.22	17.3
5	ATTOC_LTGCGUAUCTTOT_LCCCAAGGCUGCU-CY7	13.7	1.1	0.2	2.6	0.37	30.1
6	AT$_L$TOCUGCGUAUCTTOT_LCCCAAGGCUGCU-CY7	14.5	1.3	0.1	1.5	0.24	19.7

Conditions: 0.5 µM probe and 5 eq. RNA target (5'-AUACUGCGUAUCUGUCCCAAGGCUGCUGGC-3') were measured to determine fluorescence enhancement $E = I / I_0$ for thiazole orange (E_{535}) and for Cy7 (E_{773}). Single strand ratio r_0 and double strand ratio r were calculated as I_{535} / I_{773}. Enhancement factors and ratios were measured at 37 °C, quantum yield ϕ_{535} and brightness $Br_{535} = \varepsilon_{535} \cdot \phi_{535} / 1000$ in $M^{-1} \cdot cm^{-1}$ at 25 °C. Cy7: λ_{ex} = 650 nm, λ_{em} = 773 nm; TO: λ_{ex} = 485 nm, λ_{em} = 535 nm; $slit_{ex/em}$ = 5 nm. All measurements were conducted in buffer (100 mM NaCl, 10 mM Na_2HPO_4, pH 7.0). Underscored letters = 2'OMe-RNA; subscript L = LNA.

In the same way, the two probes with a distance of 7 nt (ca. 1.8 nm) between the two TO base surrogates were compared. For **CEM-TO^2-Cy7-3** and **-4**, TO fluorescence enhancements of 36.2 and 33.7 were reached (**Table 7**). The enhancement factors for Cy7 equalled 1.3. This is slightly higher than the previous two probes, but emission may still be considered independent of the hybridization state. Interestingly, the single strand Cy7/TO ratios were very low (r_0 = 0.1). Upon hybridisation, this value increased to 2.8 for **CEM-TO^2-Cy7-3** and 1.9 for **CEM-TO^2-Cy7-4**. This was considerably higher than for **CEM-TO^2-Cy7-1** and **-2**, a result also reflected by their more pronounced TO enhancement. For **CEM-TO^2-Cy7-3**, the fluorescence gain upon hybridization was 28-fold, the highest value of the whole probe set. Likewise, the quantum yields and brightness values of these 7 nt spaced probes were distinctively higher, with 37 % and 22 %, respectively, for the TO quantum yield, and 29.3 and 17.3, respectively, for probe brightness. Comparing the fluorophore microenvironment created by the different LNA positioning, it is striking that, again, adding the LNA to the 3' side of the cyanine dye (**CEM-TO^2-Cy7-3**) provides overall better fluorescence properties than a placement on the 5' side. Both probes, **CEM-TO^2-Cy7-3** and **-4** surpassed the fluorescence properties of **CEM-TO^2-Cy7-1** and **-2,** which have 9 nt between the dyes. This is in good accordance with the data from the analysis of the GlyRα2 FIT^2 probes (see **Chapter 5.1.2**). It can be speculated that the optimal distance is a general property that is independent of the sequence of interest. So far, FIT probes

had to be specifically designed, tested, and optimised for each target. With sufficient data gathered, it is imaginable that the amount of work needed for screening can be reduced in the future if design principles can be applied more universally. This is essential for making RNA FIT probes a more versatile tool that can be easily adapted to different biologic questions.

Curiously, when the TO-TO spacing was further increased to 10 nt (2.6 nm), the probe performance improved again slightly. **CEM-TO^2-Cy7-5** and **-6** reached TO enhancements of 13.7 and 14.5, respectively. This is significantly lower than **CEM-TO^2-Cy7-3** and **-4** (E_{535} = 36.2 and 33.7), but somewhat higher than the values obtained for **CEM-TO^2-Cy7-1** and **-2** (E_{535} = 11.5 and 10.2). Likewise, the Cy7/TO double strand ratio increased to 2.6 and 1.5, respectively – the former value being close to the result of the best candidate **CEM-TO^2-Cy7-3** (r = 2.8). Also, the TO quantum yield of both probes reached favourable levels of 0.37 and 0.24.

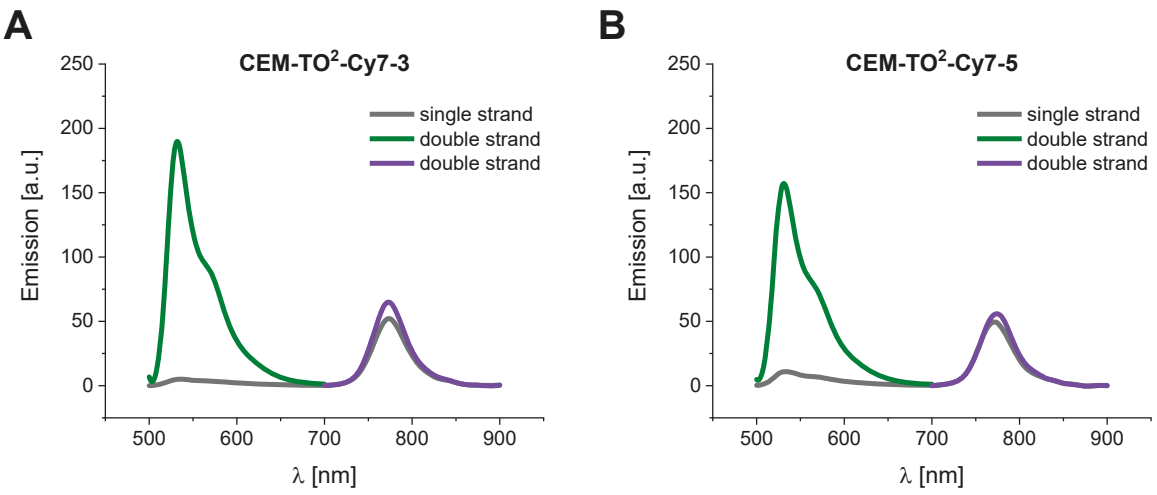

CCRF-CEM CDR3 RNA target: 5' AUA CUG CGU AUC UGU CCC AAG GCU GCU GGC 3'

Figure 38: Fluorescence emission spectra of two different qFIT^2 probes specific for the CCF-CEM CDR3 region. Spectra of (**A**) **CEM-TO^2-Cy7-3** and (**B**) **CEM-TO^2-Cy7-5** recorded at 37 °C in phosphate buffer (100 mM NaCl, 10 mM Na_2HPO_4, pH = 7.0). Depicted are the double strand fluorescence of thiazole orange (green) and Cy7 (purple), as well as the single strand emission (grey). Cy7: λ_{ex} = 650 nm, λ_{em} = 700–900 nm; TO: λ_{ex} = 485 nm, λ_{em} = 500–700 nm, $slit_{ex/em}$ = 5 nm.

In terms of brightness, **CEM-TO^2-Cy7-5** even surpassed **CEM-TO^2-Cy7-3** (Br_{535} = 30.1 vs. 29.3), despite a lower peak emission intensity (see **Figure 38**). The reasons for the observed performance increase are unclear. However, it seems that the longer spaced probes absorb light slightly more efficient, which results in higher extinction coefficients. It is possible that at a certain distance there is less interference between the dyes, allowing them to absorb light more independently. Finally, consistent with the previously observed pattern, probe performance was best when the LNA building block was placed on the 3' side of the dye.[324]

Probe responsiveness does not only depend on the dye-dye distance and the placement of the LNA building block, it may also be improved by fine-tuning the affinity for the target sequence. From previous works by Felix Hövelmann[324] and Jasmine Chamiolo,[305] as well as data presented in **Chapters 5.1.2.1** of this work (see **Table 3** and **Table 4**), it is known that 2'OMe-RNA nucleotides, although strengthening double strand interaction, reduce the responsiveness of FIT probes. However, this may be mitigated by use of a *wingmer* design. This concept is often applied in antisense oligonucleotides (ASOs), where the 5' and 3' ends are chemically stabilized against enzymatic degradation, while the unmodified middle part of the oligomer allows nuclease H recruitment. Similarly, it was thought that 2'OMe-based FIT probes could benefit from introducing deoxy nucleotides. In the following data set, probes based on this consideration are presented (**Table 8**; **CEM-TO^{2}Cy7-7** to **-9**). In these *semi-wingmers*, only the 5' end (or the 3' and 5' end for **CEM-TO^2-Cy7-10**) was stabilized with 2'OMe-nucleosides, while the rest of the sequence is composed of deoxynucleotides. Despite the reduced 2'OMe RNA content, it was assumed that these probes would still possess increased enzymatic stability, as the terminal Cy7 dye likely provides some degree of protection against exonuclease digestion and the TO base surrogate shields the middle part of the sequence against endonucleases.

Four *semi-wingmer* qFIT^2 probes based on the sequences **CEM-TO^2-Cy7-1**, **-3**, and **-5** were synthesized, with the aim to further increase their enhancement E_{535} compared to the parent compounds. Unfortunately, as the results below (**Table 8**) show, this was not achieved. For **CEM-TO^2-Cy7-7** to **-10**, the TO enhancement only reached values between 8.9 and 18.0. This is significantly lower than what was measured for **CEM-TO^2-Cy7-3** (E_{535} = 36.2) and **-4** (E_{535} = 33.7). Interestingly, the Cy7/TO ratios of the *semi-wingmers* (both in the single and double strand) were higher than for the sequences presented in **Table 7**. Theoretically, a high Cy7/TO ratio would be desirable for a live-cell imaging setup, as it allows better discrimination between non-hybridised and hybridised qFIT^2 probe. But considering that the single strand ratio of these sequences was increased as well, this advantage is likely nullified. It appears that TO is affected less strongly by probe composition than QB (which has drastically higher enhancements in DNA-based FIT^2 probes than in 2'OMe-based ones). Conceivably, QB-based wingmer FIT^2 probes might be more effective, however this was not tested in this work. A positive aspect of this dataset was the improved quantum yield and brightness of TO. For the wingmer qFIT^2 probes, an average brightness of about 29.5 was determined, which is higher than the mean brightness of the probes presented in **Table 7** (average Br_{535} = 21.8).

Table 8: Spectroscopic properties of *semi-wingmer* qFIT^2 probes against CCRF-CEM CDR3 mRNA.

	Sequence 5' – 3'	E_{535}	E_{773}	r_0	r	ϕ_{535}	Br_{535}
CEM-TO^2-Cy7							
7	AUATOT_LGCGTATCTTOT_LCCCAAGGCTGCTGGC-Cy7	12.4	1.0	0.5	5.8	0.34	26.7
8	AUACTTOC_LGTATCTTOT_LCCCAAGGCTGCTGGC-Cy7	18.0	1.0	0.6	9.7	0.43	30.9
9	ATTOC_LTGCGTATCTTOT_LCCCAAGGCTGCTGGC-Cy7	10.8	1.0	0.4	4.9	0.37	26.5
10	ATTOC_LTGCGTATCTTOT_LCCCAAGGCUGCUGGC-Cy7	8.9	1.0	0.5	4.5	0.43	34.1

Conditions: 0.5 µM probe and 5 eq. RNA target (5'-AUACUGCGUAUCUGUCCCAAGGCUGCUGGC-3') were measured to determine fluorescence enhancement $E = I / I_0$ for thiazole orange (E_{535}) and for Cy7 (E_{773}). Single strand ratio r_0 and double strand ratio r were calculated as I_{535} / I_{773}. Enhancement factors and ratios were measured at 37 °C, quantum yield ϕ and brightness $Br = \varepsilon_{535} \cdot \phi_{535} / 1000$ in $M^{-1} \cdot cm^{-1}$ at 25 °C. Cy7: λ_{ex} = 650 nm, λ_{em} = 773 nm; TO: λ_{ex} = 485 nm, λ_{em} = 535 nm, $slit_{ex/em}$ = 5 nm. All measurements were conducted in buffer (100 mM NaCl, 10 mM Na_2HPO_4, pH 7.0). Underscored letters = 2'OMe-RNA; subscript L = LNA.

In summary, it could be shown that a combination of the qFIT concept with the FIT^2 approach is straight-forward. Equipping dual dye probes with an additional Cy7 reference dye can enhance the ratio value compared to previously reported qFIT probes.[305] Unfortunately, it was not possible to further increase probe enhancement by partially replacing 2'OMe nucleotides with deoxy nucleotides in a *wingmer* design. Although quantum yield and brightness were somewhat elevated, a high responsiveness would be preferable for a use in a biological setting. It must also be noted, in the experiment, the RNA target was added in excess to guarantee full saturation of the FIT probe, whereas in a cellular environment target concentration would most likely be more limited. Based on literature values for the number of potential mRNA target molecules in the cytoplasm (moderately abundant mRNAs typically have copy numbers in the range of 10-1000 transcripts per cell[349]), it must be assumed that there are probe molecules than target and thus enhancement and high brightness values will be most critical when performing live-cell imaging on native levels of target RNA. To test these considerations and assess qFIT^2 probe performance in a biological system, experiments with TCR mRNA-expressing lymphoid cell lines were conducted next.

5.2.3 Biological Application of qFIT^2 Probes in Jurkat- and CCRF-CEM Cells

For visualisation of a target mRNA in cells, the gene of interest is often introduced by stable transfection and a sufficiently high expression is achieved by subjecting it to a strong promotor or by introducing it in repeats.[316, 350] In contrast, the envisioned T-cell discrimination using qFIT^2 probes has to take place in unmodified cells with native expression levels of target mRNA. This is much more challenging, as the amount of target is significantly lower. In previous works, the expression of T-cell receptor mRNA could be somewhat increased by stimulation of cell proliferation.[305] For this purpose, phorbol 12-myristate 13-acetate (PMA), a potent protein kinase C activator, has been added to the growth medium of T cells. Previously, the best results were achieved using a concentration of 3 ng/mL and an incubation time of 12 h. With this treatment regime, TCR mRNA expression was enhanced by up to factor 4 for Jurkat cells and 2.5 for CCRF-CEM cells. For comparability and to facilitate the experiments, the same protocol was adopted in this work.

Another important consideration for the following experiments was that lymphoid cells like T-cells are notoriously "hard-to-transfect" and few reliable methods exist that can introduce adequate concentrations of oligonucleotides, while maintaining cell viability.[351] A commonly used technique is lipofection. Unfortunately, this method is not easily applicable to suspension cell lines like T-cells.[352, 353] An alternative is electroporation. Here, a cell suspension is placed in a cuvette containing two electrodes. A short electric pulse is applied, which is thought to lead to structural changes in the cell membrane and cause temporarily increased permeability. In addition, the negatively charged phosphate backbone of oligonucleotides may cause them to move along the electric field gradient into the cells.[354] Although in principle applicable to most types of cell lines, electroporation requires laborious optimization to provide consistent results and achieve a good balance between delivery efficiency and cell survival. The key parameters for this are the number of pulses, their shape (square or exponential), voltage and duration, as well as the distance between the electrodes and the conductivity of the medium in which the cells are suspended.[355]

Before testing whether different T-cell lines could be distinguished using qFIT^2 probes, the electroporation conditions had to be optimized. In these initial experiments, the probe concentration was fixed at 500 nM to reduce complexity and allow a focus on the settings of the electroporator (GenePulser MXcell Electroporation System, Bio-Rad, CA, USA). Fyrberg *et al*. described a method development protocol for this instrument, in which different parameters

like cell diameter and permeation voltage are taken into account to establish a working electroporation protocol.[356] For this they used the following formula:

$$E_c = \frac{V_c}{0.75 \cdot d_{cell}} \quad (7)$$

Here, E_c is the critical field strength ($V \cdot cm^{-1}$), V_c the permeation voltage of the cell membrane (1 V at 20 °C, 2 V at 4 °C) and d_{cell} the cell diameter (cm). Using E_c, the optimal voltage setting for the electroporator can be estimated as

$$V = E_c \cdot d_{cuv} \quad (8)$$

where d_{cuv} is the electrode distance in cm, defined by the cuvette options of the manufacturer. Inserting the average diameter of both cell lines to be used in the experiment (Jurkat = 15.0 µm; CCRF-CEM = 14.8 µm) into the equations above, theoretical optimum voltages of 355 V for Jurkat and 360 V for CCRF-CEM were calculated.

Importantly, as described above voltage is not the only parameter that influences electroporation efficiency. Pulse length, shape, number and interval, as well as temperature and the cell medium during and after the pulse also have to be considered. In short, the best conditions for qFIT^2 probe delivery into both cell lines were using a pre-chilled (4 °C) electroporation medium consisting of RPMI-1640 medium supplemented with 1.2 % DMSO and a slightly lower voltage than calculated (330 V). Two 10 ms long, square wave pulses with a pause of 10 s in between were applied. DMSO helps to increase cell membrane flexibility, facilitate membrane fusion processes, while also allowing cells to tolerate stress more readily, lowering the barrier for molecular transport, and assisting in pore formation, as found by Notman *et al.*[357, 358]

A common observation following electroporation is a dramatic increase in cellular volume. This swelling is caused by an influx of liquid during and after the pulse, due to the different osmotic potentials between cytoplasm and cell medium. This is problematic, as the cell loses homeostasis and the salt concentration in the cytoplasm suddenly decreases.[359] It was found that in electroporation most cells do not die during the pulse, but in the steps that follow afterwards – arguably, due to improperly closed cell membranes.[360] To promote cell recovery, different post-electroporation treatments were tested. Cells were placed in a special recovery medium, consisting of RPMI-1640 supplemented with 4 mM glutamine and 20 % FCS. In addition, electroporated cells were either kept at either room temperature or at 37 °C for 30 min before being transferred to the microscopy slide. The highest viability was found with the first

treatment. With suitable electroporation conditions found, probe concentration adjustment could take place. The previous *in cuvette* experiments had been conducted on an excess of RNA-target. However, in live-cell experiments, it must be assumed that the probe to target ratio is reversed. Therefore, the goal was to achieve a bright TO fluorescence on the one hand, but also a high ratio of TO and Cy7 fluorescence after hybridisation.

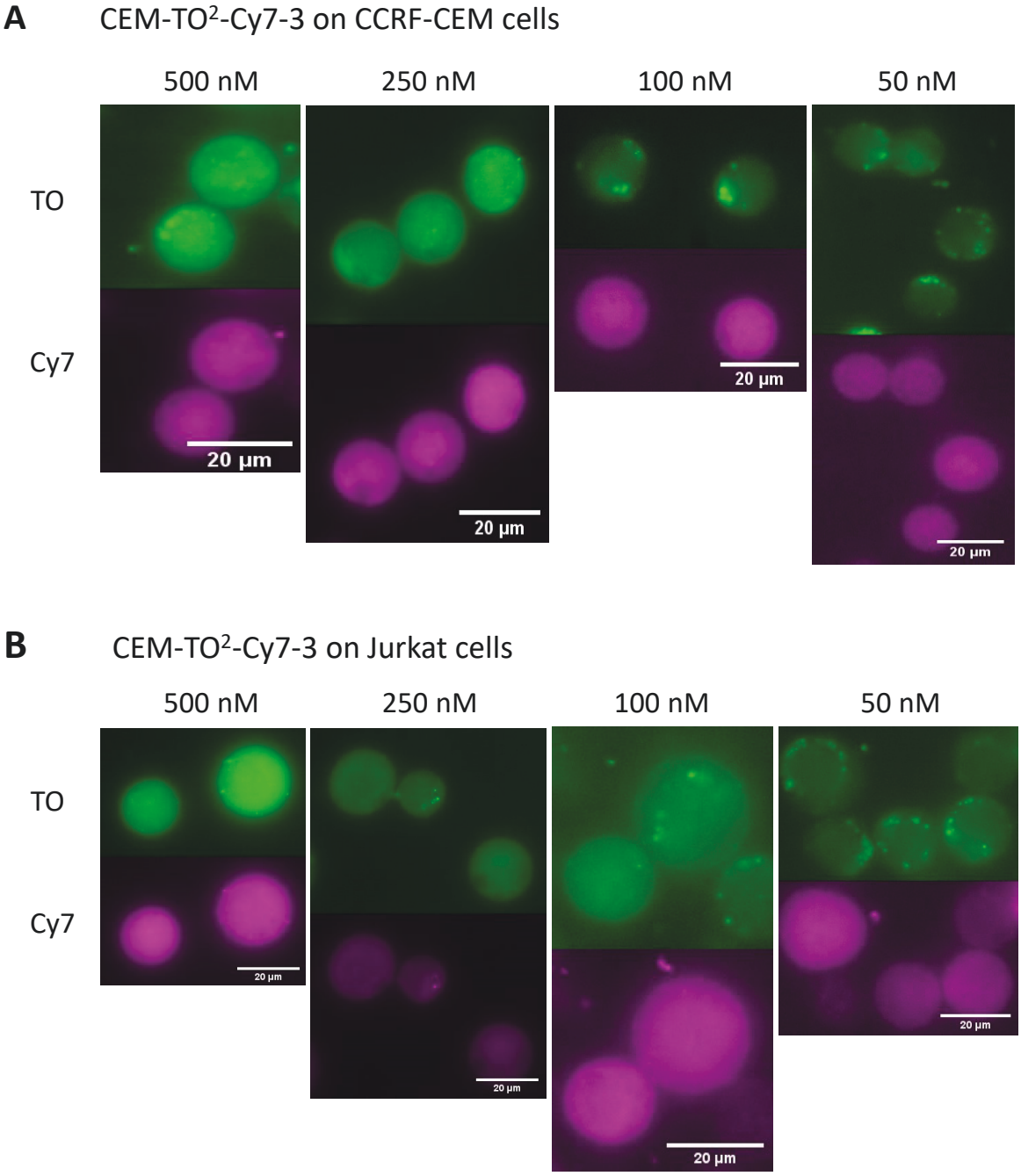

Figure 39: Influence of qFIT[2] probe concentrations during electroporation. CCRF-CEM (**A**) and Jurkat (**B**) cells were stimulated with PMA (3 ng/mL, 12 h) and then electroporated with **CEM-TO[2]-Cy7-3** (2x 330V, 10 ms square wave pulses with an interval of 10 s, in 0.4 cm cuvettes, 50-500 nM probe). Top row: thiazole orange fluorescence (green), bottom row: Cy7 fluorescence (magenta). Filters: TO: λ_{ex} = 500/24 nm; λ_{em} = 545/40 nm; Cy7: λ_{ex} = 740/73 nm; λ_{em} = 810/90 nm. For visualisation purposes, contrast and brightness have been enhanced.

Using the protocol described above the qFIT^2 concentration was lowered from 500 nM to 50 nM (with 250 nM and 100 nM as intermediate steps). **Figure 39** shows enlarged images of CCRF-CEM and Jurkat cells transfected under the same electroporation conditions, but with different **CEM-TO^2-Cy7-3** (**Figure 39A**) and **JK-TO^2-Cy7-3** (**Figure 39B**) probe concentrations. Remarkably, with decreasing qFIT^2 probe concentration, TO fluorescence changes from being evenly distributed throughout the cell (500 nM), to a more granular, sub-cellular localization (50 nM). Importantly, the fluorescence of Cy7 remains homogeneously distributed. This observation gives reason to believe that the qFIT^2 probes find and binds to their target, turning on TO fluorescence. As probe concentration decreases, the excessively distributed single-strand fluorescence of thiazole orange disappears and only isolated, but brightly illuminated spots of hybridized probe remain. However, it should be noted that it is a possibility that these speckles are the result of non-specific binding to other cellular components, as faint spots were often also observed in non-target cells. To prove the colocalization of the target mRNA and the observed granular spots, FISH experiments could be performed on fixed cells, but this experiment was not performed in this work.

How well two different cell lines can be discriminated not only depends on probe brightness in the cell, but also the ratio between thiazole orange and Cy7. This value was calculated for each pixel of each recorded image by dividing the fluorescence intensity of the TO channel by

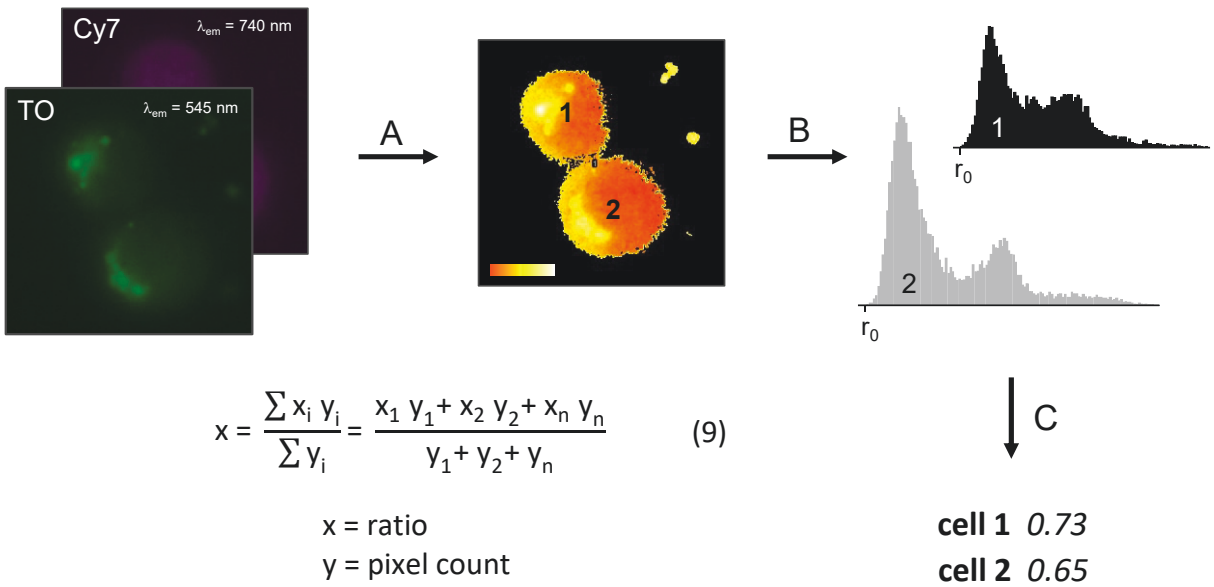

$$x = \frac{\sum x_i\, y_i}{\sum y_i} = \frac{x_1\, y_1 + x_2\, y_2 + x_n\, y_n}{y_1 + y_2 + y_n} \qquad (9)$$

x = ratio
y = pixel count

Figure 40: Schematic overview of the data processing for the qFIT^2 microscopy experiments. (**A**) For each image, the fluorescence intensity of the TO channel (filter: λ_{ex} = 500/24 nm; λ_{em} = 545/40 nm) was divided by that of the Cy7 channel (λ_{ex} = 740/73 nm; λ_{em} = 810/90 nm), to obtain ratiometric heatmaps. Values below a certain threshold were removed. (**B**) The frequency distributions of the individual pixels of each cell were exported as a separate histograms and corrected to the r_0 value of the probe, previously determined in the cuvette experiments. (**C**) The histograms were then summarized as a single values by calculating the weighted mean of all pixels (equation 9).

the one of the Cy7 channel using *ImageJ* software. The resulting image visualizes the ratio values of each cell as heatmap, colour-coded red (low ratio) to yellow (high ratio). For each cell, a histogram was generated and exported as well. The data revealed a cellular distribution, with the nuclei typically having lower ratios than the cytoplasm. Surprisingly, TO/Cy7 ratios above those previously determined in the cuvette experiments were found. This was likely a consequence of the presence of cell autofluorescence and background. Unfortunately, the range of values changed depending on the day the image was recorded and the cell line used. To compare date from different experiments, it was thus decided to subtract the background. For this, the histograms were corrected in a way that the first ratio pixel with the lowest ratio value would match to the r_0 of the corresponding probe that was determined in the cuvette experiments. For **CEM-TO^2-Cy7-3** this value was 0.1, for **JK-TO^{2}Cy7-3** 0.4.

Following background correction, each cell was summarized as a singular value. The average ratio was calculated by dividing the scalar product of the pixel count and associated ratio values by the total number of pixels (**Figure 40**, equation 9). The data of all cells was then statistically evaluated and graphed in a violin-plot (**Figure 41**). This numerical data visualization represents a hybrid of a histogram and a box plot. Like in a box plot, the median and quartiles of the data are depicted as a box with whiskers, but in addition, the value distribution is indicated by a density curve. The width of the curve corresponds to the number of data points.

Figure 41A-D shows the data obtained from the previous experiment with varying concentrations of **CEM-TO^2-Cy7-3** (500, 250, 100, and 50 nM). Using the highest probe concentration (500 nM; **Figure 41A**), both cell lines exhibit a very low average TO/Cy7 ratio, with most cells being spread around the same value. This indicates that the measured emission is probably TO single strand fluorescence and a discrimination between both cell lines is not possible. When the **CEM-TO^2-Cy7-3** concentration is halved (250 nM; **Figure 41B**), differences between the samples begin to emerge. Although still not significant, the shape of the plot begins to stretch upwards, towards higher TO/Cy7 ratios. It is conceivable that now higher ratio double strand fluorescence is now also being picked up as well, raising the mean values of the sample. With 100 nM probe (**Figure 41C**), this effect is even more pronounced. The box for CCRF-CEM cells is now vertically stretched out and a second cell population emerges as an additional bulge in the violet plot, while the data for Jurkat cells keeps the same shape. An unpaired Student's t-test on the two data sets gave a p-value of <0.001, thus discrimination between those two cell lines appears possible within the experimental setup. With 50 nM qFIT^2 probe

the discrimination is even better, now with a p-value of <0.0001. It is also visible, that the first bulge disappeared in favour of the second bulge. This could be interpreted as most of the probe now residing in a hybridized state. An important caveat to the data is that the count of Jurkat cells is rather low. However, it must be noted that due to decreasing viability during the experiment, few surviving cells could be found by the time the data was collected.

The same experiment was repeated with a qFIT^2 probe complementary to the TCR mRNA of Jurkat cells (**Figure 42A-D**). As before, electroporation with the highest concentration (500 nM) of **JK-TO^2-Cy7-3** probe (**Figure 42A**) failed to produce significant difference between the two cell lines. Of note, the plots start at a slightly higher TO/Cy7 ratio, as the r_0 value of

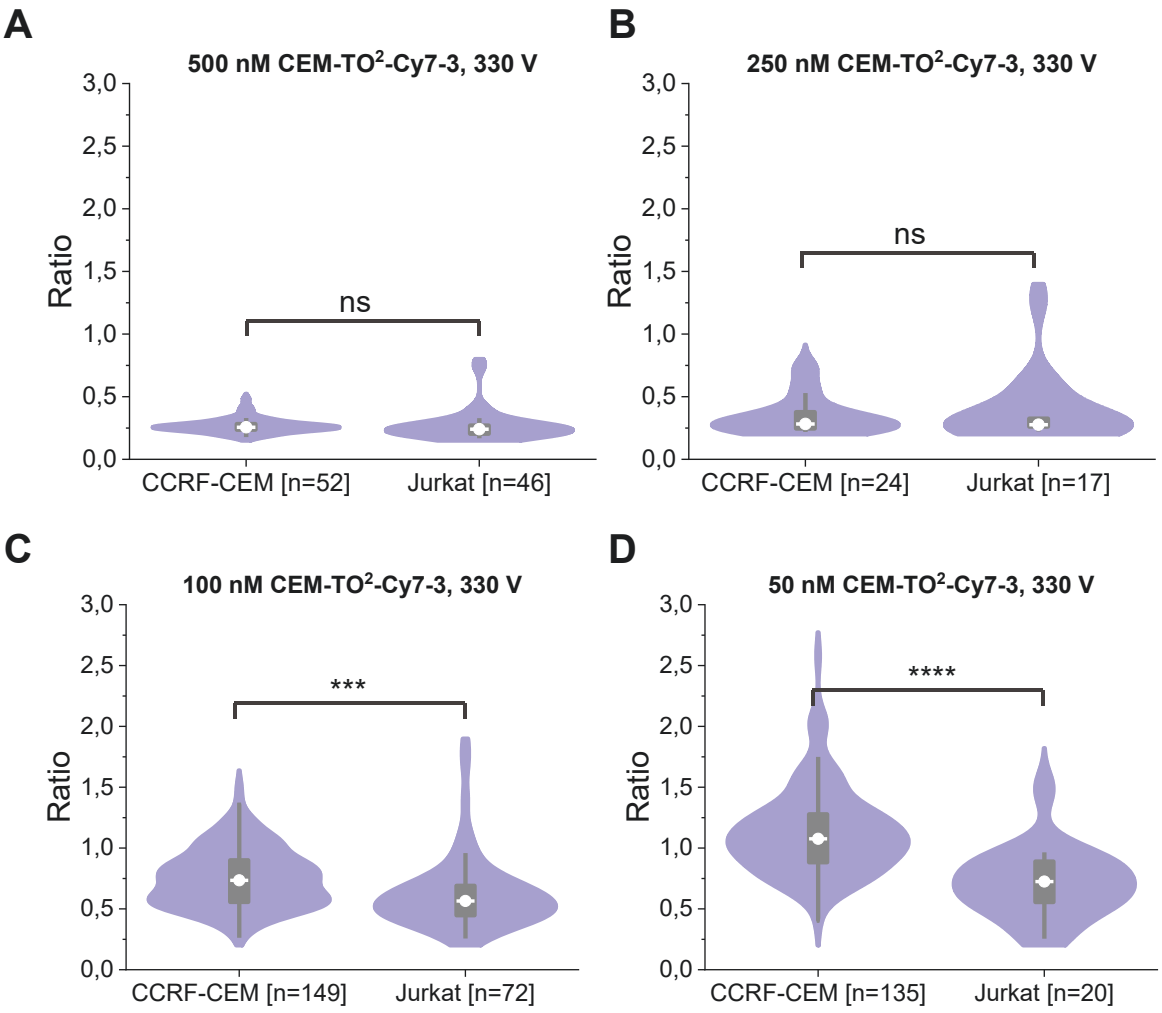

Figure 41 Violin plots of data from CCRF-CEM and Jurkat cell populations treated with **CEM-TO^{2}Cy7-3.** The same electroporation conditions were applied to both cell lines (2x 330 V, 10 ms square wave with an interval of 10 s in 0.4 cm cuvettes) with a probe concentration of (**A**) 500 nM, (**B**) 250, (**C**) 100 or (**D**) 50 nM. Plots comprise the weighted mean TO/Cy7-ratio for each cell analysed. The dark grey box indicates the position of 50 % of the data, with 1.5x interquartile range whiskers. The white line represents the median of the sample population. Data density is given as the width of the violet wings. Statistical evaluation was performed using an unpaired Student's t-test (ns = not significant, * p > 0.05, ** p <0.01, *** p < 0.001 and **** p < 0.0001. A and B show data of one experiment, C the combined data of three experiments and D the combined data of two experiments.

JK-TO^2-Cy7-3 was 0.4 in the cuvette experiments and therefore the histograms were corrected to a higher starting point. The data distribution for the CCRF-CEM cells appears to be the largely the same as in **Figure 41A**, with only one population being concentrated near a value of about 0.6. Interestingly, the data obtained for the Jurkat cells is more stretched out than that of the CCRF-CEM cells. By reduction of the probe concentration to 250 nM, the data points are narrowly distributed around a limited range of TO/Cy7 values, resulting in a compressed violin blot. Regardless, the resulting t-test gave a p-value of < 0.001 (**Figure 42B**).

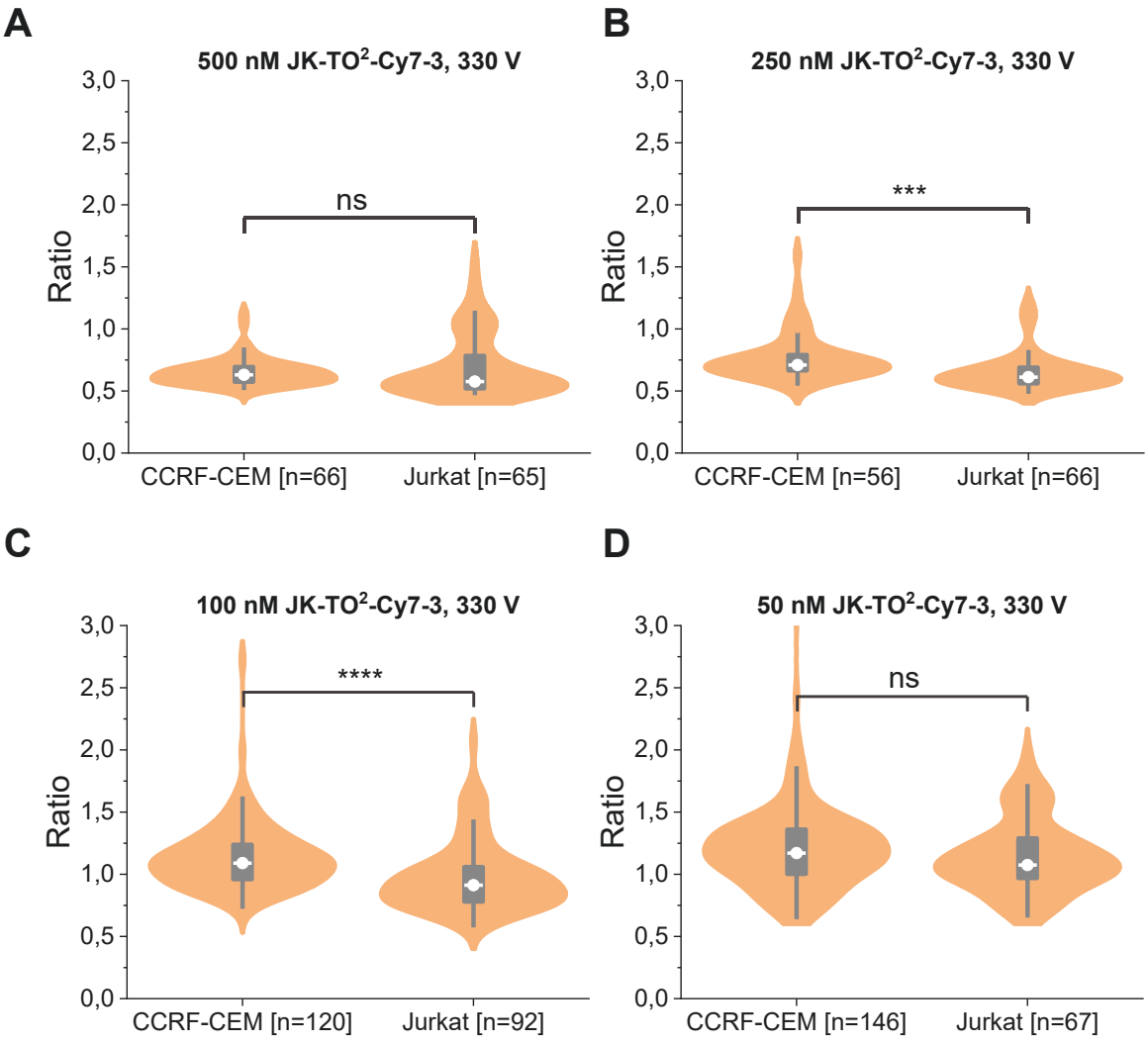

Figure 42 Violin plots of data from CCRF-CEM and Jurkat cell populations treated with **JK-TO^{2}CY7-3.** The same electroporation conditions were applied to both cell lines (2x 330 V, 10 ms square wave with an interval of 10 s in 0.4 cm cuvettes) with a probe concentration of (**A**) 500 nM, (**B**) 250, (**C**) 100 or (**D**) 50 nM. Plots comprise the weighted mean TO/Cy7-ratio of all cells analysed. The dark grey box indicates the position of 50 % of the data with 1.5x interquartile range whiskers. The white line represents the median of the sample population. Data density is given as the width of the violet wings. Statistical evaluation was performed using an unpaired Student's t-test (ns = not significant, * p > 0.05, ** p <0.01, *** p < 0.001 and **** p < 0.0001. A and B show data of one experiment, C the combined data of three experiments and D the combined data of two experiments.

Surprisingly, the median of the **JK-TO^2-Cy7-3** treated CCRF-CEM cells was higher than that of the Jurkat cells. This means that **JK-TO^2-Cy7-3** is more likely to positively tag CCRF-CEM cells than the cell line it was designed to label. When the probe concentration is reduced further to 100 nM or 50 nM (**Figure 42C-D**), this issue becomes even more evident. A reason behind this observation might be that **JK-TO^2-Cy7-3** is not exclusively staining TCR mRNA of Jurkat cells. It seems that in a cellular environment this qFIT^2 probe is not selective enough and thus may find other targets in CCRF-CEM cells.

Cell viability following electroporation was a limiting factor in the experiments described above. During the initial optimization it was found that reducing the voltage to 325 V can improve viability at the expense of transfection efficiency. As a compromise it was tested if the quality of the experiment can be improved by reducing the voltage of the electroporation pulse while increasing probe concentration to 100 nM to compensate for the reduction in transfection efficiency. **Figure 43A** summarizes data from both cell lines treated with **CEM-TO^2-Cy7-3** using this alternative protocol.

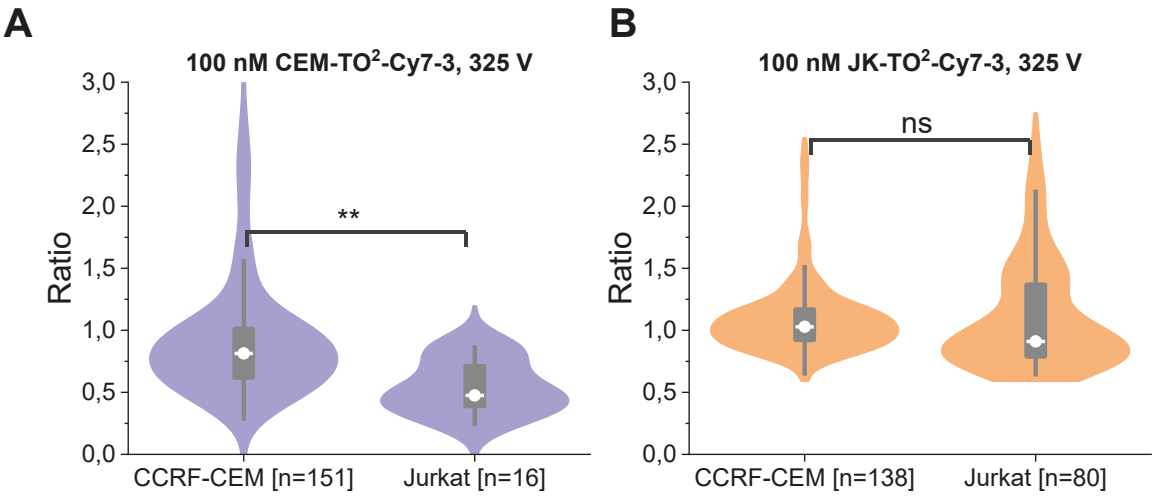

Figure 43 Violin plots of data from CCRF-CEM and Jurkat cells treated with **CEM-TO^{2}Cy7-3** and **JK-TO^{2}CY7-3** using an alternative electroporation protocol. The same electroporation conditions were applied to both cell lines (2x 330 V, 10 ms square wave with an interval of 10 s in 0.4 cm cuvettes) with a probe concentration of 100 nM. Plots comprise the weighted mean TO/Cy7-ratio for each cell analysed. The dark grey box indicates the position of 50 % of the data, with 1.5x interquartile range whiskers. The white line represents the median of the sample population. Data density is given as the width of the violet wings. Statistical evaluation was performed using an unpaired Student's t-test (ns = not significant, * $p > 0.05$, ** $p < 0.01$, *** $p < 0.001$ and **** $p < 0.0001$. Both plots show the combined data of two experiments.

It is evident that, although the p-value for the CCRF-CEM cell is not as low as before (see **Figure 41D**), the box and Whiskers remain stretched out, indicating that some of the probe may be bound to the target. On the other side, the violin plot of Jurkat cells gave a more clinched shape with very few outliers. When the cells were electroporated with 100 nM of **JK-TO^2-Cy7-**

3, it is remarkable that, despite not being statistically significant, a second data point population appears above the data, likely representing single stranded probe. It is possible that with the lower voltage protocol, uptake of the qFIT^2 probe by Jurkat cells is less affected, while the transfection efficiency for CCRF-CEM cells is lowered. This might lead to less false positive staining. It can be speculated that a discrimination between the cell lines could become possible if probe concentration can be lowered enough without compromising delivery.

In summary, the results above show that under the right experimental conditions, it is possible to discriminate CCRF-CEM cells from Jurkat cells using a qFIT^2 probe containing two thiazole orange dyes as hybridization marker in combination with a Cy7 reference dye. A statistically significant difference in the mean cellular TO/Cy7 ratio was measured when cells were electroporated with 50 nM **CEM-TO^2-Cy7-3**. Unfortunately, the inverse labelling with **JK-TO2-Cy7-3** could not be achieved. A potential reason for this could be insufficient sequence specificity.

6 Summary and Outlook

The present work sought to investigate whether the performance of FIT hybridization probes can be enhanced by incorporating two cyanine dyes of the same type into the probe sequence (FIT^2 approach). This aimed at increasing the fluorescence output upon hybridization with the target sequence, while simultaneously reducing background emission of the single strand and mismatch duplexes through collisional quenching and homo-FRET.

In the first part of the work, different designs for QB- and TO-based FIT and FIT^2 probes targeting unedited and C-to-U edited GlyRα mRNA were compared. Aside from determining a suitable dye-dye spacing and probe length, probe pairs should be identified that may be used together to detect edited and unedited target simultaneously in two channels. In an initial screening, a mono-QB FIT probe set created by Andrea Knoll was complemented with matching TO probes. The comparison confirmed a previous observation that QB-based probes have high specificity and enhancement but fail to reach the same brightness as TO-based ones. In contrast, TO probes have high emission intensity but also fluoresce in the mismatch state, resulting in lower specificity. Both deficits were hoped to be overcome with a dual dye design.

For the FIT^2 probes, the same sequence as for the mono-dye probes was used, but with an extended 5'-end to incorporate a second QB fluorophore. Two dye-dye distances (7 or 9 nt) and three different 5'-overhang sizes (3, 4 and 5 nt) were screened. It could be confirmed that QB FIT^2 probes have higher extinction coefficients (up to 246 000 $M^{-1} \cdot cm^{-1}$), greater enhancement (up to 131) and better selectivity (up to 78.8) than their mono-dye counterparts (**Figure 44**). Generally, a shorter dye-dye spacing of 7 nt resulted in more responsive and selective probes, as did increasing the length of the probe. The selectivity gain was the result of a significantly decreased mismatch emission, which was attributed to the appearance of a second, red-shifted emission maximum in the single strand and mismatch duplex. This indicated the formation of cyanine dye aggregates and confirmed the postulated self-quenching mechanism of the FIT^2 approach. The concept was then applied to nuclease-resistant 2'OMe-RNA probes, which have higher binding affinity per nucleoside, but are known to be less discriminative.[324] Two sets of QB- and TO-based FIT^2 probes and matching mono-dye controls were prepared. As expected, the 2'OMe-RNA sequences exhibited lower enhancement (up to 125 for QB and 16 for TO) and specificity (up to 14.8 for QB and 5.7 for TO) than the DNA-based congeners, but they retained an increased brightness compared to the mono dye probes.

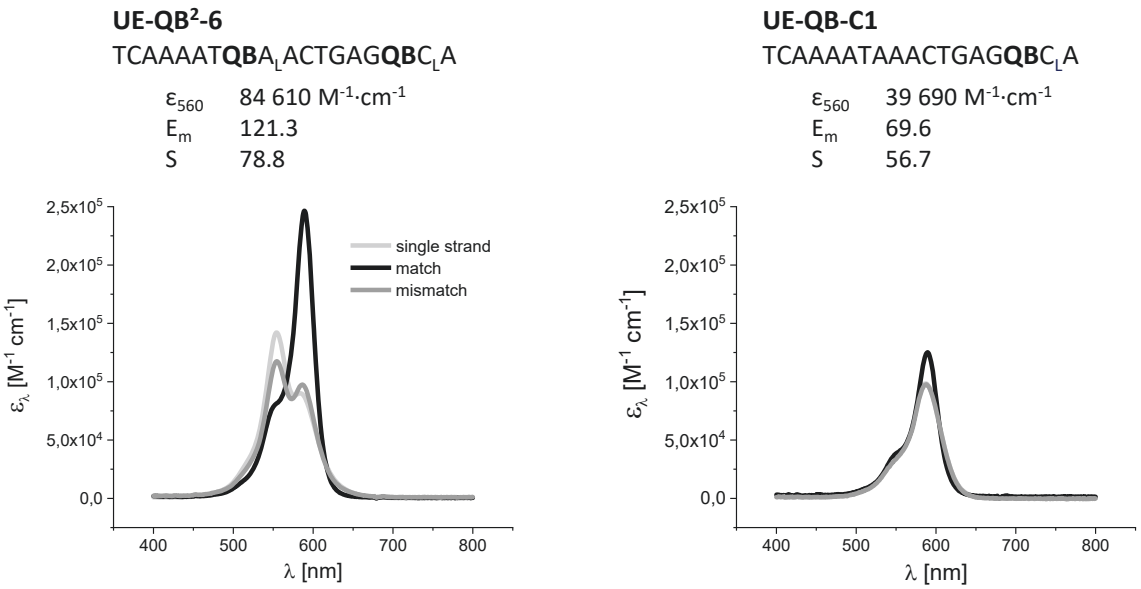

Figure 44: Comparison between an exemplary dual-dye FIT^2 and mono-dye FIT probe. **UE-QB^2-6** has a higher extinction coefficient (ε_{560}), match duplex enhancement (E_m) and specificity (S) than its mono-dye counterpart **UE-QB-C1**, due to the presence of a pronounced H-band that blue-shifts the absorption wavelength in the single strand and mismatch duplex.

This was especially true for the QB^2 set, for which values up to 29.4 were determined. In comparison, mono dye QB FIT probes were only half as bright. The intensity increase for the TO^2 set was somewhat smaller, except for **ED-TO^2-OMe-1**, for which an impressive brightness of 46.6 was measured. It was demonstrated that brightness can be elevated not only by increasing quantum yield, but also the extinction coefficient. Although the maximum achievable quantum yield is limited by the nature of the dye, introduction of additional fluorophores can lead to increased absorption and therefore higher extinction coefficients. Interestingly, the previously observed H-bands were much weaker for the 2'OMe-RNA QB FIT^2 probes, providing a rationale for their lower selectivity, whereas they remained detectable for the 2'OMe-RNA-based TO FIT^2 probes. The reason for this behaviour is unclear, but it is possible that 2'OMe-RNA nucleosides somehow suppress the formation of QB but not TO aggregates. If this effect could be prevented in the future, e.g. by exploring the use of alternative nuclease-resistant building blocks (such as 2'-F RNA), it may be possible to further enhance the already good performance of QB-based FIT^2 probes. Alternatively, the incorporation of additional dye molecules into a sequence (FIT^n approach) could promote H-aggregate formation, while simultaneously increasing the brightness of the probes further. Such FIT^n approaches might be a worthwhile strategy to investigate (**Figure 45**).

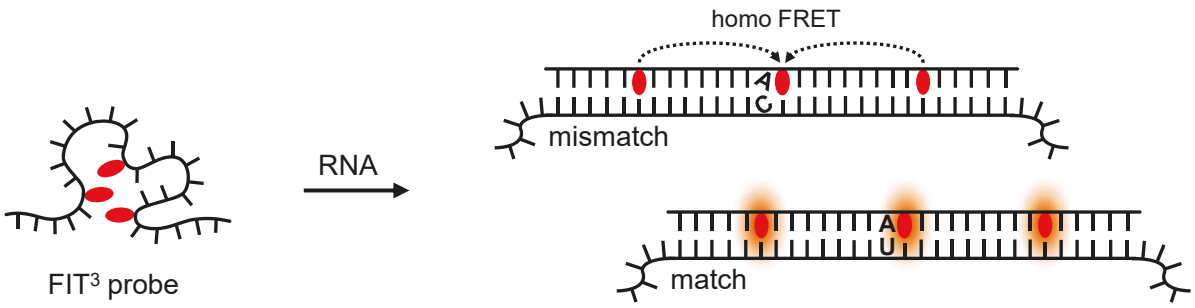

Figure 45: Concept for FIT^n probes, which might benefit from increased H-aggregate formation in the single strand and even further enhanced emission in the match duplex.

In a competitive experiment suitable probe combinations for a use in a cell-like environment were tested. For this, probes were measured in buffer supplemented with different amounts (0, 20 or 100 %) of HEK 293 embryonic kidney cell lysate. In this increased viscosity environment, background fluorescence of all probes was higher, but due to their self-quenching properties the FIT^2 probes were less affected by this effect than their mono-dye counterparts. They also retained a higher selectivity and in 100 % lysate all FIT^2 probes tested were more discriminative than the corresponding mono-dye probes.

To investigate how the probes perform in an actual live-cell imaging setup, HEK293 cells should be stably transfected with an overexpressed GlyRα gene in a future experiment. In contrast to transient transfection with plasmids, this will result in a more homogenous expression of the target mRNA and facilitate evaluation of the data. Similarly to a method described in a recent publication, an MS2 system should be introduced as an in-cell reference, to map FIT^2 probe fluorescence intensity to the hybridization state, independently of probe concentration.[316]

In **Chapter 5.2**, it was investigated if the FIT^2 concept could be further enhanced by combining it with a ratiometric approach (qFIT^2 probes). For this, a Cy7 reference dye was appended to the 3'-end of TO-FIT^2 probes designed to bind TCR mRNA of two different human T-cell lines. Cy7 emits independently of the hybridization state of the probe and a change in the TO/Cy7 ratio can be interpreted as successful hybridization. Relying on a relative value instead of an intensity change allows for background correction.

For the qFIT^2 probes, three different distances between reporter and reference dye (13, 15 or 17 nt) and between the two TO dyes (7, 8 or 10 nt) were screened. In addition, it was tested if the LNA effect originally described by Felix Hövelmann is more effective when the LNA unit is placed 3' or 5' of the reporter dye. The results of these experiments showed that the spacing

between reporter and reference does not have significant impact on probe performance (enhancement, brightness, and quantum yield) within the range tested. From previous experiments conducted by Jasmine Chamiolo it was known that distances smaller than 13 nt can result in detrimental energy transfer between TO and Cy7 but extending the 3'-end any further seems to be of negligible benefit. Regarding the reporter dye spacing, the shortest distance of 7 nt resulted in probes with the highest enhancement (E_{535} = 33.7) and largest TO/Cy7 ratio increase (r = 2.8) upon hybridization to the target. This agrees with the results of the first part of the thesis and reinforces the hypothesis that the optimal distance of 7 nt is a general property that might be independent of the probe sequence. This is an important finding that, if true, could substantially reduce the optimization effort required to prepare probes against other targets. For future experiments, it would be interesting to test where the lower limit of the dye spacing is. Data from others,[324] as well as own experiments not presented in this thesis suggests that probe performance decreases again for distances shorter than 7 nt. Another apparently general property is the optimal positioning of the LNA unit relative to the reporter dye. In all probes tested (including the mono-dye probes of **Chapter 5.1.1**), placement on the 3' side of TO consistently produced probes with higher quantum yield and brightness then-placement on the 5' side. This matches observations made by Felix Hövelmann and others.[305, 324] Finally, a *semi-wingmer* design was tested, in which only the 5' end of the probes was stabilized with 2'OMe building blocks, while the rest of the probe comprised unmodified deoxy nucleosides. This was hoped to alleviate the shortcomings of 2'OMe-RNA nucleosides regarding probe specificity and fluorescence enhancement. Unfortunately, despite slightly higher average quantum yields and brightness of these probes, no improvement in responsiveness was found. On the contrary, the enhancement factors of the wingmers were 2-4 times lower than those of the full 2'-OMe-RNA qFIT^2 probes.

Two qFIT^2 probes, one specific for Jurkat (**JK-TO^2-Cy7-3**) cells and one for CCRF-CEM (**CEM-TO^2-Cy7-3**) cells were selected for live-cell imaging experiments. Cell delivery was achieved by electroporation and a preliminary protocol optimization revealed that two 330 V, 10 ms square wave pulses with an interval of 10 s in 0.4 cm cuvettes is a suitable condition for both cell lines. Jurkat and CCRF-CEM cells were treated with both probes at four different concentrations (500, 250, 100 and 50 nM) and analysed by fluorescence microscopy. To obtain ratiometric results, each pixel in the TO-channel was divided by the corresponding pixel in the Cy7 channel for each image recorded. Histograms of the TO/Cy7 ratios found within each cell

were exported and evaluated in a data analysis software. Here, a method was found that allows the representation of each cell as a single value. Statistical analysis of the data revealed that **CEM-TO^2-Cy7-3** produces significantly higher ratios in CCRF-CEM cells than in Jurkat cells, when 50 nM qFIT^2 probe were used for transfection. If one were to apply these conditions to an actual flow cytometry-based cell sorting experiment, it may be possible to enrich CCRF-CEM cells from a mixture with Jurkat cells. To get an idea of how successful this could be, enrichment factors can be calculated for the results presented in **Chapter 5.2.3**, assuming the application of different ratio thresholds (**Table 9**). The data suggests that, with the very low r_0 of **CEM-TO^2-Cy7-3**, enrichment might be possible if a threshold of 10 times r_0 is applied. Under such conditions, 82 % of all CCRF-CEM cells would have been positively tagged, but only 5 % of the Jurkat cells. This corresponds to a theoretical enrichment of over 90 %. Applying even stricter selection criteria (such as 15 x r_0), an enrichment close to 100 % might be possible (albeit at the expense of a lower cell yield).

Table 9: Theoretically achievable CCRF-CEM cell enrichment from a mixture with Jurkat cells using CEM-TO^2-Cy7-3.

CEM-TO^2-Cy7-3	CCRF-CEM [n=135]	Jurkat [n= 20]	Enrichment factor
5 x r_0 (r = 0.5)	134 (99 %)	16 (80 %)	55 %
10 x r_0 (r = 1.0)	82 (61 %)	1 (5 %)	92 %
15 x r_0 (r = 1.5)	17 (12.5 %)	0 (0 %)	100 %

Number of positively tagged cells (and relative share of the total cells) using different ratio thresholds. Values calculated based on the results presented in Figure 41D, where CCRF-CEM and Jurkat cells were transfected with 50 nM CEM-TO^2-Cy7-3. Enrichment factor calculated as the proportion of positively tagged CCRF-CEM cells divided by the total percentage of positively tagged cells, assuming a 50:50 mixture of both cell lines.

Unfortunately, the inverse experiment using the **JK-TO^2-Cy7-3** probe was unsuccessful, as no statistically significant differences between the two cell lines could be found. It is possible, that **JK-TO^2-Cy7-3** fails to bind its TCR mRNA target specifically enough. This might lead to a false-positive ratio increase in CCRF-CEM cells. To further explore the potential of qFIT^2 probes, it would be advisable to repeat the experiment using flow cytometry. This way, the throughput and sample size could be increased significantly, improving statistical power. It would also be possible to attempt a real-time cell sorting to confirm suitable ratio thresholds to enrich one specific cell line from a mixture.

In summary, it can be concluded that FIT probes generally benefit from the addition of a second fluorophore of the same type. FIT^2 probes are often brighter, more responsive and more selective than their mono-dye congeners. This is mostly due to a significantly reduced emission in the single strand and mismatch, which persists in viscous environments with many competing molecules and will likely also improve probe performance in cells. The concept appears to be somewhat less dependent on probe sequence and several seemingly fundamental design aspects could be identified: Optimal probe performance is achieved by keeping the dye-dye distance at about 7 nt and placing an LNA unit on the 3' side of the fluorophore. In addition, a longer 5' extension (5 nt) appears to benefit probe quantum yield and brightness. Like the mono-dye qFIT system, FIT^2 probes can be modified with hybridization insensitive dyes to allow ratiometric imaging, which facilitates discrimination between bound and unbound probe in live-cell experiments. This can be used, for example, to discriminate between two cell lines. Finally, the preparation of FIT^2 probes does not require increased synthetic effort compared to mono-dye probes, so the concept should be easy to implement into existing workflows.

7 Experimental Section

7.1 General Information

Materials: All solvents used were of analytical grade or higher. Solvents used for DNA synthesis were dried over 3 Å molecular sieves (*Carl Roth,* Karlsruhe, Germany) prior to use. Unless specified otherwise, chemicals were purchased from *Sigma-Aldrich* (St. Louis. USA), *TCI Deutschland* (Eschborn, Germany) or *Carl Roth* (Karlruhe, Germany). Synthetic oligoribonucleotides were obtained from *Biomers* (Ulm, Germany). Aqueous solutions were made from ultrapure water prepared on an Astacus system (*membraPure*, Henningsdorf, Germany). Reaction tubes and pipette tips were purchased from *Sarstedt* (Nümbrecht, Germany).

Biological Consumables and Reagents: For biological procedures only autoclaved materials and buffers were used. For cell culture, fetal calf serum (*Merck*, Berlin, Germany) and Penicillin/Streptavidin mixture (*Biochrome*, Berlin, Germany) were added to RPMI-1640 cell medium (*Merck*, Darmstadt, Germany). Cell culture flasks were obtained from *Greiner* (Kremsmünster, Austria). For microscopy, channel *µ-slides IV 0.4* from *ibidi* (Planegg, Germany) were used.

HPLC Purification and Analysis: Semi-preparative and analytical HPLC was carried out on a 1105 HPLC system (321 Pump, 402 Dilutor, GX-271 Liquid Handler) equipped with a 171-diode array detector (*Gilson,* Limburg, Germany). The mobile phase used consisted of a binary mixture of eluent A (0.1 M aq. triethylammonium acetate buffer, pH = 7.4.) and eluent B (acetonitrile). For purification, a Triart C_{18} column (10 x 250 mm, 5 µm, 120 Å; *YMC Europe,* Dinslaken, Germany) was used, operated at 55 °C with a flow rate of 8 mL/min and a linear gradient (gradient 1 (*DMT-on*): 15-40 % B in 10 min; gradient 2 (*DMT-off*): 5–20 % B in 10 min). qFIT^2 probes were purified on a Triart C_{18} column (4.6 x 250 mm, 5 µm, 120 Å; *YMC Europe*) operated at 55 °C with a flow rate of 1.5 mL/min and a linear gradient of 20-70 % B in 15 min (gradient 3). For analytical measurements, a Triart C_{18} column (4.6 x 250 mm, 5 µm, 120 Å; *YMC Europe*) was used, operated at 55 °C with a flow rate of 1.5 mL/min and a linear gradient of 5-50 % B in 10 min (gradient 4). Probes marked with an asterisk (*) were analysed on an Acquity ultra-high-performance liquid chromatography (UPLC) system (*Waters Corporation,* Milford, MA, USA) equipped with a UV-detector (λ = 260 nm) and an FLR fluorescence detector, using an Acquity UPLC Oligonucleotide BEH C_{18} Column (2.1 x 50 mm; 1.7 µm; 130 Å; *Waters Corporation*), operated at 70 °C with a flow rate of 0.4 ml/min and a linear gradient of 3-20 % B in 7 min (gradient 4).

MALDI-TOF mass spectrometry: MALDI-TOF mass spectra were measured on an AXIMA Confidence spectrometer (*Shimadzu*, Kyoto, Japan) in positive ion mode. As matrix, a 50 mg/ml solution of 3-hydroxypicolinic acid in acetonitrile/water (1:1 v/v) mixed with a 100 mg/ml solution of diammonium hydrogen citrate (10:1 v/v) was used. For measurements, 0.5 µl of matrix solution and 0.5 µl analyte were mixed on a 96-spot ground steel MALDI target and dried at room temperature. The instrument was operated with an ion gate of 600 Da and the pulsed extraction setting optimized for the analyte mass. The laser was set to a frequency of 50 Hz and operated at a power of 90–120. For each spectrum between 100 and 500 single shots were accumulated. Spectra were calibrated using the Oligonucleotide Calibration Standard (*Bruker Daltonics,* Bremen, Germany)

7.2 Synthesis

7.2.1 TO and QB Phosphoroamidite Building Blocks

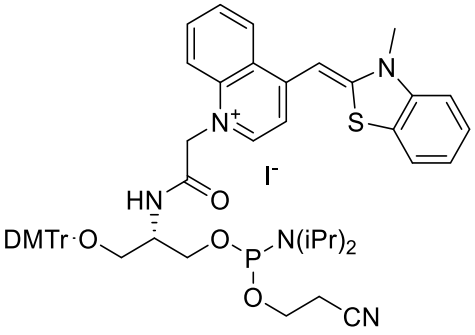

TO phosphoroamidite

$C_{53}H_{59}IN_5O_6PS$

1052.02 g/mol

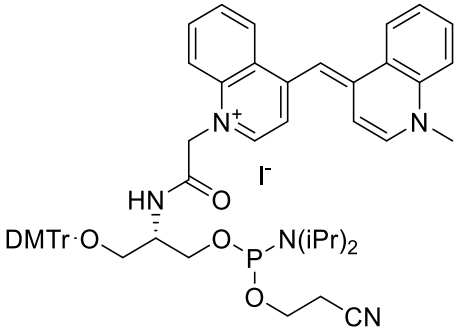

QB phosphoroamidite

$C_{55}H_{61}IN_5O_6P$

1046.00 g/mol

The synthesis of the QB- and TO-containing phosphoroamidite building blocks was conducted in a 10 step procedure as described by Hövelmann *et al.*[293] and Bethge *et al.*[289], starting from *N*-Methyl-4-chlorquinoline (QB) or 2-methylbenzothiazole (TO) and L-serine. The yields and NMR-spectroscopic data were in accordance with the literature.

7.2.2 FIT and FIT^2 Probe Solid-Phase Synthesis

FIT and FIT^2 probes were assembled on a 3'-C3-spacer-modified, universal CPG solid support (1 µmol, 500 Å pore size; *LGC, Biosearch Technologies,* Hoddeston, UK) or alkyne-modified CPG (1 µmol, 500 Å pore size; *Lumiprobe GmbH*, Hannover, Germany) using a MerMade-4 oligonucleotide synthesizer (*Bioautomation*, Irving, Texas). DMT-protected DNA and 2'OMe-RNA phosphoramidites were purchased from *LGC, Biosearch Technologies* (Hoddeston, UK), LNA phosphoramidites from *Exiqon* (Vedbak, Denmark). DNA, 2'-OMe-RNA and LNA phosphoramidites were dissolved in dry acetonitrile at a concentration of 0.1 M, TO- and QB-phosphoroamidites at a concentration of 0.15 M. All building blocks were coupled with DNA synthesis reagents (deblocking solution: 3 % TCA in DCM; activator: 0.25 M 5-benzylmercaptotetrazole in acetonitrile; capping A: 25 % Ac_2O in MeCN; capping B: 10 % *N*-methylimidazole, 10 % pyridine in MeCN; oxidizer: 0.1 M I_2 in THF/pyridine/water) obtained from *EMP-Biotech* (Berlin, Germany) according to the manufacturer's instructions. For the TO- and QB-building blocks, the coupling time was extended to 2x 4 min. The quality of each coupling step was monitored by measuring the absorbance (λ = 498 nm) of the DMT cleavage solution. The synthesis was programmed to yield oligomers carrying a terminal DMT protective group ("DMT-on" strategy). After synthesis, the oligonucleotide-bearing solid supports were dried under reduced pressure and transferred into 2 ml tubes. 1 ml of aqueous ammonia (32 %) was added, and the tubes were agitated at 55 °C for 2 h. The volatiles were removed using a vacuum centrifuge) and the remaining resin was filtered off. The crude product was purified by RP-HPLC (gradient 1) and the product-containing fractions were lyophilized. DMT cleavage was carried out by adding 300 µl aqueous AcOH (80 %) for 30 min at room temperature. The deprotected oligonucleotides were purified again by RP-HPLC (gradient 2) and lyophyllized. Finally, the pure oligonucleotides were desalted by precipitation from 0.1 volume sodium acetate buffer (3 M, pH 5.4) and 1 volume isopropanol, washed with 70 % (v/v) ethanol, dried and dissolved in ultrapure water. Products were characterized by MALDI-TOF mass spectrometry and analytical RP-HPLC (see **Appendix 8.1**). Typical yields after purification ranged around 10 %.

7.2.3 Modification of qFIT^2 Probes with Cy7

For the modification of qFIT^2 probes with a 3'-terminal Cy7 reference dye, the probe sequence was prepared according to the standard protocol on an alkyne-modified CPG solid support. After cleavage, purification and desalting, the oligonucleotides were dissolved in PUS buffer (100 mM Tris, 100 mM NaOAc, 1 mM $MgCl_2$, pH 8.0) at a concentration of 200 µM. Sodium ascorbate (100 eq.) as well as tris-hydroxypropyltriazolylmethylamine (55 eq.), each dissolved in 0.3 volumes PUS buffer, were added. Azide-modified Cyanine 7 (*Lumiprobe GmbH*, Hannover, Germany) was dissolved in DMSO at a concentration of 200 µM (10 eq.) and added to the mixture, followed by $CuSO_4$ (11.25 eq.) in PUS buffer. The reaction vessel was flushed with argon and agitated at 30 °C for 20 h. A spatula tip of sodium hydrogen sulfide hydrate was added, and the mixture incubated for another 10 min. The resulting precipitate was filtered off and the filtrate subjected to RP-HPLC purification (gradient 1). Product-containing fractions were combined, lyophilized, and desalted by precipitation from sodium acetate and isopropanol as described above.

7.3 Experimental Procedures

7.3.1 Fluorescence Spectroscopy

Fluorescence emission and excitation spectra were recorded on a Varian Cary Eclipse fluorescence spectrometer (Agilent Technologies, Santa Clara, CA, USA) in 10 mm, clear (1.4 ml) or black (140 µl) high performance quartz glass cuvettes (*Hellma,* Müllheim, Germany). The cuvettes were filled with phosphate buffer (100 mM NaCl, 10 mM Na_2HPO_4, pH 7.0) and, after measuring a blank, FIT probes were added as specified. Probe concentration was verified by determining the absorption at 260 nm in the same cuvette (see **7.3.2**) on an UV/VIS spectrometer (*Jasco*, Tokio, Japan). The relative deviation from the target concentration was later used as a correction factor for the obtained fluorescence intensities. Fluorescence spectra were recorded at 25 or 37 °C. Prior to each measurement, samples were allowed to equilibrate for 5 min to reach the specified temperature. To determine the spectroscopic properties of the double strand, RNA target was added to the cuvette and the mixture resuspended thoroughly with a pipette. For proper hybridization, the cuvette was briefly heated up to 90 °C and cooled down again to the desired temperature prior the measurement.

For each probe, three spectra were recorded and averaged. Quantum yields were calculated according to formula 5 (see **Chapter 3.2**), using ATTO 590 (for QB-probes; ϕ_{560} = 80 %; *ATTO-Tec GmbH*, Siegen, Germany) or ATTO 485 (for TO-probes; ϕ_{485} = 90 %) as reference. All fluorescence measurements were corrected according to the probe concentration in the cuvette.

7.3.2 UV-Vis Spectroscopy

UV-Vis absorption measurements of the probes were conducted on a V-750 spectrophotometer equipped with a PAC-743R Peltier cell changer (*Jasco*, Tokio, Japan) and connected to a F250 recirculating cooler (*Julabo*, Seelbach, Germany).

For concentration determination, an absorption spectrum (800–220 nm, 1 nm steps) of the respective solution was recorded. Probe concentration was calculated from the absorption at 260 nm according to the Beer-Lambert law (equation 1, see **Chapter 3.2**). The molar extinction coefficients of the probes were calculated with the OligoAnalyzer (*Integrated DNA Technologies*, Coralville, IA, USA). QB and TO base surrogates were treated as adenosine.

For melting temperature experiments, 1 µM probe and 1 µM synthetic RNA target were diluted in 1 ml phosphate buffer (100 mM NaCl, 10 mM Na_2HPO_4, pH 7.0). Duplex absorption

(λ = 260 nm) was determined between 20 °C and 90 °C with a heating rate of 1.0 °C/min and a sampling rate of 5 data points/°C. For each experiment three measurements were averaged and the T_m was calculated as the maximum of the first derivative of a sigmoidal fit (for melting curves see **Appendix 8.2.4**). Curve fitting was performed with Origin 2019 (*OriginLab*, Northhampton, MA, USA).

7.3.3 Preparation of Cell Lysate

HEK 293 embryonic kidney cells were grown in DMEM supplemented with 10 % fetal calf serum, 4 mM L-glutamine and 1 % Penicillin/Streptavidin mixture at 37 °C in a humidified 5 % CO_2 atmosphere and sub-cultivated twice a week. $2 \cdot 10^8$ HEK 293 cells were pelleted by centrifugation (500 x g, 5 min), washed with PBS buffer and lysed by 15 min incubation in 4 ml lysis buffer (10 mM Na_2HPO_4, 100 mM NaCl, 0.5 % Triton X-100, pH 7.0, 1 U/µl RNAsin Plus RNAse inhibitor [*Promega,* Madison, WI, USA], 1 tbl/10 ml cOmplete Mini protease inhibitor cocktail [*Sigma-Aldrich,* St. Louis, MO, USA]) on ice for 20 min with sonification every 5 min. Cell debris and nuclei were removed by centrifugation (14 000 x g, 10 min; 4 °C) and the supernatant was aliquoted and stored at -80 °C.

7.3.4 Competitive Experiments in Cell Lysate

A black 140 µl high performance quartz glass cuvette (*Hellma*, Müllheim, Germany) was filled with buffer (10 mM Na_2HPO_4, 100 mM NaCl, pH 7.0), PBS buffer + 20 % HEK293 cell lysate or 100 % HEK293 cell lysate and a blank measurement was recorded. 500 nM of UE-QB, ED-TO (or UE-TO and ED-QB) probe and edited or unedited RNA target were added sequentially. After addition of each oligonucleotide, the concentration was verified by measuring the absorption at 260 nm, as described in chapter 7.3.2. Then, TO (λ_{ex} = 485 nm, λ_{em} = 500–700 nm, readout at 535 nm) and QB (λ_{ex} = 560 nm, λ_{em} = 570–800 nm, readout at 605 nm) fluorescence were measured consecutively at 37 °C.

7.3.5 Cell Culture and Treatment of Jurkat and CCRF-CEM Cells

Cell Culture

Lymphoid cell lines (CCRF-CEM, Jurkat) were obtained from Prof. Dr. Frohme (TH Wildau, Germany). Both cell lines were grown in RPMI-1640 supplemented with 10 % fetal calf serum and 1 % Penicillin/Streptomycin mix at 37 °C and 5 % CO_2. The growth medium was replaced every 3-4 days, according to cell density. Cells were passaged at a cell density of $2 \cdot 10^6$ cells $\cdot$ ml^{-1}. For Jurkat passaging, cell media was taken out of the flask and transferred to a tube and centrifuged at 100 rcf for 5 min. As CCRF-CEM cells only showed partial attachment, for passaging the cell suspension was transferred to a tube and the remaining attached cells were trypsinated and combined. The cells were centrifuged at 100 rcf for 5 min, counted in a Neubauer chamber and resuspended in fresh growth medium at a concentration of $4 \cdot 10^5$ cells $\cdot$ ml^{-1} (Jurkat) or $3 \cdot 10^5$ cells $\cdot$ ml^{-1} (CCRF-CEM). Cell lines were stored in RPMI-1640 supplemented with 10 % FCS, 1 % Penicillin/Streptomycin and 10% DMSO in liquid nitrogen at -196 °C. Cells were grown for 28-30 passages, then a new batch of cells was thawed.

Electroporation

For electroporation a *GenePulserXcell™ system* from *Biorad* (Kalifornien, USA) was used in conjunction with 0.4 cm *GenePulser Cuvette*s. 12 hours prior to each experiment, cells were treated with a 10 µM PMA solution in cell culture flask (3 ng/mL final concentration). The following day cells were counted using a Neubauer chamber. $1.0 \cdot 10^6$ cells were pelleted and resuspended in 200 µL RPMI-1640 (+4 mM L-glutamine, 1.2% DMSO, on ice) and $qFIT^2$ (500, 250, 100 or 50 nM) were transfected with $qFIT^2$ probes. For electroporation the the instrument was operated in square wave mode and the cells were subjected to 2x 10 ms pulses at a voltage of 330 or 325 V and with a 10 s interval. Afterwards cells were immediately treated with 1 mL *post-electroporation- medium* (RPMI-1640, 4 mM L-glutamine and 20 % FCS, @RT) in the electroporation cuvette. Cells were allowed to recover at room temperature for 30 min. Afterwards, cells were washed with RPMI-1640 (2 x 5 mL, 3 min at 200 rcf), then PI was added (5 µL of 1.5 µM / 100 µL cell suspension) and cells were transferred into an ibidi µ-slide for fluorescent microscopy.

Fluorescence Microscopy

Fluorescence microscopy was conducted on an inverse *IX83* microscope from *Olympus* (Hamburg, Germany) equipped with a 10X/0.25 and a 60x/1.35 UPLSAPO oil objective (Hamburg, Germany) and an *Orca Flash 4.0 V2* camera *Hamamatsu* (Ammersee, Germany). A JC12V100W halogen lamp from *Traydon* (Frechen, Germany) was used for brightfield microscopy. Fluorescence measurements were obtained using a pE-4000 LED lamp from *Cool LED* (Andover, United Kingdom) with the following filters from *AHF* (Pfrondorf, Germany): TO: λ_{ex} = 500/24 nm; λ_{em} = 545/40 nm; QB/PI: λ_{ex} = 572/24 nm; λ_{em} = 628/40 nm; Cy7: λ_{ex} = 740/73 nm; λ_{em} = 810/90 nm.

Data Analysis using *ImageJ* Software

Fluorescence microscopy images were taken in the brightfield-, TO-, QB- (emission of propidium iodide) and Cy7 channel (in this order) and saved as tif *merge stack* using the *Olympus IX3* (*Olympus*, Hamburg, Germany) software. This format allowed further analysis with the open-source software *ImageJ* bundle *Fiji* (Wayne Rasband).[361] The stack was opened and the background fluorescence was subtracted using a custom macro (**macro_1**; see below). Further processing required a manual set threshold (3-4 %), and the apply button was hit. With a second macro (**macro_2**), the ratio between thiazole orange and Cy7 was calculated by dividing the intensity of each pixel in the TO channel by that of the corresponding pixel in the Cy7 channel and displayed in a new image as heat map. The data readout was executed by generating a histogram for each individual cell and exporting the pixel counts of the TO/Cy7 ratio as text file. Using *OriginPro* software (*OriginLab Corporation*, Northhampton, MA, USA), the ratio of the first detected pixel >0 was normalized to the TO/Cy7 single strand ratio r_0 determined in **Chapter 5.2** (**CEM-TO^2-Cy7-3** = 0.1; **JK-TO^2-Cy7-3** = 0.4). This allowed correction of background fluorescence in cells. Subsequently, the weighted mean values of the TO/Cy7 ratio were calculated for each individual cell and the data population was displayed as a violin blot. Finally, statistical analysis (unpaired Student's t-test) was performed on the data using *OriginPro* software.

ImageJ Macros

macro_1

```
t=getTitle();
t=substring(t,0,indexOf(t,"."));
run("Subtract Background...",
"rolling=200 sliding");
run("Gaussian Blur...", "sigma=1 stack");
run("Stack to Images");
selectWindow(t+"-0004");
run("Add...", "value=1");
selectWindow(t+"-0002");
run("Duplicate...", " ");
rename(t);
run("Threshold...");
```

macro_2

```
t=getTitle();
run("Create Selection");
selectWindow(t+"-0002");
run("Restore Selection");
run("Clear Outside");
run("Select None");
selectWindow(t);
close();
imageCalculator("Divide create 32-bit",
t+"-0002",t+"-0004");
selectWindow(t+"-0002");
run("Add Slice");
run("Add Slice");
run("32-bit");
run("Stack to Hyperstack...", "order=xyczt(default)
channels=3 slices=1 frames=1 display=Color");
Stack.setChannel(1);
run("Yellow");
selectWindow(t+"-0004");
run("Select All");
run("Copy");
selectWindow(t+"-0002");
Stack.setChannel(2);
run("Paste");
run("Grays");
selectWindow("Result of "+t+"-0002");
run("Select All");
run("Copy");
selectWindow(t+"-0002");
Stack.setChannel(3);
run("Paste");
run("Red Hot");
```

8 Appendix

8.1 Characterization Data

8.1.1 Characterization of FIT and FIT^2 Probes Targeting GlyRα2

Table 10: GlyRα2 Probe Characterisation by HPLC-MS and MALDI-TOF-MS

FIT-Probe	Sequence 5′ – 3′	MALDI-TOF-MS calc. $[M+H]^+$	MALDI-TOF-MS found	HPLC t_R [min]
UE-TO-OMe-1	AAUAAACUGAGTOC$_L$A-C3	4912.5	4915.7	8.79
UE-TO-OMe-2	AAUAAACUGAGTOC$_L$AG-C3	5271.7	5271.0	8.66
UE-TO-OMe-3	AAUAAACUGAGLTOCA-C3	4898.4	4902.1	8.97
UE-TO-OMe-4	AAUAAACUGAG$_L$TOCAG-C3	5257.7	5261.6	8.83
UE-TO-OMe-5	AAUAAACUGTOG$_L$GC-C3	4571.2	4573.5	8.85
UE-TO-OMe-6	AAUAAACTG$_L$TOGGC-C3	4585.2	4587.7	8.76
ED-TO-OMe-1	AAUAAACUGAATOC$_L$A-C3	4896.5	4900.0	3.13*
ED-TO-OMe-2	AAUAAACUGAATOC$_L$AG-C3	5255.7	5252.0	3.09*
ED-TO-OMe-3	AAUAAACUGAA$_L$TOCA-C3	4882.4	4905.5†	3.32*
ED-TO-OMe-4	AAUAAACUGAA$_L$TOCAG-C3	5241.6	5264.1†	3.23*
ED-TO-OMe-5	AAUAAACUGTOA$_L$GC-C3	4555.2	4555.5	3.14*
ED-TO-OMe-6	AAUAAACTG$_L$TOAGC-C3	4569.2	4568.5	3.16*
UE-QB^2-1	AAAQBT$_L$AAACTGAGQBC$_L$A-C3	5438.9	5440.4	8.88
UE-QB^2-2	CAAAQBT$_L$AAACTGAGQBC$_L$A-C3	5742.0	5742.5	8.81
UE-QB^2-3	TCAAAQBT$_L$AAACTGAGQBC$_L$A-C3	6046.2	6046.8	8.86
UE-QB^2-4	AAAATQBA$_L$ACTGAGQBC$_L$A-C3	5451.0	5452.6	7.48
UE-QB^2-5	CAAAATQBA$_L$ACTGAGQBC$_L$A-C3	5742.0	5747.0	7.16
UE-QB^2-6	TCAAAATQBA$_L$ACTGAGQBC$_L$A-C3	6046.2	6050.4	7.39
UE-QB-C1	TCAAAAT$_L$AAACTGAGQBC$_L$A-C3	5854.0	5851.8	2.72*
UE-QB-C2	TCAAAQBT$_L$AAACTGAGGC$_L$A-C3	5854.0	5856.4	2.81*
UE-QB-C3	TCAAAATQBA$_L$ACTGAGGC$_L$A-C3	5854.0	5852.9	2.81*

UE-QB^2-OMe-1	UCAAAQBT$_L$AAACUGAGQBC$_L$A-C3	6318.4	6321.6	8.97
UE-QB^2-OMe-2	AAAATQBA$_L$ACUGAGQBC$_L$A-C3	5679.0	5680.3	7.94
UE-QB^2-OMe-3	CAAAATQBA$_L$ACUGAGQBC$_L$ A-C3	5998.2	5999.2	7.75
UE-QB^2-OMe-4	UCAAAATQBA$_L$ACUGAGQBC$_L$A-C3	6318.4	6317.3	8.97
UE-QB-OMe-C1	UCAAAAUAAACUGAGQBC$_L$A-C3	6232.3	6230.8	3.15*
UE-QB-OMe-C2	UCAAAQBT$_L$AAACUGAGGCA-C3	6248.3	6244.4	3.16*
UE-QB-OMe-C3	UCAAAATQBA$_L$ACUGAGGCA-C3	6248.3	6248.5	3.20*
ED-TO^2-OMe-1	UCAAATOT$_L$AAACUGAATOC$_L$A-C3	6314.5	6312.5	8.96
ED-TO^2-OMe-2	AAAATTOA$_L$ACUGAATOC$_L$A-C3	5675.1	5672.4	9.11
ED-TO^2-OMe-3	CAAAATTOA$_L$ACUGAATOC$_L$A-C3	5994.3	5991.1	8.93
ED-TO^2-OMe-4	UCAAAATTOA$_L$ACUGAATOC$_L$A-C3	6314.5	6312.2	9.00
ED-TO-OMe-C1	UCAAAAUAAACUGAATOC$_L$A-C3	6222.3	6221.4	3.15*
ED-TO-OMe-C2	UCAAATOT$_L$AAACUGAAGCA-C3	6238.3	6236.7	3.11*
ED-TO-OMe-C3	UCAAAATTOA$_L$ACUGAAGCA-C3	6238.3	6238.5	3.33*
UE-TO^2-OMe-1	UCAAATOT$_L$AAACUGAGTOC$_L$A-C3	6330.5	6326.8	8.77
UE-TO^2-OMe-2	AAAATTOA$_L$ACUGAGTOC$_L$A-C3	5691.1	5694.7	8.95
UE-TO^2-OMe-3	CAAAATTOA$_L$ACUGAGTOC$_L$ A-C3	6010.3	6013.1	8.83
UE-TO^2-OMe-4	UCAAAATTOA$_L$ACUGAGTOC$_L$A-C3	6330.5	6330.0	3.25*
UE-TO-OMe-C1	UCAAAAUAAACUGAGTOC$_L$A-C3	6238.3	6239.1	3.11*
UE-TO-OMe-C2	UCAAATOT$_L$AAACUGAGGCA-C3	6254.3	6254.7	3.09*
UE-TO-OMe-C3	UCAAAATTOA$_L$ACUGAGGCA-C3	6254.4	6253.3	3.12*
ED-QB^2-OMe-1	UCAAAQBT$_L$AAACUGAAQBC$_L$A-C3	6302.4	6300.7	7.95
ED-QB^2-OMe-2	AAAATQBA$_L$ACUGAAQBC$_L$A-C3	5663.0	5665.6	8.02
ED-QB^2-OMe-3	CAAAATQBA$_L$ACUGAAQBC$_L$A-C3	5982.2	5981.3	7.95
ED-QB^2-OMe-4	UCAAAATQBA$_L$ACUGAAQBC$_L$A-C3	6302.4	6300.0	3.13*
ED-QB-OMe-C1	UCAAAAUAAACUGAAQBC$_L$A-C3	6216.3	6214.3	3.22*
ED-QB-OMe-C2	UCAAAQBT$_L$AAACUGAAGCA-C3	6232.3	6230.8	3.20*
ED-QB-OMe-C3	UCAAAATQBA$_L$ACUGAAGCA-C3	6232.3	6232.0	3.21*

* Probe measured on the Acquity UPLC system using gradient 4. † Mass detected as Na^+ adduct. Underscored letters = 2'-OMe-RNA building blocks, subscript L = LNA. QB and TO base surrogates are indicated with bold letters. C3 = 1,3-propanediol spacer.

8.1.2 Characterization of qFIT^2 Probes Targeting TCR mRNA

Table 11: TCR mRNA Probe Characterisation by HPLC-MS and MALDI-TOF-MS

FIT-Probe	Sequence 5′ – 3′	MALDI-TOF-MS calc. $[M+H]^+$	MALDI-TOF-MS found	HPLC t_R [min]
JK-TO^2-Cy7-1	GGTTOTLAGCCAUATOTLTAGCCGAACAGG-CY7	9856.5	9858.8	3.54*
JK-TO^2-Cy7-2	GGTTOTLAGCCAUATOTLTAGCCGAACAGGUC-CY7	10495.9	10496.8	3.54*
JK-TO^2-Cy7-3	GGTTOTLAGCCAUATOTLTAGCCGAACAGGUCGA-CY7	11198.4	11196.7	3.51*
CEM-TO^2-Cy7-1	AUATOTLGCGUAUCTTOTLCCCAAGGCUGCU-CY7	10036.5	10033.1	3.58*
CEM-TO^2-Cy7-2	ATALTOTGCGUAUCTTOTLCCCAAGGCUGCU-CY7	10370.7	10368.3	3.58*
CEM-TO^2-Cy7-3	AUACTTOCLGUAUCTTOTLCCCAAGGCUGCU-CY7	10010.5	10004.9	3.58*
CEM-TO^2-Cy7-4	AUACTLTOCGUAUCTTOTLCCCAAGGCUGCU-CY7	9996.5	9999.0	3.58*
CEM-TO^2-Cy7-5	ATTOCLTGCGUAUCTTOTLCCCAAGGCUGCU-CY7	10040.6	10042.0	3.59*
CEM-TO^2-Cy7-6	ATLTOCUGCGUAUCTTOTLCCCAAGGCUGCU-CY7	10012.5	10016.2	3.59*
CEM-TO^2-Cy7-7	AUATOTLGCGTATCTTOTLCCCAAGGCTGCTGGC-Cy7	10529.7	10525.6	3.50*
CEM-TO^2-Cy7-8	AUACTTOCLGTATCTTOTLCCCAAGGCTGCTGGC-Cy7	10563.8	10566.7	3.51*
CEM-TO^2-Cy7-9	ATTOCLTGCGTATCTTOTLCCCAAGGCTGCTGGC-Cy7	10503.7	10510.5	3.51*
CEM-TO^2-Cy7-10	ATTOCLTGCGTATCTTOTLCCCAAGGCUGCUGGC-Cy7	10896.1	10891.9	3.52*

* Probe measured on the Acquity UPLC system using gradient 4. Underscored letters = 2′-OMe-RNA building blocks; subscript L = LNA. QB and TO base surrogates and the Cy7 reference dye are indicated with bold letters.

8.1.3 UPLC Chromatograms

Compounds marked with an asterisk (*) were analysed on the *Waters* Acquity UPLC system (gradient 4). Their chromatograms (λ = 260 nm) are shown below. The data of probes analysed on the *Gilson* HPLC system could not be exported due to software limitations. Trace amounts (<5 %) of unlabelled nucleic acid sequence, which could sometimes be detected for the TO probes, are marked with an asterisk.

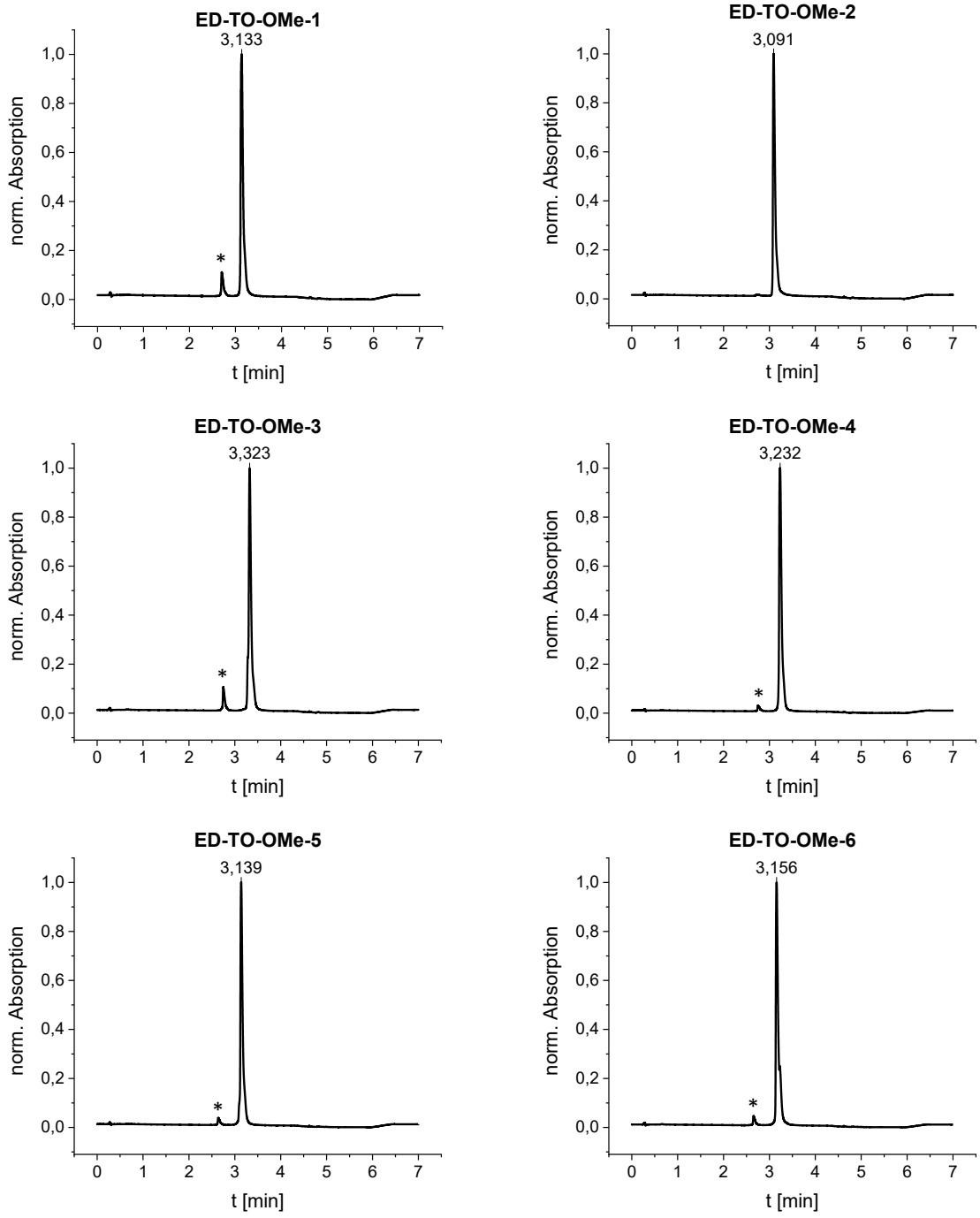

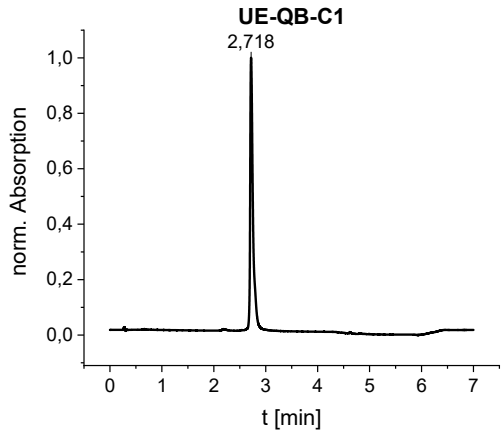
UE-QB-C1
2,718
norm. Absorption
t [min]

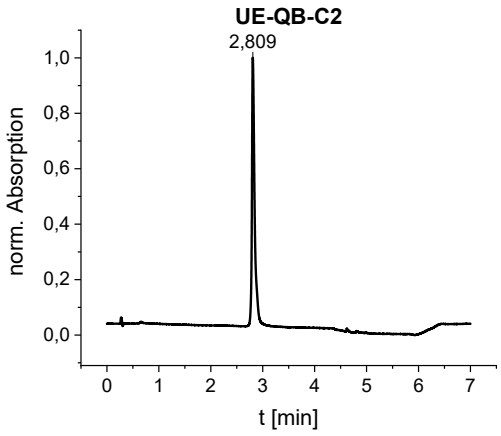
UE-QB-C2
2,809
norm. Absorption
t [min]

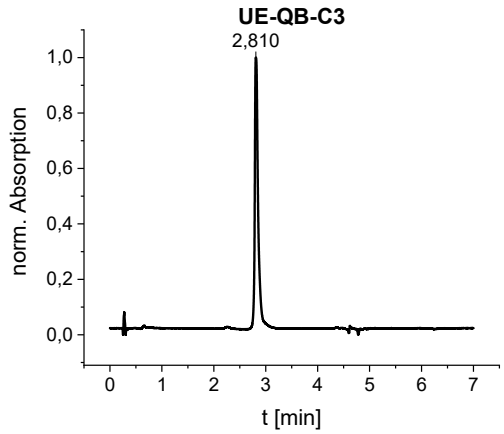
UE-QB-C3
2,810
norm. Absorption
t [min]

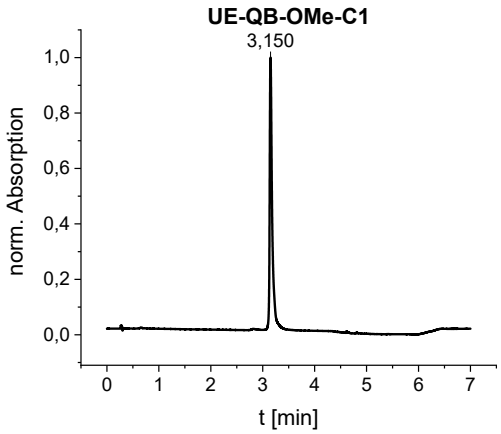
UE-QB-OMe-C1
3,150
norm. Absorption
t [min]

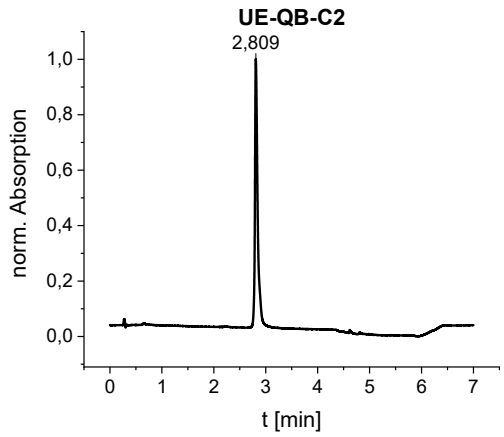
UE-QB-C2
2,809
norm. Absorption
t [min]

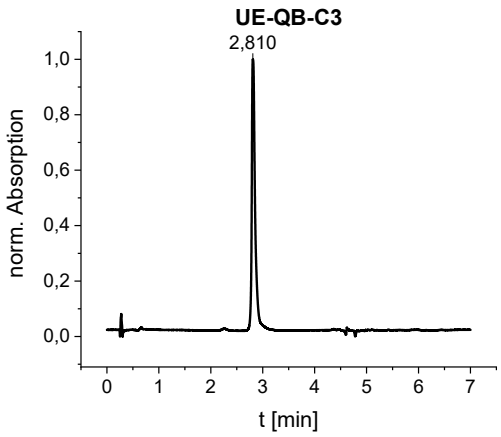
UE-QB-C3
2,810
norm. Absorption
t [min]

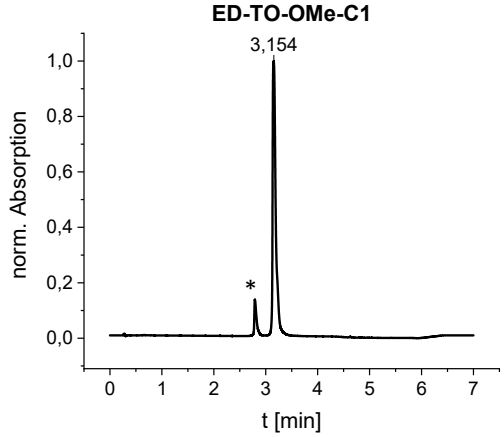
ED-TO-OMe-C1
3,154
*
norm. Absorption
t [min]

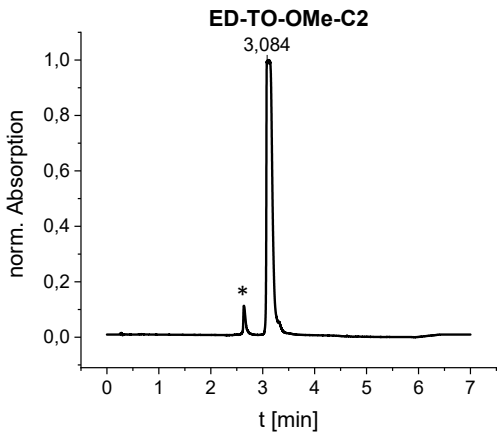
ED-TO-OMe-C2
3,084
*
norm. Absorption
t [min]

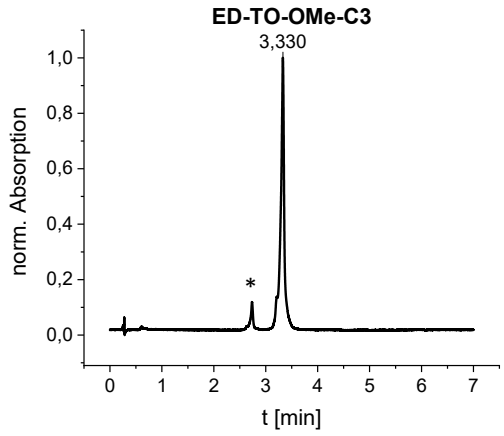
ED-TO-OMe-C3
3,330
norm. Absorption
t [min]
*

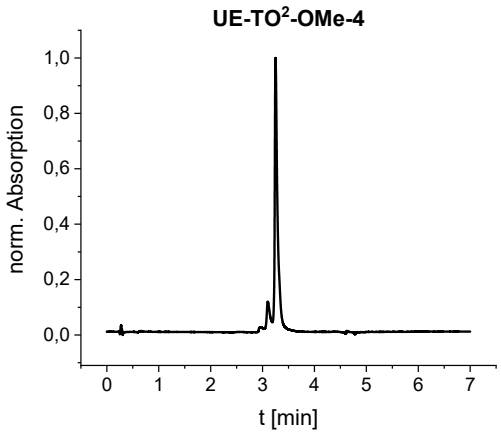
UE-TO²-OMe-4
norm. Absorption
t [min]

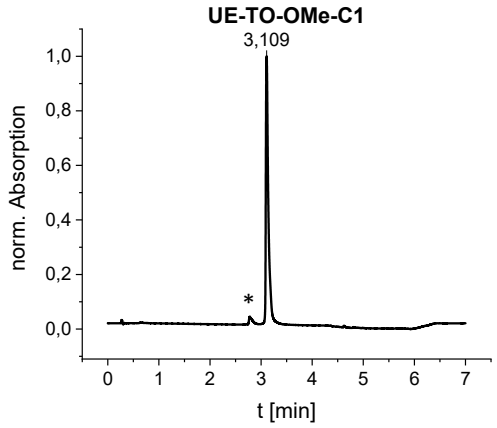
UE-TO-OMe-C1
3,109
norm. Absorption
t [min]
*

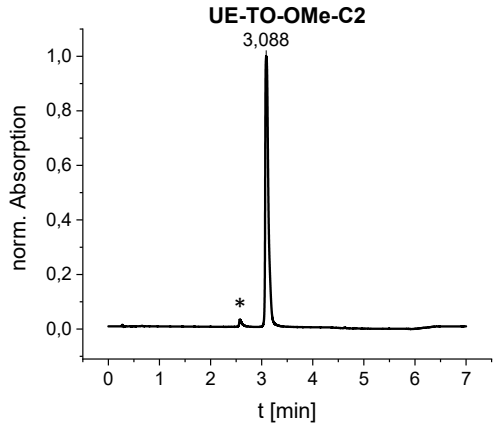
UE-TO-OMe-C2
3,088
norm. Absorption
t [min]
*

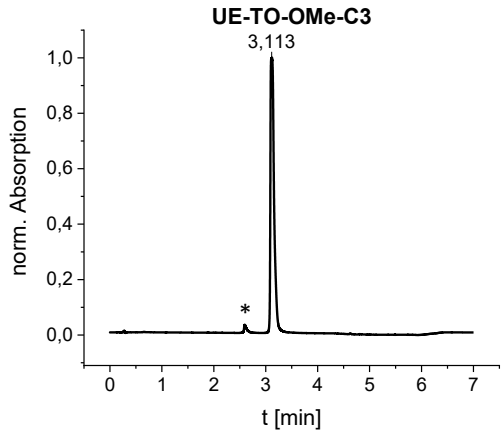
UE-TO-OMe-C3
3,113
norm. Absorption
t [min]
*

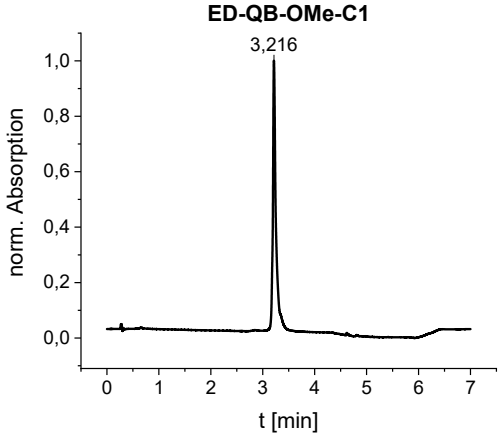
ED-QB-OMe-C1
3,216
norm. Absorption
t [min]

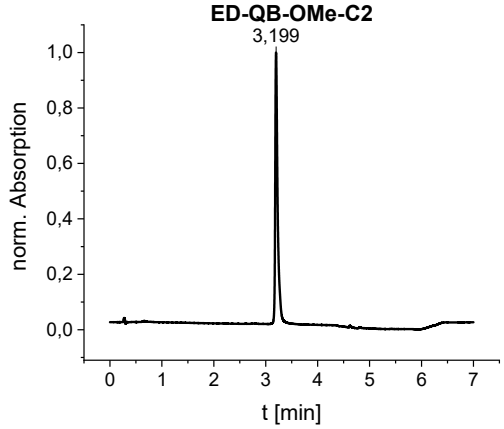
ED-QB-OMe-C2
3,199
norm. Absorption
t [min]

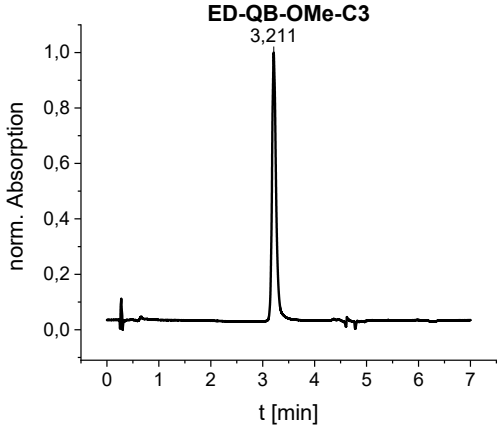
ED-QB-OMe-C3
3,211
norm. Absorption
t [min]

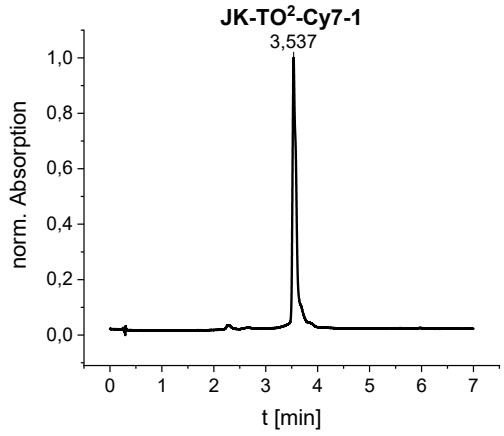
JK-TO²-Cy7-1
3,537
norm. Absorption
t [min]

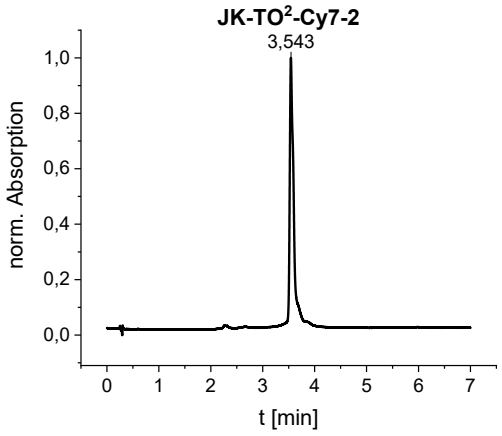
JK-TO²-Cy7-2
3,543
norm. Absorption
t [min]

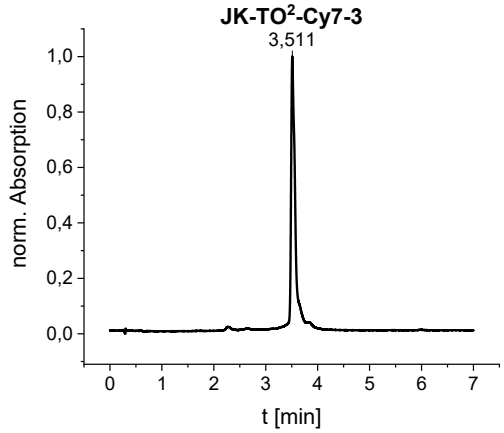
JK-TO²-Cy7-3
3,511
norm. Absorption
t [min]

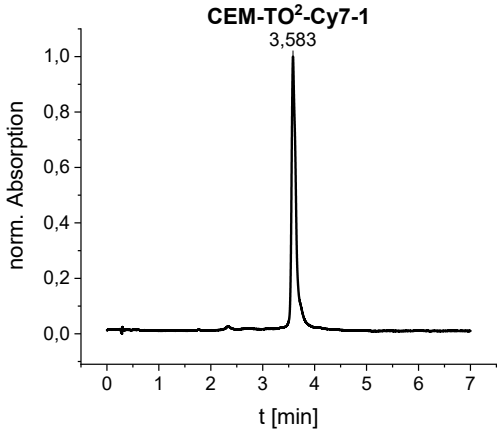
CEM-TO²-Cy7-1
3,583
norm. Absorption
t [min]

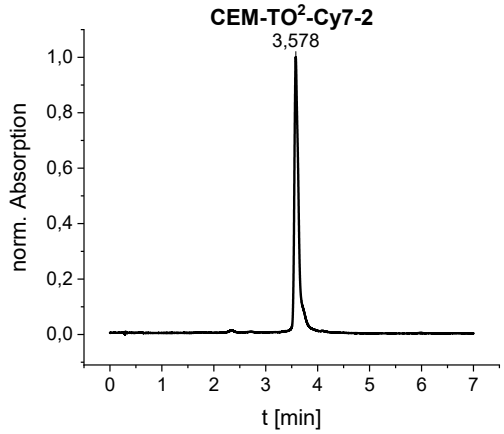
CEM-TO²-Cy7-2
3,578
norm. Absorption
t [min]

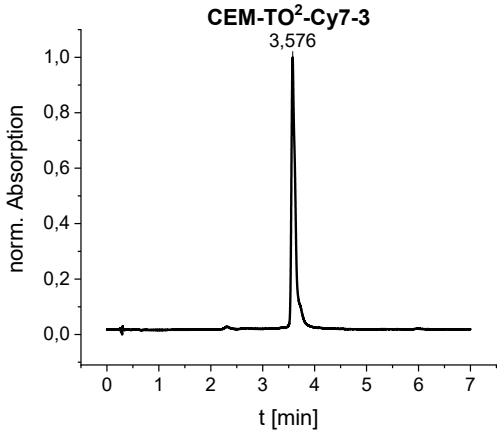
CEM-TO²-Cy7-3
3,576
norm. Absorption
t [min]

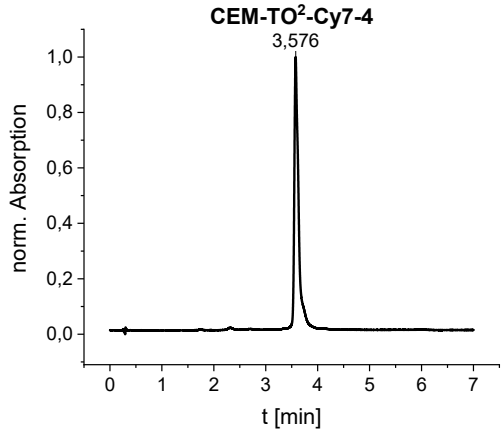
CEM-TO²-Cy7-4
3,576
norm. Absorption
t [min]

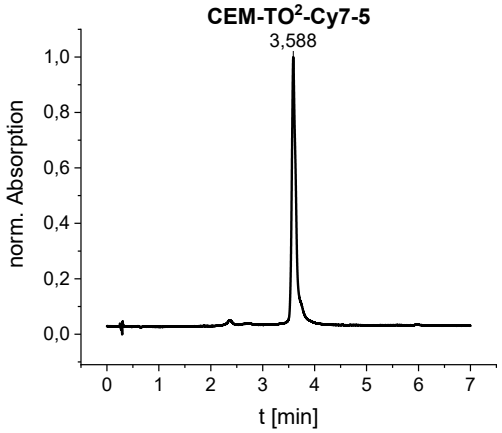
CEM-TO²-Cy7-5
3,588
norm. Absorption
t [min]

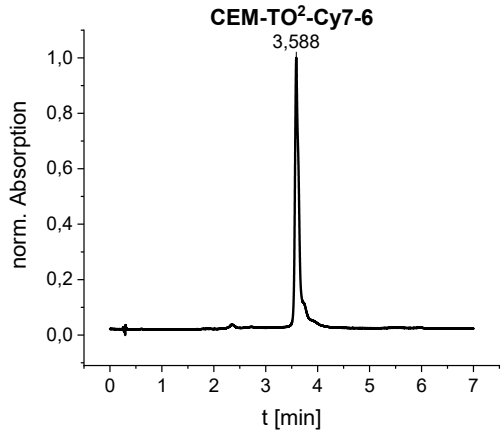
CEM-TO²-Cy7-6
3,588
norm. Absorption
t [min]

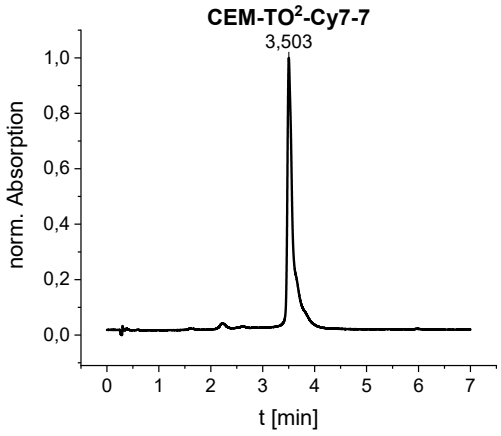
CEM-TO²-Cy7-7
3,503
norm. Absorption
t [min]

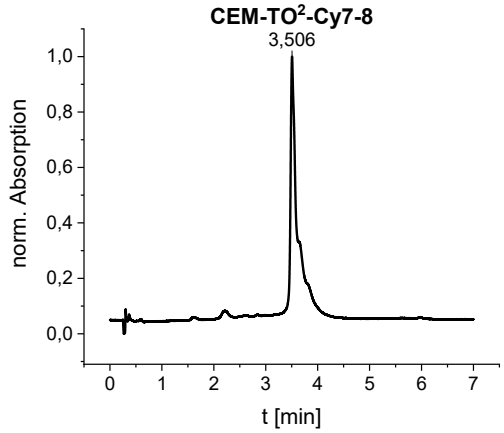
CEM-TO²-Cy7-8
3,506
norm. Absorption
t [min]

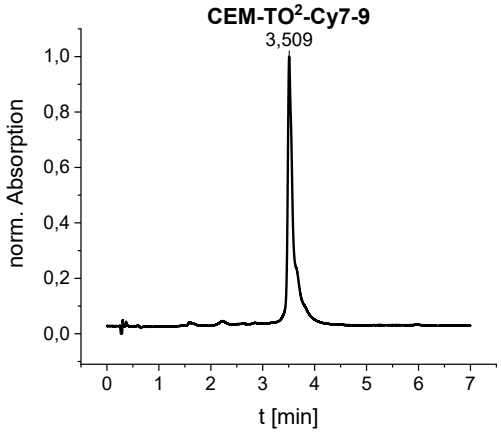
CEM-TO²-Cy7-9
3,509
norm. Absorption
t [min]

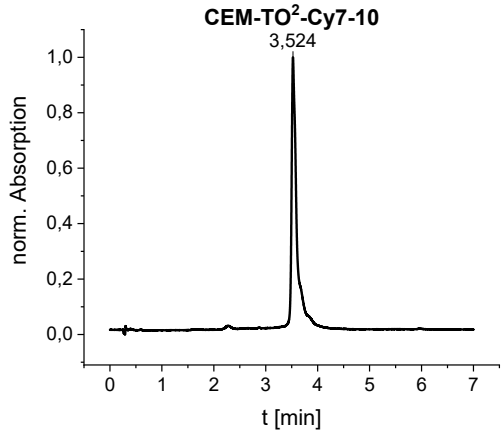
CEM-TO²-Cy7-10
3,524
norm. Absorption
t [min]

8.1.4 MALDI-TOF-MS Spectra

MALDI-TOF-MS Spectra of FIT-Probes Presented in Chapter 5.1.1

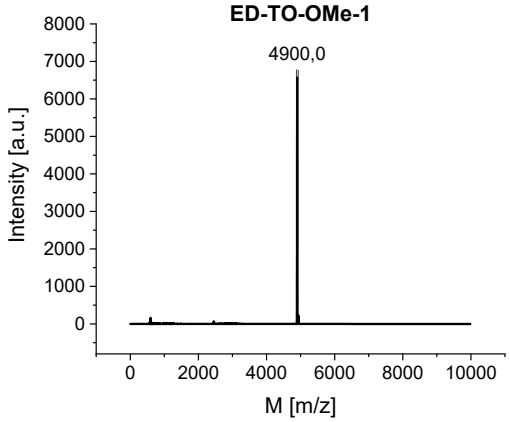

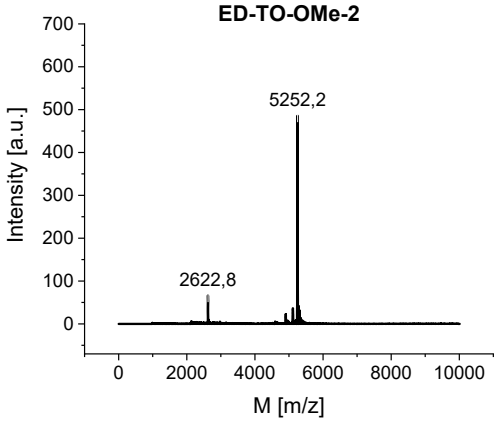

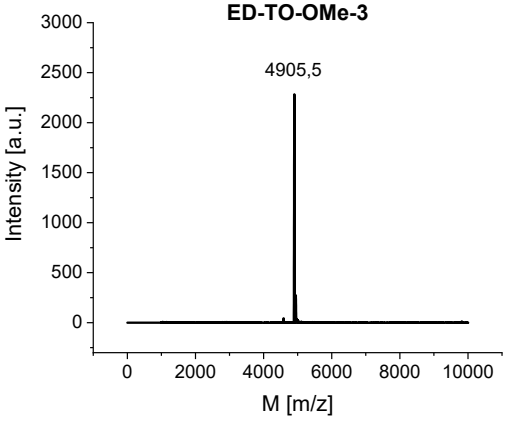

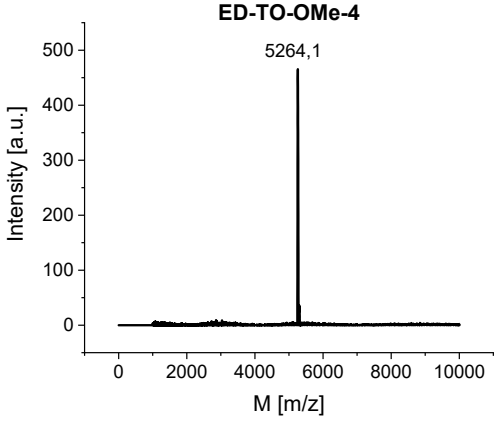

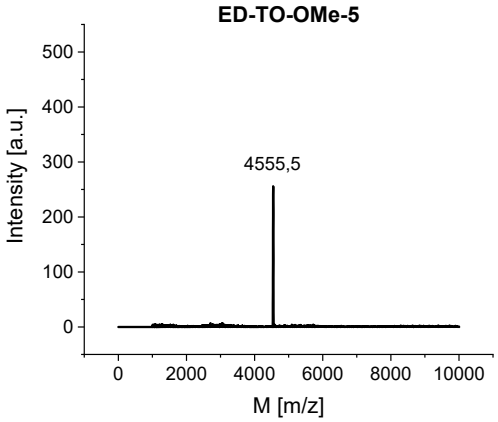

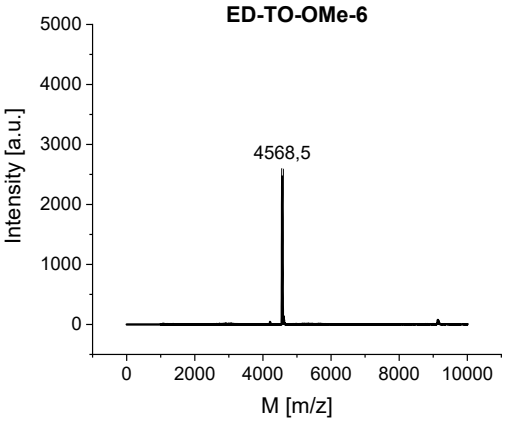

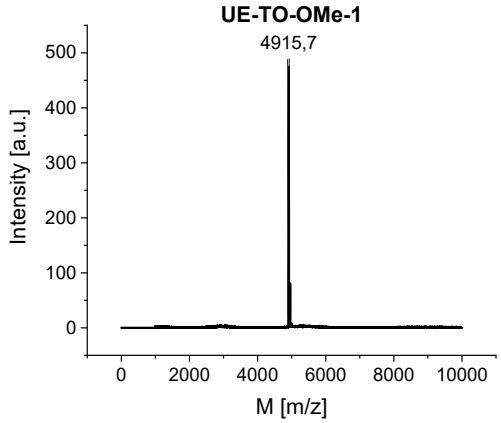
UE-TO-OMe-1
4915,7
Intensity [a.u.]
M [m/z]

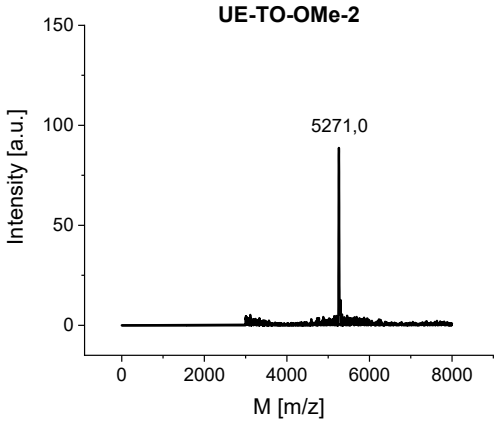
UE-TO-OMe-2
5271,0
Intensity [a.u.]
M [m/z]

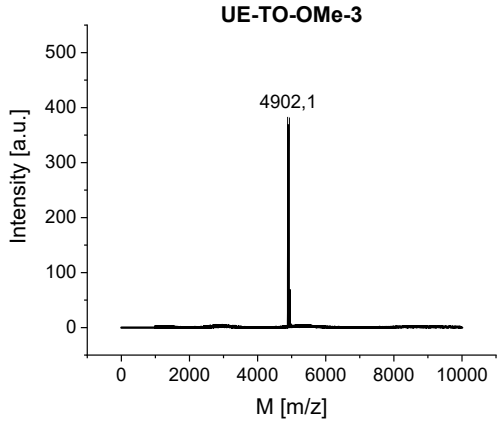
UE-TO-OMe-3
4902,1
Intensity [a.u.]
M [m/z]

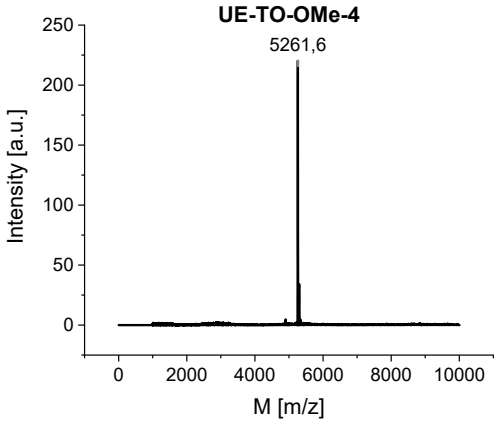
UE-TO-OMe-4
5261,6
Intensity [a.u.]
M [m/z]

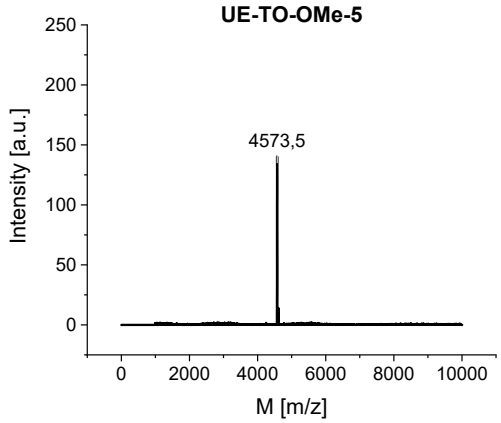
UE-TO-OMe-5
4573,5
Intensity [a.u.]
M [m/z]

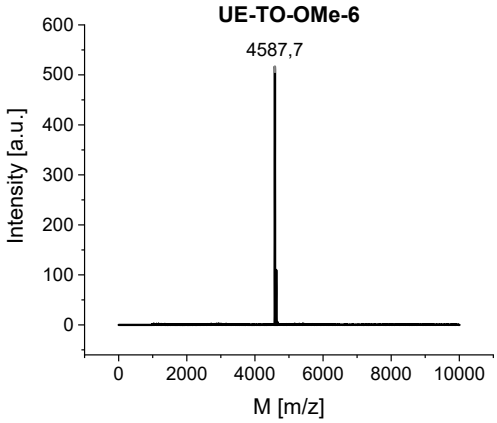
UE-TO-OMe-6
4587,7
Intensity [a.u.]
M [m/z]

MALDI-TOF-MS Spectra of FIT^2-Probes Presented in Chapter 5.1.2

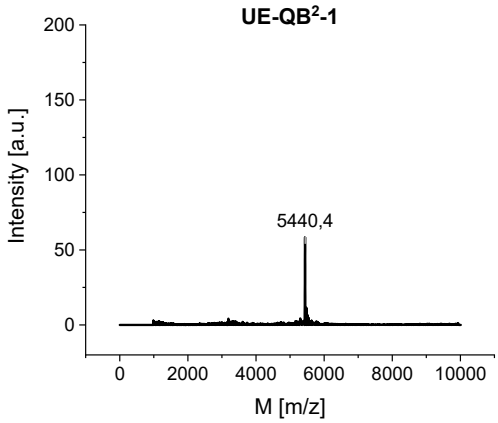

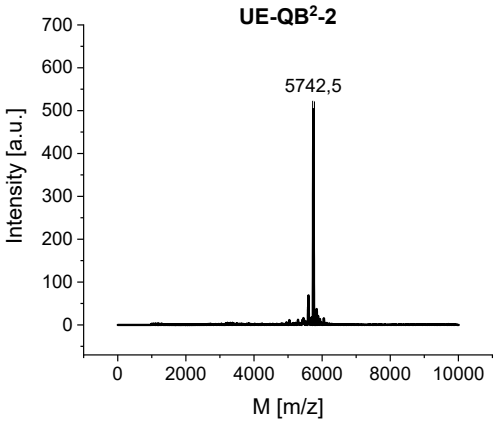

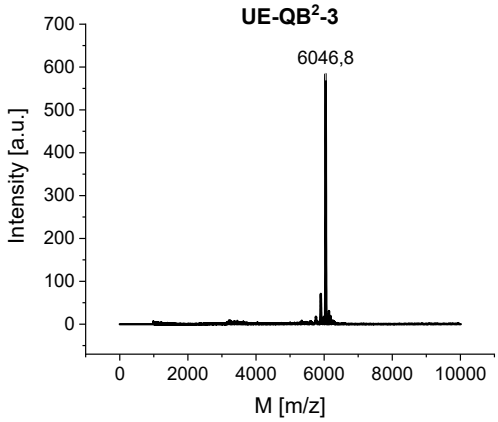

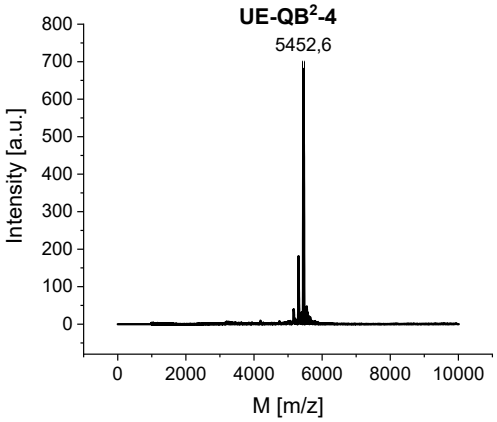

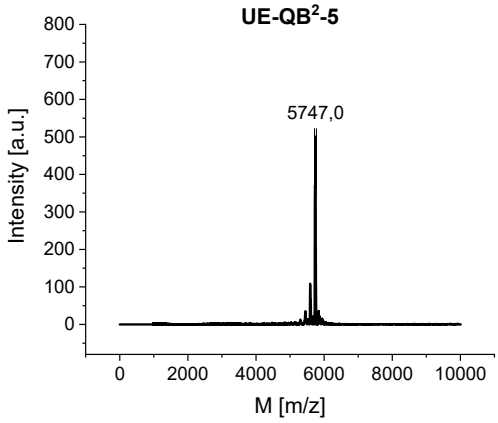

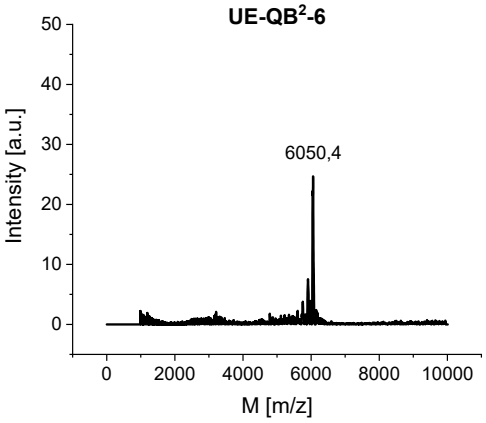

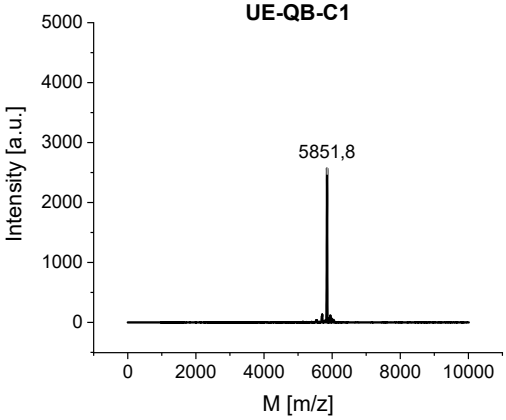

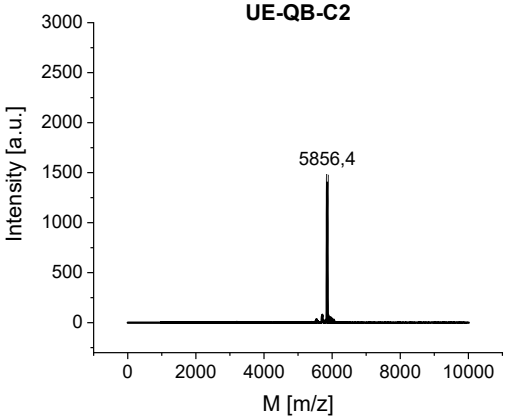

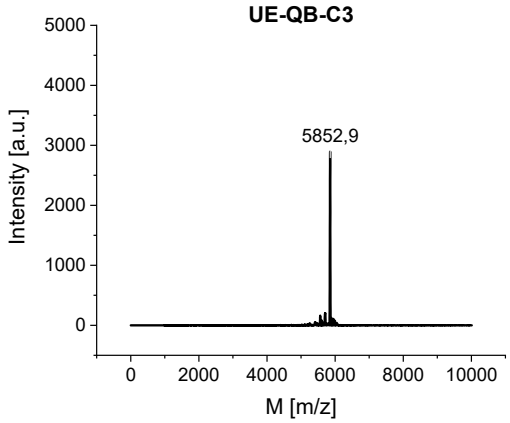
UE-QB-C3
5852,9
Intensity [a.u.]
M [m/z]

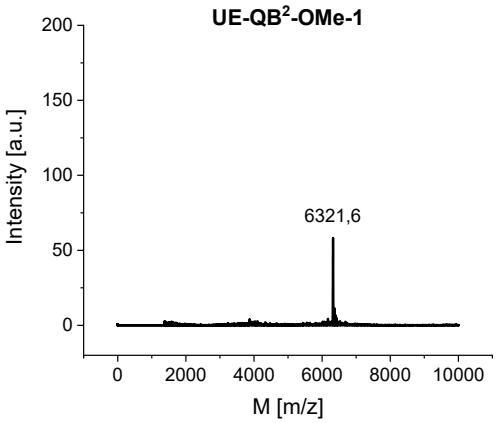
UE-QB²-OMe-1
6321,6
Intensity [a.u.]
M [m/z]

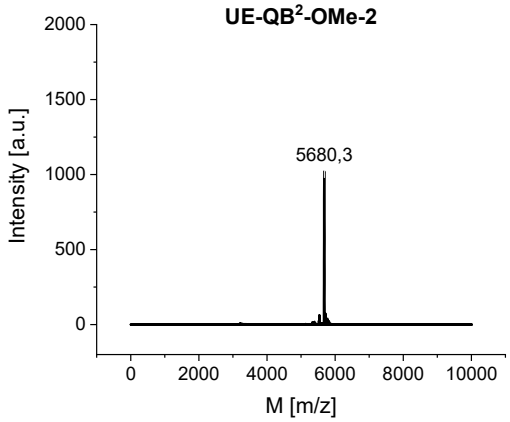
UE-QB²-OMe-2
5680,3
Intensity [a.u.]
M [m/z]

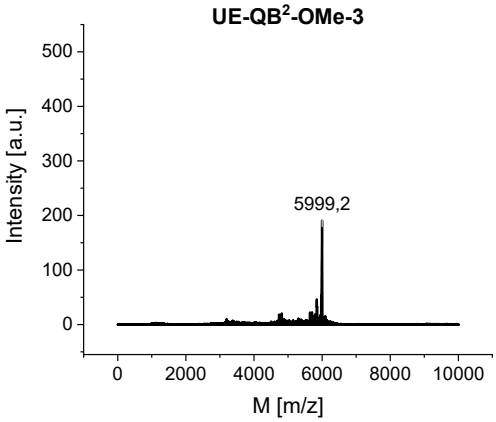
UE-QB²-OMe-3
5999,2
Intensity [a.u.]
M [m/z]

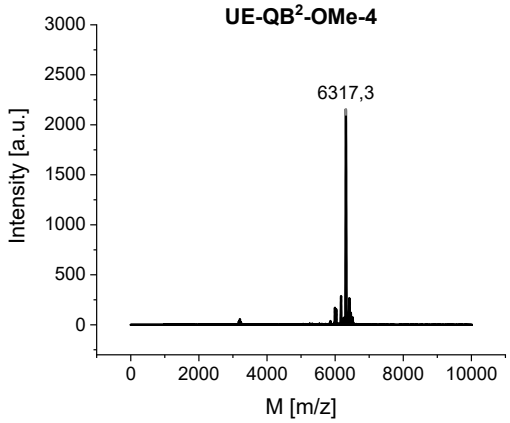
UE-QB²-OMe-4
6317,3
Intensity [a.u.]
M [m/z]

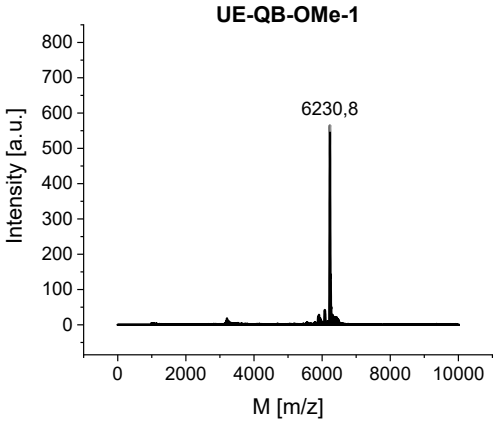
UE-QB-OMe-1
6230,8
Intensity [a.u.]
M [m/z]

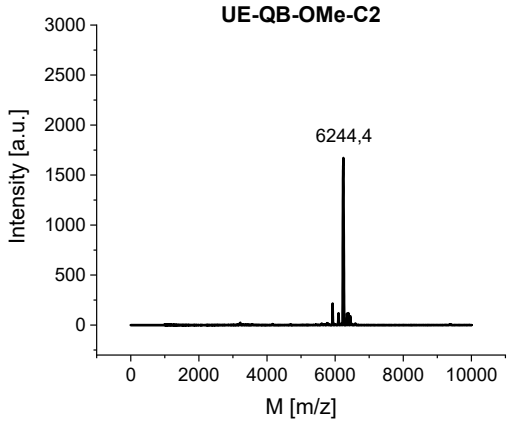
UE-QB-OMe-C2
6244,4
Intensity [a.u.]
M [m/z]

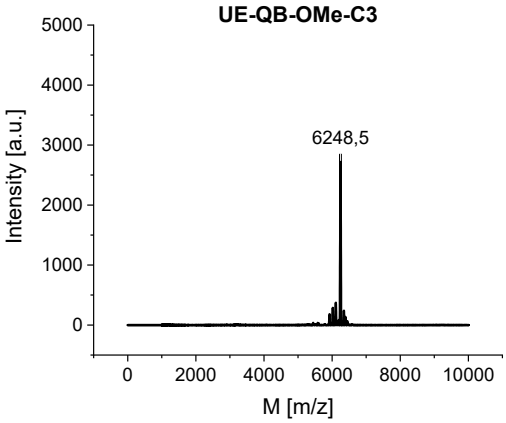
UE-QB-OMe-C3
6248,5
Intensity [a.u.]
M [m/z]

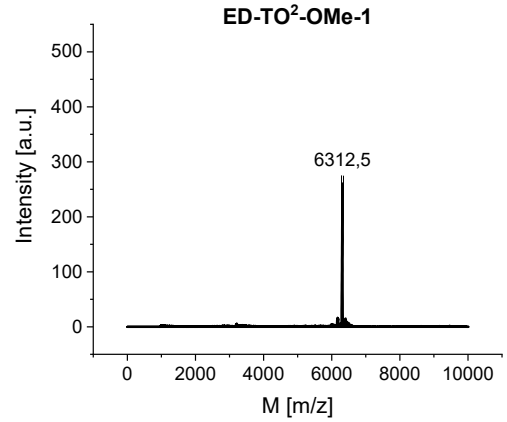
ED-TO2-OMe-1
6312,5
Intensity [a.u.]
M [m/z]

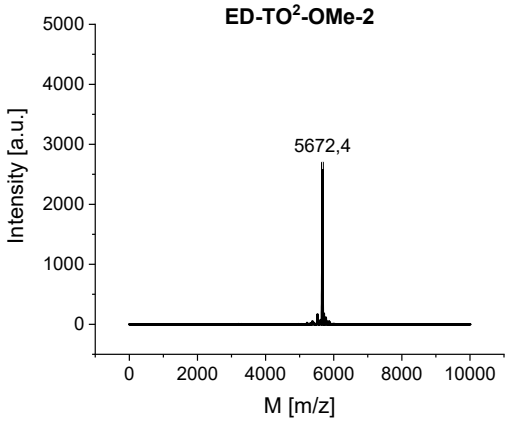
ED-TO2-OMe-2
5672,4
Intensity [a.u.]
M [m/z]

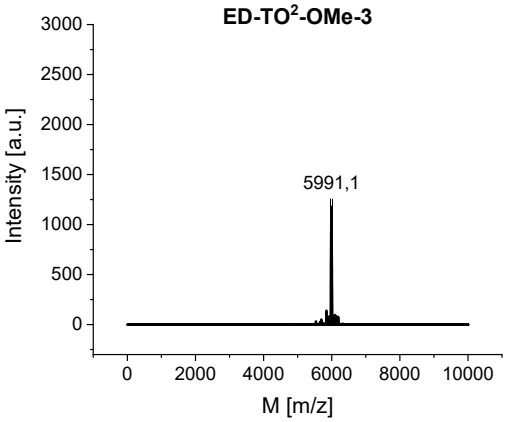
ED-TO2-OMe-3
5991,1
Intensity [a.u.]
M [m/z]

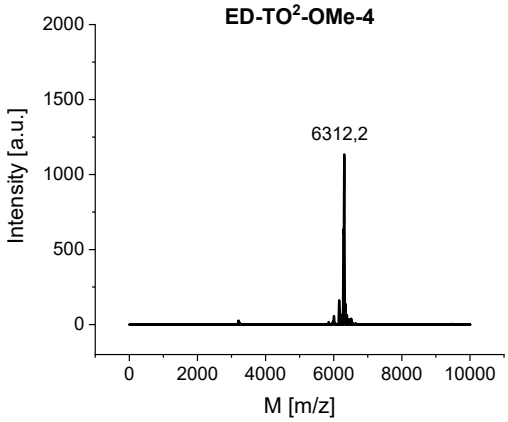
ED-TO2-OMe-4
6312,2
Intensity [a.u.]
M [m/z]

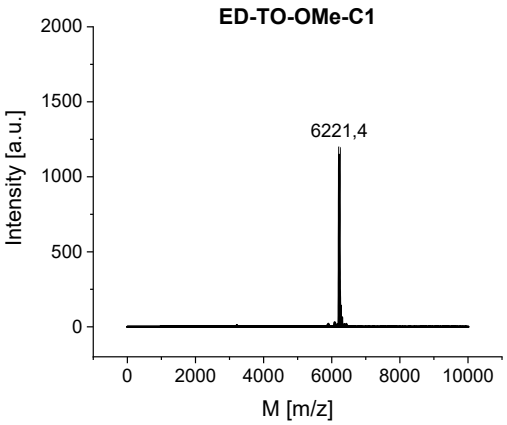
ED-TO-OMe-C1
6221,4
Intensity [a.u.]
M [m/z]

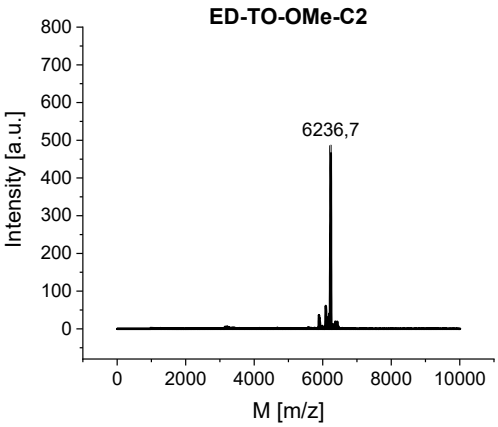
ED-TO-OMe-C2
6236,7
Intensity [a.u.]
M [m/z]

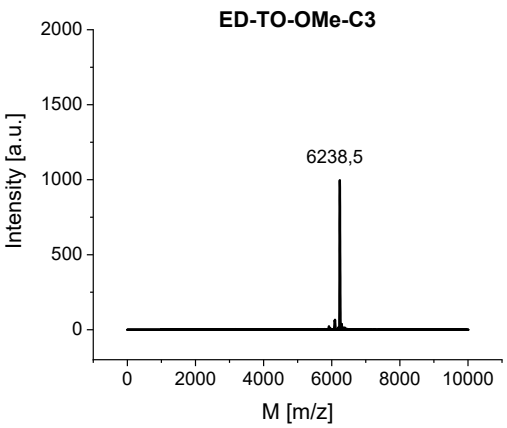
ED-TO-OMe-C3
6238,5
Intensity [a.u.]
M [m/z]

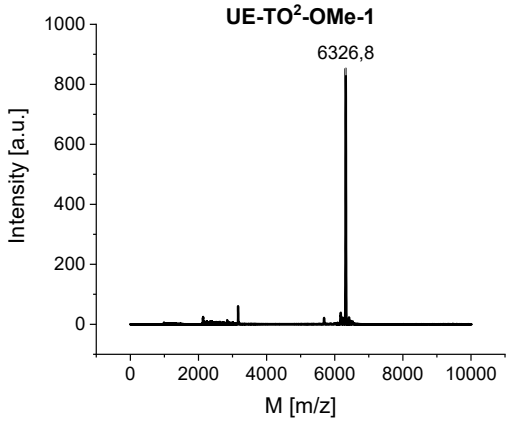
UE-TO²-OMe-1
6326,8
Intensity [a.u.]
M [m/z]

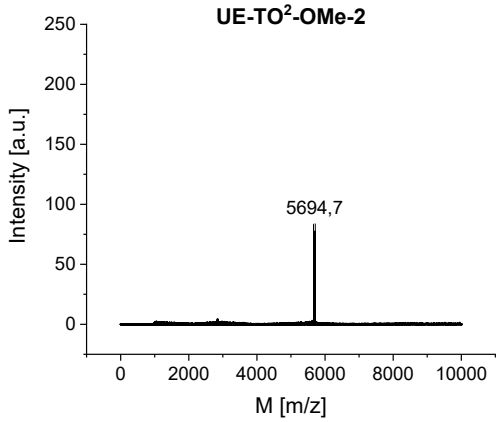
UE-TO²-OMe-2
5694,7
Intensity [a.u.]
M [m/z]

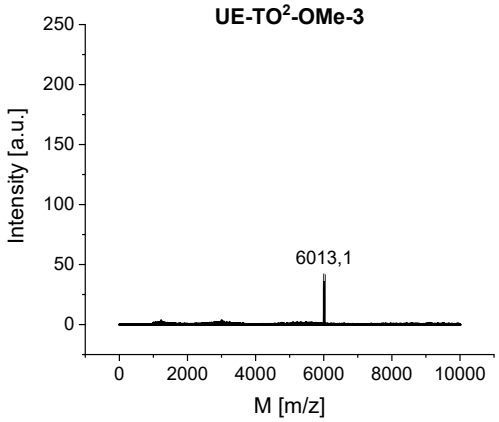
UE-TO²-OMe-3
6013,1
Intensity [a.u.]
M [m/z]

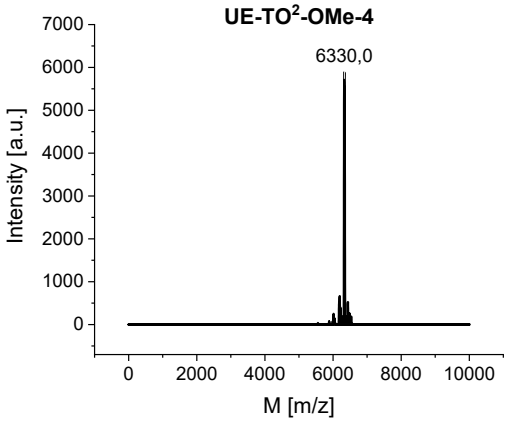
UE-TO²-OMe-4
6330,0
Intensity [a.u.]
M [m/z]

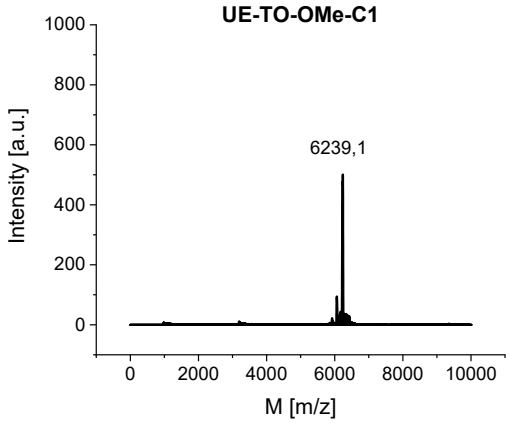
UE-TO-OMe-C1
6239,1
Intensity [a.u.]
M [m/z]

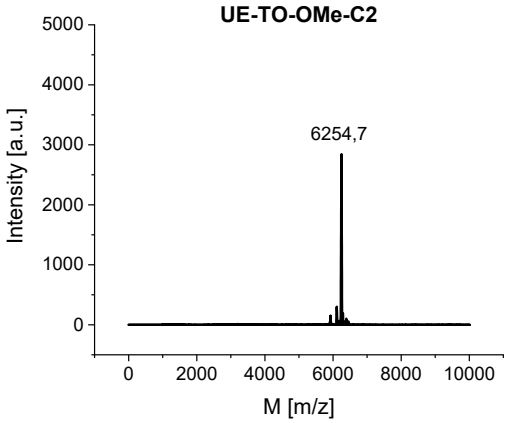
UE-TO-OMe-C2
6254,7
Intensity [a.u.]
M [m/z]

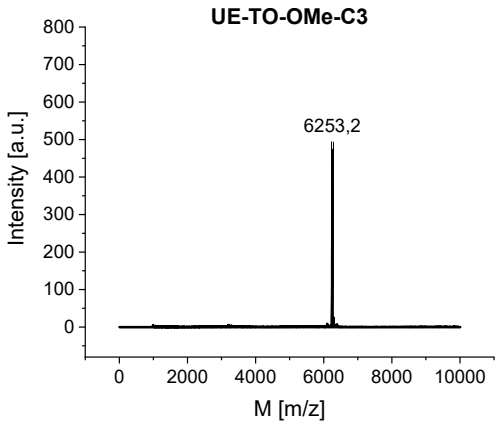
UE-TO-OMe-C3
6253,2
Intensity [a.u.]
M [m/z]

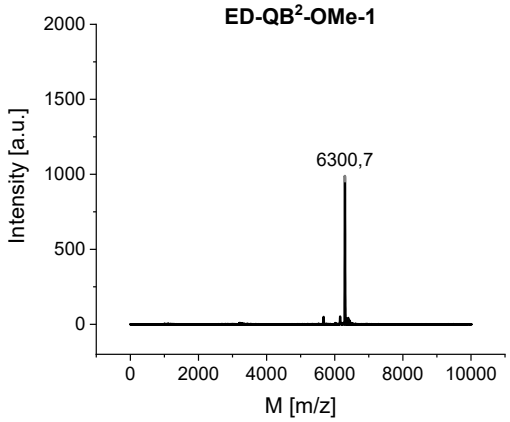
ED-QB²-OMe-1
6300,7
Intensity [a.u.]
M [m/z]

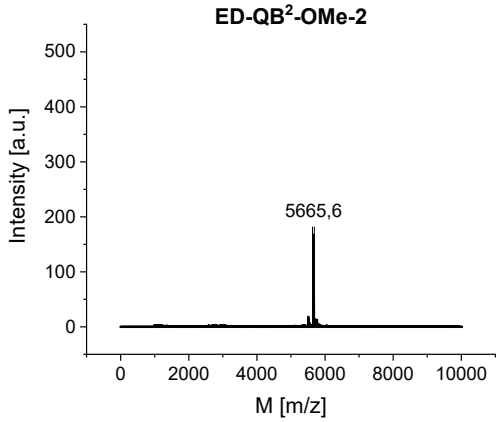
ED-QB²-OMe-2
5665,6
Intensity [a.u.]
M [m/z]

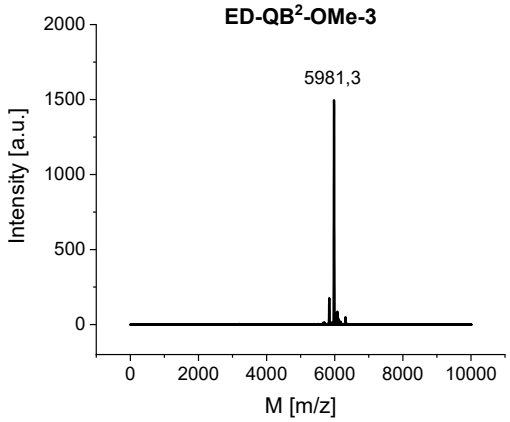
ED-QB²-OMe-3
5981,3
Intensity [a.u.]
M [m/z]

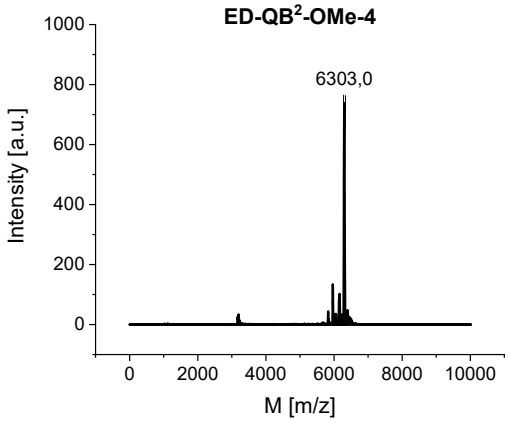
ED-QB²-OMe-4
6303,0
Intensity [a.u.]
M [m/z]

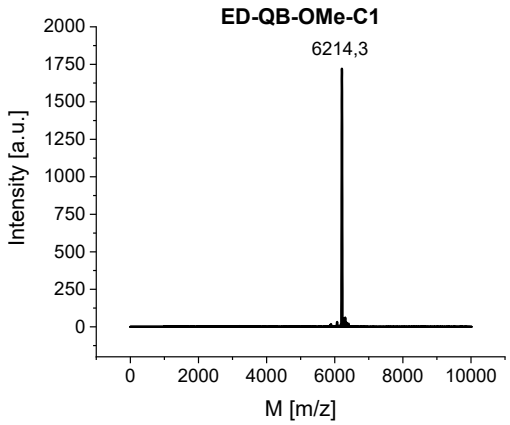
ED-QB-OMe-C1
6214,3
Intensity [a.u.]
M [m/z]

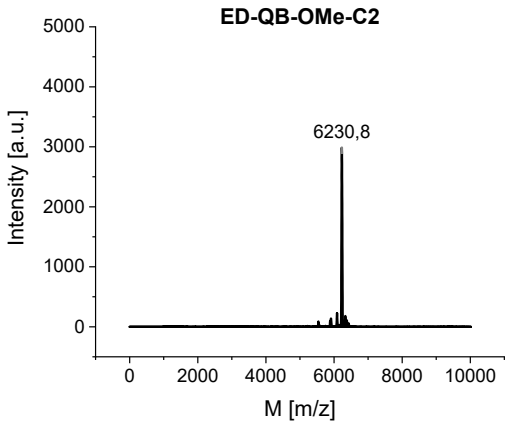
ED-QB-OMe-C2
6230,8
Intensity [a.u.]
M [m/z]

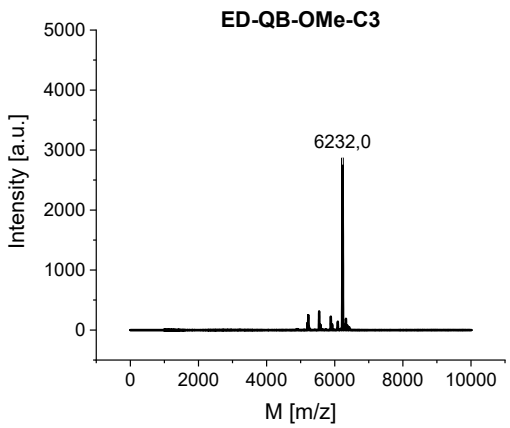
ED-QB-OMe-C3
6232,0
Intensity [a.u.]
M [m/z]

MALDI-TOF-MS Spectra of qFIT^2-Probes Presented in **Chapter 5.2.**

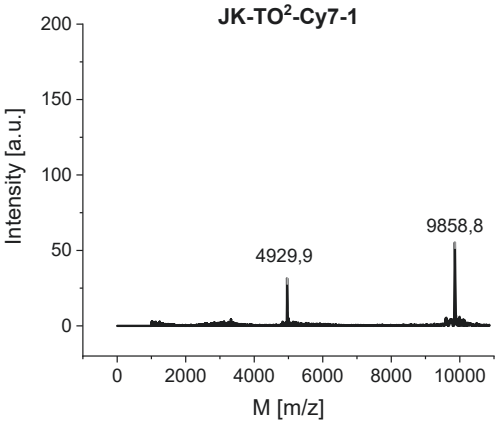

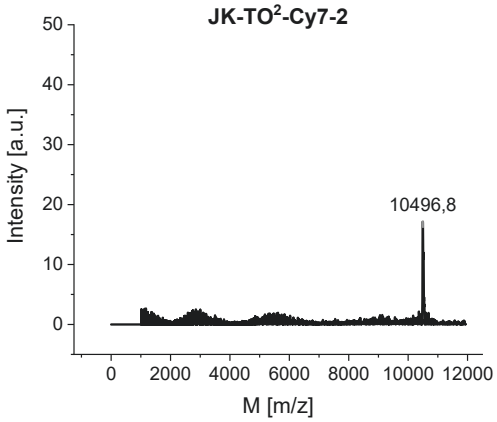

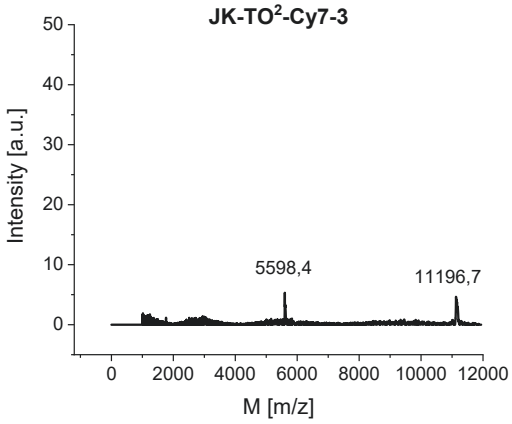

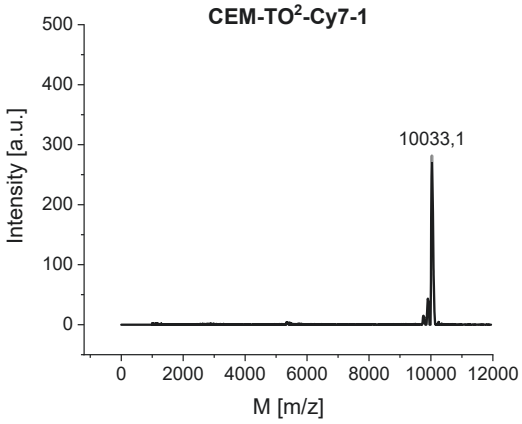

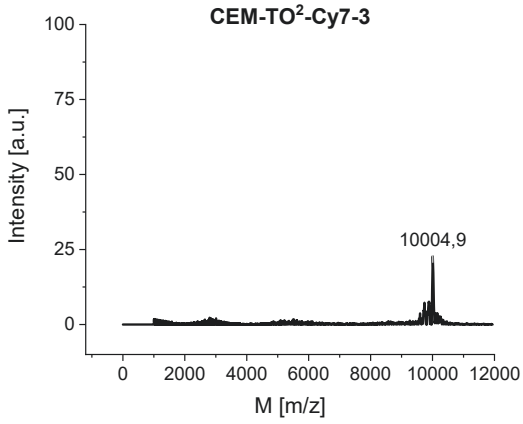

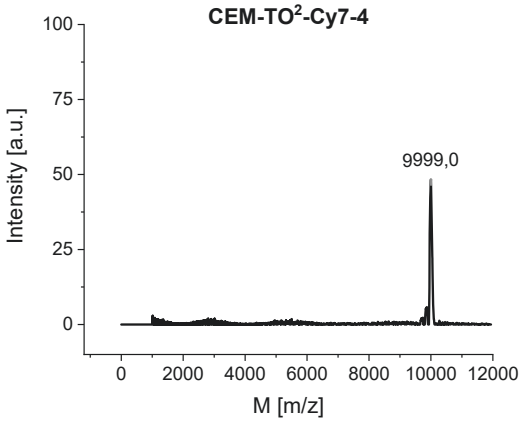

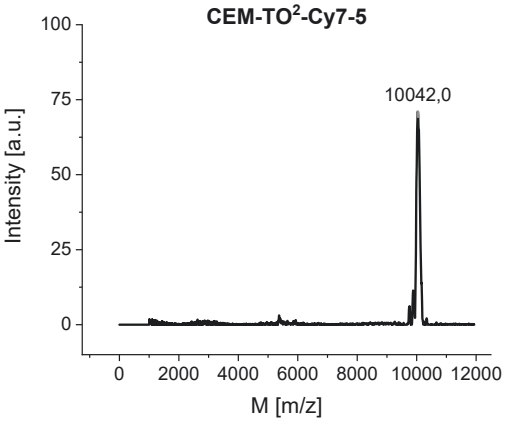

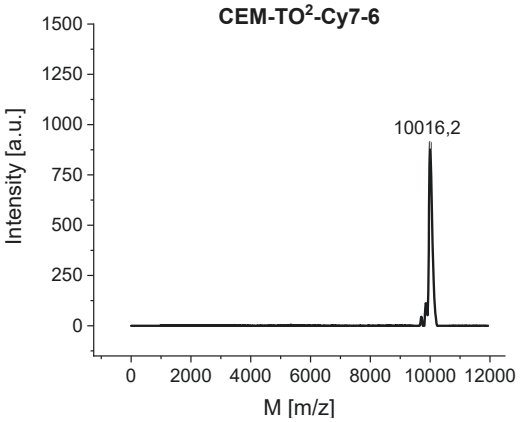

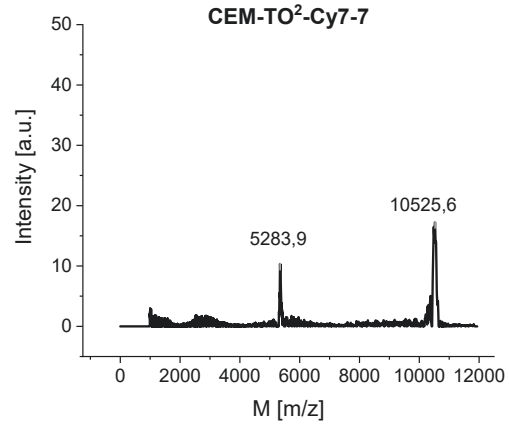
CEM-TO2-Cy7-7
Intensity [a.u.]
M [m/z]
5283,9
10525,6

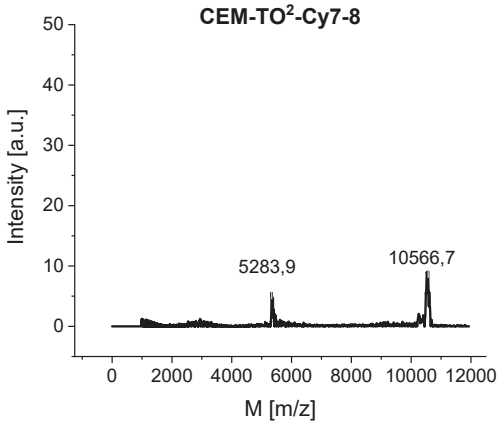
CEM-TO2-Cy7-8
Intensity [a.u.]
M [m/z]
5283,9
10566,7

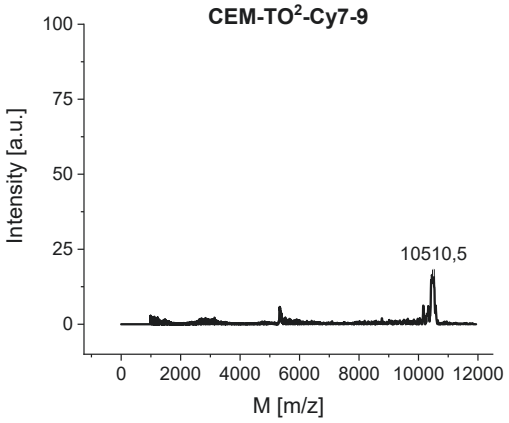
CEM-TO2-Cy7-9
Intensity [a.u.]
M [m/z]
10510,5

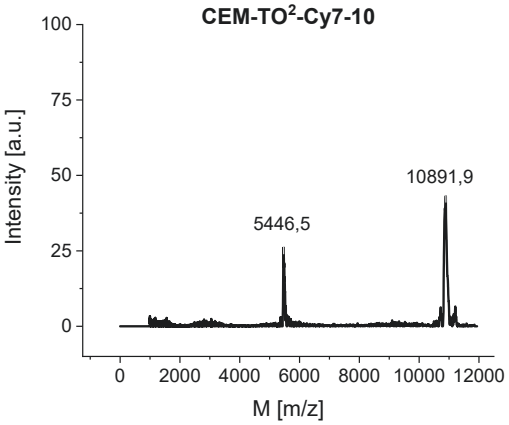
CEM-TO2-Cy7-10
Intensity [a.u.]
M [m/z]
5446,5
10891,9

8.2 Spectroscopic Properties of FIT and FIT^2 Probes Targeting GlyRα2 mRNA

8.2.1 Mono-Dye FIT Probes

Table 12: Spectroscopic properties of GlyRα2 UE-TO-OMe and ED-QB-OMe FIT probes.

	Sequence 5' – 3'	RNA target	I_0	SD	I	E	S	ϕ	ϕ/ϕ$_0$	Br	T_m
UE-TO-OMe											
1	AATAAACTGA***G***TOC$_L$A	m mm	6.17	0.18	110.2 57.0	17.5 9.4	1.9	0.44 0.31	5.7 4.2	21.7 14.6	55.5 42.5
2	AATAAACTGA***G***TOC$_L$AG	m mm	40.4	0.69	124.9 84.1	3.1 2.1	1.5	0.49 0.38	2.0 1.6	22.9 21.1	57.1 46.7
3	AATAAACTGA***G$_L$***TOCA	m mm	7.51	0.17	63.9 30.3	8.7 4.0	2.5	0.31 0.22	6.0 3.8	14.1 10.8	52.3 40.2
4	AATAAACTGA***G$_L$***TOCAG	m mm	5.24	0.24	77.2 45.3	14.3 8.9	1.6	0.30 0.25	7.0 6.0	13.9 11.2	53.3 41.8
5	AATAAACTG**TO*G$_L$***GC	m mm	7.49	0.06	77.1 41.7	10.5 5.1	2.0	0.44 0.30	6.8 3.8	17.5 13.6	51.9 47.6
6	AATAAAC TG$_L$**TO*G***GC	m mm	3.11	0.02	42.5 21.2	13.7 6.8	2.2	0.23 0.14	9.4 5.3	9.8 6.1	52.7 49.8
ED-QB-OMe											
1	AATAAACTGA***A*****QB**C$_L$A	m mm	2.05	0.07	84.9 11.5	41.2 5.8	7.1	0.29 0.10	24.8 18.1	10.0 2.8	48.8 40.8
2	AATAAACTGA **QB**C$_L$AG	m mm	6.85	0.92	113.1 14.9	15.0 2.4	6.3	0.31 0.11	9.6 4.1	15.0 4.6	50.4 42.1
3	AATAAACTGAA***A$_L$*****QB**CA	m mm	0.4	0.00	22.2 0.9	63.3 2.4	26.4	0.11 0.02	29.3 7.1	4.3 0.6	45.1 37.0
4	AATAAACTGAA***A$_L$*****QB**CAG	m mm	2.6	0.00	32.8 3.6	12.8 1.4	9.1	0.24 0.03	14.1 2.6	6.2 1.0	46.7 37.0

Conditions: 0.5 µM probe and 4 eq. RNA target (5'-CUGC**Y**UCAGUUUAUU-3', UE: Y = C; ED: Y = U) were measured in PBS buffer (100 mM NaCl, 10 mM Na_2HPO_4, pH 7.0) at 37 °C to determine fluorescence enhancement E = I / I_0 with SD as standard deviation and specificity S = E_m / E_{mm}. Quantum yield ϕ and brightness Br = $\varepsilon_{\lambda ex} \cdot$ ϕ / 1000 in $M^{-1} \cdot cm^{-1}$ were measured at 25 °C. QB: λ_{ex} = 560 nm, λ_{em} = 605 nm; TO: λ_{ex} = 485 nm, λ_{em} = 535 nm, $slit_{ex/em}$ = 5 nm. Melting temperature T_m in °C was measured with 1 µM probe and 1 eq. (1 µM) target RNA. Underscored letters = 2'OMe-RNA; subscript L = LNA; bold italic letters = editing site and bold letters = base surrogates. Match and mismatch target are indicated with m and mm.

Table 13: Spectroscopic properties of GlyRα2 ED-TO-OMe and UE-QB-OMe FIT probes.

	Sequence 5′ – 3′	RNA target	I_0	SD	I	E	S	ϕ	ϕ / $ϕ_0$	Br	T_m
ED-TO-OMe											
1	AATAAACTGA***A**TO*C$_L$A	m mm	3.87	0.12	71.8 13.4	18.2 3.6	5.0	0.43 0.19	3.8 1.6	25.0 8.8	46.4 39.2
2	AATAAACTGA***A**TO*C$_L$AG	m mm	39.3	1.15	94.8 22.5	2.4 0.6	4.0	0.67 0.26	1.6 0.6	32.3 12.7	49.0 43.0
3	AATAAACTGA***A**$_L$TO*CA	m mm	2.48	0.12	35.3 14.0	14.7 5.5	2.7	0.24 0.17	7.5 4.9	14.8 8.1	45.7 38.2
4	AATAAACTGA***A**$_L$TO*CAG	m mm	4.11	0.89	43.5 11.3	12.5 2.4	5.3	0.28 0.18	3.3 1.8	12.5 8.4	46.8 38.7
5	AATAAACTG**TO*A**$_L$GC	m mm	2.87	0.08	30.5 6.9	10.8 2.4	4.6	0.52 0.16	4.0 1.2	18.6 5.8	47.5 40.5
6	AATAAAC**T**G$_L$**TO*A***GC	m mm	3.92	0.05	42.2 7.1	10.9 1.8	6.0	0.38 0.11	9.1 2.3	16.0 5.6	44.3 36.7
UE-QB-OMe											
1	AATAAACTGA***G**QB*C$_L$A	m mm	1.75	0.21	143.4 53.6	87.5 28.4	3.1	0.45 0.35	65.2 79.5	16.8 14.6	56.3 43.9
2	AATAAACTGA***G**QB*C$_L$AG	m mm	10.7	1.06	146.2 79.6	12.8 8.1	1.5	0.48 0.47	13.2 12.2	24.5 26.0	60.5 47.0
3	AATAAACTGA***G**$_L$QB*CA	m mm	3.3	0.42	55.2 24.3	15.3 8.0	1.9	0.18 0.27	42.3 59.6	6.1 8.3	47.3 39.0
4	AATAAACTGA***G**$_L$QB*CAG	m mm	1.65	0.07	57.9 36.0	37.4 21.2	1.7	0.22 0.32	43.7 42.7	7.5 11.5	52.9 41.8

Conditions: 0.5 µM probe and 4 eq. RNA target (5′-CUGC**Y**UCAGUUUAUU-3', UE: Y = C; ED: Y = U) were measured in PBS buffer (100 mM NaCl, 10 mM Na_2HPO_4, pH 7.0) at 37 °C to determine fluorescence enhancement E = I / I_0 with SD as standard deviation and specificity S = E_m / E_{mm}. Quantum yield ϕ and brightness Br = $\varepsilon_{\lambda ex} \cdot$ ϕ / 1000 in $M^{-1} \cdot cm^{-1}$ were measured at 25 °C. QB: λ_{ex} = 560 nm, λ_{em} = 605 nm; TO: λ_{ex} = 485 nm, λ_{em} = 535 nm, $slit_{ex/em}$ = 5 nm. Melting temperature T_m in °C was measured with 1 µM probe and 1 eq. (1 µM) target RNA. Underscored letters = 2′OMe-RNA; subscript L = LNA; bold italic letters = editing site and bold letters = base surrogates. Match and mismatch target are indicated with m and mm.

8.2.2 Dual-Dye FIT^2 Probes

In addition to match and mismatch targets, the QB FIT^2 probes listed below were tested against a partially matched RNA (5'-AGGACCAU**UCACCCUGCCUCAG**GAUCUAAGCAGGA-3') with a 14 nt overlap.

Table 14: Spectroscopic properties of DNA-based UE-QB^2 FIT^2 probes and their respective controls.

	Sequence 5' – 3'	RNA target	I_0	SD	I	E	S	ϕ	ϕ / ϕ$_0$	Br	T_m
UE-QB^2											
1	AAA**QB**T$_L$AAACTGA***G*** **QB**C$_L$A	m mm pm	1.35	0.11	92.3 3.1 1.4	66.1 2.6 1.0	22.0	0.18 0.03 0.007	45.3 5.6 1.2	13.5 3.2 0.8	49.9 50.9 nd
2	CAAA**QB**T$_L$AAACTGA***G*** **QB**C$_L$A	m mm pm	1.06	0.03	110.3 4.2 1.3	106.7 3.8 1.3	26.5	0.15 0.03 0.004	45.0 6.7 1.3	13.1 2.8 0.5	51.2 48.5 nd
3	TCAAA**QB**T$_L$AAACTGA ***G*****QB**C$_L$A	m mm pm	1.09	0.14	116.1 4.3 1.2	131.7 4.4 1.0	32.7	0.15 0.03 0.004	53.8 6.7 1.1	12.3 2.7 0.4	52.0 48.7 nd
4	AAAAT**QB**A$_L$ACTGA ***G*****QB**C$_L$A	m mm pm	0.80	0.01	66.1 1.1 0.6	82.2 1.3 1.1	63.1	0.11 0.01 0.004	45.8 2.4 1.3	8.9 0.7 0.5	49.6 50.9 nd
5	CAAAAT**QB**A$_L$ACTGA ***G*****QB**C$_L$A	m mm pm	0.60	0.21	81.5 1.0 1.0	110.0 2.6 1.5	36.6	0.12 0.01 0.004	54.6 4.2 1.2	10.3 1.4 0.5	48.3 50.6 nd
6	TCAAAAT**QB**A$_L$ACTGA ***G*****QB**C$_L$A	m mm pm	0.68	0.06	83.8 1.5 0.9	121.3 2.4 1.2	78.8	0.13 0.01 0.004	54.2 3.7 1.2	11.0 1.0 0.5	49.2 51.1 nd
UE-QB											
C1	TCAAAATAAACTGA ***G*****QB**C$_L$A	m mm	1.61	0.27	98.9 2.2	69.6 1.2	56.7	0.32 0.03	34.7 2.8	12.7 1.0	48.4 53.3
C2	TCAAA**QB**T$_L$AAACTGA ***G***GCA	m mm	1.9	0.07	49.4 5.5	26.1 3.0	8.7	0.19 0.07	16.6 6.4	7.4 2.8	49.8 49.0
C3	TCAAAAT**QB**A$_L$AC-TGA***G***GCA	m mm	1.34	0.05	61.2 3.4	47.1 2.5	18.9	0.30 0.08	37.3 9.4	10.3 3.2	49.2 51.1

Conditions: 0.5 µM probe and 5 eq. RNA target (match / mismatch: 5'-CUGAAGGACUCACCCUGC**Y**UCAGUUUAUUU UGA-3', UE: Y = C; ED: Y = U; partial match: 5'- AGGACCAU**UCACCCUGCCUCAG**GAUCUAAGCAGGA-3') were measured in PBS buffer (100 mM NaCl, 10 mM Na_2HPO_4, pH 7.0) at 37 °C to determine fluorescence enhancement $E = I_{ds} / I_{ss}$ with SD as standard deviation and specificity $S = E_m / E_{mm}$. Quantum yield ϕ and brightness $Br = \varepsilon_{\lambda ex} \cdot \phi_{ds} / 1000$ in $M^{-1} \cdot cm^{-1}$ were measured at 25 °C. QB: λ_{ex} = 560 nm, λ_{em} = 605 nm; TO: λ_{ex} = 485 nm, λ_{em} = 535 nm. Melting temperature T_m in °C was measured with 1 µM probe and 1 eq. (1 µM) target RNA. Underscored letters = 2'OMe-RNA; subscript L = LNA; bold italic letters = editing site and bold letters = base surrogates. Match, mismatch and partial match RNA target are indicated with m, mm and pm.

Table 15: Spectroscopic properties of nuclease-resistant UE-QB²-OMe probes and their respective controls.

	Sequence 5' – 3'	RNA target	I_0	SD	I	E	S	ϕ	ϕ / $ϕ_0$	Br	T_m
UE-QB²-OMe											
1	UCAAA**QB**T_LAAACUGA***G*** **QB**C_LA	m mm pm	1.58	0.70	156.3 13.7 3.5	124.8 8.5 2.3	14.8	0.38 0.09 0.03	41.6 1.5 1.5	29.4 7.0 2.7	49.6 49.6 nd
2	AAAA**T**QBA_LACUGA ***G***QBC_LA	m mm pm	0.96	0.06	99.7 17.6 3.0	109.0 17.6 3.0	6.2	0.23 0.10 0.01	17.8 15.1 4.4	16.2 7.3 1.0	49.8 49.3 nd
3	CAAAA**T**QBA_LACUGA ***G***QBC_L A	m mm pm	0.97	0.04	119.0 41.0 3.4	119.0 41.0 3.4	2.9	0.24 0.15 0.01	39.9 9.4 3.7	16.8 11.2 0.9	48.3 48.6 nd
4	UCAAAA**T**QBA_LACUGA***G*** **QB**C_LA	m mm pm	1.34	0.22	117.0 37.9 2.9	108.2 26.4 1.9	4.1	0.25 0.13 0.01	48.6 19.8 2.7	17.1 9.0 1.4	48.6 48.2 nd
UE-QB-OMe											
C1	UCAAAAUAAACUGA ***G***QBC_LA	m mm	1.79	0.02	164.4 133.4	91.2 75.1	1.2	0.58 0.53	69.9 16.9	23.1 21.2	62.1 53.2
C2	UCAAA**QB**T_LAAACUGAG ***G***CA	m mm	2.78	0.30	85.2 81.7	28.4 31.8	0.9	0.30 0.26	13.3 11.0	9.9 9.2	66.5 59.6
C3	UCAAAA**T**QBA_LACUGAG ***G***CA	m mm	1.93	0.17	73.9 76.3	36.0 42.2	0.9	0.19 0.17	15.1 13.7	7.6 6.4	65.3 58.2

Conditions: 0.5 µM probe and 5 eq. RNA target (match / mismatch: 5'-CUGAAGGACUCACCCUGC**Y**UCAGUUUAUUU UGA-3', UE: Y = C; ED: Y = U; partial match: 5'- AGGACCAU**UCACCCUGCCUCAG**GAUCUAAGCAGGA-3') were measured in PBS buffer (100 mM NaCl, 10 mM Na_2HPO_4, pH 7.0) at 37 °C to determine fluorescence enhancement $E = I / I_0$ with SD as standard deviation and specificity $S = E_m / E_{mm}$. Quantum yield ϕ and brightness $Br = \varepsilon_{\lambda ex} \cdot \phi / 1000$ in $M^{-1} \cdot cm^{-1}$ were measured at 25 °C. QB: λ_{ex} = 560 nm, λ_{em} = 605 nm; TO: λ_{ex} = 485 nm, λ_{em} = 535 nm. Melting temperature T_m in °C was measured with 1 µM probe and 1 eq. (1 µM) target RNA. Underscored letters = 2'OMe-RNA; subscript L = LNA; bold italic letters = editing site and bold letters = base surrogates. Match and mismatch RNA target are indicated with m and mm.

Table 16: Spectroscopic properties of nuclease-resistant ED-TO^2-OMe FIT^2 probes and their respective controls.

	Sequence 5' – 3'	RNA target	I_0	SD	I	E	S	ϕ	ϕ / $ϕ_0$	Br	T_m
ED-TO^2-OMe											
1	UCAA***A***TOT_LAAACUGA ***A***TOC_LA	m mm	41.67	0.22	270.2 89.8	6.5 2.1	3.0	0.44 0.25	3.4 1.8	46.6 27.4	52.3 45.1
2	AAAAT***T***OA_LACUGA ***A***TOC_LA	m mm	15.74	0.47	126.2 22.9	8.2 1.4	5.7	0.19 0.09	4.5 2.0	18.7 9.3	50.5 45.6
3	CAAAAT***T***OA_LACUGA ***A***TOC_LA	m mm	13.45	2.28	105.8 29.1	7.0 2.5	2.9	0.19 0.10	4.7 3.0	19.5 7.5	50.3 42.4
4	UCAAAAT***T***OA_LACUGA ***A***TOC_LA	m mm	12.24	2.54	106.6 24.2	7.6 2.3	3.3	0.19 0.08	4.9 2.8	19.3 6.3	50.0 42.3
ED-TO-OMe											
C1	UCAAAAUAAACUGA ***A***TOC_LA	m mm	12.87	0.12	169.1 52.2	13.2 4.0	3.3	0.38 0.17	3.1 7.8	18.2 7.8	56.1 49.5
C2	UCAA***A***TOT_LAAACUGA ***A***GCA	m mm	19.15	0.18	195.4 191.2	10.3 9.9	1.0	0.54 0.46	27.5 23.0	27.5 23.0	60.4 53.4
C3	UCAAAAT***T***OA_LACUGA ***A***GCA	m mm	15.09	0.02	116.7 223.8	7.7 14.8	0.5	0.28 0.43	12.8 20.1	12.8 20.1	52.4 61.8

Conditions: 0.5 µM probe and 5 eq. RNA target (5'-CUGAAGGACUCACCCUGC***Y***UCAGUUUAUUUUGA-3', UE: Y = C; ED: Y = U) were measured in PBS buffer (100 mM NaCl, 10 mM Na_2HPO_4, pH 7.0) at 37°C to determine fluorescence enhancement E = I / I_0 with SD as standard deviation and specificity S = E_m / E_{mm}. Quantum yield ϕ and brightness Br = $ε_{λex} \cdot ϕ$ / 1000 in $M^{-1} \cdot cm^{-1}$ were measured at 25 °C. QB: $λ_{ex}$ = 560 nm, $λ_{em}$ = 605 nm; TO: $λ_{ex}$ = 485 nm, $λ_{em}$ = 535 nm. Melting temperature T_m in °C was measured with 1 µM probe and 1 eq. (1 µM) target RNA. Underscored letters = 2'OMe-RNA; subscript L = LNA; bold italic letters = editing site and bold letters = base surrogates. Match and mismatch RNA target are indicated with m and mm.

Table 17: Spectroscopic properties of nuclease-resistant UE-TO^2-OMe probes and their respective controls.

	Sequence 5' – 3'	RNA target	I_0	SD	I	E	S	ϕ	ϕ / $ϕ_0$	Br	T_m
UE-TO^2-OMe											
1	UCAAA**TO**T_LAAACUGA ***G*TO**C_LA	m mm	22.46	0.50	363.5 128.7	16.1 5.8	2.8	0.37 0.25	**5.6** **4.1**	37.1 25.2	56.9 50.2
2	AAAAT**TO**A_LACUGA ***G*TO**C_LA	m mm	15.60	0.09	159.0 38.1	10.2 2.4	4.2	0.22 0.11	5.5 2.5	22.2 11.8	52.5 51.3
3	CAAAAT**TO**A_LACUGA ***G*TO**C_L A	m mm	14.59	0.34	145.8 55.8	10.2 3.8	2.7	0.24 0.16	5.7 3.6	23.8 15.9	54.4 50.2
4	UCAAAAT**TO**A_LACUGA ***G*TO**C_LA	m mm	13.34	0.27	134.4 13.2	9.9 3.8	2.6	0.23 0.14	5.5 3.5	22.3 13.8	47.6 42.1
UE-TO-OMe											
C1	UCAAAATAAACUGA ***G*TO**C_LA	m mm	16.59	0.54	245.9 131.3	15.2 7.7	2.0	0.59 0.32	4.5 2.8	23.0 14.8	58.4 48.2
C2	UCAAA**TO**T_LAAACUGA ***G*GCA**	m mm	18.36	0.63	196.7 19 3.2	11.0 10.3	1.1	0.43 0.44	7.5 7.5	21.2 21.4	63.5 56.5
C3	UCAAAAT**TO**A_LACUGA ***G*GCA**	m mm	12.63	0.11	63.1 61.4	5.0 4.8	1.0	0.16 0.15	2.7 2.6	6.9 6.8	61.7 55.9

Conditions: 0.5 µM probe and 5 eq. RNA target (5'-CUGAAGGACUCACCCUGC**Y**UCAGUUUAUUUUGA-3', UE: Y = C; ED: Y = U) were measured in PBS buffer (100 mM NaCl, 10 mM Na_2HPO_4, pH 7.0) at 37°C to determine fluorescence enhancement E = I / I_0 with SD as standard deviation and specificity S = E_m / E_{mm}. Quantum yield ϕ and brightness Br = $ε_{λex}$ · ϕ / 1000 in M^{-1} · cm^{-1} were measured at 25 °C. QB: $λ_{ex}$ = 560 nm, $λ_{em}$ = 605 nm; TO: $λ_{ex}$ = 485 nm, $λ_{em}$ = 535 nm. Melting temperature T_m in °C was measured with 1 µM probe and 1 eq. (1 µM) target RNA. Underscored letters = 2'OMe-RNA; subscript L = LNA; bold italic letters = editing site and bold letters = base surrogates. Match and mismatch RNA target are indicated with m and mm.

Table 18: Spectroscopic properties of nuclease-resistant ED-EB^2-OMe probes and their respective controls.

	Sequence 5' – 3'	RNA target	I_0	SD	I	E	S	ϕ	ϕ / ϕ$_0$	Br	T_m
ED-QB^2-OMe											
1	UCAAA**QB**T$_L$AAACUGA ***A*QB**C$_L$A	m mm	2.05	0.11	125.5 26.6	59.0 13.5	4.4	0.24 0.13	26.1 15.3	20.5 8.3	50.7 43.2
2	AAAAT**QB**A$_L$ACUGA ***A*QB**C$_L$A	m mm	1.81	0.30	53.4 5.2	26.4 3.2	8.1	0.17 0.04	20.9 6.3	14.1 2.6	49.3 45.0
3	CAAAAT**QB**A$_L$ACUGA ***A*QB**C$_L$A	m mm	1.78	0.21	104.6 21.6	63.8 11.2	5.7	0.22 0.10	26.6 13.6	18.2 6.1	48.8 41.9
4	UCAAAAT**QB**A$_L$ACUGA ***A*QB**C$_L$A	m mm	1.89	0.10	97.2 30.6	49.7 16.8	3.0	0.22 0.10	25.2 14.3	17.8 6.2	48.6 43.6
ED-QB-OMe											
C1	UCAAAAUAAACUGA ***A*QB**C$_L$A	m mm	1.42	0.07	84.6 22.8	61.7 15.5	4.0	0.36 0.13	20.0 7.6	13.9 4.7	56.3 49.1
C2	UCAAA**QB**T$_L$AAACUGA ***A*GCA	m mm	3.11	0.03	86.1 82.6	27.9 26.4	1.1	0.33 0.31	13.5 13.5	14.9 14.2	60.1 53.2
C3	UCAAAAT**QB**A$_L$ACUGA ***A*GCA	m mm	2.97	0.19	35.0 23.4	11.3 8.3	1.4	0.17 0.13	8.1 6.9	6.2 5.3	54.7 49.1

Conditions: 0.5 µM probe and 5 eq. RNA target (5'-CUGAAGGACUCACCCUGC**Y**UCAGUUUAUUUUGA-3', UE: Y = C; ED: Y = U) were measured in PBS buffer (100 mM NaCl, 10 mM Na_2HPO_4, pH 7.0) at 37°C to determine fluorescence enhancement E = I / I_0 with SD as standard deviation and specificity S = E_m / E_{mm}. Quantum yield ϕ and brightness Br = $\varepsilon_{\lambda ex} \cdot \phi$ / 1000 in $M^{-1} \cdot cm^{-1}$ were measured at 25 °C. QB: λ_{ex} = 560 nm, λ_{em} = 605 nm; TO: λ_{ex} = 485 nm, λ_{em} = 535 nm. Melting temperature T_m in °C was measured with 1 µM probe and 1 eq. (1 µM) target RNA. Underscored letters = 2'OMe-RNA; subscript L = LNA; bold italic letters = editing site and bold letters = base surrogates. Match and mismatch RNA target are indicated with m and mm.

8.2.3 Fluorescence Emission and Extinction Coefficient Spectra

8.2.3.1 Mono-Dye FIT Probes

UE-TO-OMe-1 to 6

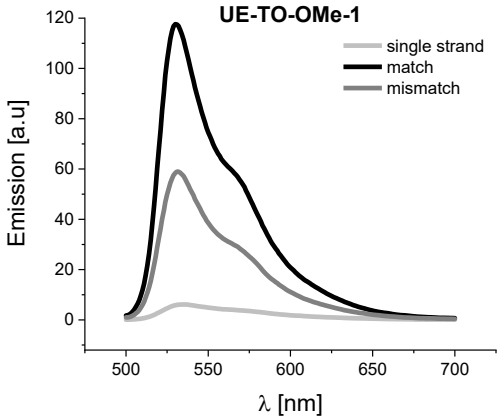

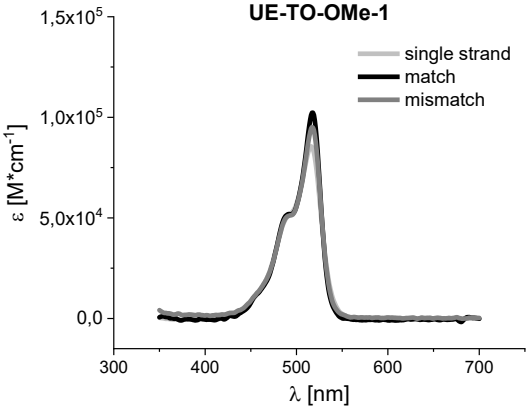

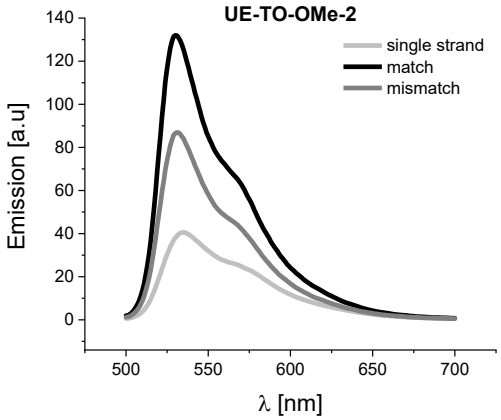

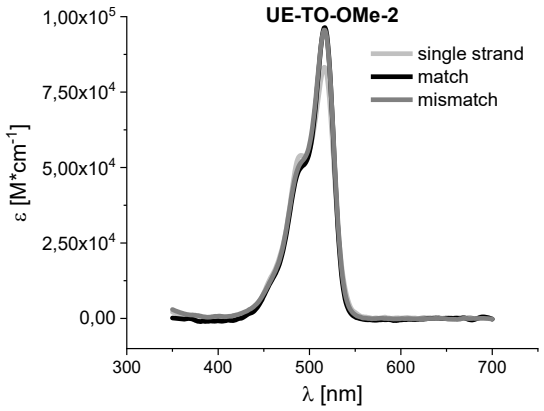

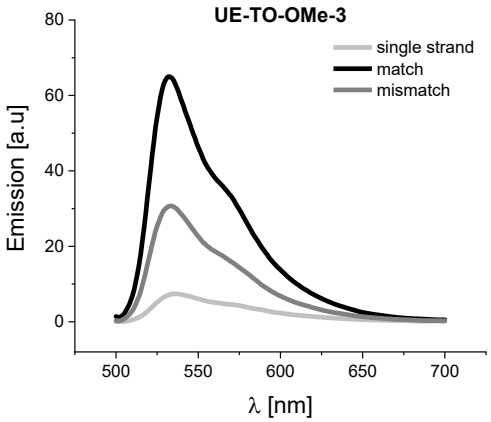

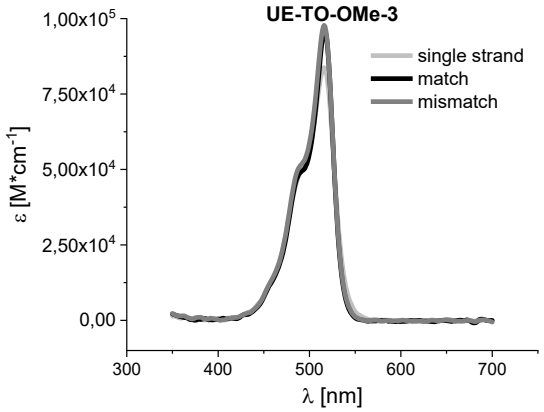

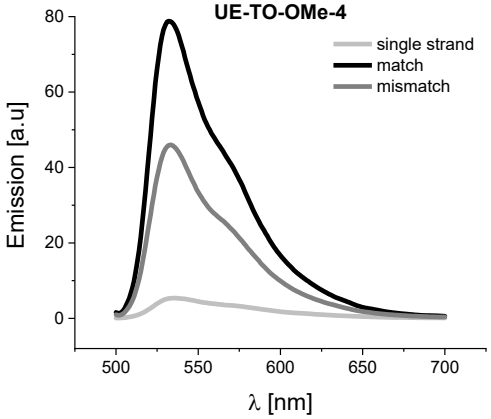
UE-TO-OMe-4
single strand
match
mismatch
Emission [a.u]
λ [nm]

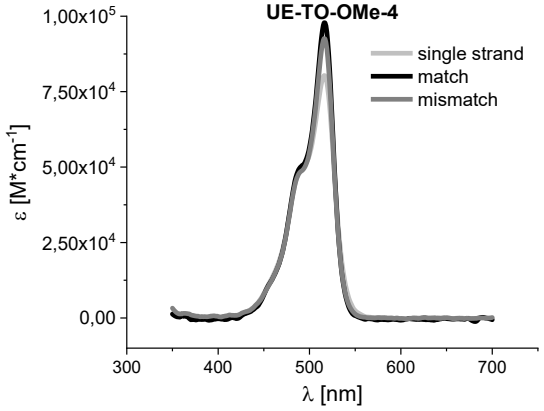
UE-TO-OMe-4
single strand
match
mismatch
ε [M*cm-1]
λ [nm]

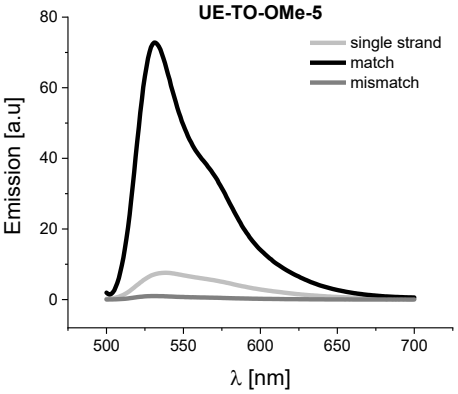
UE-TO-OMe-5
single strand
match
mismatch
Emission [a.u]
λ [nm]

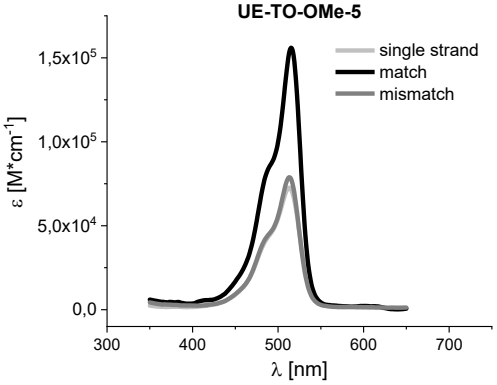
UE-TO-OMe-5
single strand
match
mismatch
ε [M*cm-1]
λ [nm]

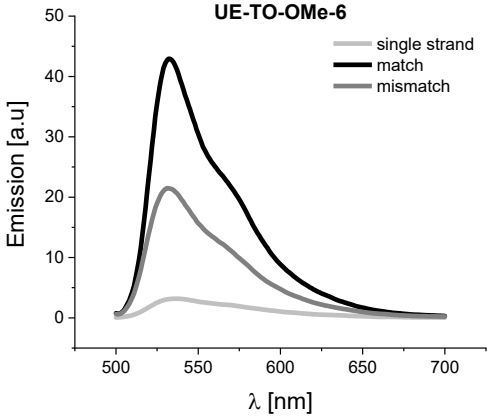
UE-TO-OMe-6
single strand
match
mismatch
Emission [a.u]
λ [nm]

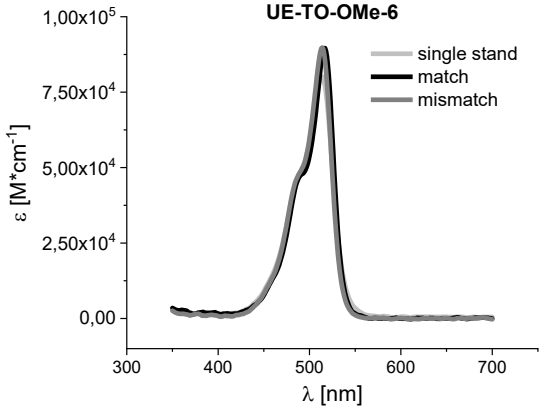
UE-TO-OMe-6
single stand
match
mismatch
ε [M*cm-1]
λ [nm]

ED-TO-OMe-1 to 6

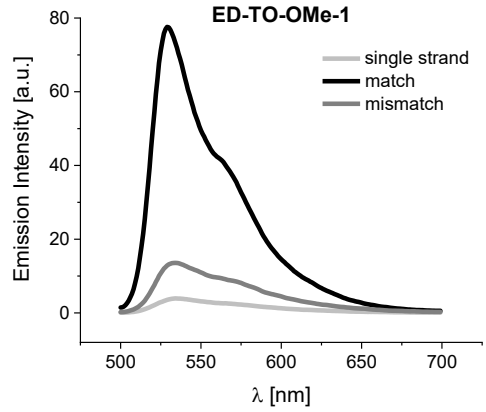

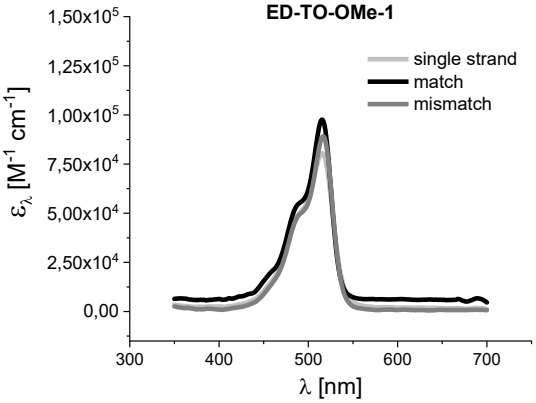

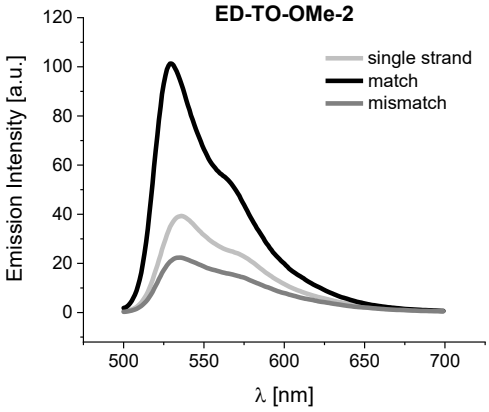

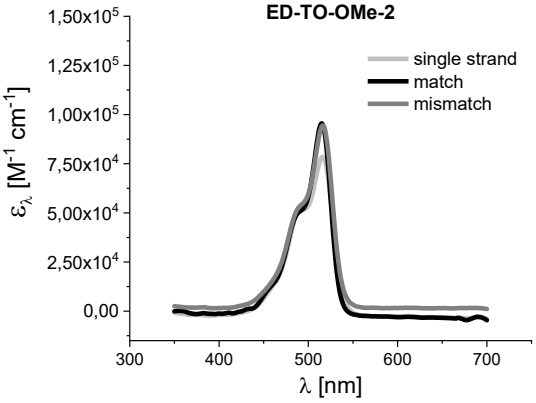

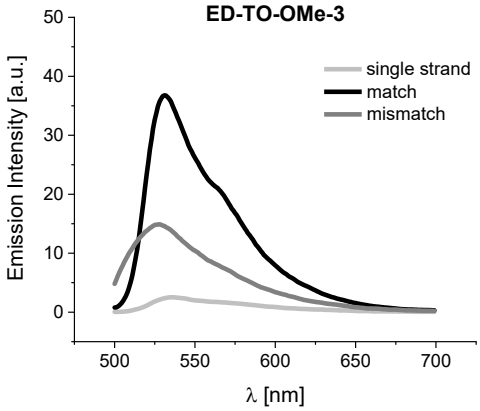

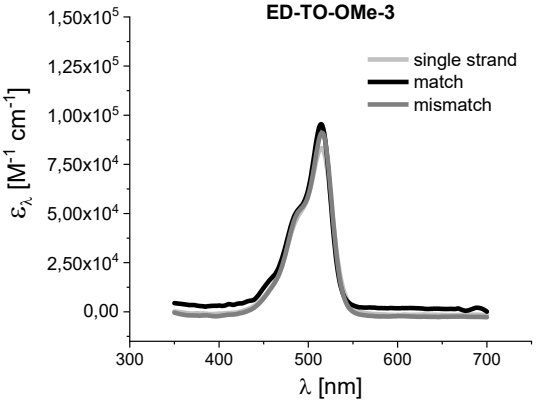

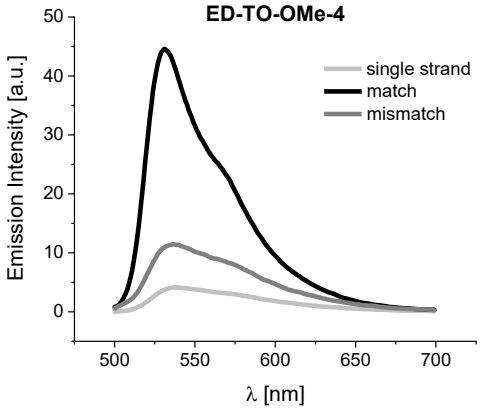

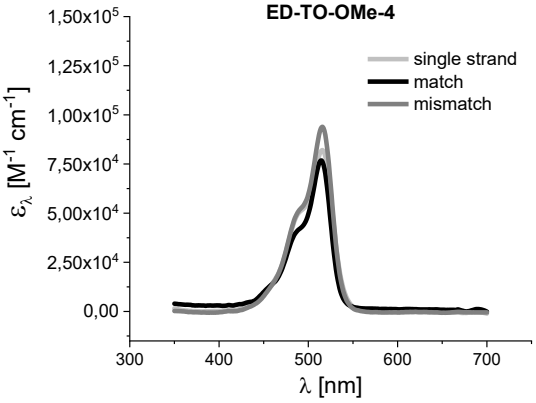

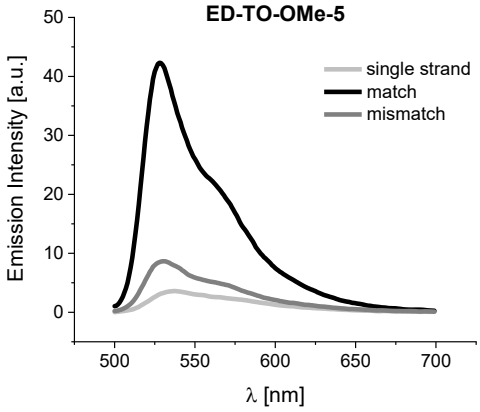
ED-TO-OMe-5
Emission Intensity [a.u.]
λ [nm]
single strand
match
mismatch

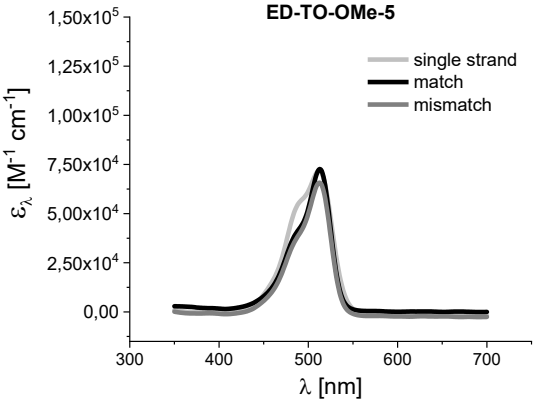
ED-TO-OMe-5
ε_λ [M^-1 cm^-1]
λ [nm]
single strand
match
mismatch

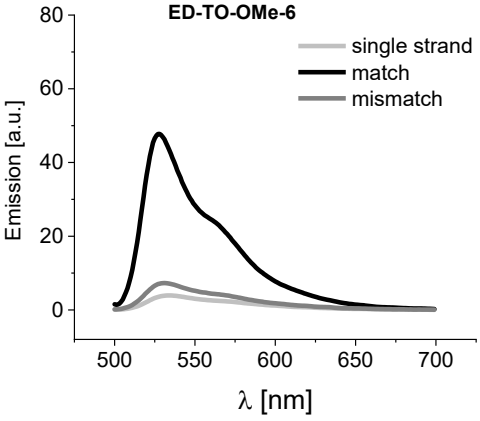
ED-TO-OMe-6
Emission [a.u.]
λ [nm]
single strand
match
mismatch

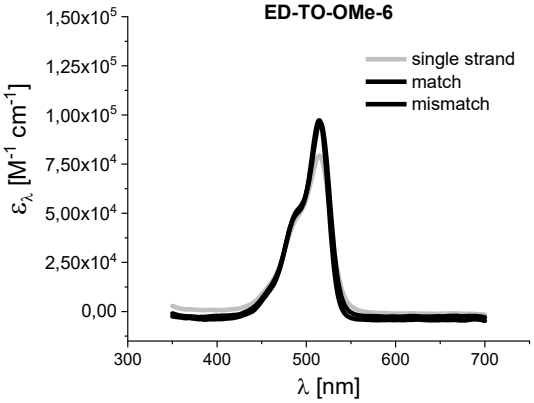
ED-TO-OMe-6
ε_λ [M^-1 cm^-1]
λ [nm]
single strand
match
mismatch

8.2.3.2 Dual-Dye FIT^2 Probes

DNA-based FIT^2 Probes UE-QB^2-1 to -6 and Mono-Dye Controls

In addition to match and mismatch targets these probes were tested against a partially matched RNA target (5'- AGGACCAU**UCACCCUGCCUCAG**GAUCUAAGCAGGA-3'). Fluorescence emission (solid line) and excitation (dashed line) spectra (left) and extinction coefficient as a function of absorption wavelength (right) are shown below.

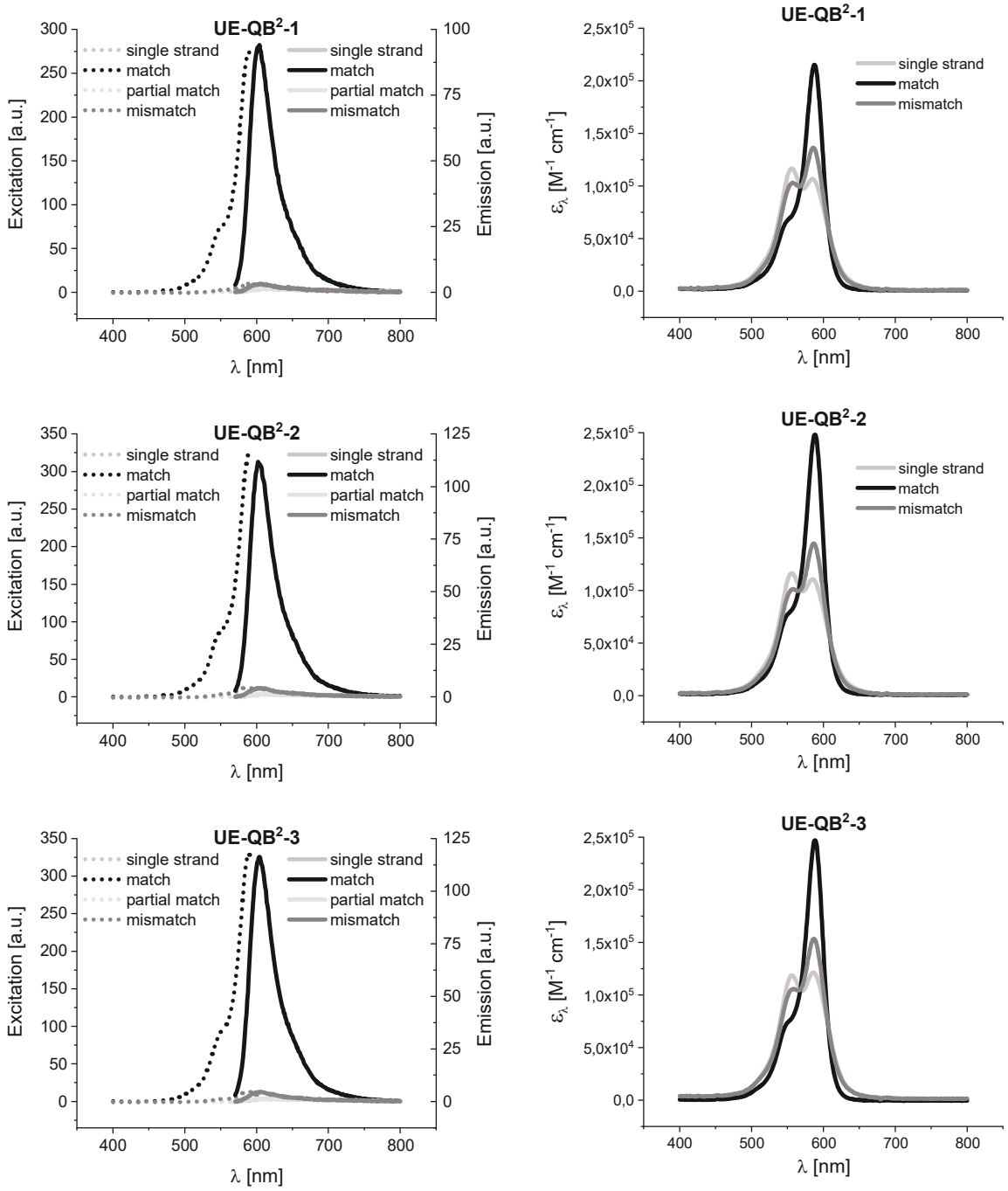

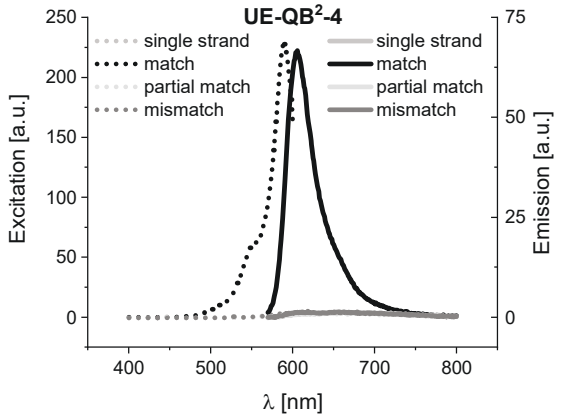
UE-QB²-4
single strand
match
partial match
mismatch
Excitation [a.u.]
Emission [a.u.]
λ [nm]

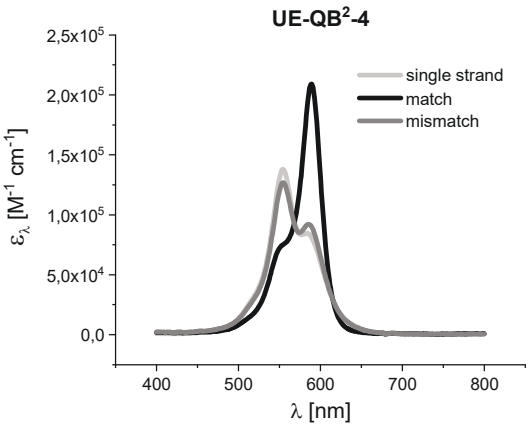
UE-QB²-4
single strand
match
mismatch
ε_λ [M⁻¹ cm⁻¹]
λ [nm]

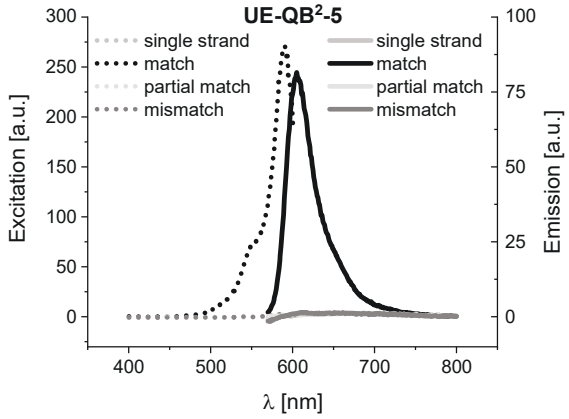
UE-QB²-5
single strand
match
partial match
mismatch
Excitation [a.u.]
Emission [a.u.]
λ [nm]

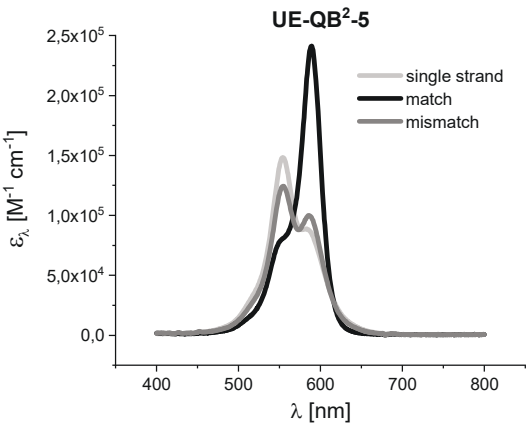
UE-QB²-5
single strand
match
mismatch
ε_λ [M⁻¹ cm⁻¹]
λ [nm]

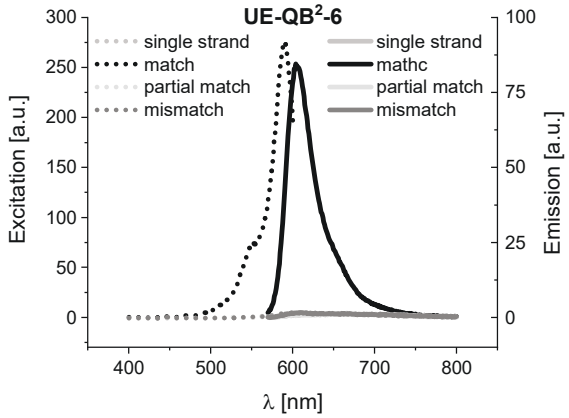
UE-QB²-6
single strand
match
partial match
mismatch
mathc
Excitation [a.u.]
Emission [a.u.]
λ [nm]

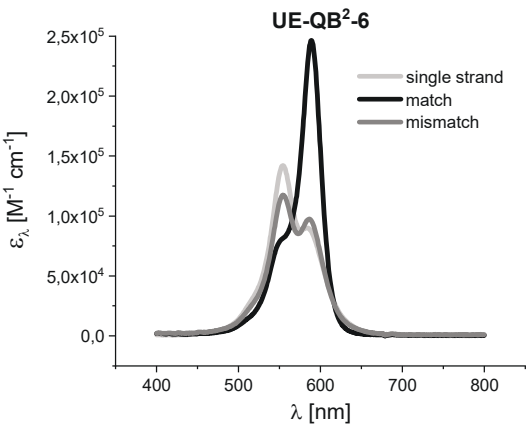
UE-QB²-6
single strand
match
mismatch
ε_λ [M⁻¹ cm⁻¹]
λ [nm]

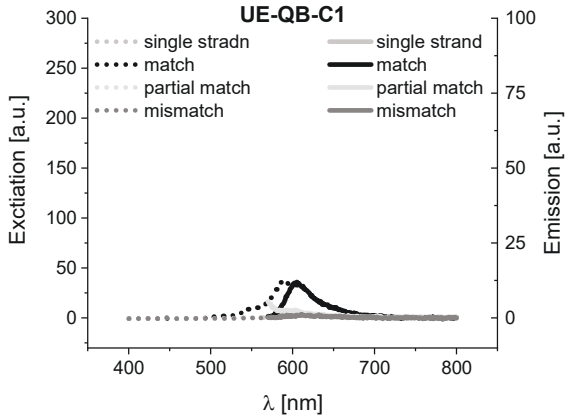
UE-QB-C1
single stradn
match
partial match
mismatch
Exctiation [a.u.]
Emission [a.u.]
λ [nm]

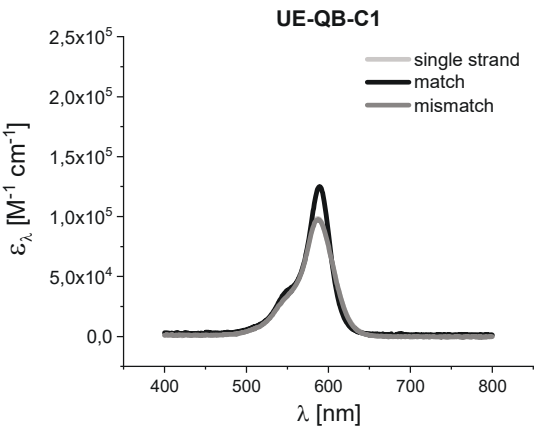
UE-QB-C1
single strand
match
mismatch
ε_λ [M⁻¹ cm⁻¹]
λ [nm]

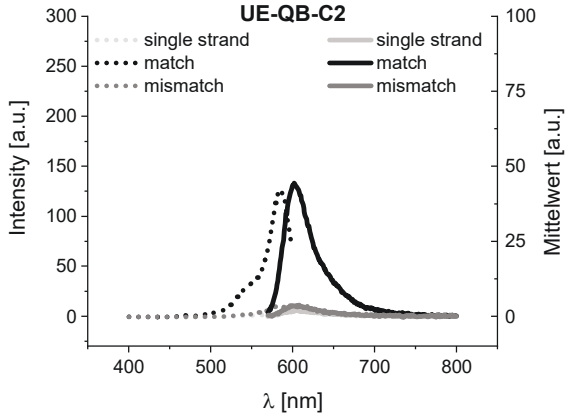
UE-QB-C2
single strand
match
mismatch
single strand
match
mismatch
Intensity [a.u.]
Mittelwert [a.u.]
λ [nm]

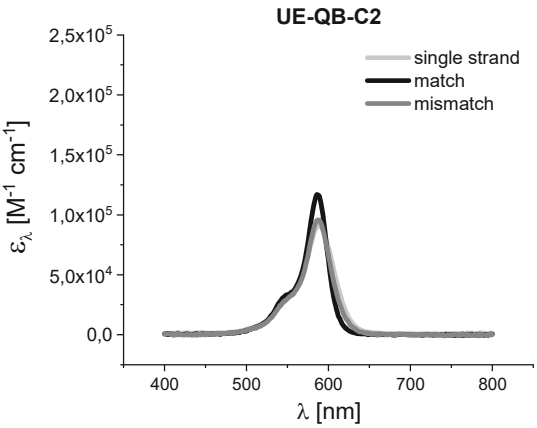
UE-QB-C2
single strand
match
mismatch
ελ [M-1 cm-1]
λ [nm]

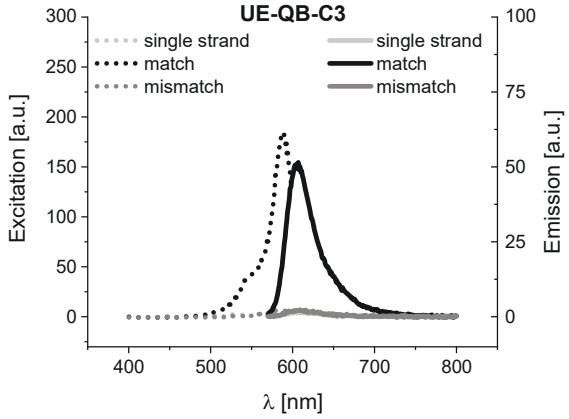
UE-QB-C3
single strand
match
mismatch
single strand
match
mismatch
Excitation [a.u.]
Emission [a.u.]
λ [nm]

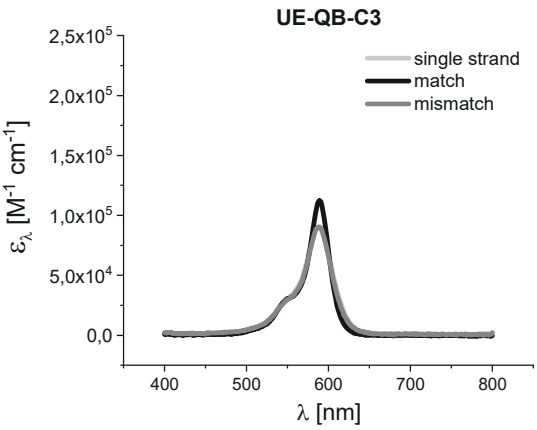
UE-QB-C3
single strand
match
mismatch
ελ [M-1 cm-1]
λ [nm]

Nuclease-Resistant FIT^2 Probes UE-QB^2-OMe-1 to -4 and Mono-Dye Controls

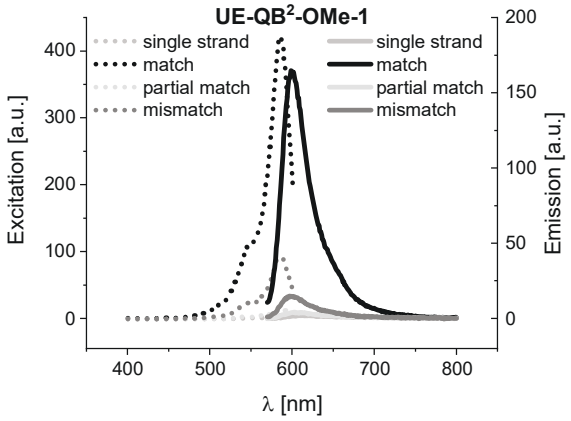

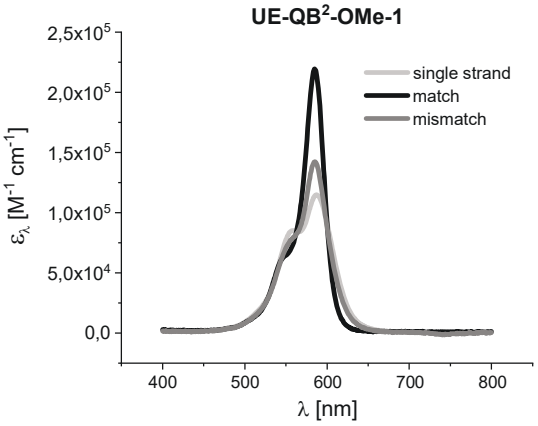

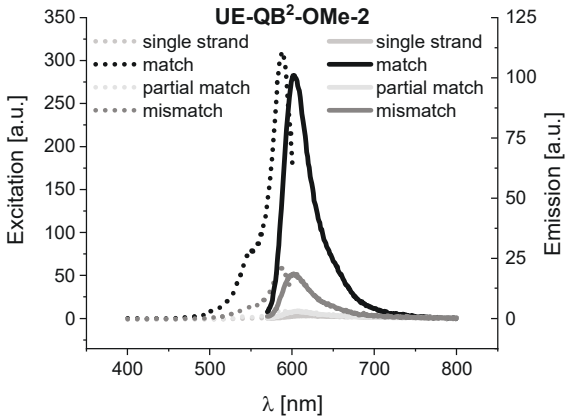

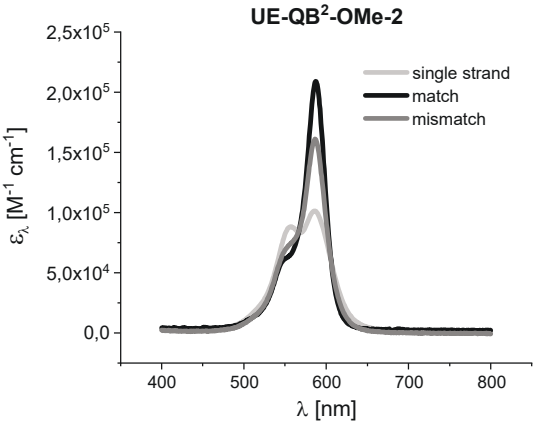

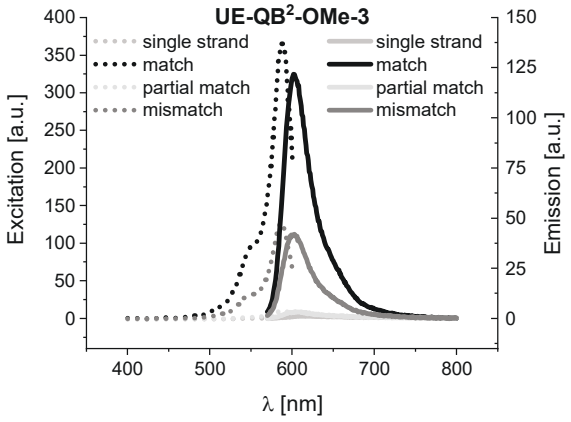

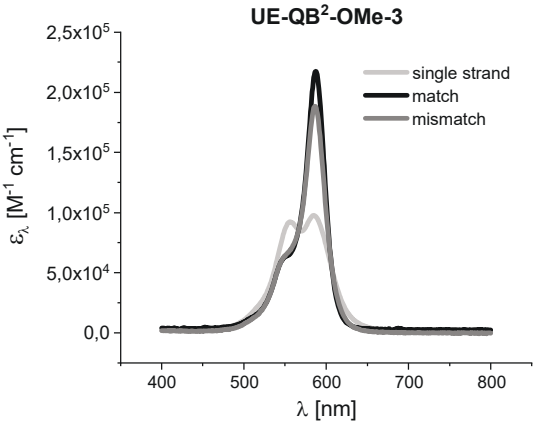

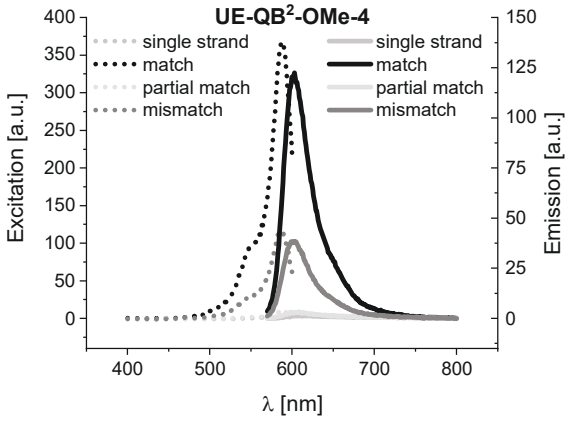

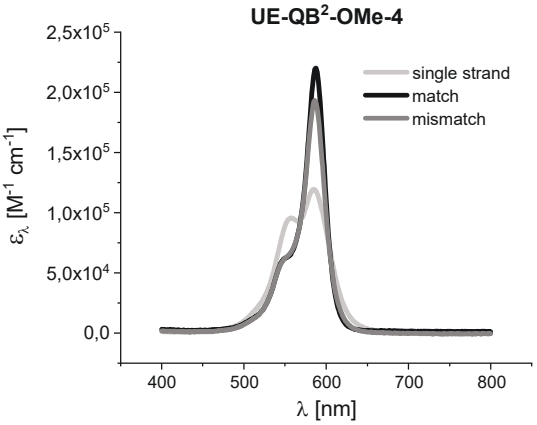

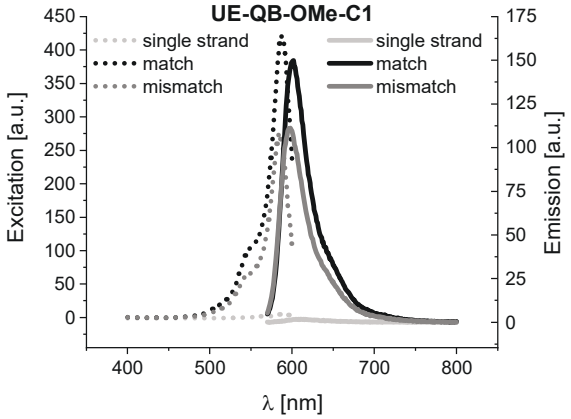
UE-QB-OMe-C1
single strand
match
mismatch
Excitation [a.u.]
Emission [a.u.]
λ [nm]

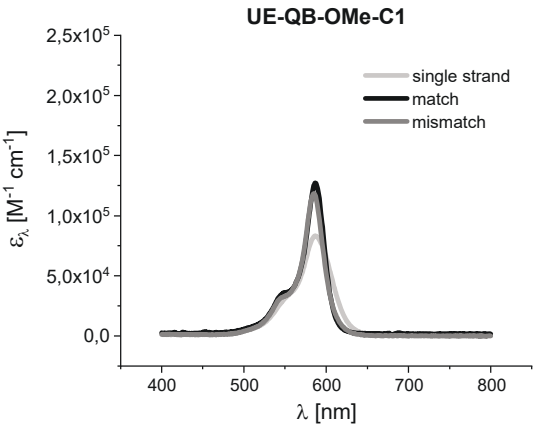
UE-QB-OMe-C1
single strand
match
mismatch
ελ [M-1 cm-1]
λ [nm]

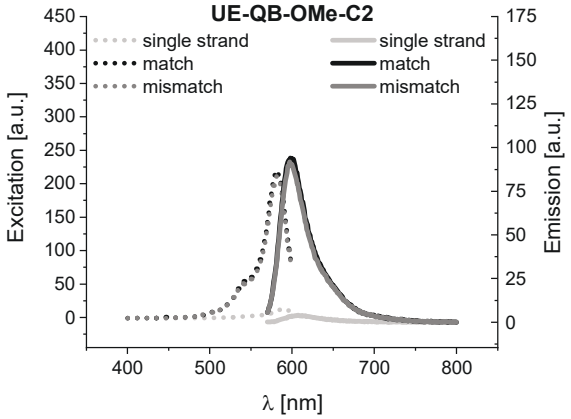
UE-QB-OMe-C2
single strand
match
mismatch
Excitation [a.u.]
Emission [a.u.]
λ [nm]

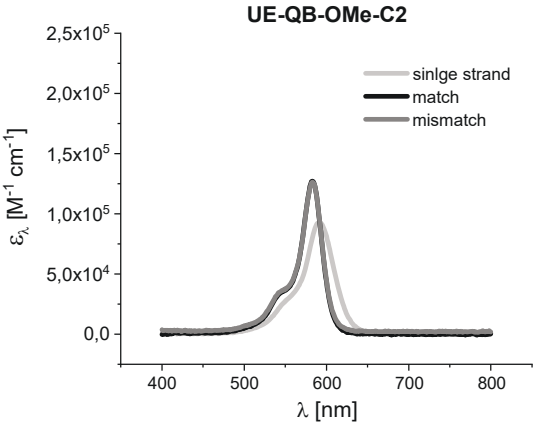
UE-QB-OMe-C2
sinlge strand
match
mismatch
ελ [M-1 cm-1]
λ [nm]

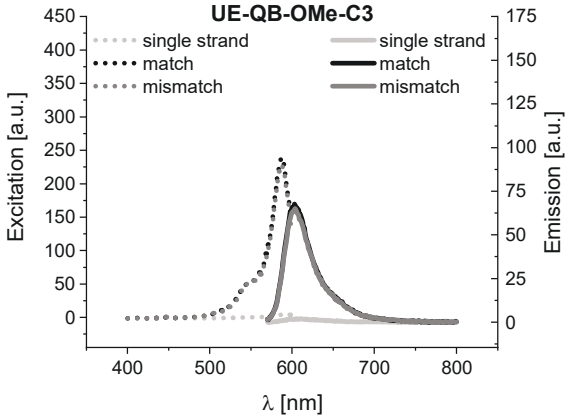
UE-QB-OMe-C3
single strand
match
mismatch
Excitation [a.u.]
Emission [a.u.]
λ [nm]

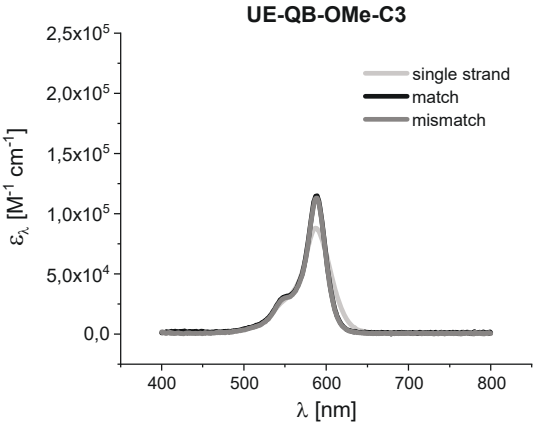
UE-QB-OMe-C3
single strand
match
mismatch
ελ [M-1 cm-1]
λ [nm]

Nuclease-Resistant FIT^2 Probes ED-TO^2-OMe-1 to -4 and Mono-Dye Controls

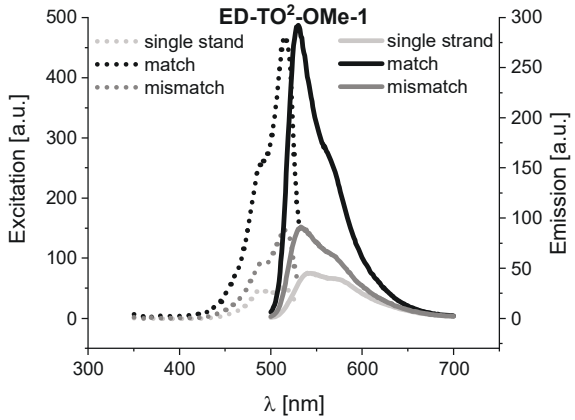

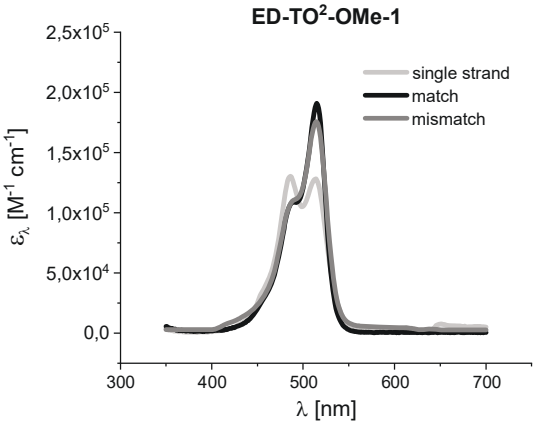

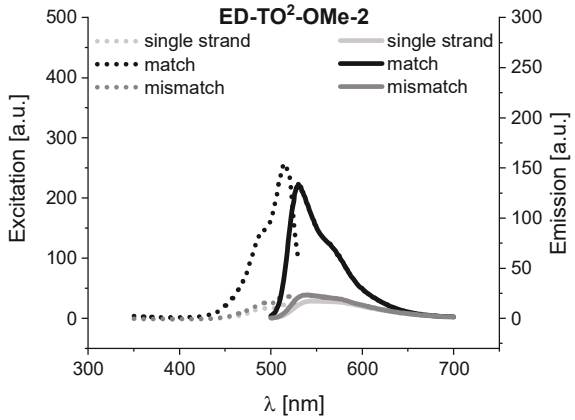

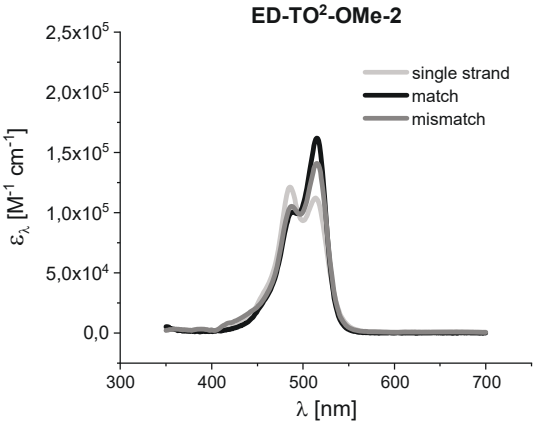

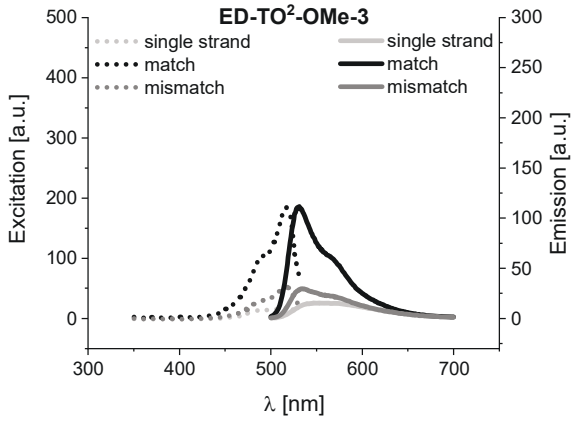

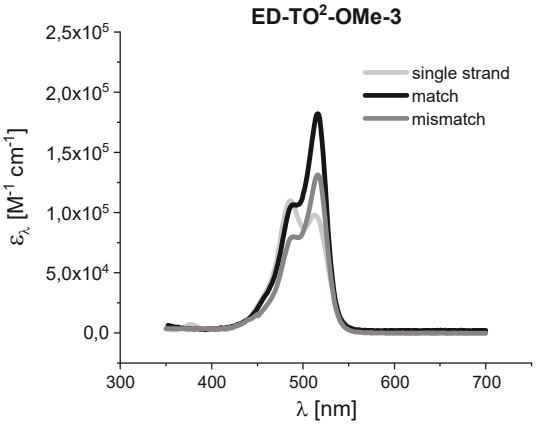

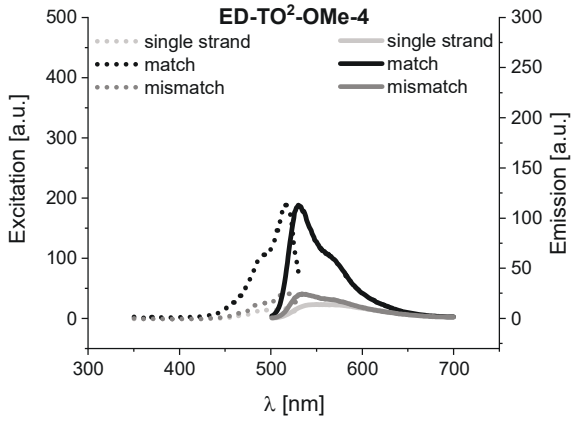

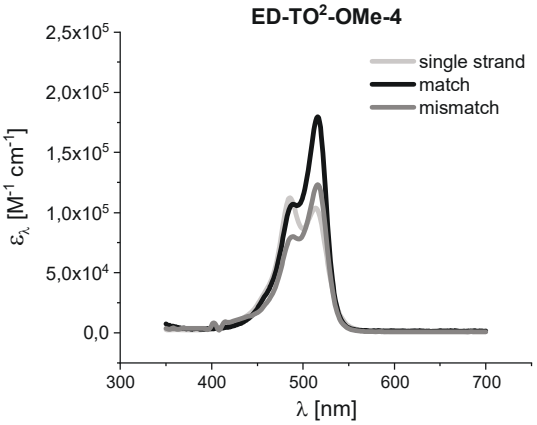

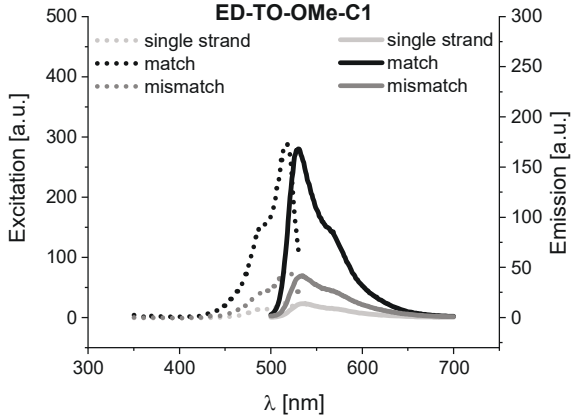
ED-TO-OMe-C1
single strand
match
mismatch
Excitation [a.u.]
Emission [a.u.]
λ [nm]

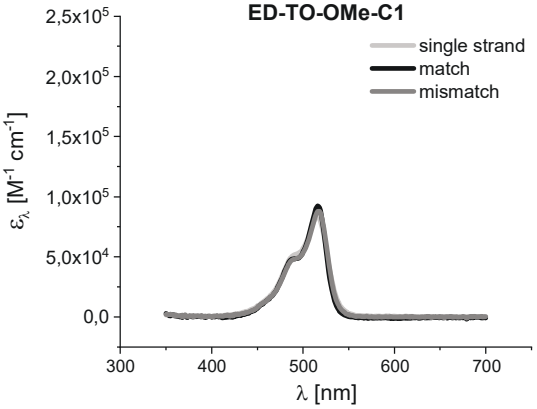
ED-TO-OMe-C1
single strand
match
mismatch
ε_λ [M^-1 cm^-1]
λ [nm]

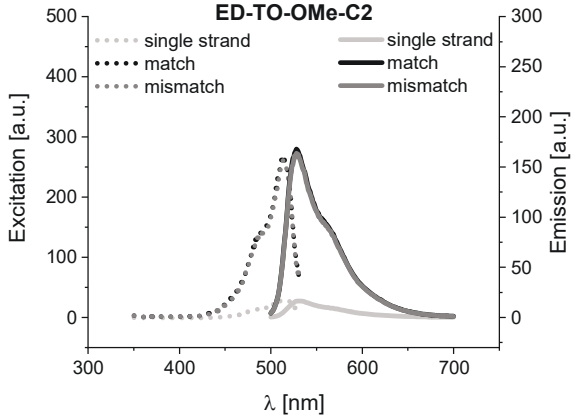
ED-TO-OMe-C2
single strand
match
mismatch
Excitation [a.u.]
Emission [a.u.]
λ [nm]

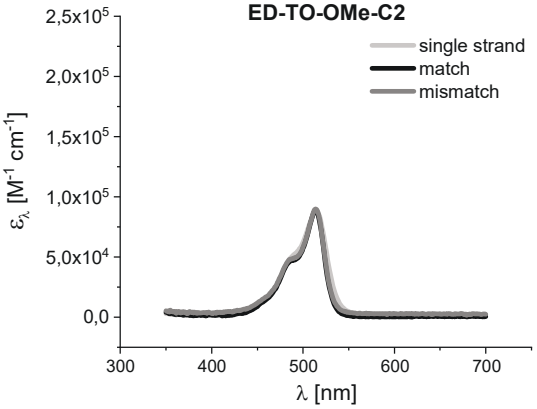
ED-TO-OMe-C2
single strand
match
mismatch
ε_λ [M^-1 cm^-1]
λ [nm]

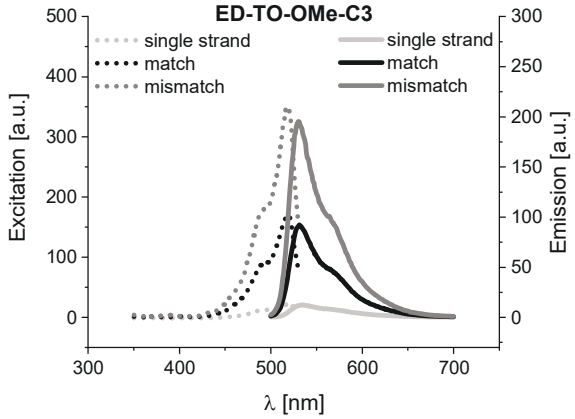
ED-TO-OMe-C3
single strand
match
mismatch
Excitation [a.u.]
Emission [a.u.]
λ [nm]

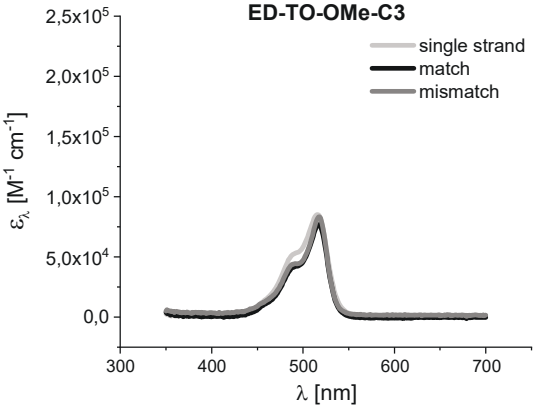
ED-TO-OMe-C3
single strand
match
mismatch
ε_λ [M^-1 cm^-1]
λ [nm]

Nuclease-Resistant FIT^2 Probes UE-TO^2-1 to -4 and Mono-Dye Controls

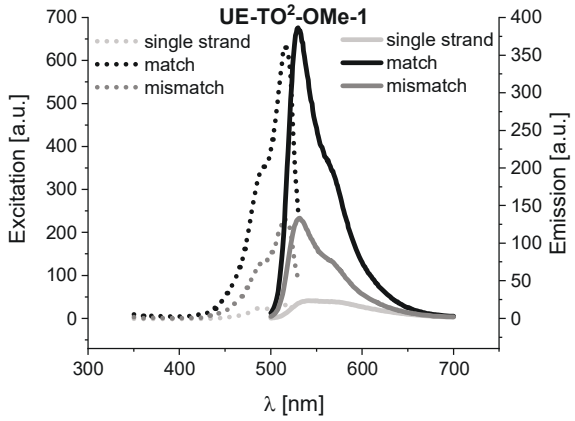

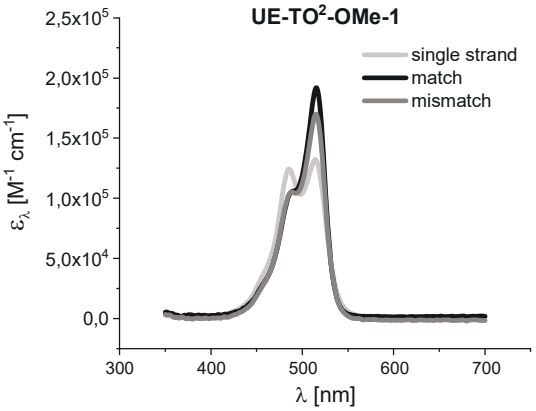

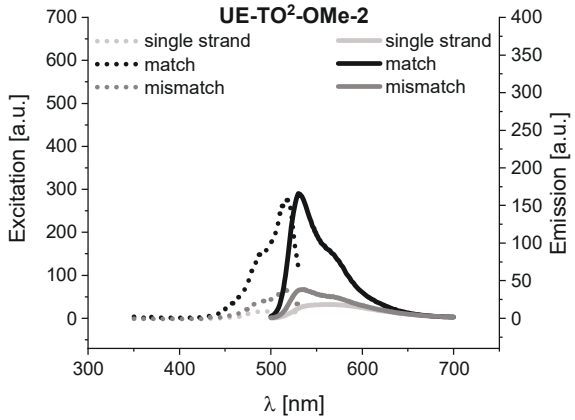

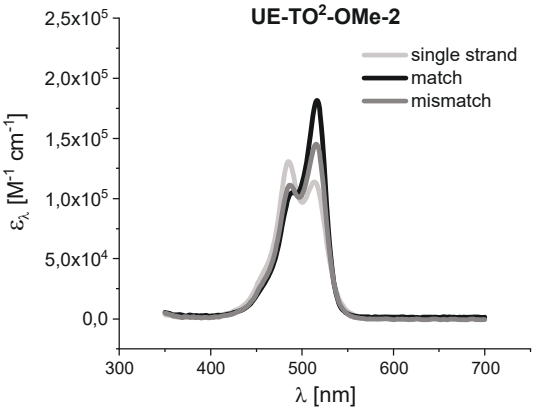

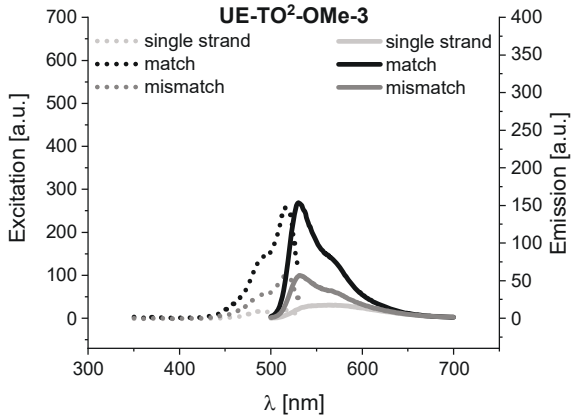

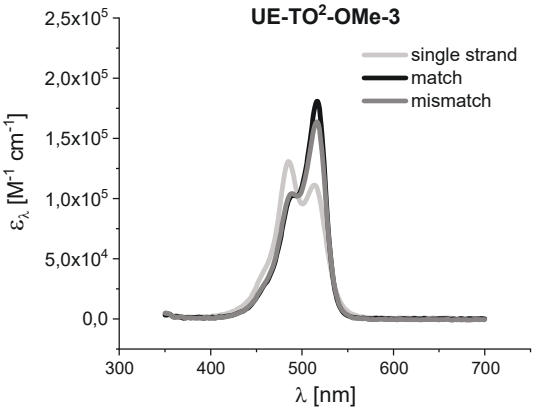

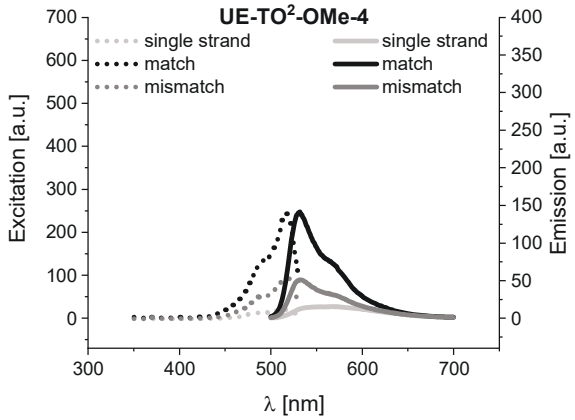

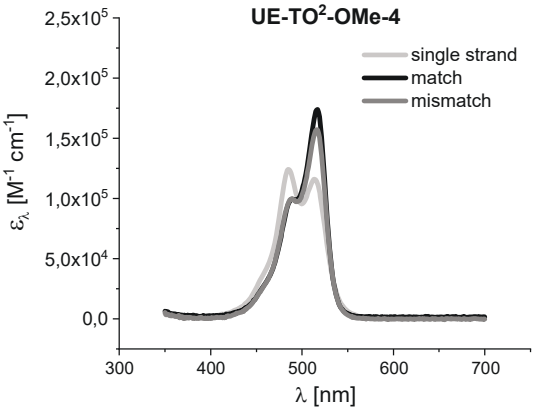

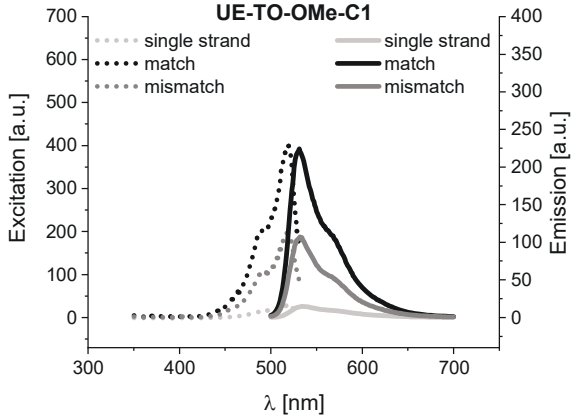
UE-TO-OMe-C1
single strand
match
mismatch
single strand
match
mismatch
Excitation [a.u.]
Emission [a.u.]
λ [nm]

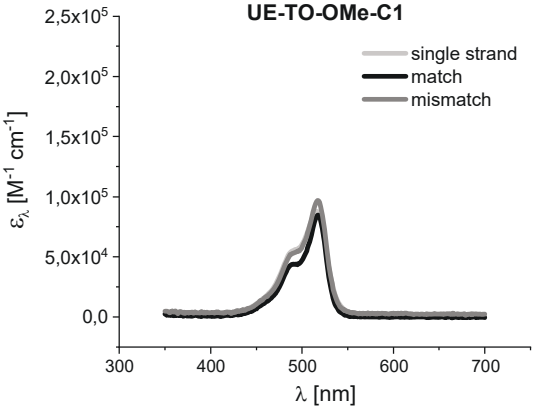
UE-TO-OMe-C1
single strand
match
mismatch
ε_λ [M^{-1} cm^{-1}]
λ [nm]

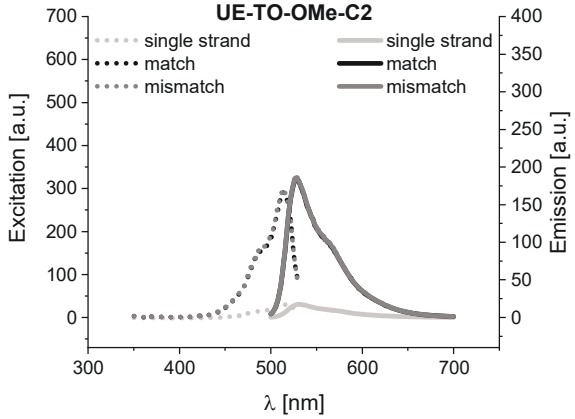
UE-TO-OMe-C2
single strand
match
mismatch
single strand
match
mismatch
Excitation [a.u.]
Emission [a.u.]
λ [nm]

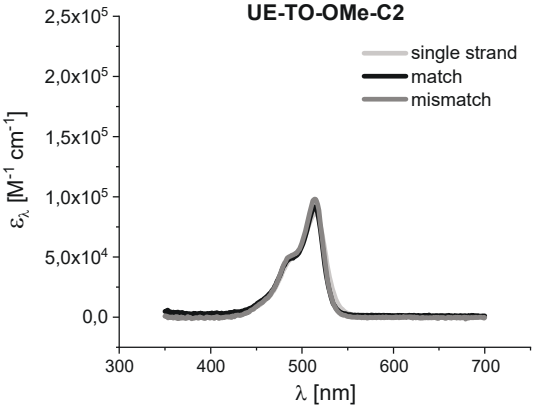
UE-TO-OMe-C2
single strand
match
mismatch
ε_λ [M^{-1} cm^{-1}]
λ [nm]

Nuclease-Resistant FIT^2 Probes ED-QB^2-1 to -4 and Mono-Dye Controls

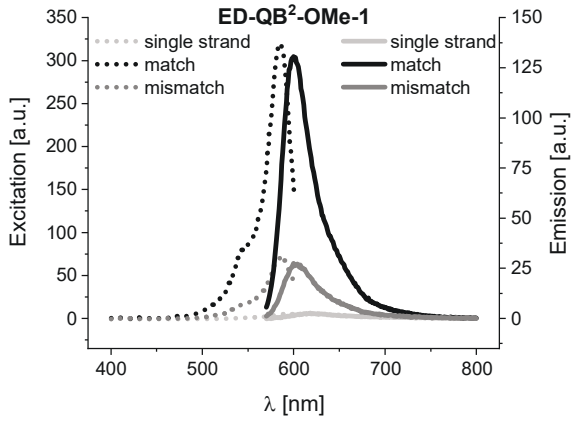

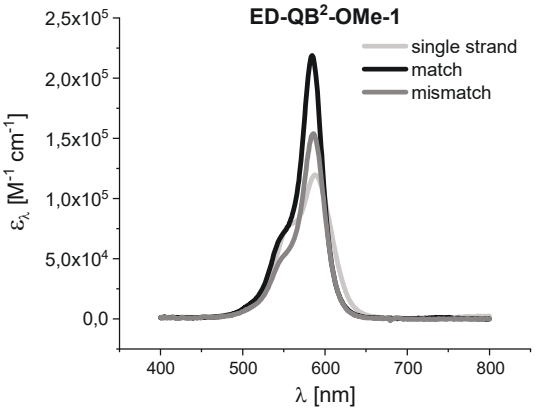

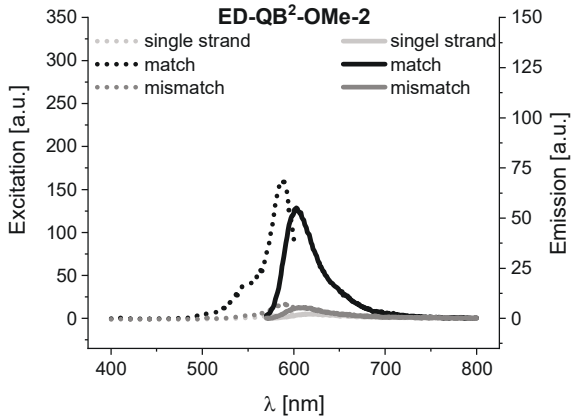

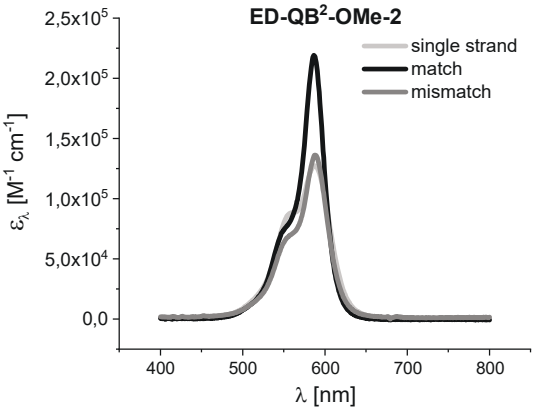

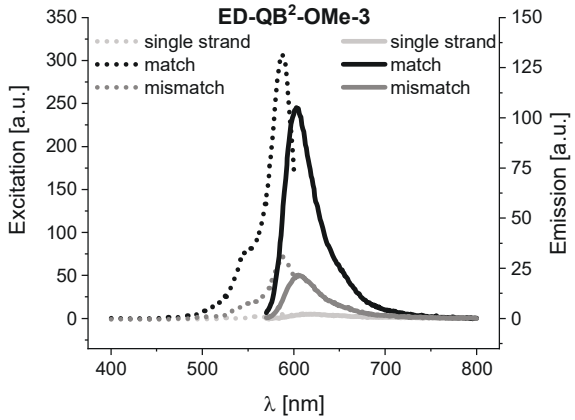

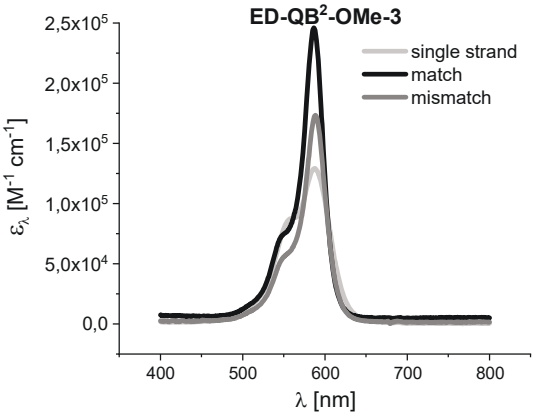

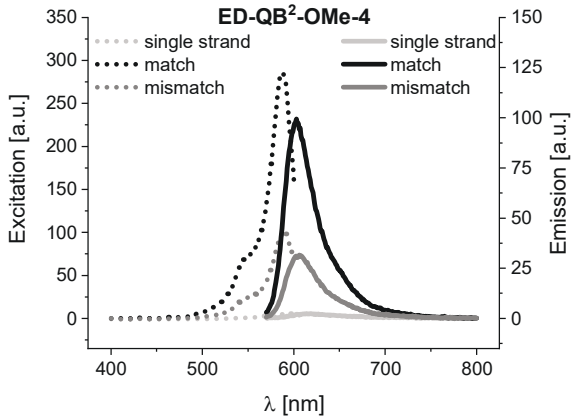

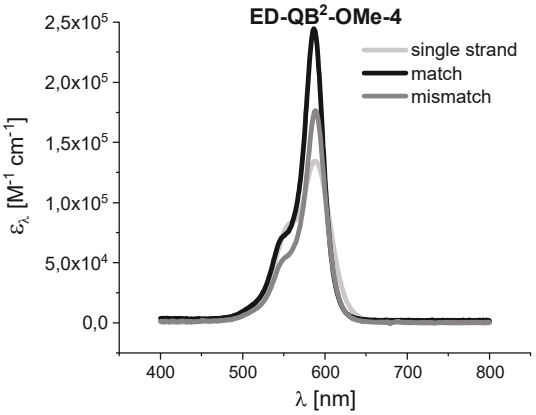

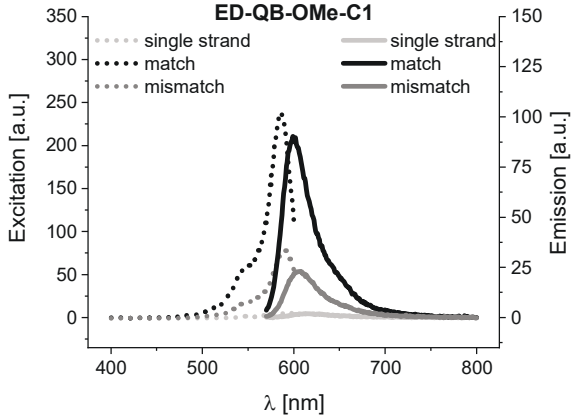
ED-QB-OMe-C1
single strand
match
mismatch
Excitation [a.u.]
Emission [a.u.]
λ [nm]

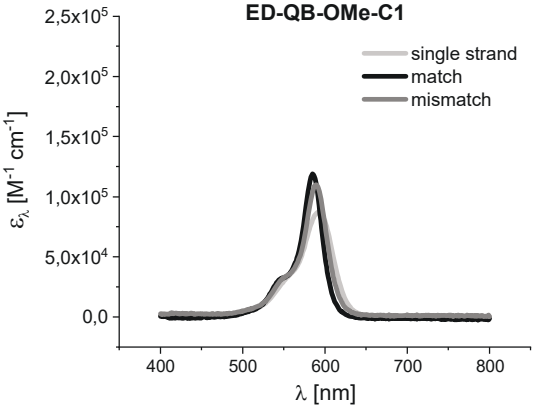
ED-QB-OMe-C1
single strand
match
mismatch
ε_λ [M^-1 cm^-1]
λ [nm]

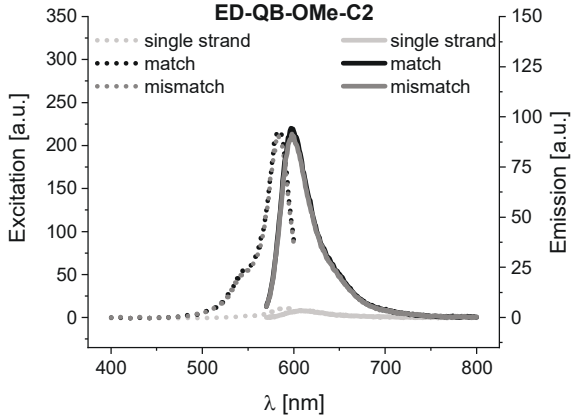
ED-QB-OMe-C2
single strand
match
mismatch
Excitation [a.u.]
Emission [a.u.]
λ [nm]

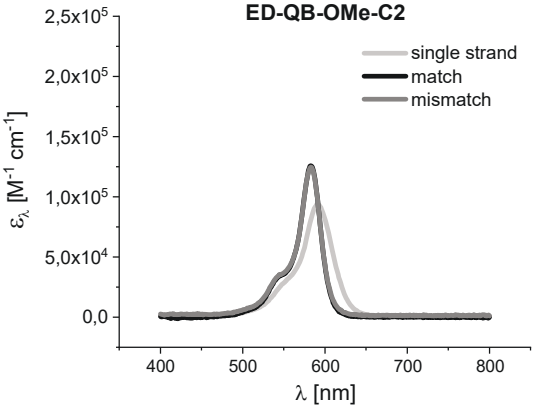
ED-QB-OMe-C2
single strand
match
mismatch
ε_λ [M^-1 cm^-1]
λ [nm]

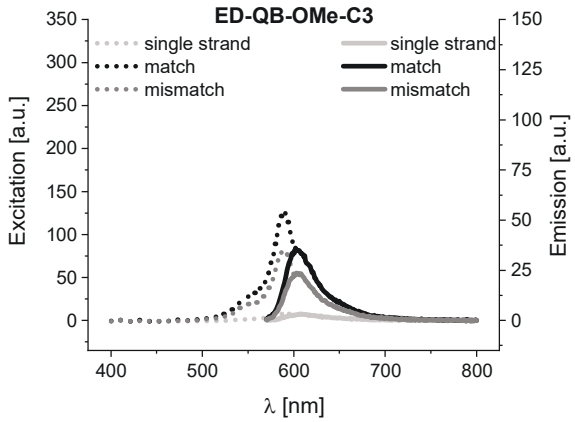
ED-QB-OMe-C3
single strand
match
mismatch
Excitation [a.u.]
Emission [a.u.]
λ [nm]

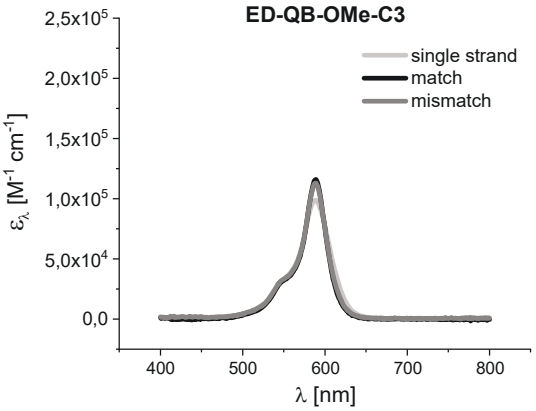
ED-QB-OMe-C3
single strand
match
mismatch
ε_λ [M^-1 cm^-1]
λ [nm]

Normalised Fluorescence Emission Spectra

All fluorescence emission traces were smoothed by a Savitzky-Golay filter using *OriginPro* software and normalised afterwards.[362]

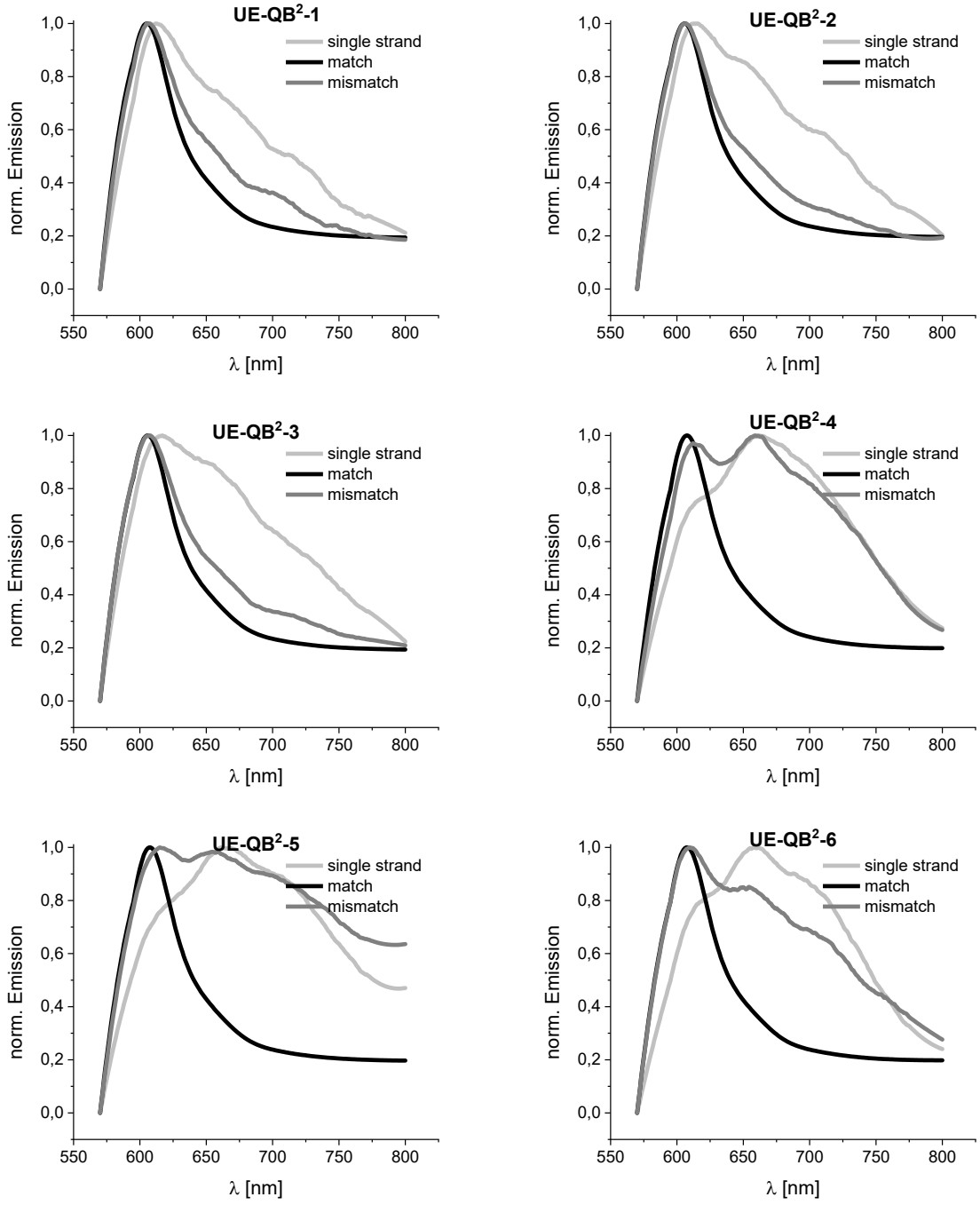

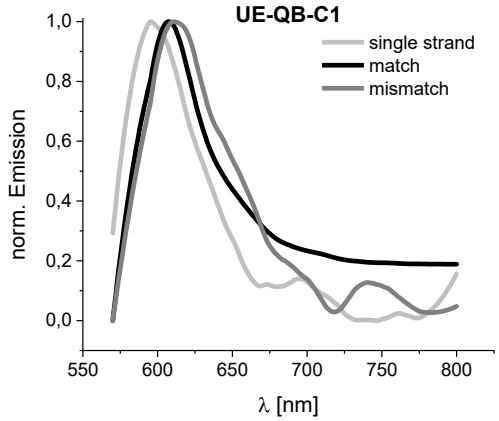
UE-QB-C1
single strand
match
mismatch
norm. Emission
λ [nm]

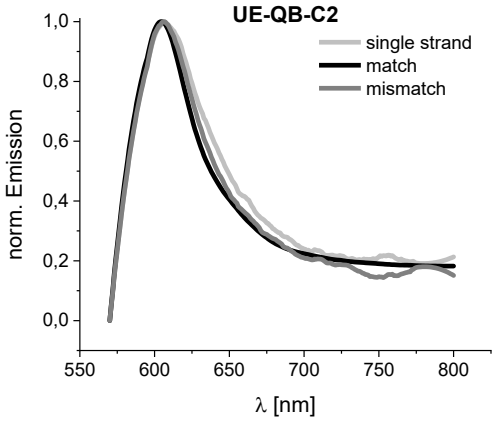
UE-QB-C2
single strand
match
mismatch
norm. Emission
λ [nm]

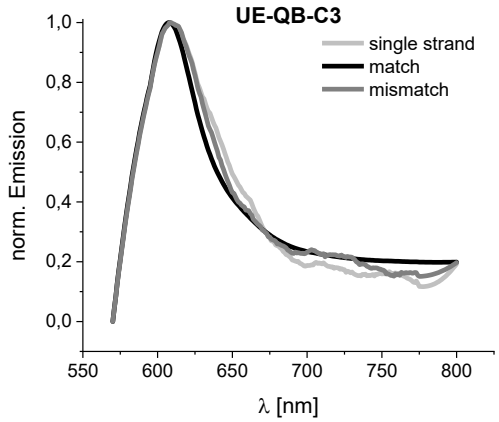
UE-QB-C3
single strand
match
mismatch
norm. Emission
λ [nm]

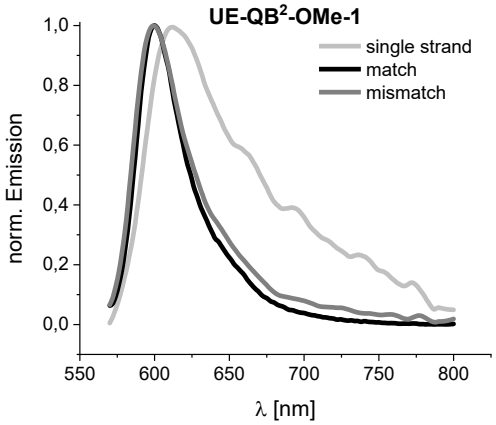
UE-QB²-OMe-1
single strand
match
mismatch
norm. Emission
λ [nm]

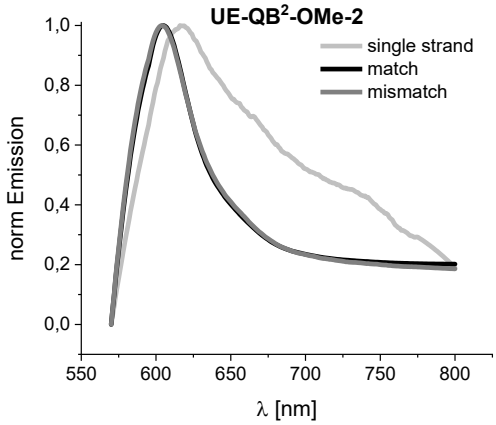
UE-QB²-OMe-2
single strand
match
mismatch
norm Emission
λ [nm]

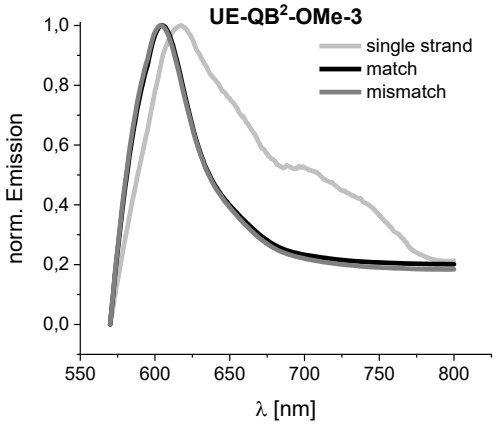
UE-QB²-OMe-3
single strand
match
mismatch
norm. Emission
λ [nm]

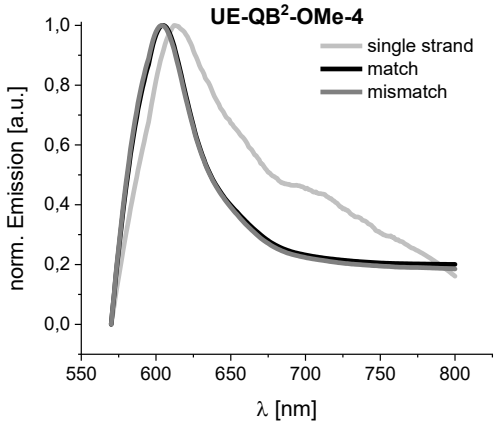
UE-QB²-OMe-4
single strand
match
mismatch
norm. Emission [a.u.]
λ [nm]

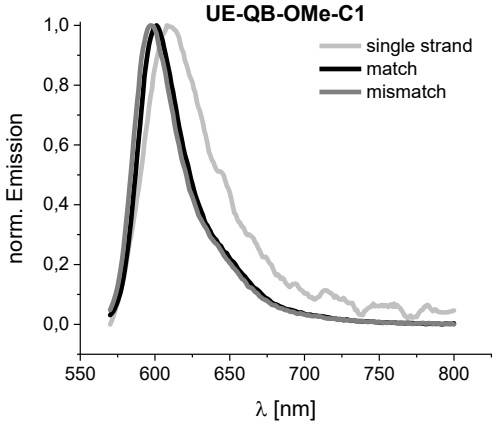
UE-QB-OMe-C1
single strand
match
mismatch
norm. Emission
λ [nm]

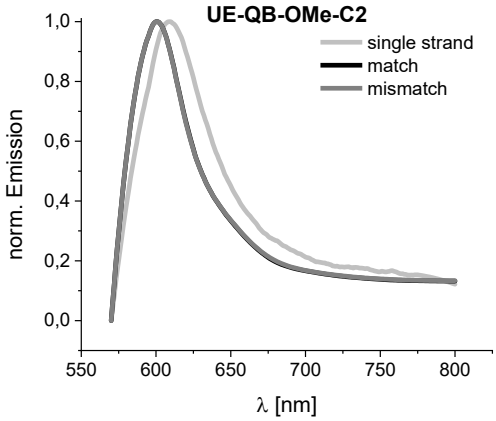
UE-QB-OMe-C2
single strand
match
mismatch
norm. Emission
λ [nm]

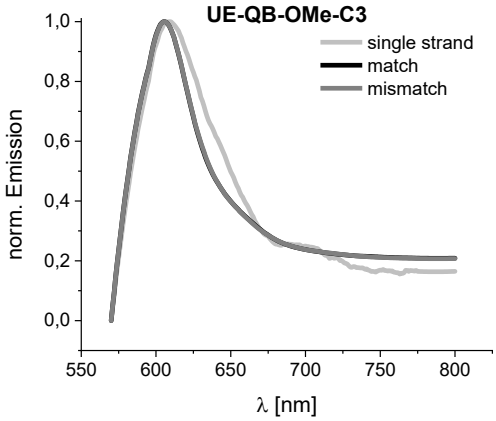
UE-QB-OMe-C3
single strand
match
mismatch
norm. Emission
λ [nm]

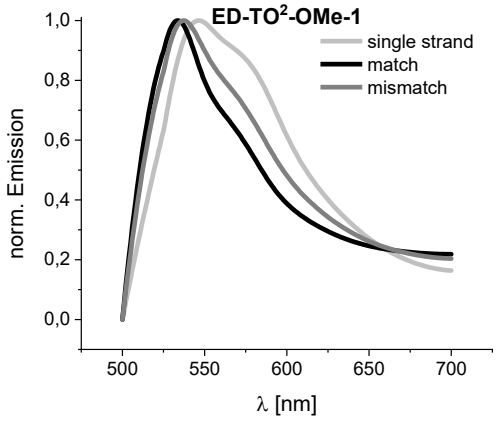
ED-TO²-OMe-1
single strand
match
mismatch
norm. Emission
λ [nm]

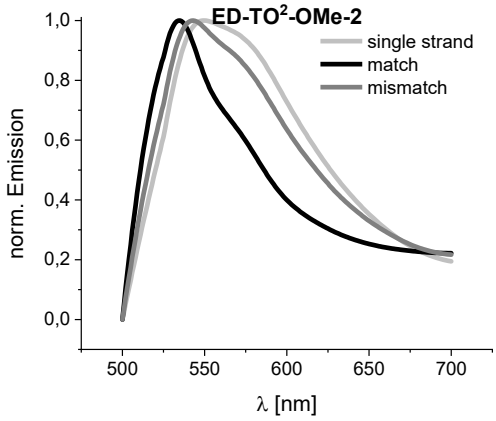
ED-TO²-OMe-2
single strand
match
mismatch
norm. Emission
λ [nm]

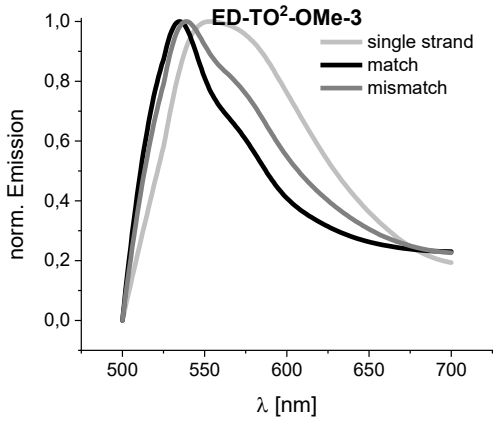
ED-TO²-OMe-3
single strand
match
mismatch
norm. Emission
λ [nm]

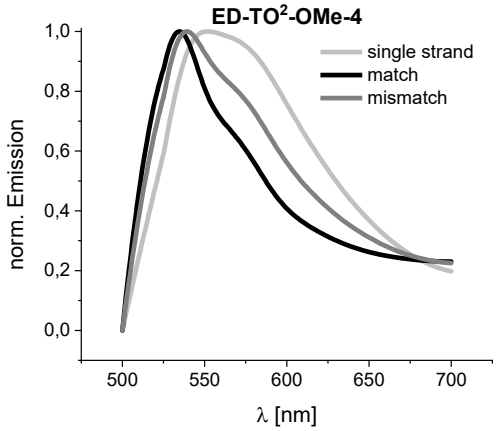
ED-TO²-OMe-4
single strand
match
mismatch
norm. Emission
λ [nm]

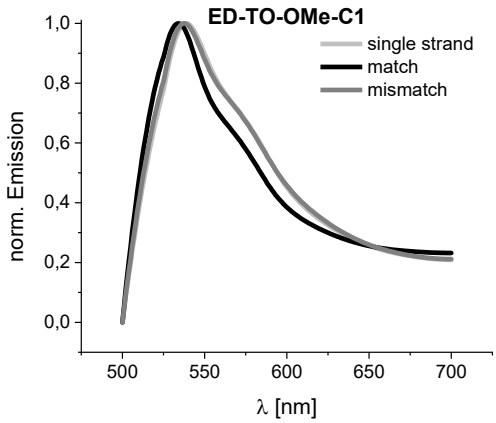
ED-TO-OMe-C1
single strand
match
mismatch
norm. Emission
λ [nm]

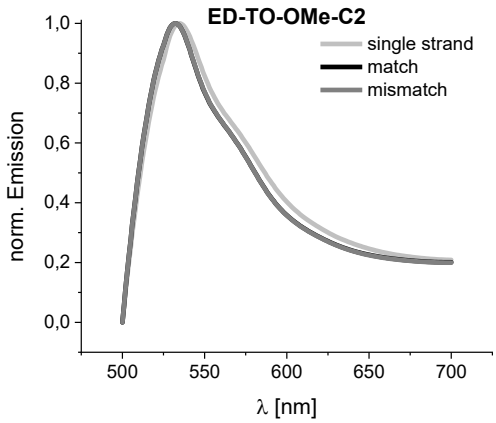
ED-TO-OMe-C2
single strand
match
mismatch
norm. Emission
λ [nm]

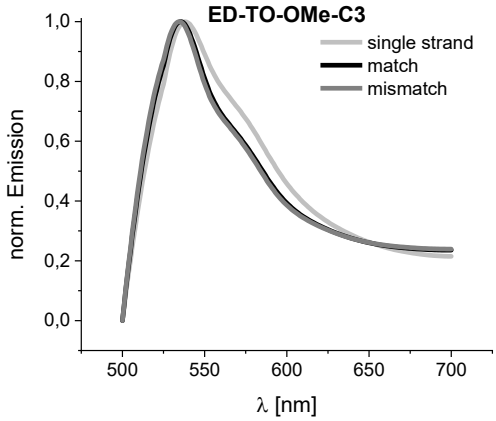
ED-TO-OMe-C3
single strand
match
mismatch
norm. Emission
λ [nm]

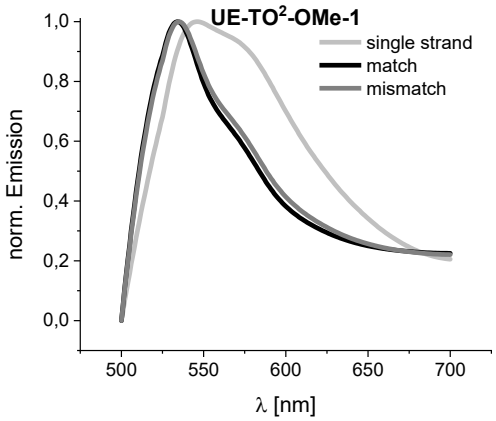
UE-TO²-OMe-1
single strand
match
mismatch
norm. Emission
λ [nm]

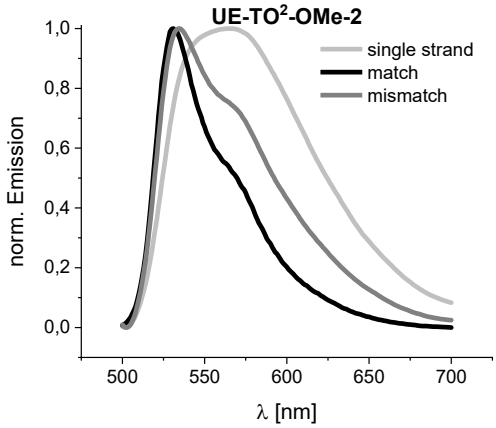
UE-TO²-OMe-2
single strand
match
mismatch
norm. Emission
λ [nm]

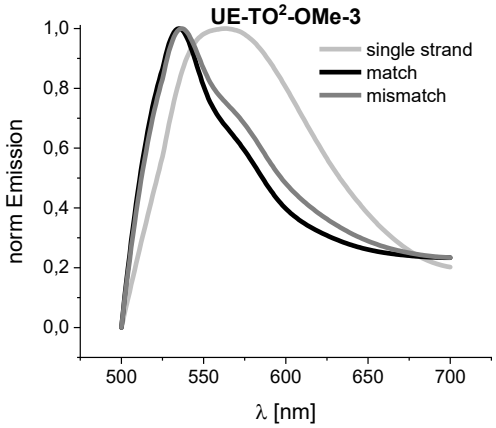
UE-TO²-OMe-3
single strand
match
mismatch
norm Emission
λ [nm]

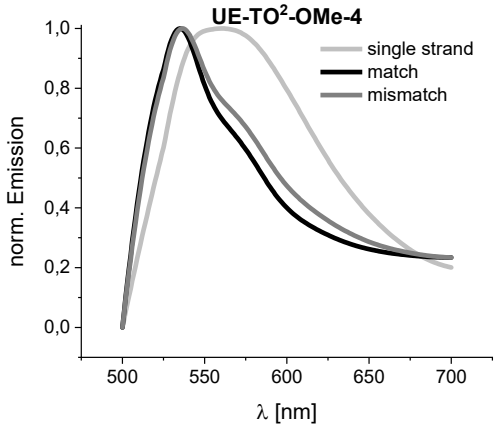
UE-TO²-OMe-4
single strand
match
mismatch
norm. Emission
λ [nm]

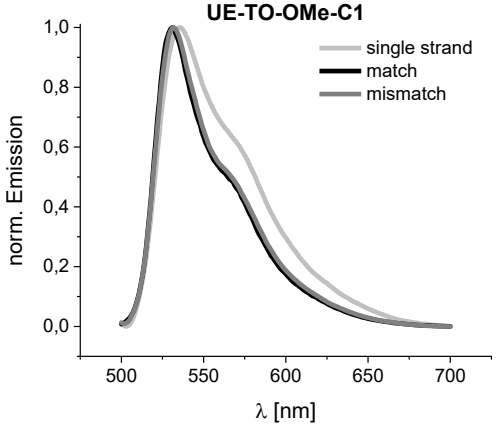
UE-TO-OMe-C1
single strand
match
mismatch
norm. Emission
λ [nm]

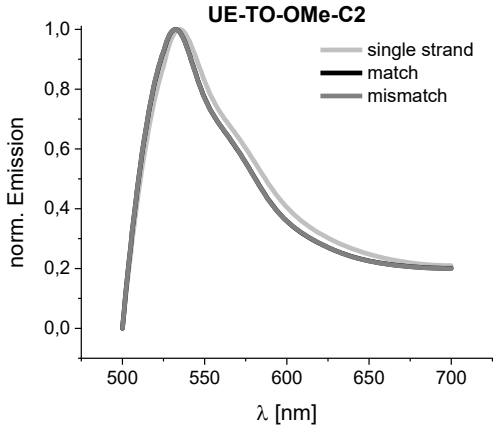
UE-TO-OMe-C2
single strand
match
mismatch
norm. Emission
λ [nm]

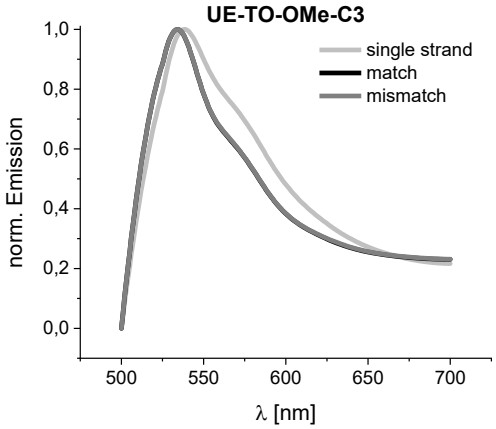
UE-TO-OMe-C3
single strand
match
mismatch
norm. Emission
λ [nm]

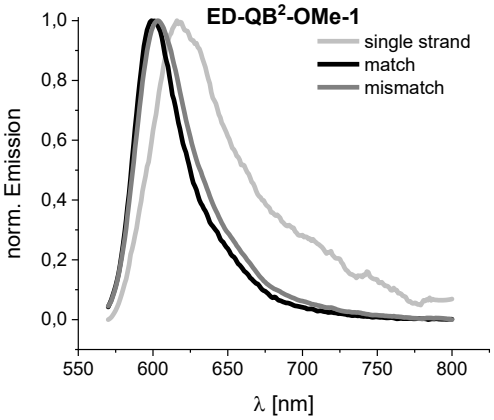
ED-QB²-OMe-1
single strand
match
mismatch
norm. Emission
λ [nm]

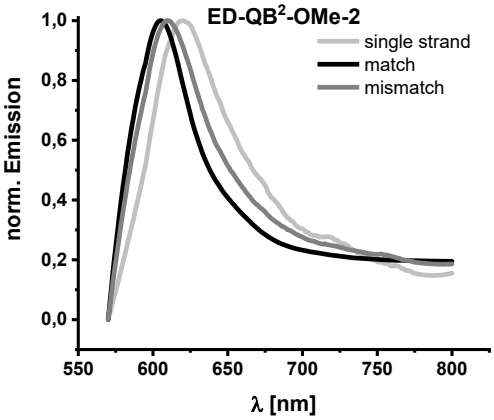
ED-QB²-OMe-2
single strand
match
mismatch
norm. Emission
λ [nm]

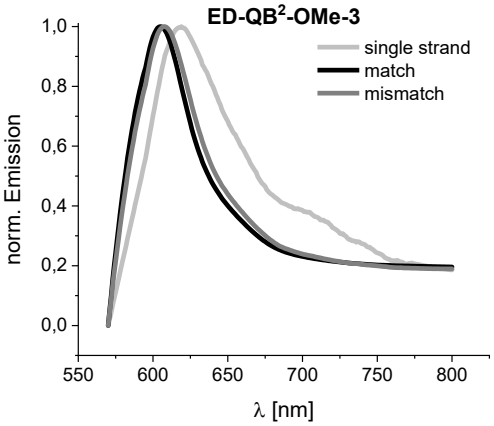
ED-QB²-OMe-3
single strand
match
mismatch
norm. Emission
λ [nm]

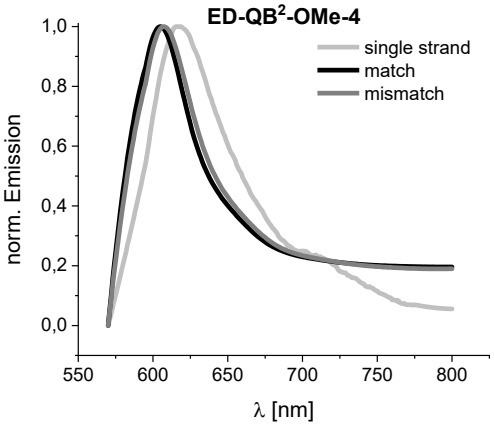
ED-QB²-OMe-4
single strand
match
mismatch
norm. Emission
λ [nm]

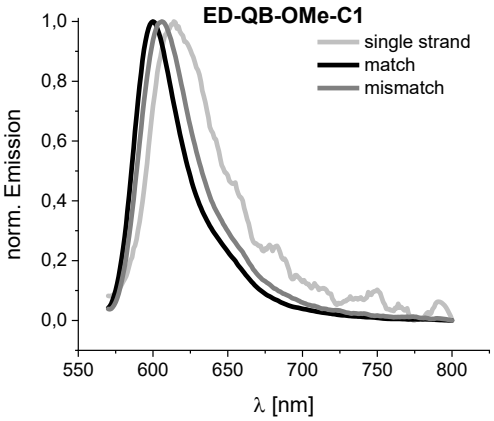
ED-QB-OMe-C1
single strand
match
mismatch
norm. Emission
λ [nm]

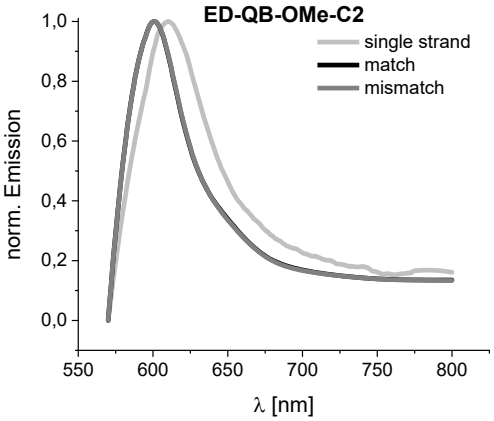
ED-QB-OMe-C2
single strand
match
mismatch
norm. Emission
λ [nm]

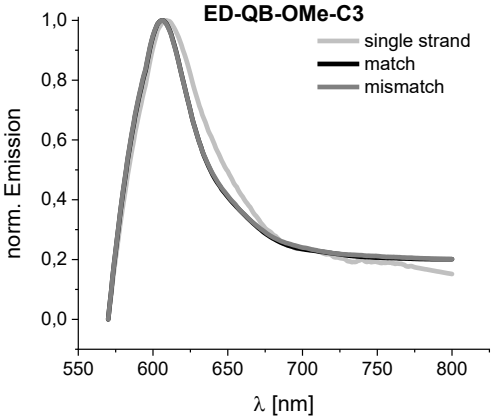
ED-QB-OMe-C3
single strand
match
mismatch
norm. Emission
λ [nm]

8.2.4 Thermal Stability Curves

Melting curves of all FIT probes (1 µM) in PBS buffer (100 mM NaCl, 10 mM Na_2HPO_4, pH 7.0) in the presence of 1 eq. match (solid lines) or mismatch (dashed lines) RNA target. Grey curves show the first derivative of a sigmoidal fit.

8.2.4.1 Mono-Dye FIT Probes

Nuclease-Resistant Mono-Dye UE-TO-OMe Probes

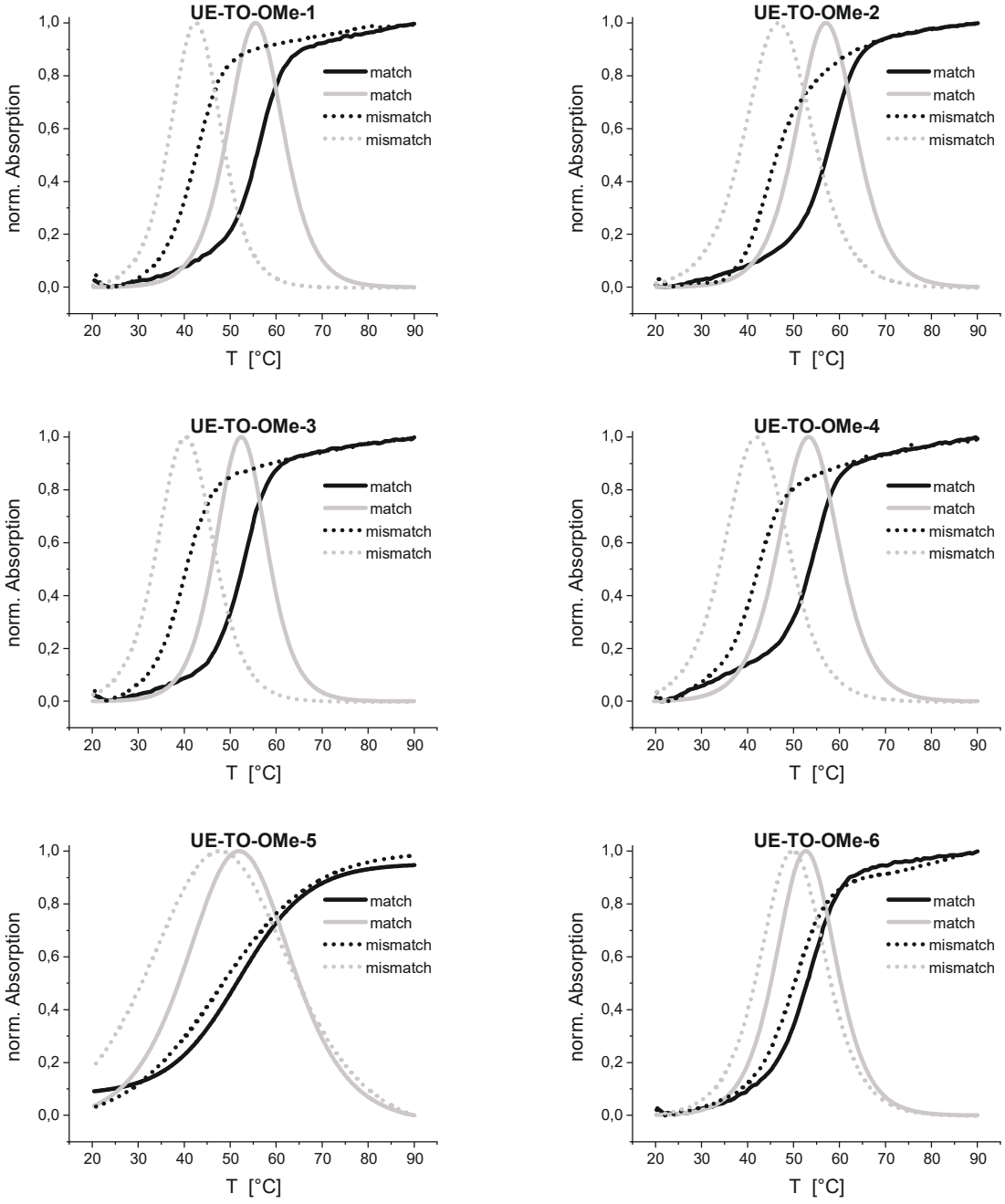

Nuclease-Resistant Mono-Dye ED-TO-OMe Probes

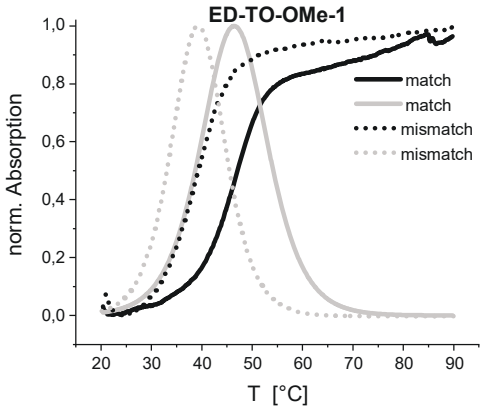

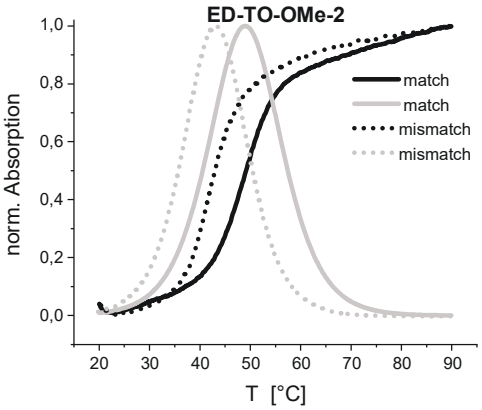

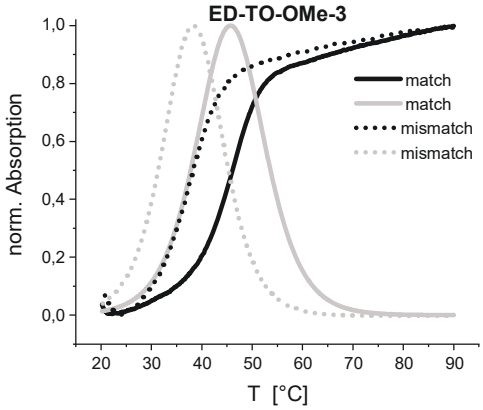

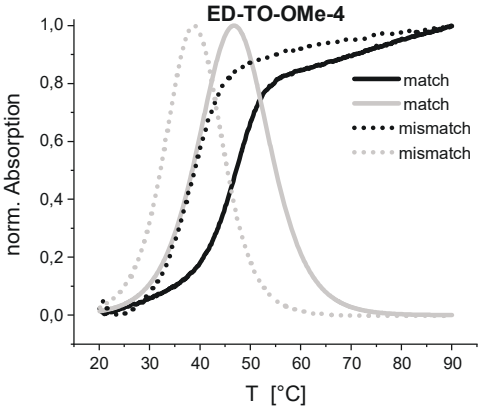

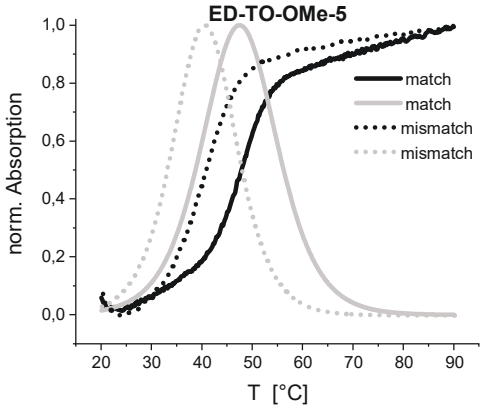

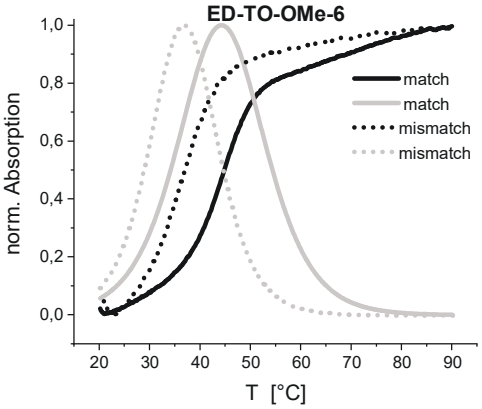

8.2.4.2 Dual-Dye FIT^2 Probes

DNA-Based FIT^2 Probes UE-QB^2-1 to -6 and Mono-Dye Controls

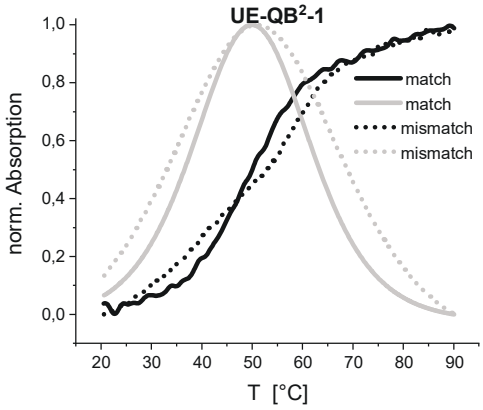

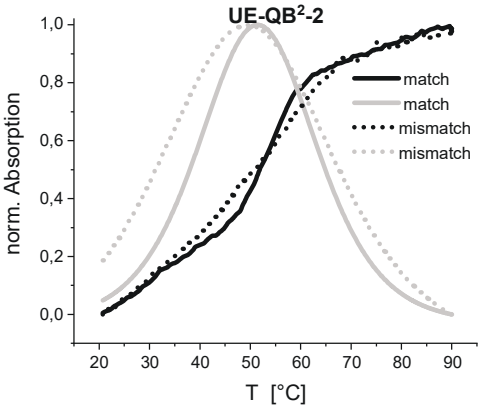

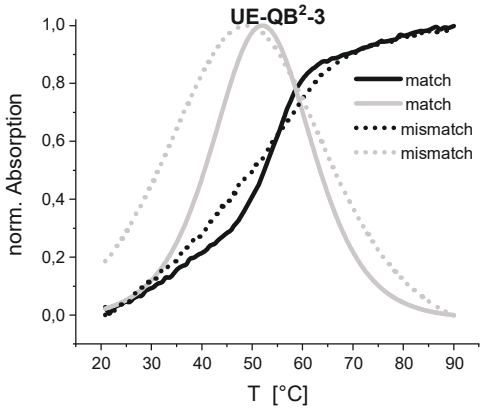

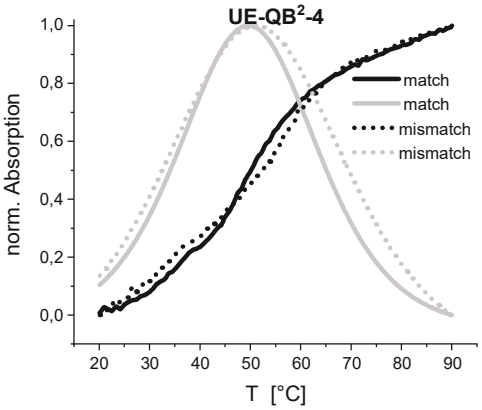

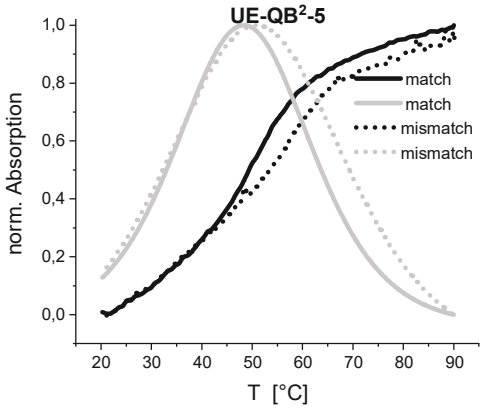

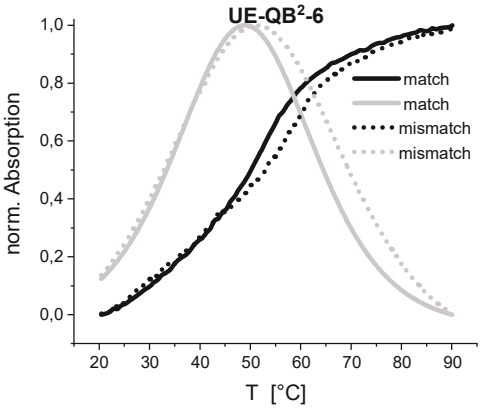

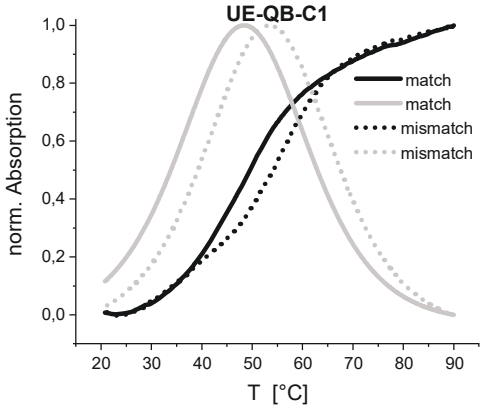
UE-QB-C1
norm. Absorption
T [°C]
match
match
mismatch
mismatch

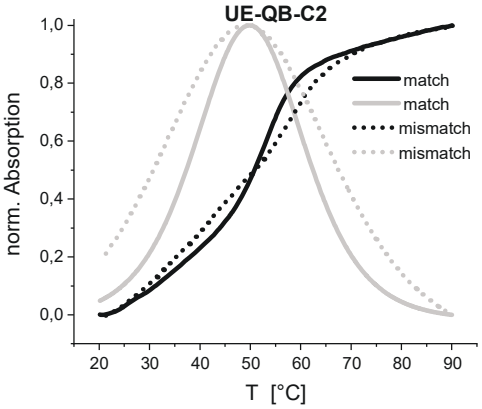
UE-QB-C2
norm. Absorption
T [°C]
match
match
mismatch
mismatch

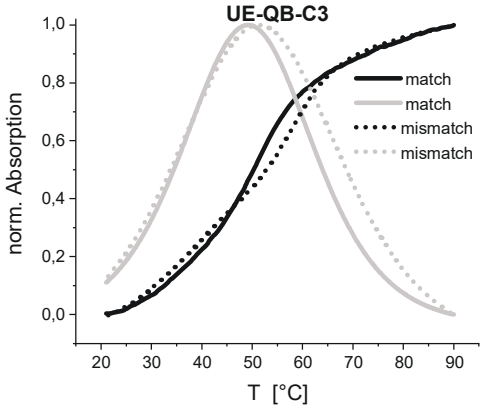
UE-QB-C3
norm. Absorption
T [°C]
match
match
mismatch
mismatch

Nuclease-Resistant FIT^2 Probes UE-QB^2-OMe-1 to -4 and Mono-Dye Controls

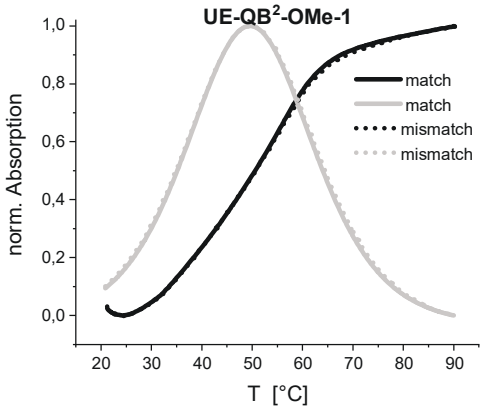

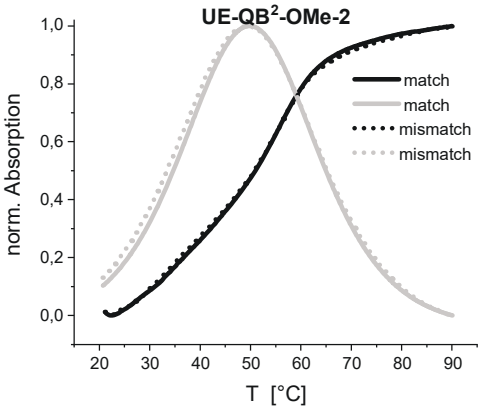

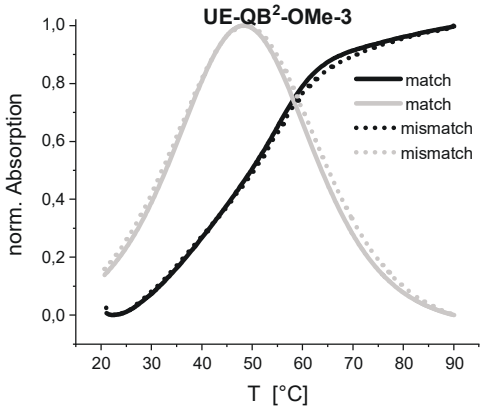

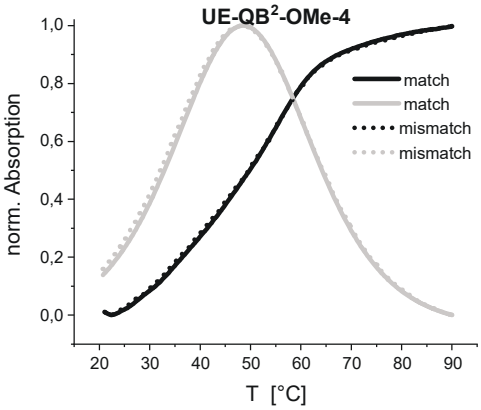

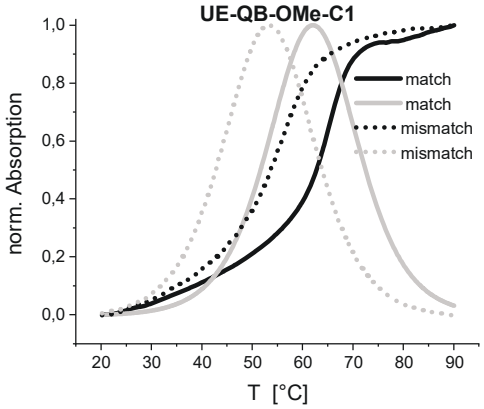

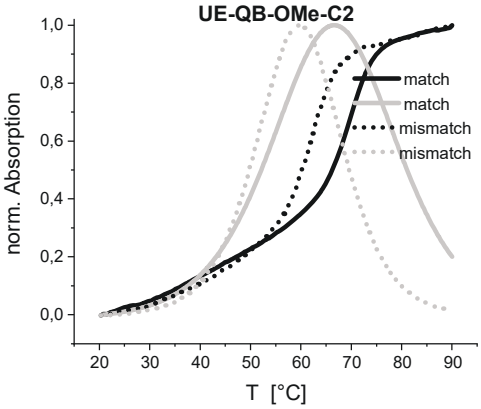

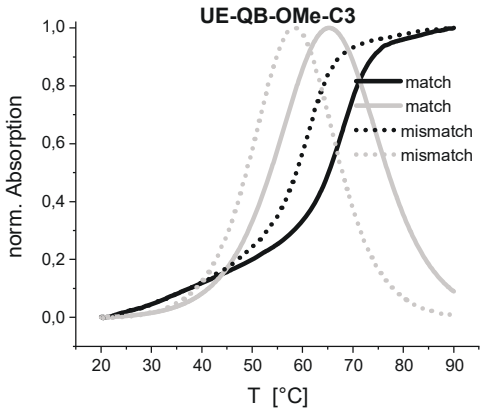

Nuclease-Resistant FIT^2 Probes ED-TO^2-OMe-1 to -4 and Mono-Dye Controls

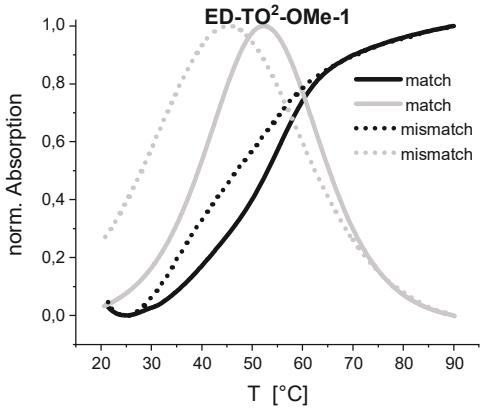

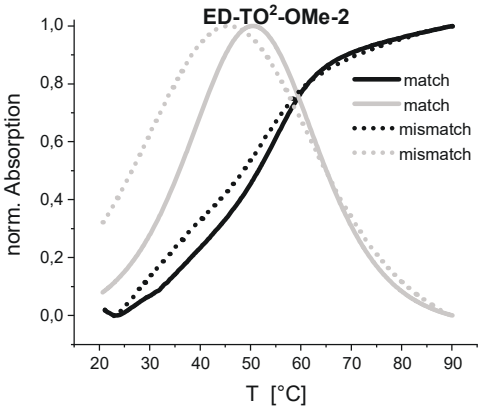

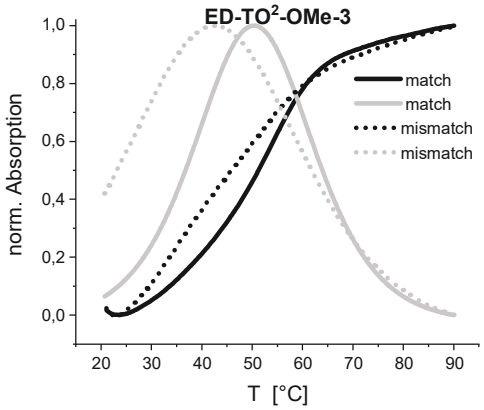

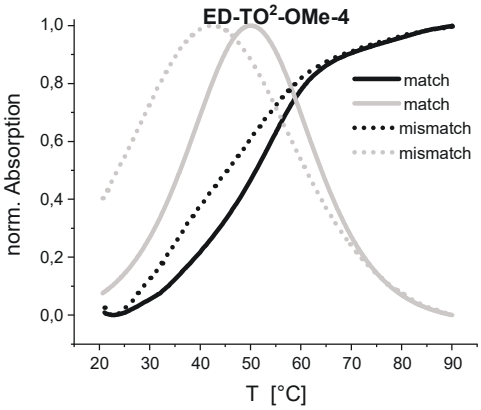

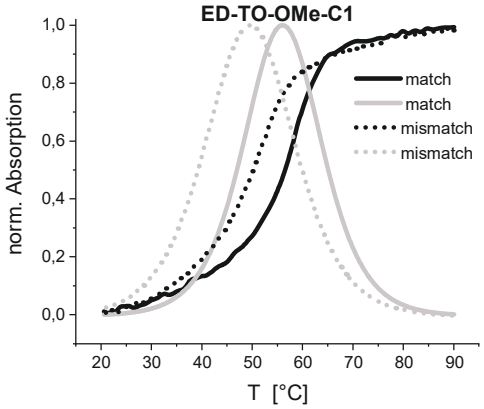

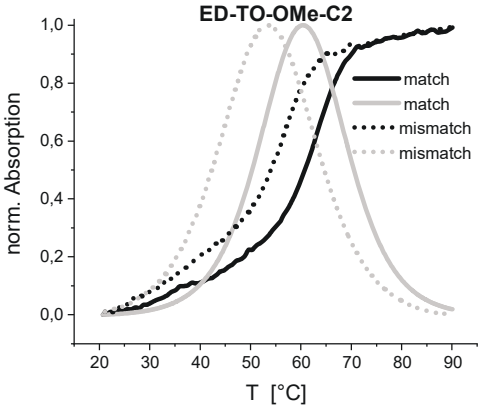

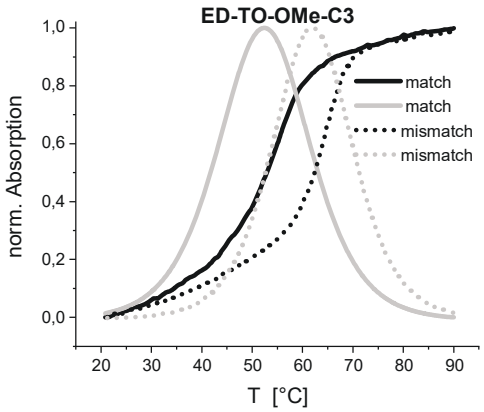

Nuclease-Resistant FIT^2 Probes UE-TO^2-OMe-1 to -4 and Mono-Dye Controls

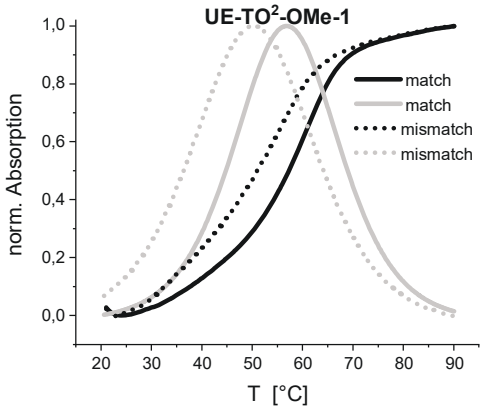

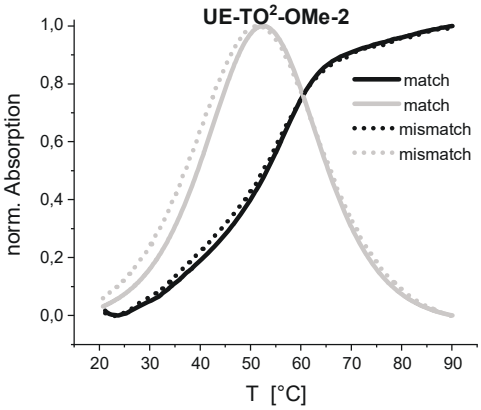

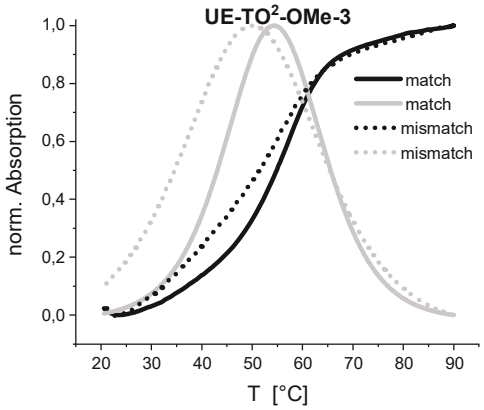

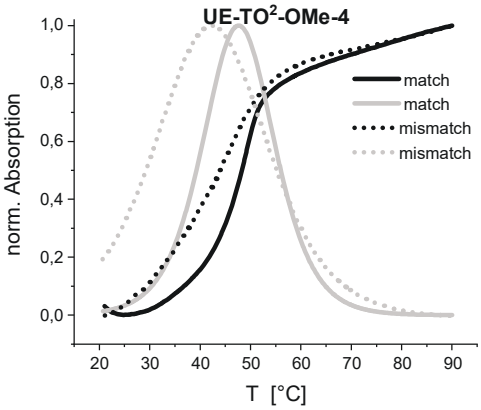

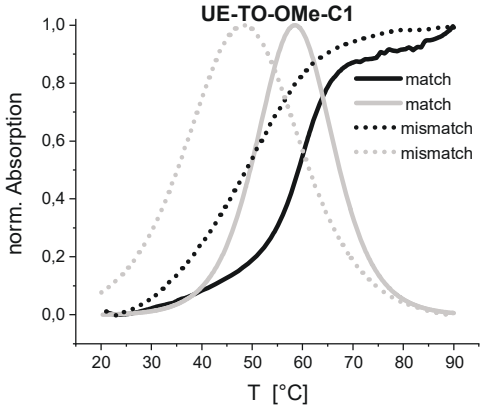

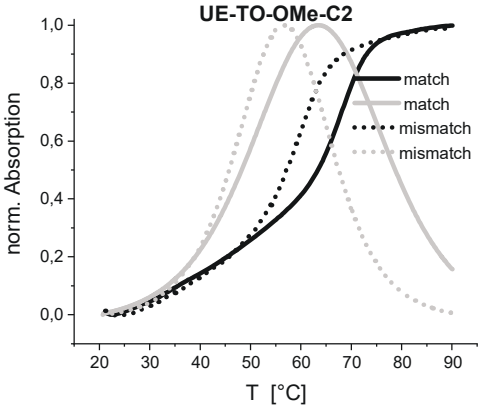

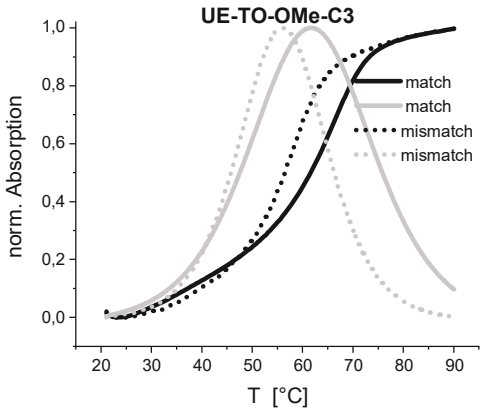

Nuclease-Resistant FIT^2 Probes ED-TO^2-OMe-1 to -4 and Mono-Dye Controls

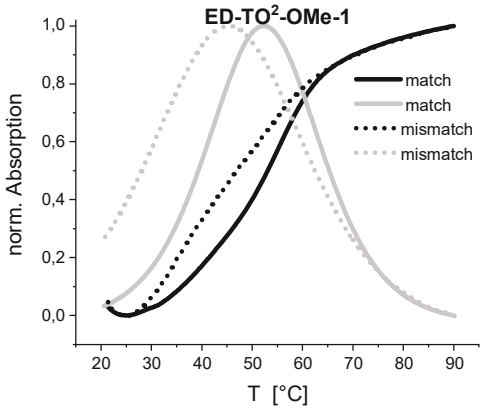

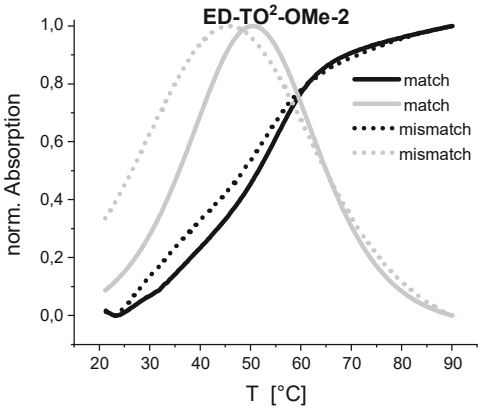

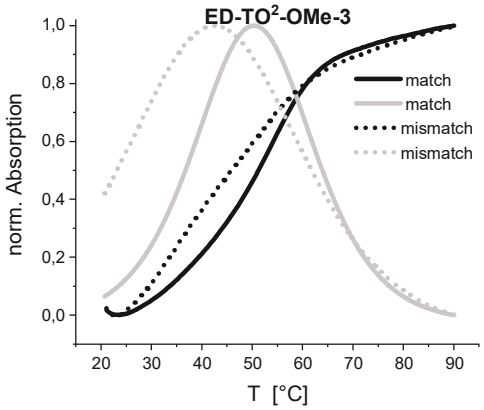

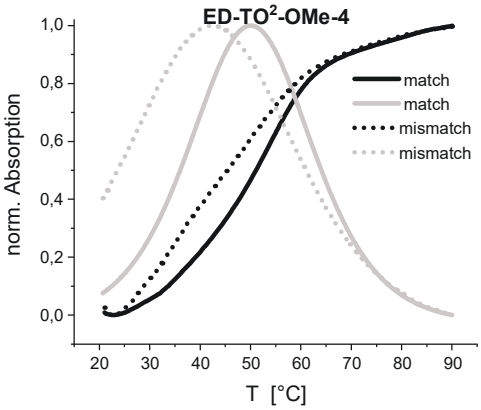

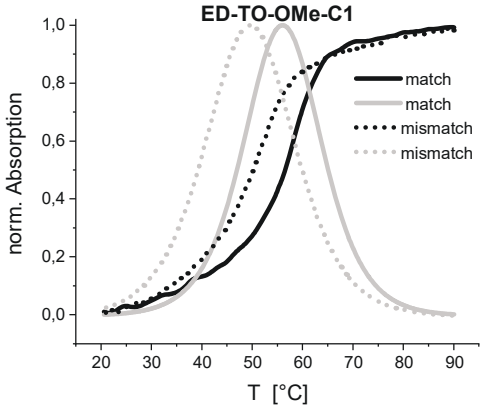

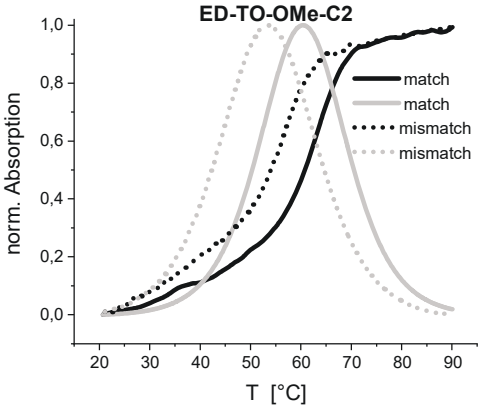

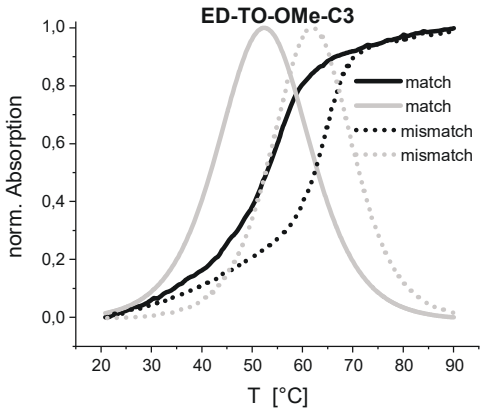

Nuclease-Resistant FIT^2 Probes ED-QB^2-OMe-1 to -4 and Mono-Dye Controls

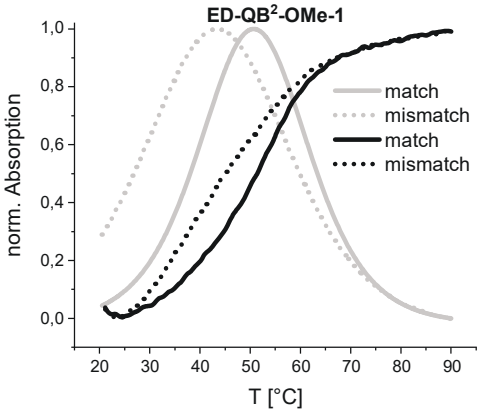

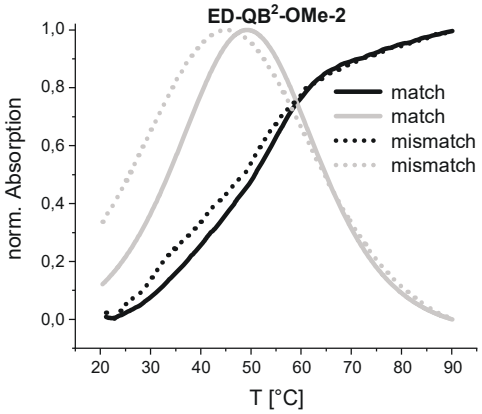

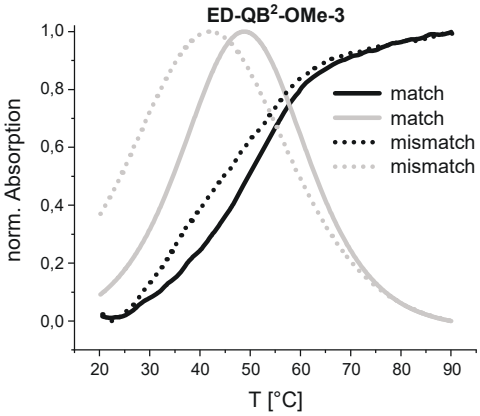

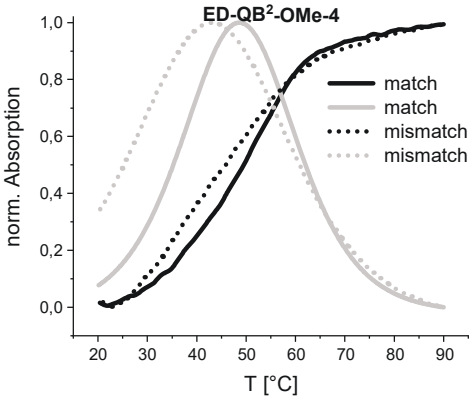

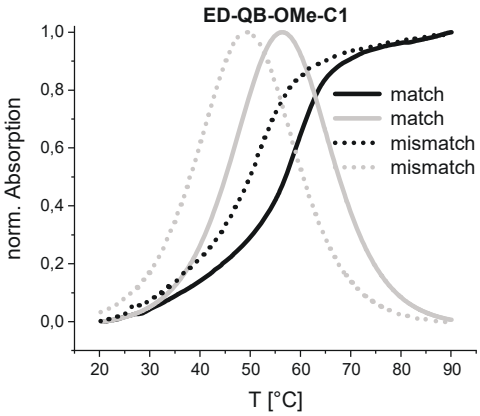

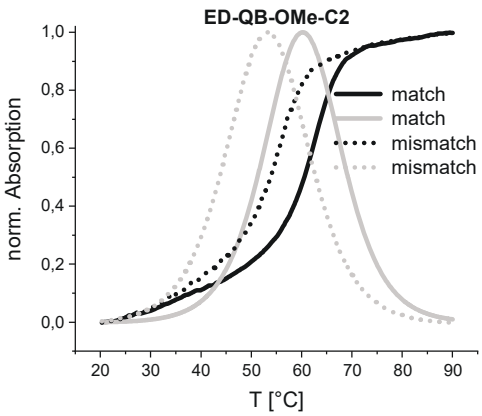

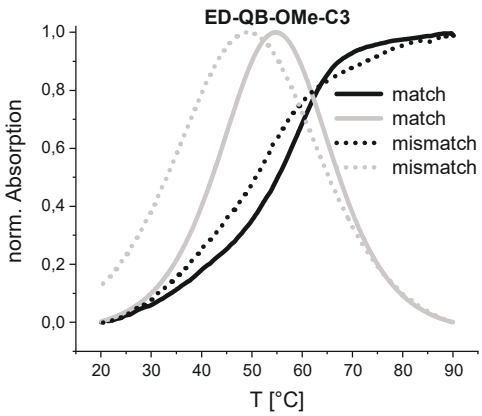

8.2.5 Competitive Experiments

8.2.5.1 Fluorescence Spectra of Competitive Measurements with Mono-Dye Probes

ED-TO-OMe-1 vs. UE-QB-OMe-1

ED-TO-OMe-1 AATAAACTGAA**TO**C$_L$A

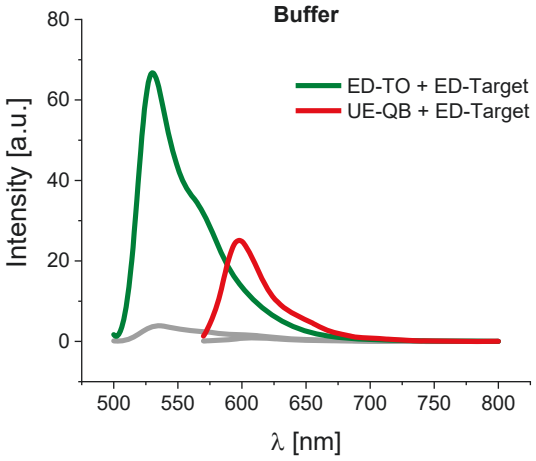

UE-QB-OMe-1 AATAAACTGAG**QB**C$_L$A

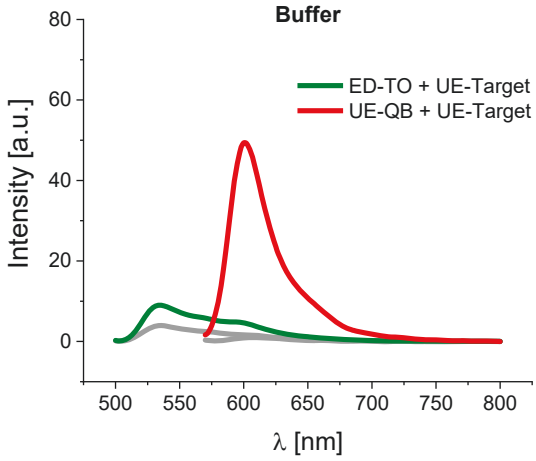

UE-TO-OMe-3 vs. ED-QB-OMe-3

UE-TO-OMe-3 5'-AATAAACTGAG$_L$**TO**CA-3'

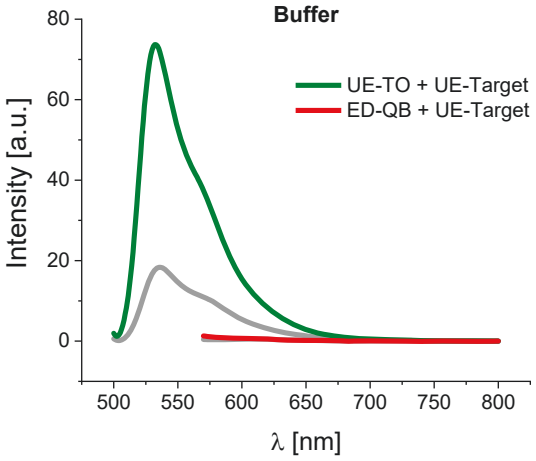

ED-QB-OMe-3 5'-AATAAACTGAA$_L$**QB**CA-3'

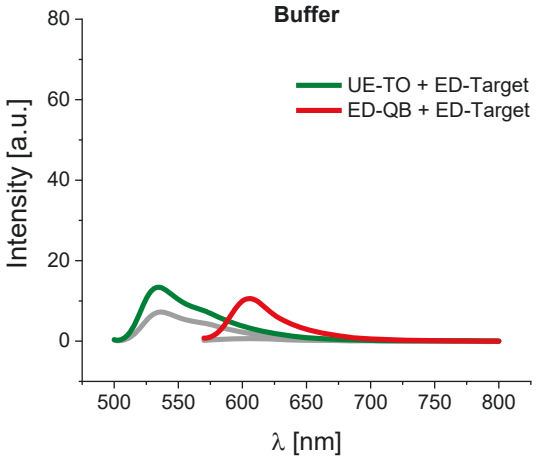

8.2.5.2 Fluorescence Spectra of Competitive Measurements with Dual-Dye Probes

UE-QB-OMe-C1 vs. ED-TO-OMe-C1

UE-QB-OMe-C1 UCAAAAUAAACUGAG**QB**C$_L$A

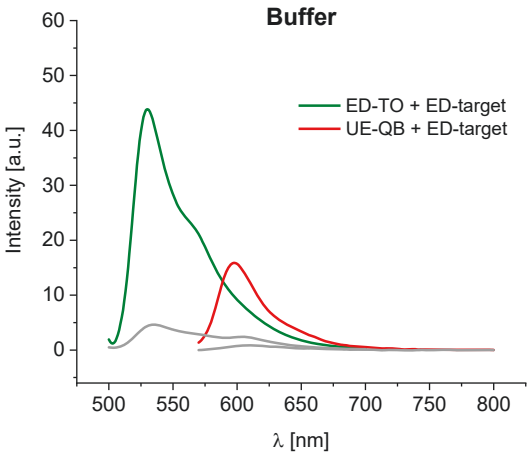

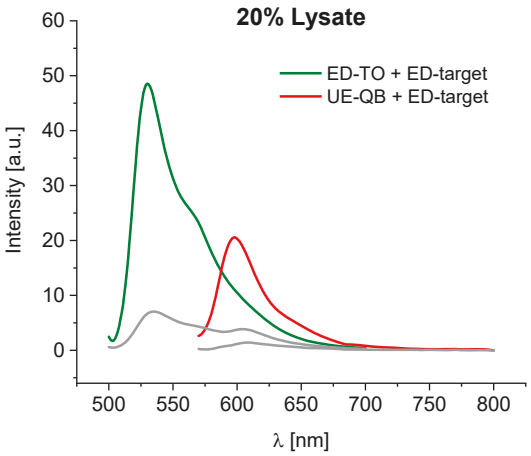

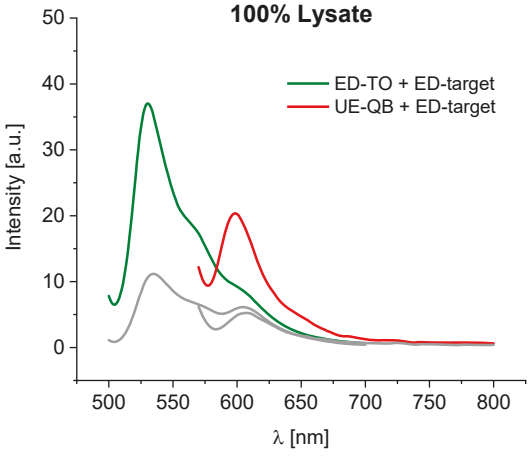

ED-TO-OMe-C1 UCAAAAUAAACUGAA**TO**C$_L$A

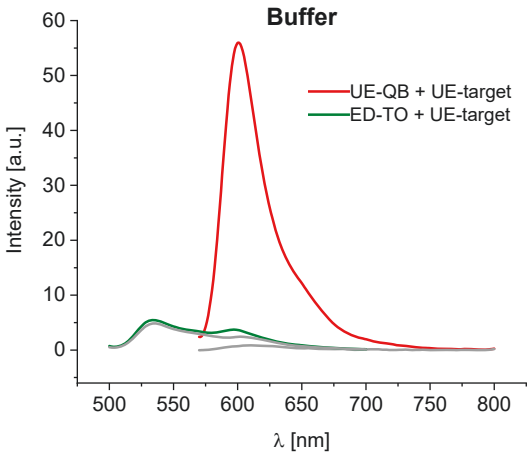

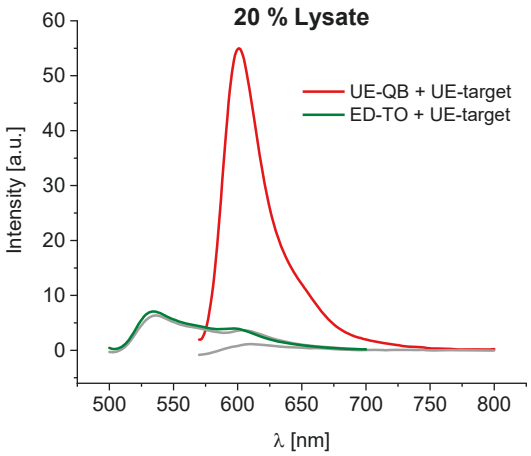

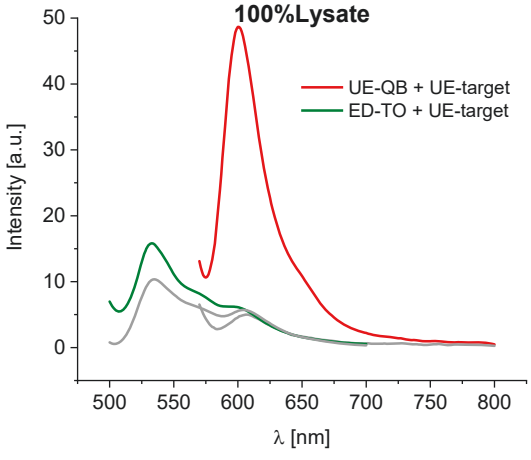

UE-QB^2-OMe-1 vs. ED-TO^2-OMe-4

UE-QB^2-OMe-1 UCAAA**QB**TLAAACUGAG**QB**CLA

ED-TO^2-OMe-4 UCAAAAT**TO**ALACUGAA**TO**CLA

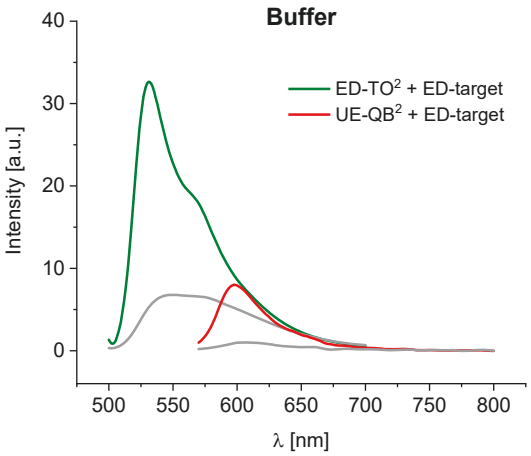

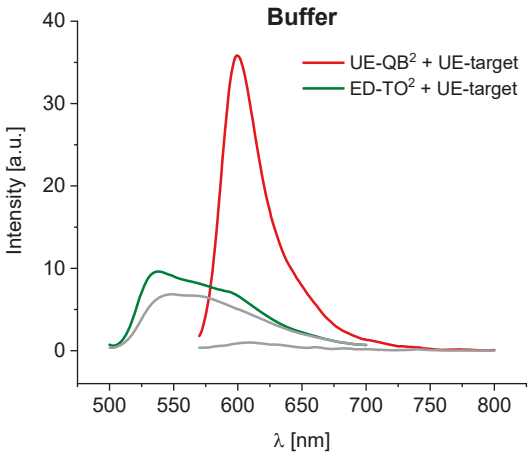

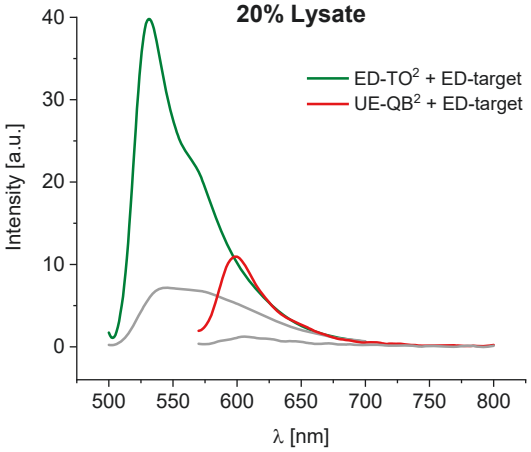

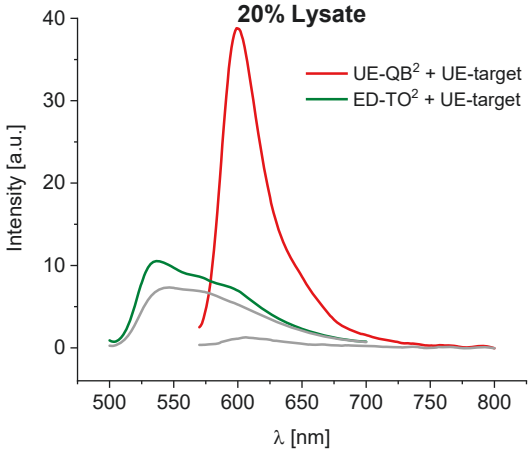

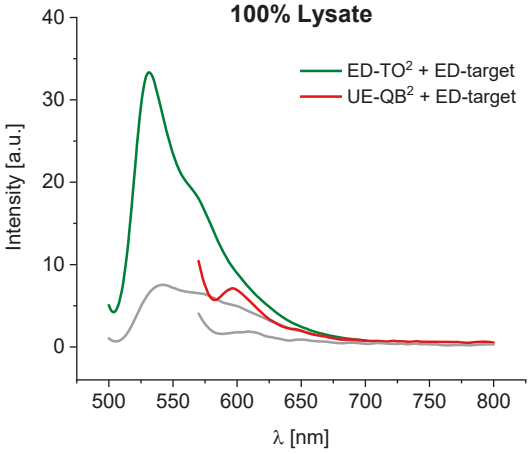

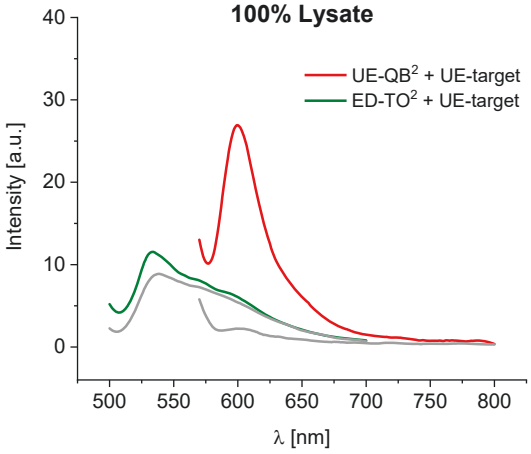

UE-TO-OMe-C1 vs. ED-QB-OMe-C1

UE-TO-OMe-C1 UCAAAATAAACUGAGTOCLA

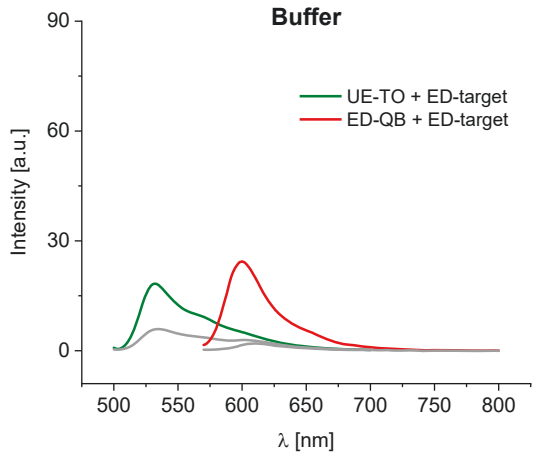

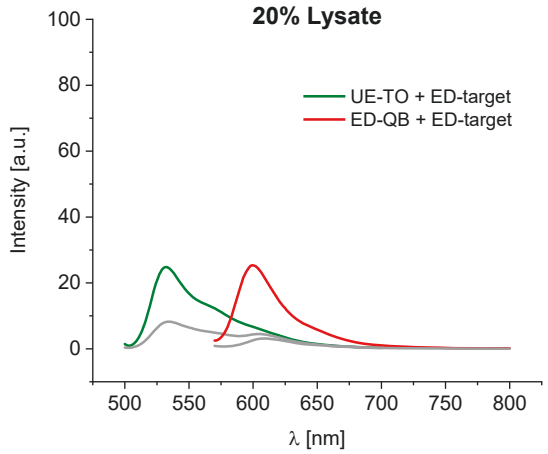

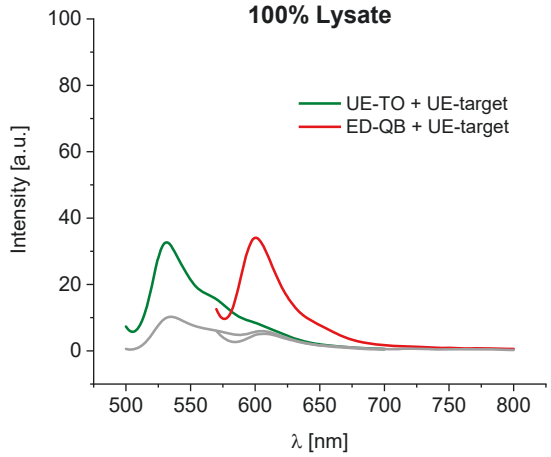

ED-QB-OMe-C1 UCAAAAUAAACUGAAQBCLA

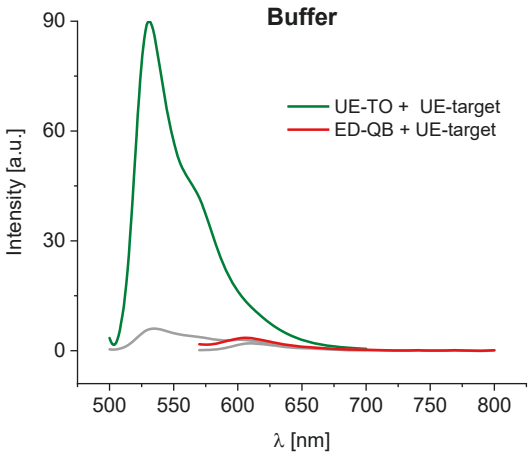

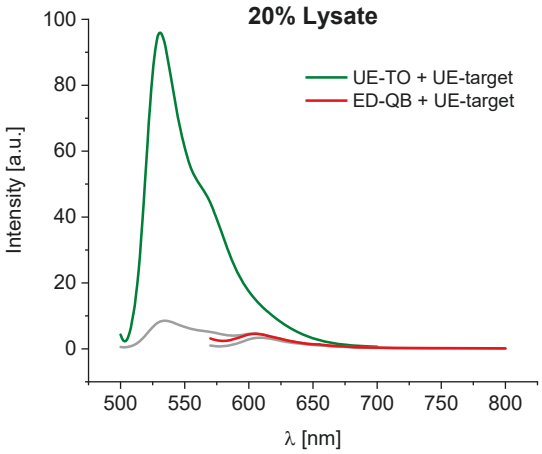

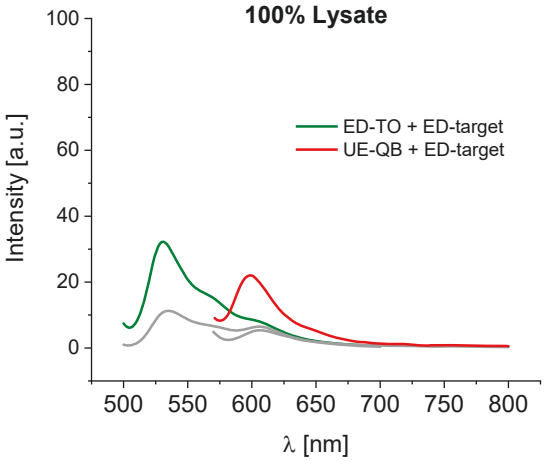

UE-TO^2-OMe-2 vs. ED-QB^2-OMe-1

UE-TO^2-OMe-2 AAAATTOALACUGAGTOCLA

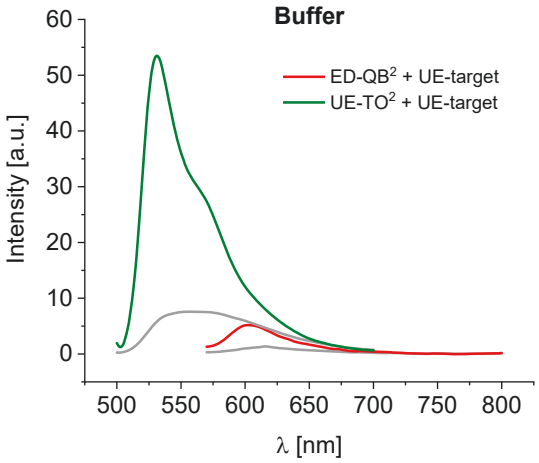

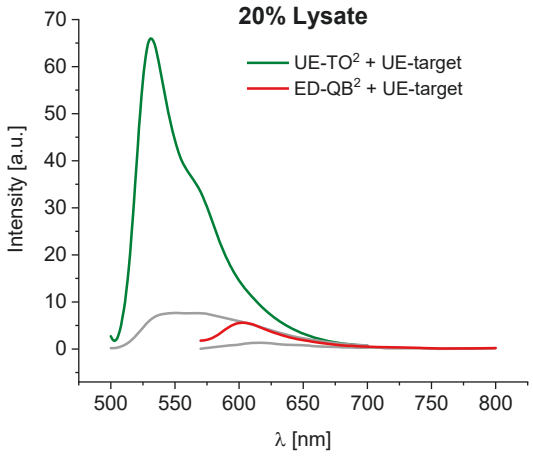

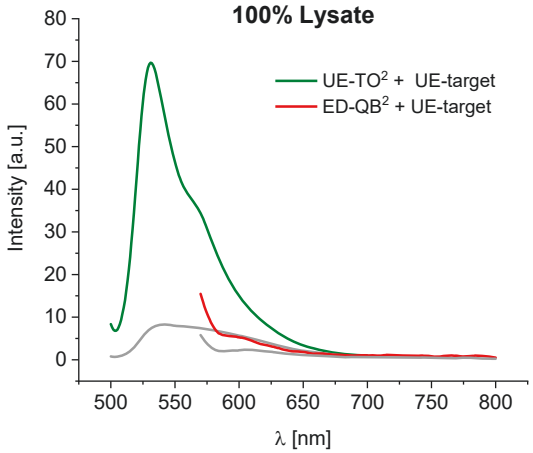

ED-QB^2-OMe-1 UCAAAQBTLAAACUGAAQBCLA

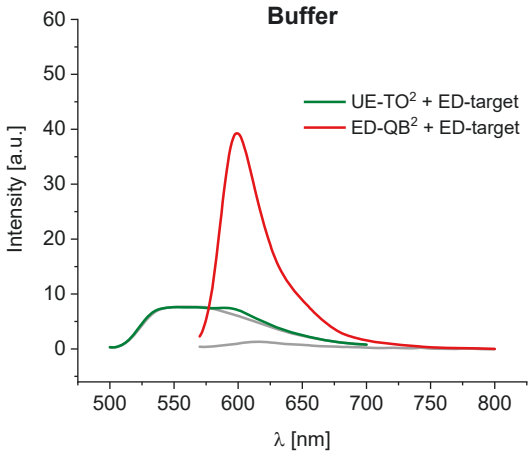

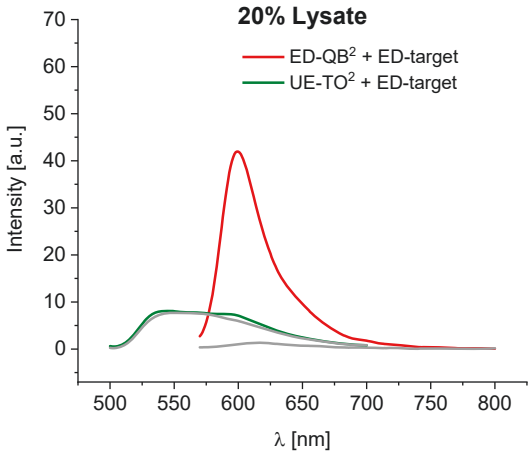

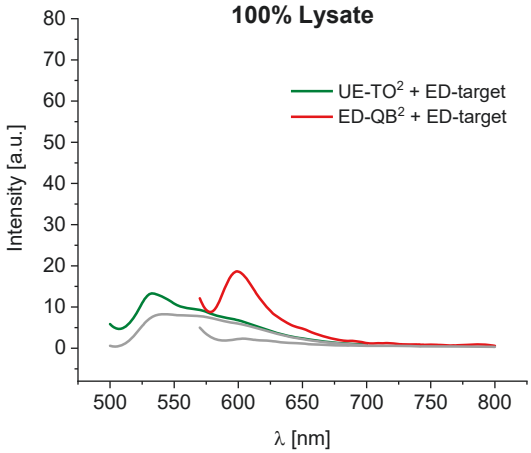

8.3 Spectroscopic Properties of qFIT^2 Probes Targeting TCR CDR3 mRNA

Table 19: Spectroscopic properties of qFIT^2 probes specific for TCR CDR3 mRNA of Jurkat and CCRF-CEM cells.

	Sequence 5' – 3'	I_0 535 nm	I 535 nm	E_{535}	I_0 733 nm	I 733 nm	E_{733}	r_0	r	ϕ_{535}	ϕ/ϕ_0 535 nm	Br_{535}
JK-TO^2-Cy7												
1	GGTTOT$_L$AGCCAUATOT$_L$T AGCCGAACAGG-CY7	11.1	183.6	16.5	49.0	56.0	1.1	0.2	3.3	0.41	11.8	38.7
2	GGTTOT$_L$AGCCAUATOT$_L$T AGCCGAACAGGUC-CY7	15.8	193.3	12.3	27.8	26.9	1.0	0.6	7.2	0.42	9.0	36.2
3	GGTTOT$_L$AGCCAUATOT$_L$T AGCCGAACAGGUCGA-CY7	13.2	195.0	14.8	35.4	41.2	1.2	0.4	4.7	0.41	11.5	36.0
CEM-TO^2-Cy7												
1	AUATOT$_L$GCGUAUCTTOT$_L$C CCAAGGCUGCU-CY7	9.1	105.0	11.5	50.0	53.2	1.1	0.2	2.0	0.25	8.9	19.0
2	ATA$_L$TOTGCGUAUCTTOT$_L$C CCAAGGCUGCU-CY7	8.7	89.0	10.2	48.0	59.3	1.2	0.2	1.5	0.20	8.5	15.8
3	AUACTTOC$_L$GUAUCTTOT$_L$C CCAAGGCUGCU-CY7	5.1	184.5	36.2	52.8	66.5	1.3	0.1	2.8	0.37	24.3	29.3
4	AUACT$_L$TOCGUAUCTTOT$_L$C CCAAGGCUGCU-CY7	3.6	121.9	33.7	49.2	63.3	1.3	0.1	1.9	0.22	22.8	17.3
5	ATTOC$_L$TGCGUAUCTTOT$_L$C CCAAGGCUGCU-CY7	10.9	149.2	14.5	51.5	56.3	1.1	0.2	2.6	0.37	10.6	30.1
6	AT$_L$TOCUGCGUAUCTTOT$_L$C CCAAGGCUGCU-CY7	6.3	90.7	13.7	49.5	62.0	1.3	0.1	1.5	0.24	10.0	19.7
7	AUATOT$_L$GCGTATCTTOT$_L$C CCAAGGCTGCTGGC-Cy7	12.4	153.6	12.4	25.7	26.5	1.0	0.5	5.8	0.34	7.8	26.7
8	AUACTTOC$_L$GTATCTTOT$_L$C CCAAGGCTGCTGGC-Cy7	11.5	207.4	18.0	20.7	21.4	1.0	0.6	9.7	0.43	10.9	30.9
9	ATTOC$_L$TGCGTATCTTOT$_L$C CCAAGGCTGCTGGC-Cy7	15.0	161.9	10.8	33.9	33.1	1.0	0.4	4.9	0.37	8.8	26.5
10	ATTOC$_L$TGCGTATCTTOT$_L$C CCAAGGCUGCUGGC-Cy7	20.3	179.7	8.9	38.0	39.7	1.0	0.5	4.5	0.43	7.7	34.1
11	AUACTTOC$_L$GCGTATCTTOT$_L$(CCAAGGCUGCUGGC-Cy7	11.7	203.2	17.4	27.4	27.1	1.0	0.4	7.5	0.39	11.6	28.2

Conditions: 0.5 µM probe and 5 eq. RNA target (Jurkat: 5'-GGUGUAGCCAUAGUUAGCCGAACAGGUCGA-3'; CEM: 5'-GGUGUAGCCAUAGUUAGCCGAACAGGUCGA-3') were measured in buffer (100 mM NaCl. 10 mM Na_2HPO_4, pH 7.0) to determine fluorescence enhancement $E = I / I_0$ for TO (E_{535}) and for Cy7 (E_{773}). Single strand r_0 and double strand ratio r were calculated as I_{535} / I_{773}. Enhancement factors and ratios were measured at 37 °C, quantum yield ϕ and brightness $Br = \varepsilon_{535} \cdot \phi_{535} / 1000$ in $M^{-1} \cdot cm^{-1}$ at 25 °C. Cy7: λ_{ex} = 650 nm, λ_{em} = 773 nm; TO: λ_{ex} = 485 nm, λ_{em} = 535 nm, $slit_{ex/em}$ = 5 nm. Underscored letters = 2'OMe-RNA; subscript L = LNA.

8.3.1.1 Spectroscopic Properties of qFIT² Probes Specific for Jurkat Cells

Extinction Coefficient Spectra for JK-TO²-Cy7-1 to -3

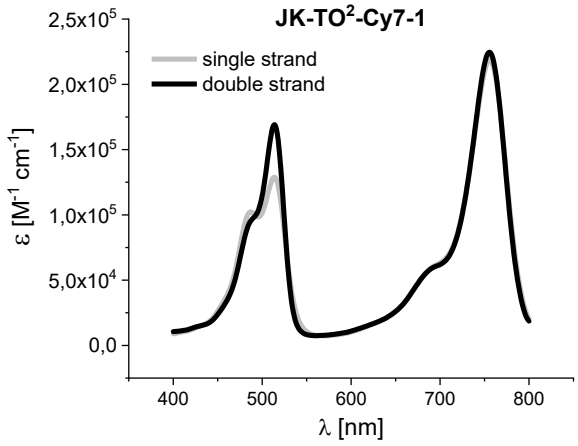

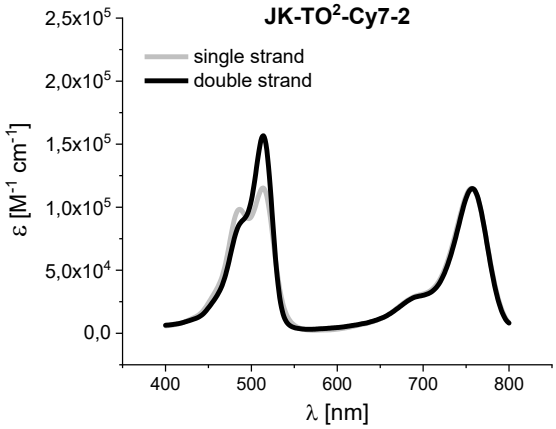

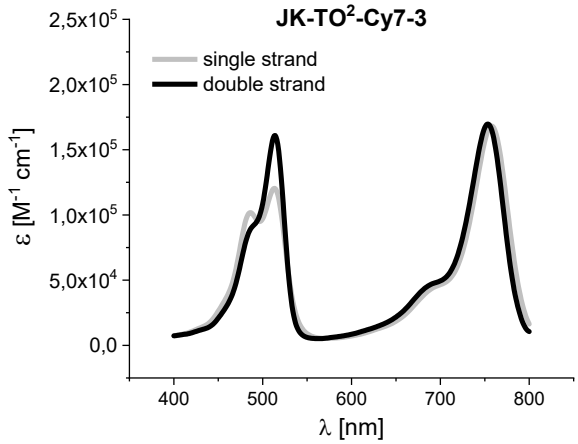

Excitation and Emission Spectra of JK-TO^2-Cy7-1 to -3

TO Excitation / Emission

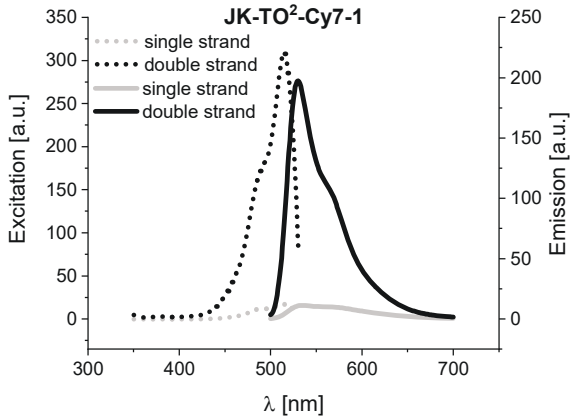

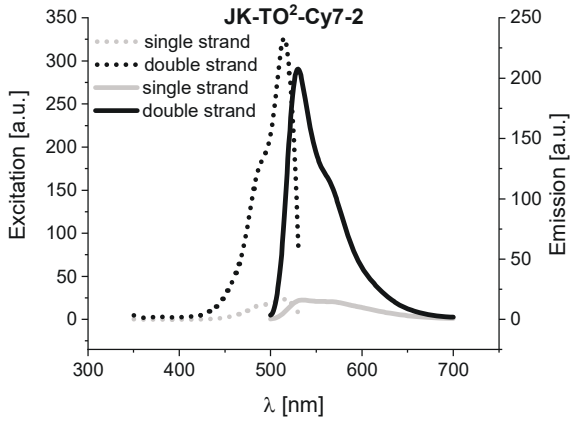

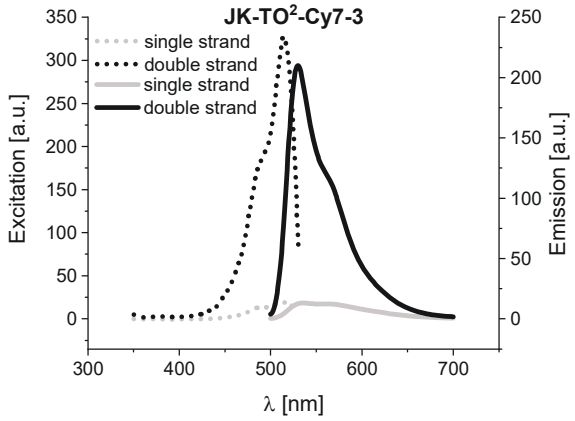

Cy7 Excitation / Emission

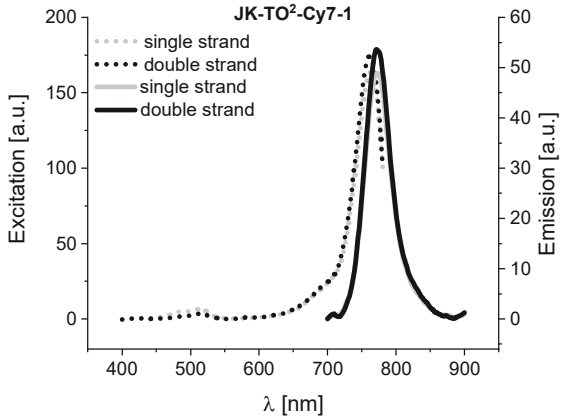

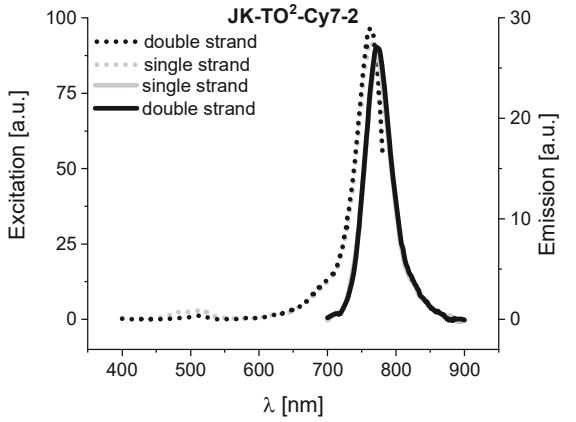

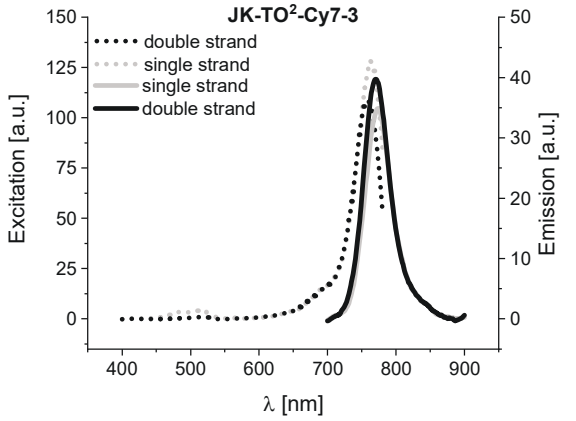

8.3.1.2 Spectroscopic Properties of qFIT² Probes Specific for CCRF-CEM Cells

Extinction Coefficient Spectra for CEM-TO²-Cy7-1 to -11

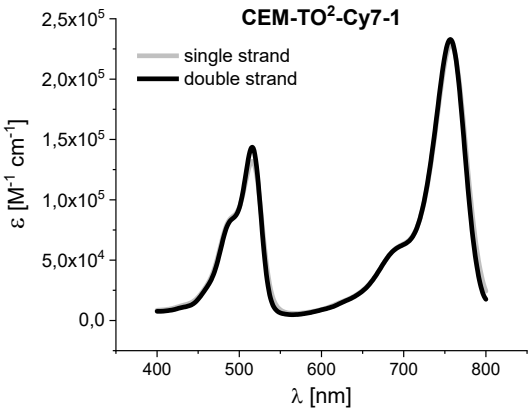

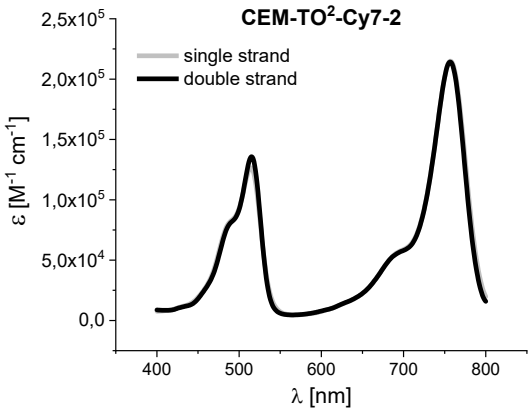

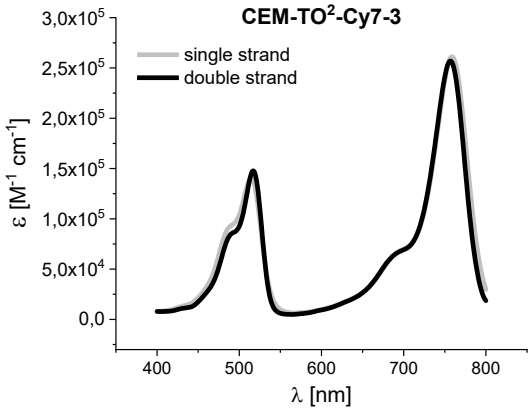

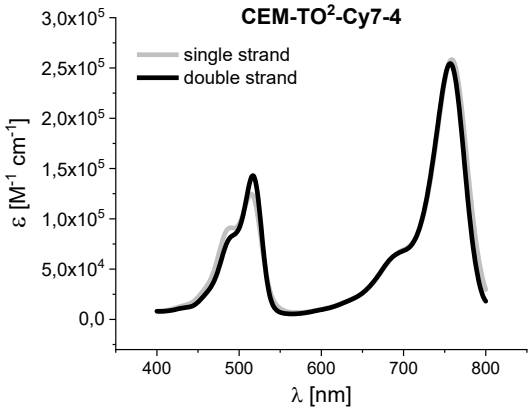

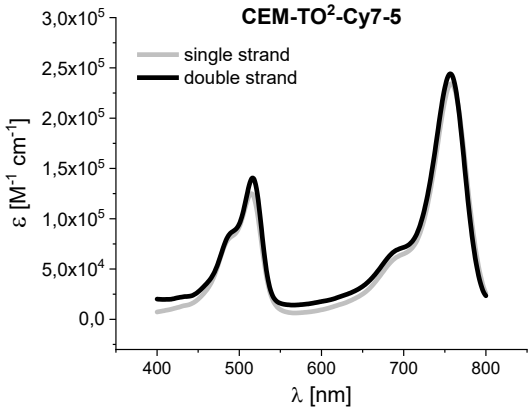

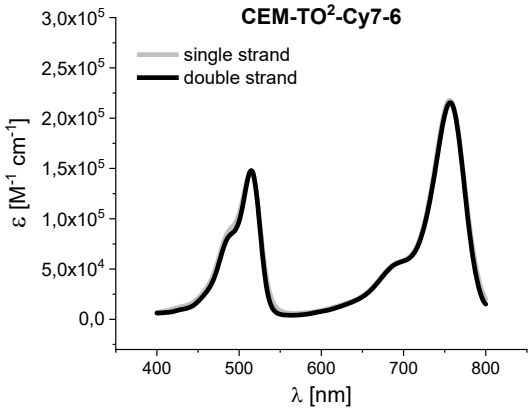

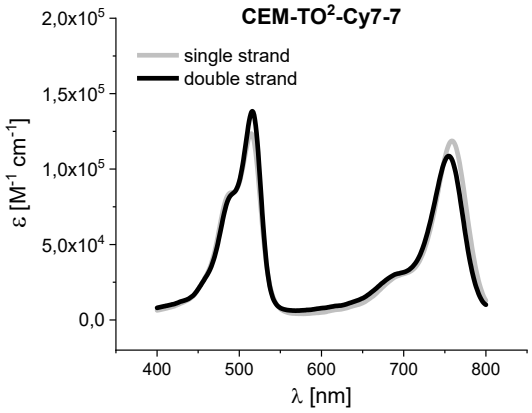
CEM-TO2-Cy7-7
single strand
double strand
ε [M-1 cm-1]
λ [nm]

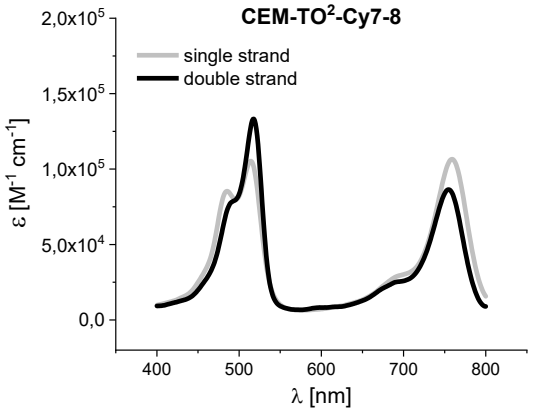
CEM-TO2-Cy7-8
single strand
double strand
ε [M-1 cm-1]
λ [nm]

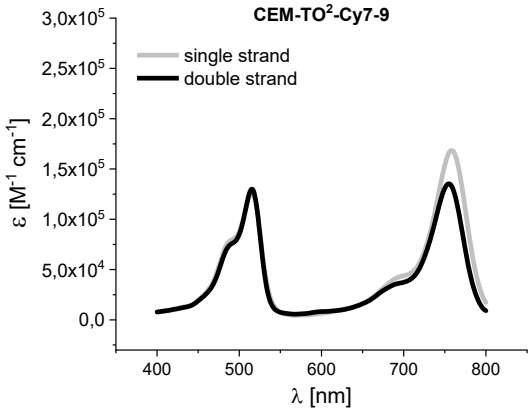
CEM-TO2-Cy7-9
single strand
double strand
ε [M-1 cm-1]
λ [nm]

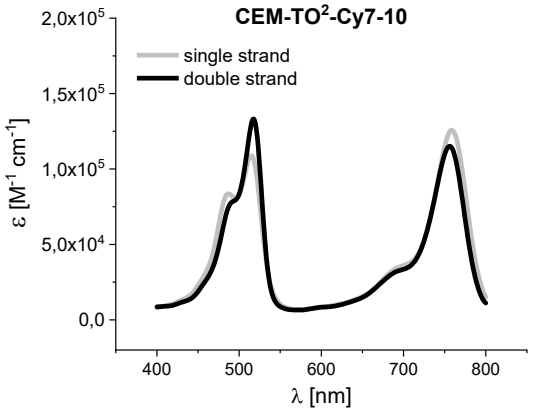
CEM-TO2-Cy7-10
single strand
double strand
ε [M-1 cm-1]
λ [nm]

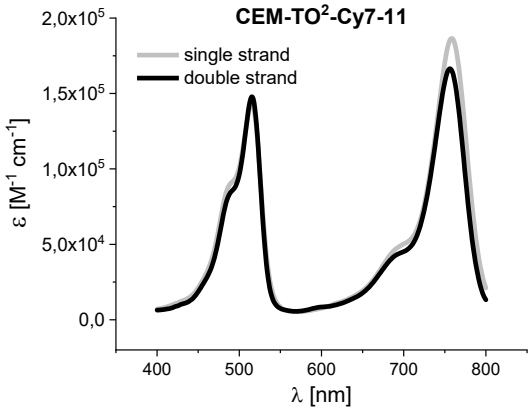
CEM-TO2-Cy7-11
single strand
double strand
ε [M-1 cm-1]
λ [nm]

Excitation and Emission Spectra of CEM-TO^2-Cy7-1 to -11

TO Excitation / Emission

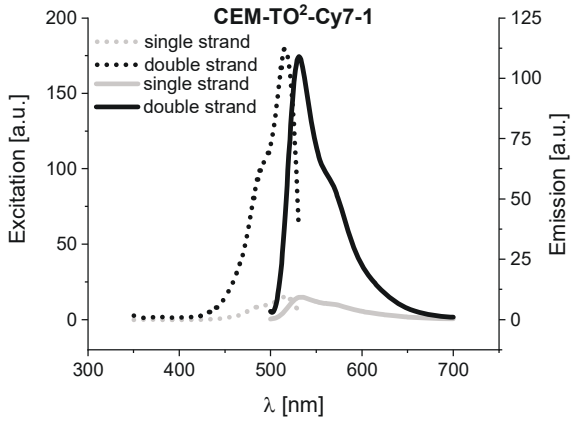

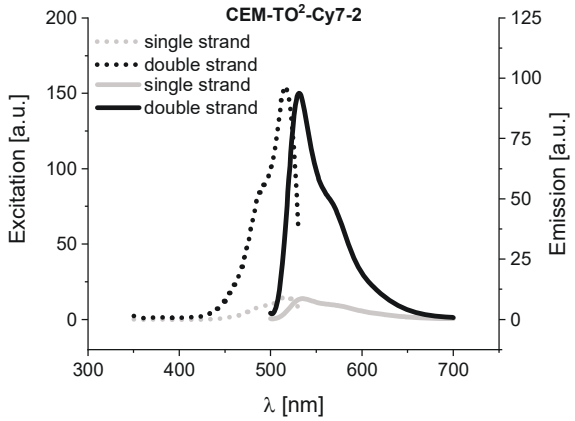

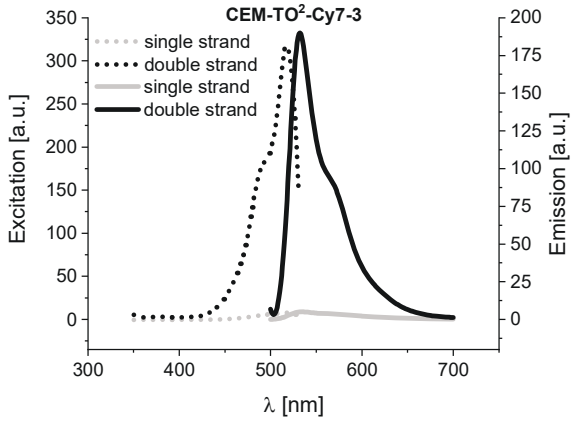

Cy7 Excitation / Emission

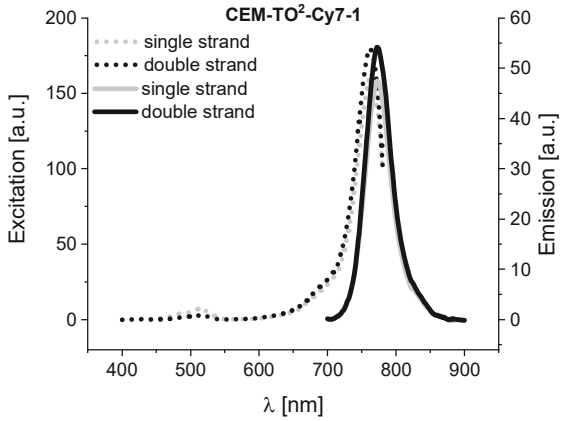

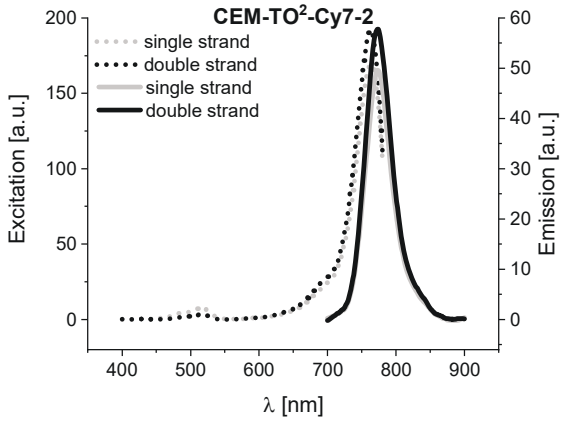

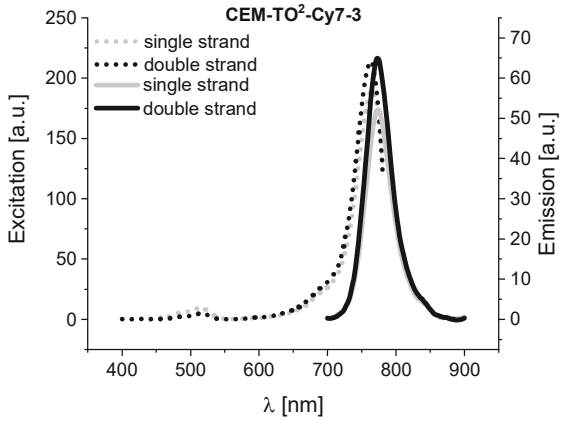

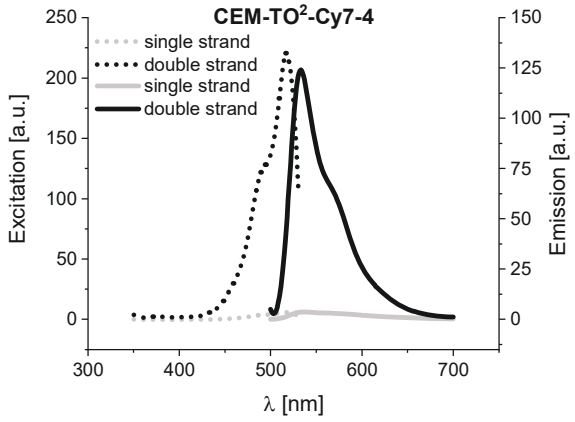
CEM-TO²-Cy7-4
single strand
double strand
single strand
double strand
Excitation [a.u.]
Emission [a.u.]
λ [nm]

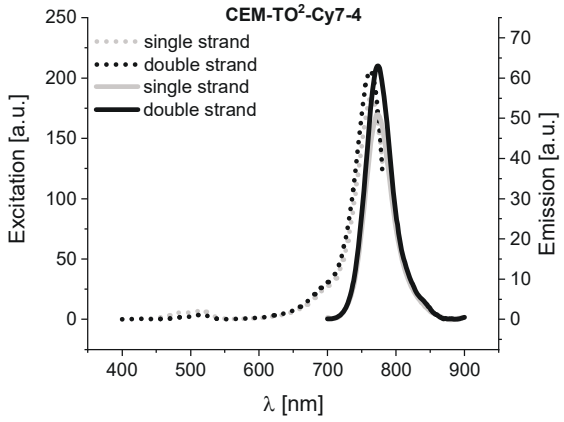
CEM-TO²-Cy7-4
single strand
double strand
single strand
double strand
Excitation [a.u.]
Emission [a.u.]
λ [nm]

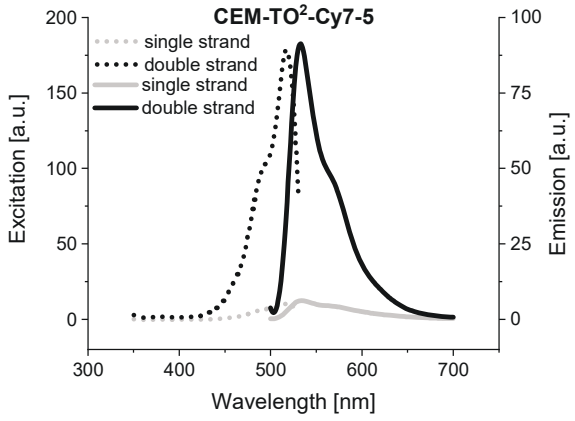
CEM-TO²-Cy7-5
single strand
double strand
single strand
double strand
Excitation [a.u.]
Emission [a.u.]
Wavelength [nm]

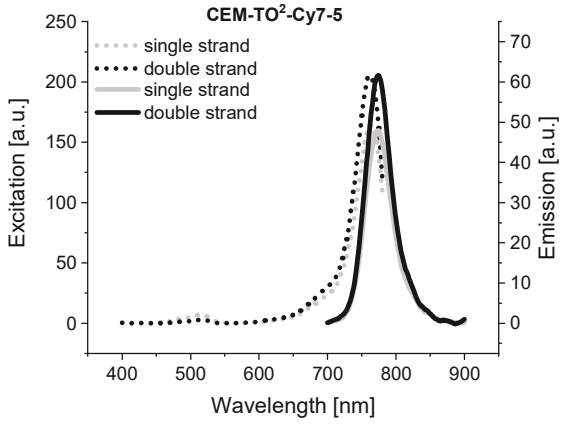
CEM-TO²-Cy7-5
single strand
double strand
single strand
double strand
Excitation [a.u.]
Emission [a.u.]
Wavelength [nm]

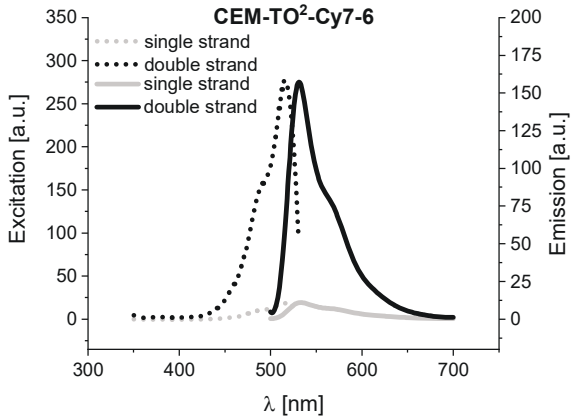
CEM-TO²-Cy7-6
single strand
double strand
single strand
double strand
Excitation [a.u.]
Emission [a.u.]
λ [nm]

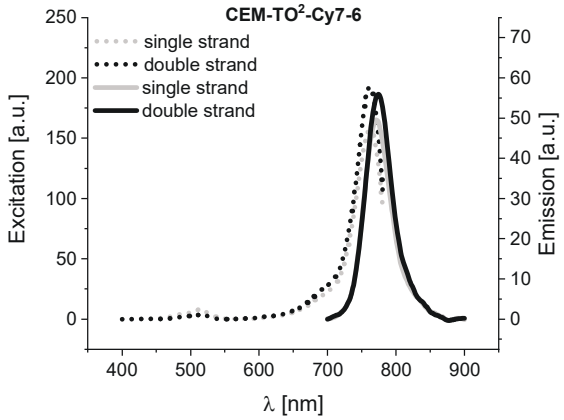
CEM-TO²-Cy7-6
single strand
double strand
single strand
double strand
Excitation [a.u.]
Emission [a.u.]
λ [nm]

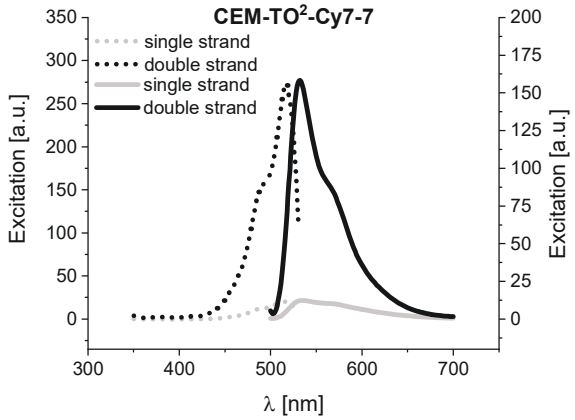
CEM-TO²-Cy7-7
single strand
double strand
single strand
double strand
Excitation [a.u.]
Excitation [a.u.]
λ [nm]

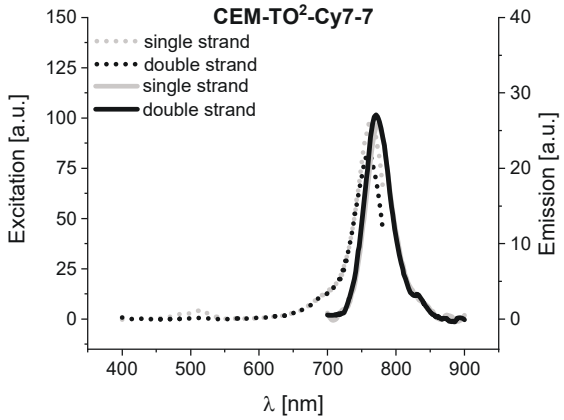
CEM-TO²-Cy7-7
single strand
double strand
single strand
double strand
Excitation [a.u.]
Emission [a.u.]
λ [nm]

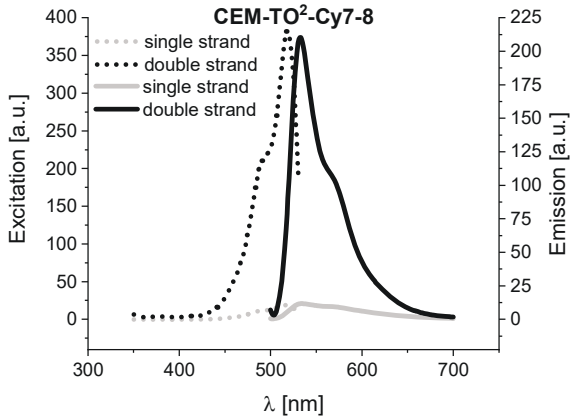
CEM-TO²-Cy7-8
single strand
double strand
single strand
double strand
Excitation [a.u.]
Emission [a.u.]
λ [nm]

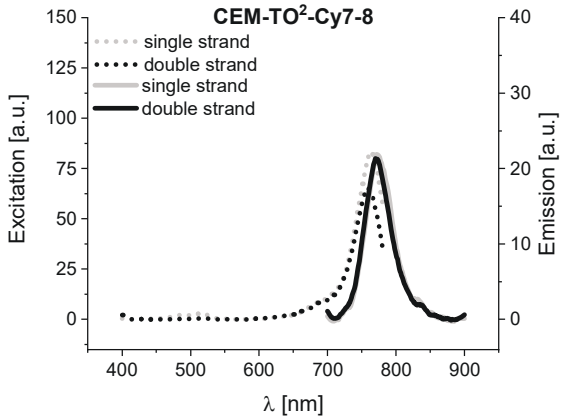
CEM-TO²-Cy7-8
single strand
double strand
single strand
double strand
Excitation [a.u.]
Emission [a.u.]
λ [nm]

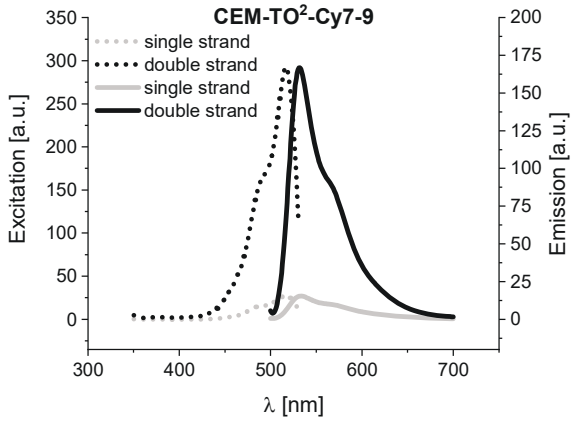
CEM-TO²-Cy7-9
single strand
double strand
single strand
double strand
Excitation [a.u.]
Emission [a.u.]
λ [nm]

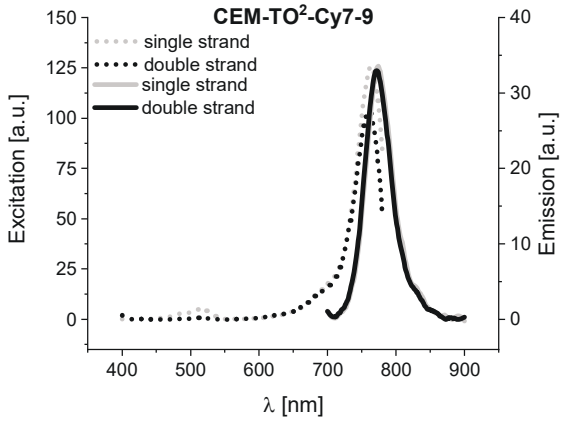
CEM-TO²-Cy7-9
single strand
double strand
single strand
double strand
Excitation [a.u.]
Emission [a.u.]
λ [nm]

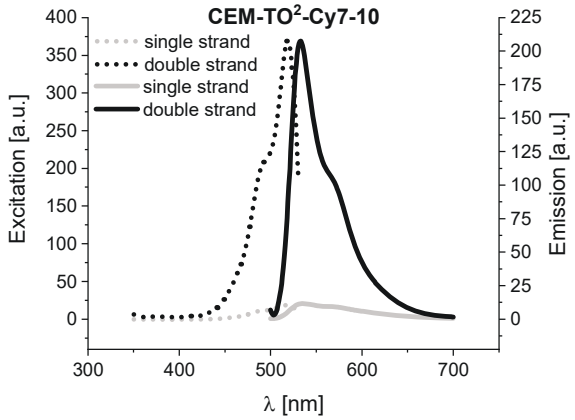
CEM-TO²-Cy7-10
single strand
double strand
single strand
double strand
Excitation [a.u.]
Emission [a.u.]
λ [nm]

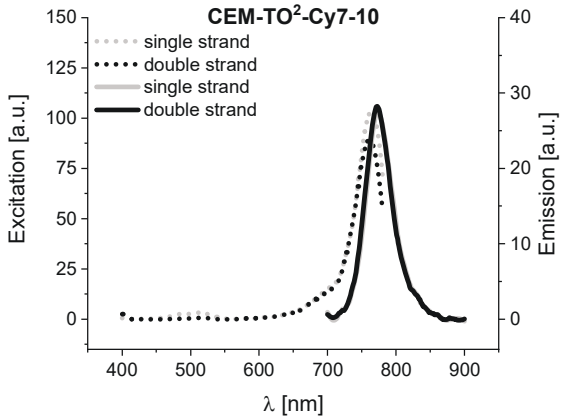
CEM-TO²-Cy7-10
single strand
double strand
single strand
double strand
Excitation [a.u.]
Emission [a.u.]
λ [nm]

8.4 Fluorescence Microscopy Images Generated by qFIT^2 Probes

The following images show a stack montage displaying the brightfield (BF), thiazole orange (TO) channel, dead cell staining with propidium bromide (PI) and Cyanine7 staining (Cy7). Of note, for presentation, image brightness and contrast have been increased. TO/Cy7 ratio analysis was performed on *native* images.

CCRF-CEM Cells Transfected with **CEM-TO^2-Cy7-3**

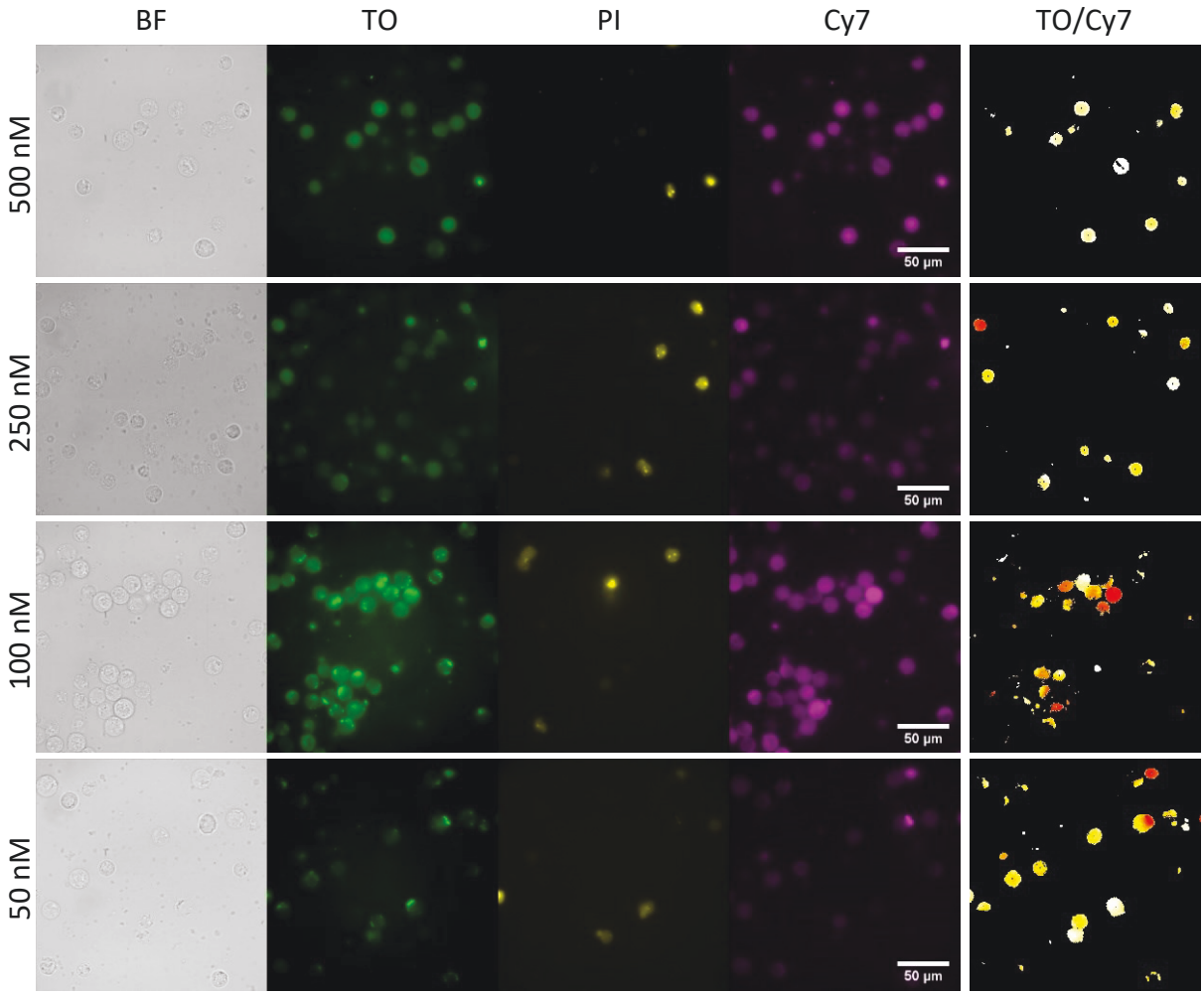

Figure 46: CCRF-CEM cells transfected with **CEM-TO^2-Cy7-3** (50, 100, 250 or 500 nM). Exemplary microscopy images recorded at 37 °C using an 60x oil immersion objective in an 0.4 µ-slide. The last column shows ratio heatmaps generated by dividing each pixel in the TO channel by the corresponding pixel in the Cy7 channel using *ImageJ*. Filters: TO: λ_{ex} = 500/24 nm; λ_{em} = 545/40 nm; QB/PI: λ_{ex} = 572/24 nm; λ_{em} = 628/40 nm; Cy7: λ_{ex} = 740/73 nm; λ_{em} = 810/90 nm.

CCRF-CEM Cells Transfected with **JK-TO^2-Cy7-3**

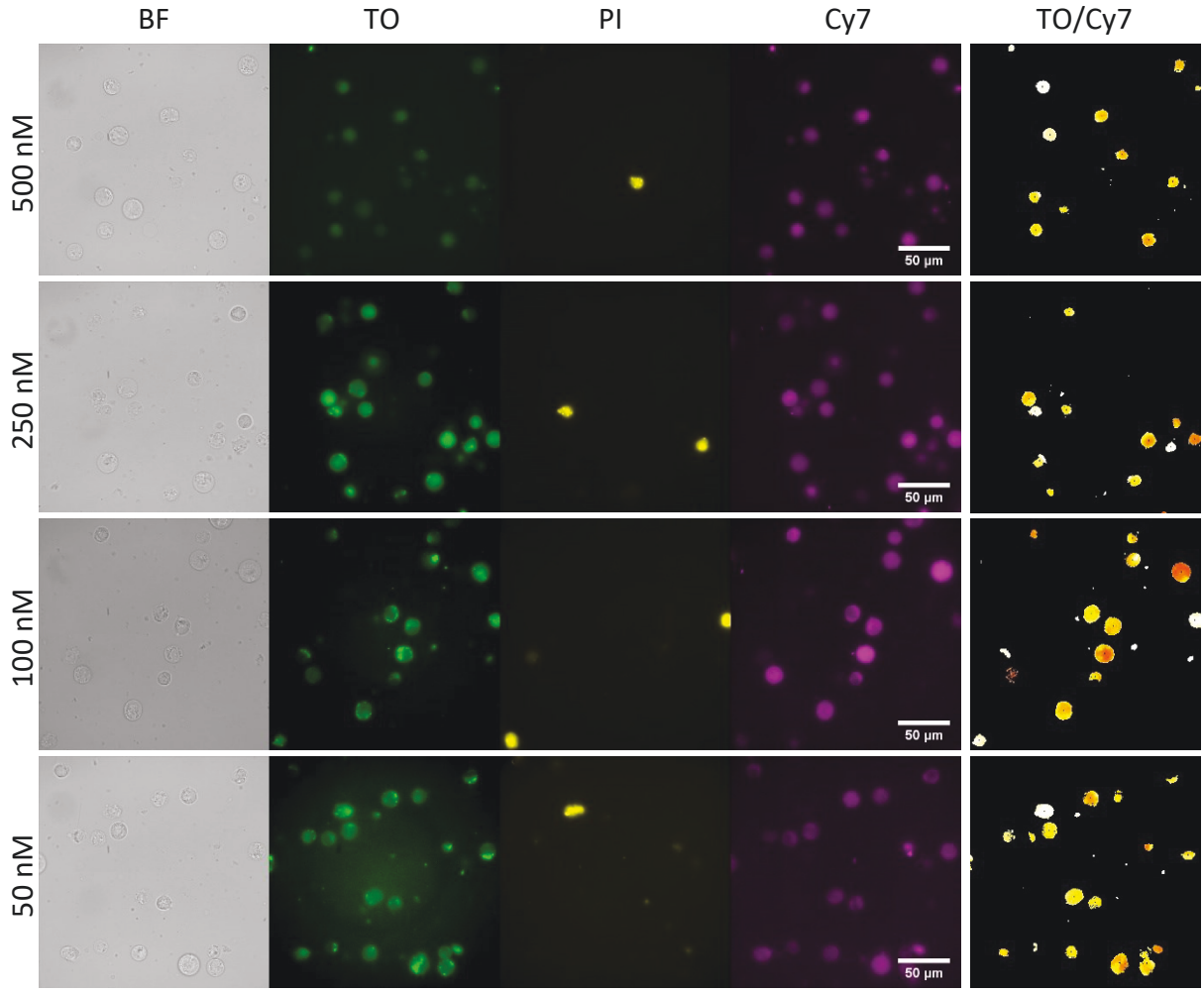

Figure 47: CCRF-CEM cells transfected with **JK-TO^2-Cy7-3** (50, 100, 250 or 500 nM). Exemplary microscopy images recorded at 37 °C using an 60x oil immersion objective in an 0.4 µ-slide. The last column shows ratio heatmaps generated by dividing each pixel in the TO channel by the corresponding pixel in the Cy7 channel using *ImageJ*. Filters: TO: λ_{ex} = 500/24 nm; λ_{em} = 545/40 nm; QB/PI: λ_{ex} = 572/24 nm; λ_{em} = 628/40 nm; Cy7: λ_{ex} = 740/73 nm; λ_{em} = 810/90 nm.

Jurkat cells transfected with **JK-TO^2-Cy7-3**

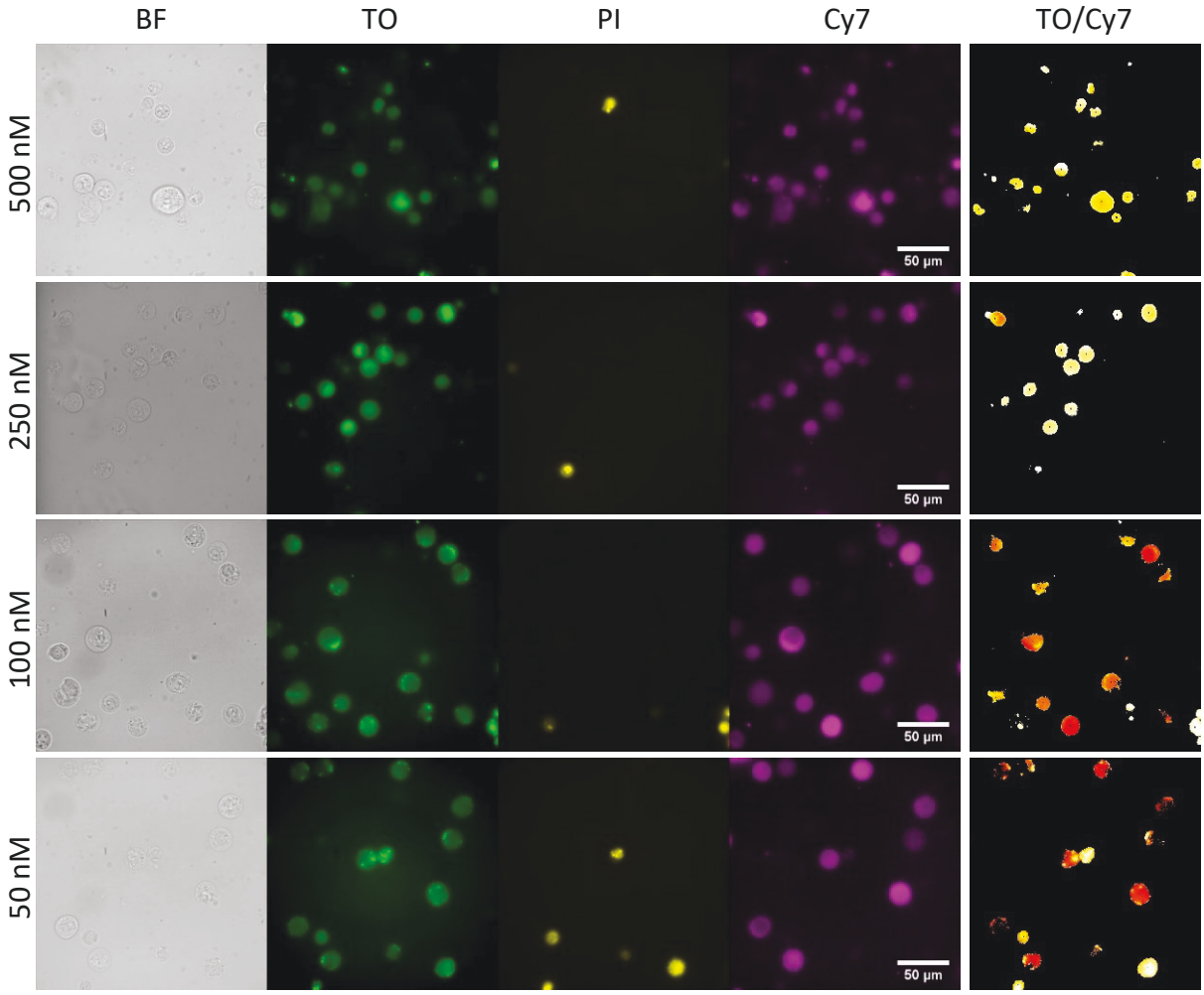

Figure 48: Jurkat cells transfected with **JK-TO^2-Cy7-3** (50, 100, 250 or 500 nM). Exemplary microscopy images recorded at 37 °C using an 60x oil immersion objective in an 0.4 µ-slide. The last column shows ratio heatmaps generated by dividing each pixel in the TO channel by the corresponding pixel in the Cy7 channel using *ImageJ*. Filters: TO: λ_{ex} = 500/24 nm; λ_{em} = 545/40 nm; QB/PI: λ_{ex} = 572/24 nm; λ_{em} = 628/40 nm; Cy7: λ_{ex} = 740/73 nm; λ_{em} = 810/90 nm.

Jurkat cells transfected with **CEM-TO^2-Cy7-3**

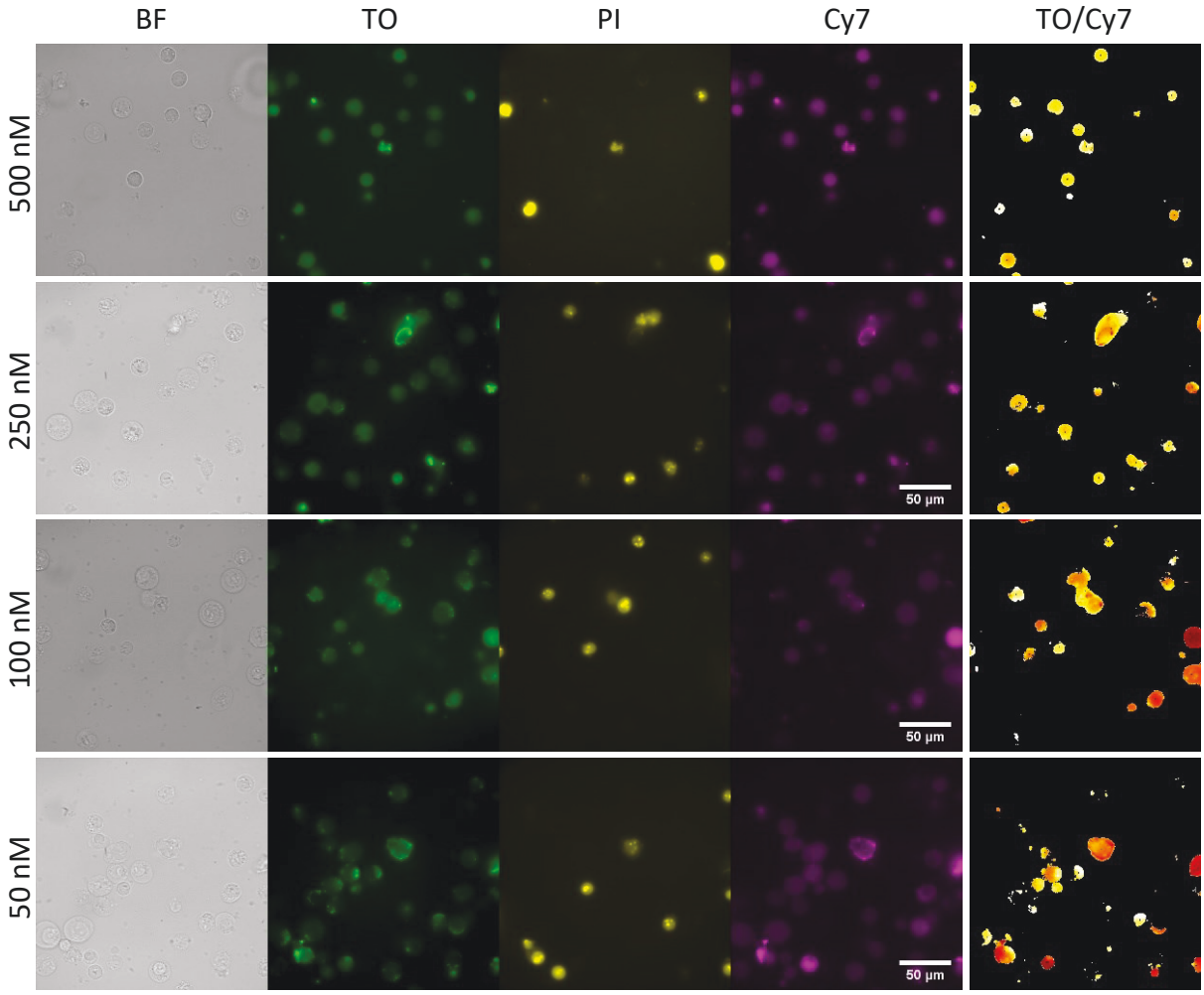

Figure 49: Jurkat cells transfected with **CEM-TO^2-Cy7-3** (50, 100, 250 or 500 nM). Exemplary microscopy images recorded at 37 °C using an 60x oil immersion objective in an 0.4 µ-slide. The last column shows ratio heatmaps generated by dividing each pixel in the TO channel by the corresponding pixel in the Cy7 channel using *ImageJ*. Filters: TO: λ_{ex} = 500/24 nm; λ_{em} = 545/40 nm; QB/PI: λ_{ex} = 572/24 nm; λ_{em} = 628/40 nm; Cy7: λ_{ex} = 740/73 nm; λ_{em} = 810/90 nm.

CCRF-CEM and Jurkat cells transfected with **CEM-TO^2-Cy7-3** at reduced voltage (325 V)

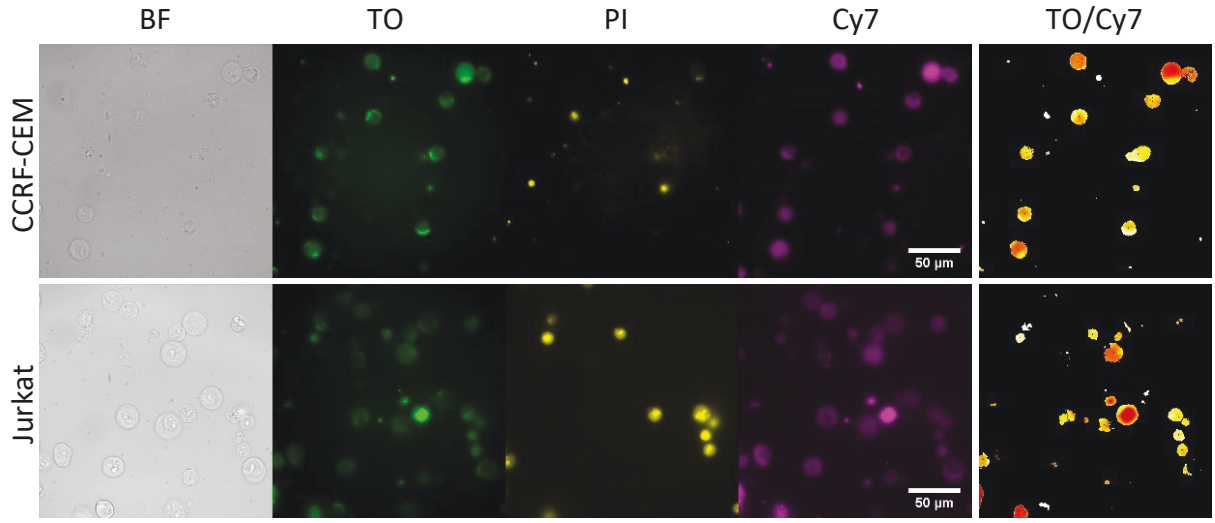

Figure 50: CCRF-CEM (top panel) and Jurkat (bottom panel) cells transfected with 100 nM **CEM-TO^2-Cy7-3** using a reduced voltage (325 V) electroporation protocol. Exemplary microscopy images recorded at 37 °C using an 60x oil immersion objective in an 0.4 µ-slide. The last column shows ratio heatmaps generated by dividing each pixel in the TO channel by the corresponding pixel in the Cy7 channel using *ImageJ*. Filters: TO: λ_{ex} = 500/24 nm; λ_{em} = 545/40 nm; QB/PI: λ_{ex} = 572/24 nm; λ_{em} = 628/40 nm; Cy7: λ_{ex} = 740/73 nm; λ_{em} = 810/90 nm.

CCRF-CEM and Jurkat cells transfected with **JK-TO^2-Cy7-3** at reduced voltage (325 V)

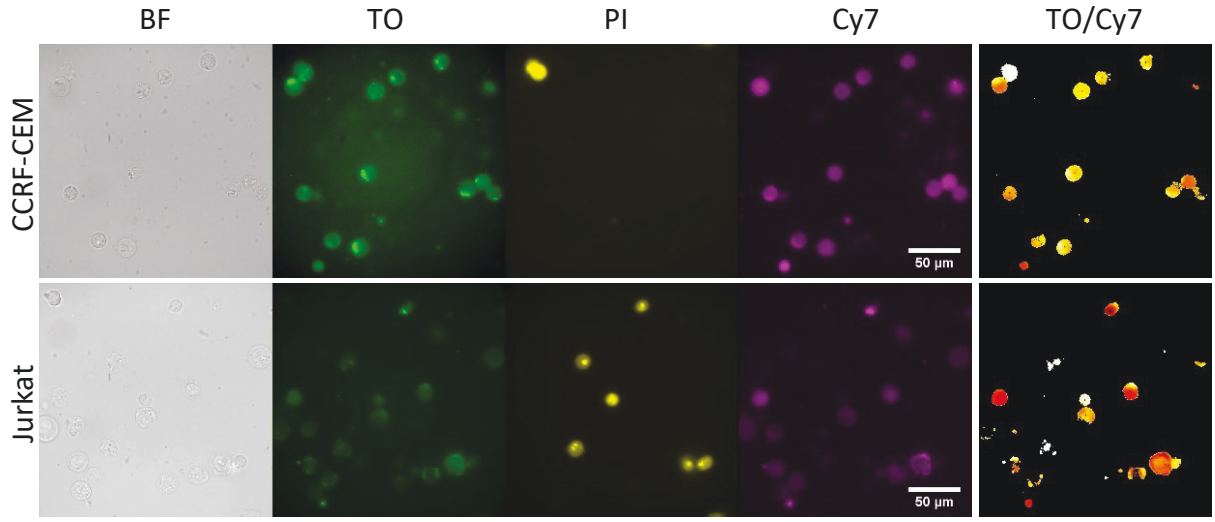

Figure 51: CCRF-CEM (top panel) and Jurkat (bottom panel) cells transfected with 100 nM JK-TO^2-Cy7-3 using a reduced voltage (325 V) electroporation protocol. Exemplary microscopy images recorded at 37 °C using an 60x oil immersion objective in an 0.4 µ-slide. The last column shows ratio heatmaps generated by dividing each pixel in the TO channel by the corresponding pixel in the Cy7 channel using *ImageJ*. Filters: TO: λ_{ex} = 500/24 nm; λ_{em} = 545/40 nm; QB/PI: λ_{ex} = 572/24 nm; λ_{em} = 628/40 nm; Cy7: λ_{ex} = 740/73 nm; λ_{em} = 810/90 nm.

8.5 Histograms

The graphs below show overlays of all individual cell histograms presented in the violin plots in **Chapter 5.2.3** after background subtraction and before mean determination. The X-axis represents different TO/Cy7 ratios, the Y-axis the number of pixels measured for each ratio. Note that mean calculation and statistical evaluation was performed on the individual data for each cell, not the combined histograms.

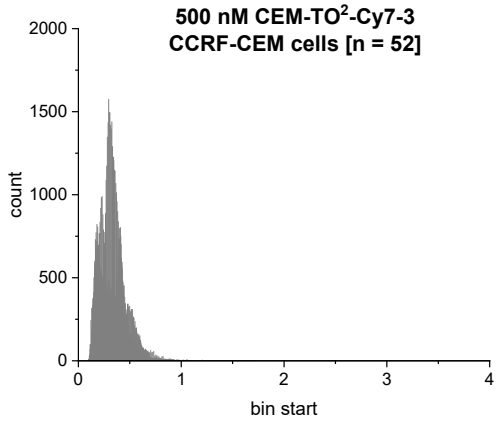

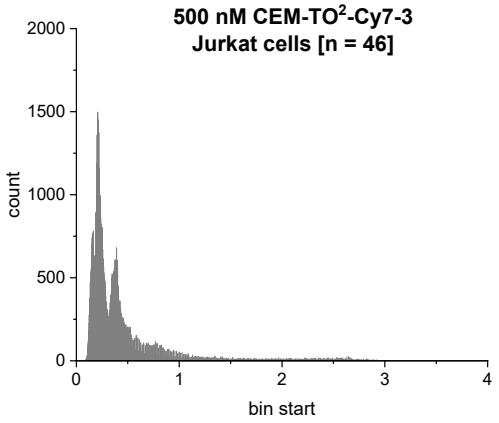

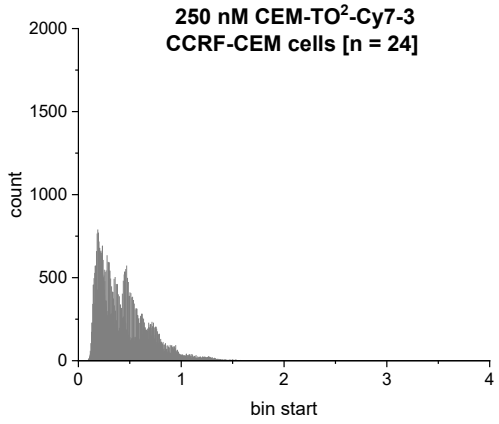

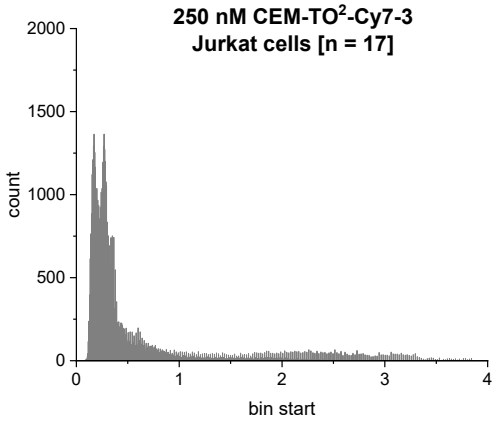

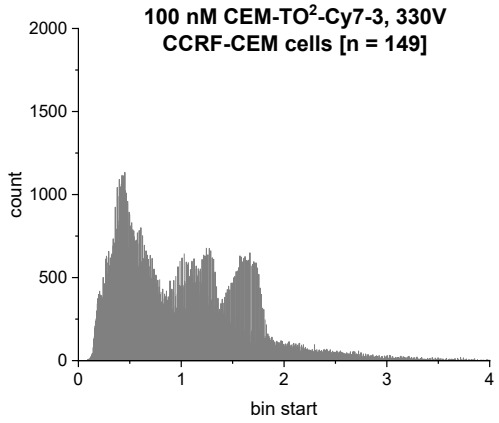

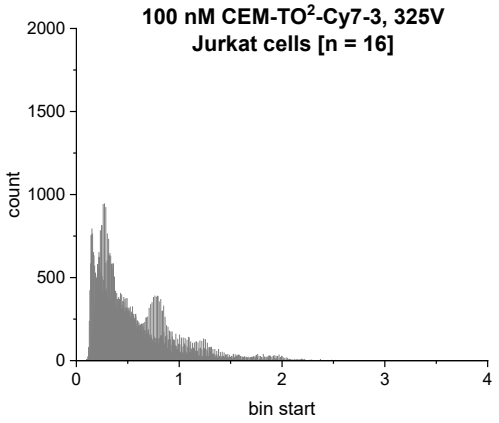

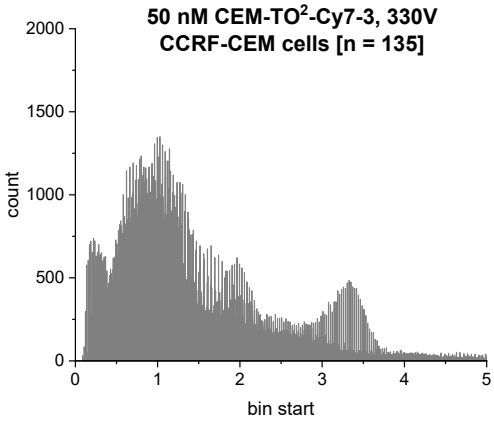
50 nM CEM-TO2-Cy7-3, 330V
CCRF-CEM cells [n = 135]
count
bin start

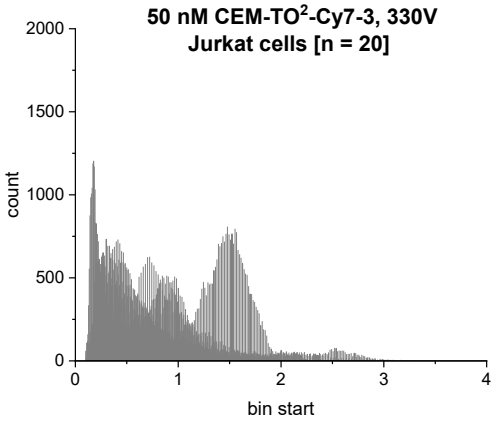
50 nM CEM-TO2-Cy7-3, 330V
Jurkat cells [n = 20]
count
bin start

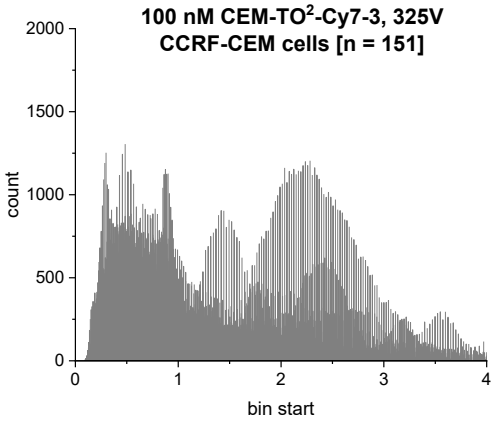
100 nM CEM-TO2-Cy7-3, 325V
CCRF-CEM cells [n = 151]
count
bin start

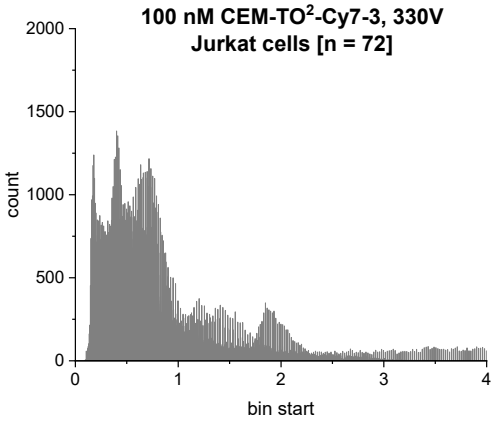
100 nM CEM-TO2-Cy7-3, 330V
Jurkat cells [n = 72]
count
bin start

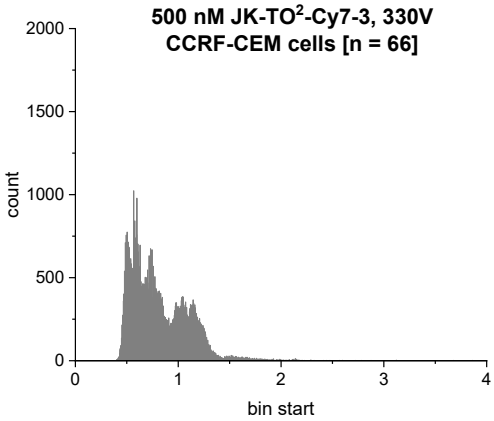
500 nM JK-TO2-Cy7-3, 330V
CCRF-CEM cells [n = 66]
count
bin start

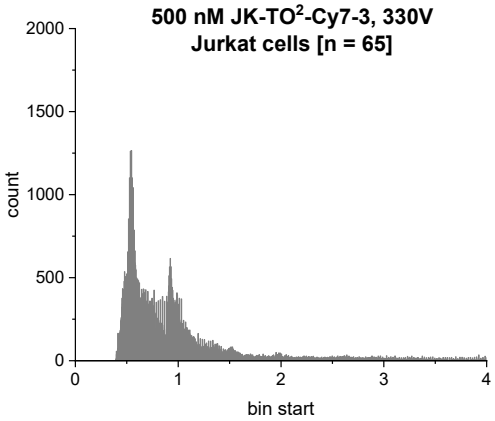
500 nM JK-TO2-Cy7-3, 330V
Jurkat cells [n = 65]
count
bin start

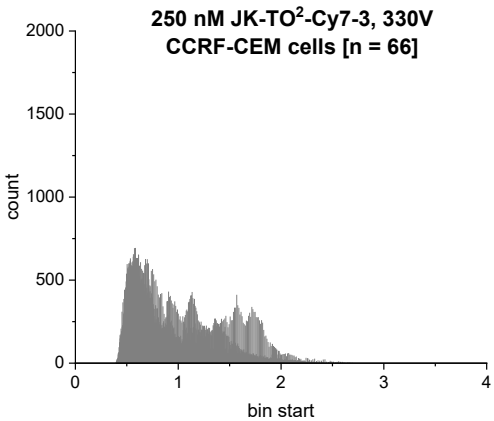
250 nM JK-TO2-Cy7-3, 330V
CCRF-CEM cells [n = 66]
count
bin start

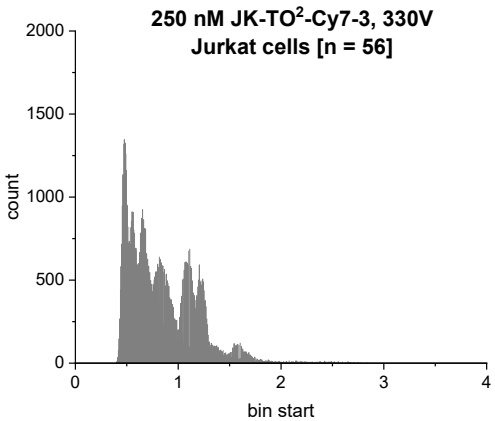
250 nM JK-TO2-Cy7-3, 330V
Jurkat cells [n = 56]
count
bin start

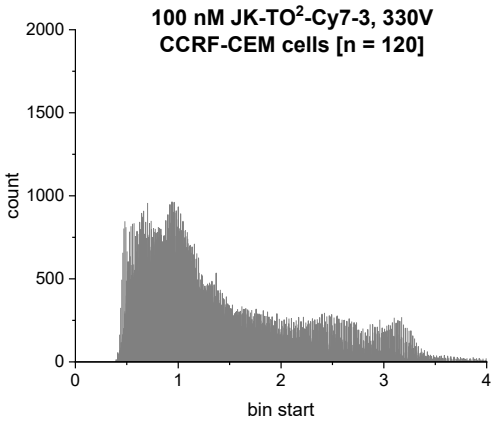
100 nM JK-TO2-Cy7-3, 330V
CCRF-CEM cells [n = 120]
count
bin start

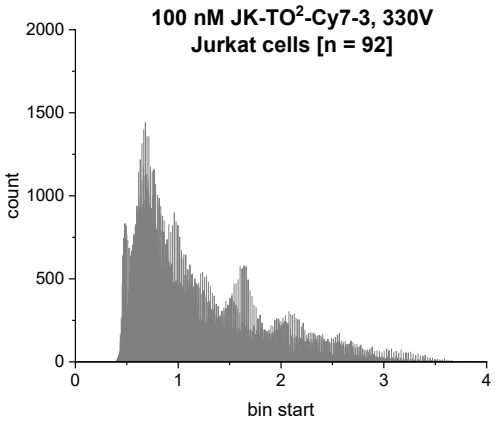
100 nM JK-TO2-Cy7-3, 330V
Jurkat cells [n = 92]
count
bin start

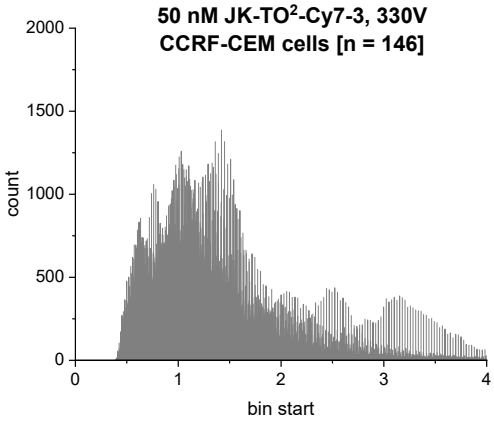
50 nM JK-TO2-Cy7-3, 330V
CCRF-CEM cells [n = 146]
count
bin start

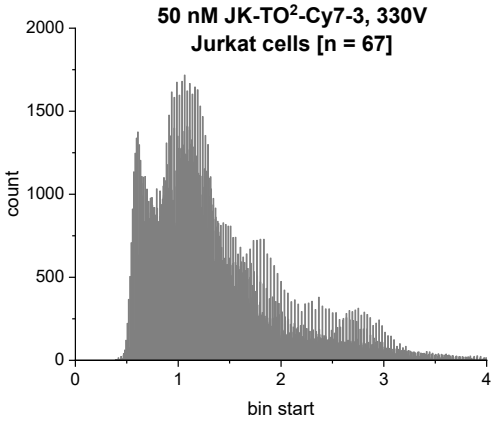
50 nM JK-TO2-Cy7-3, 330V
Jurkat cells [n = 67]
count
bin start

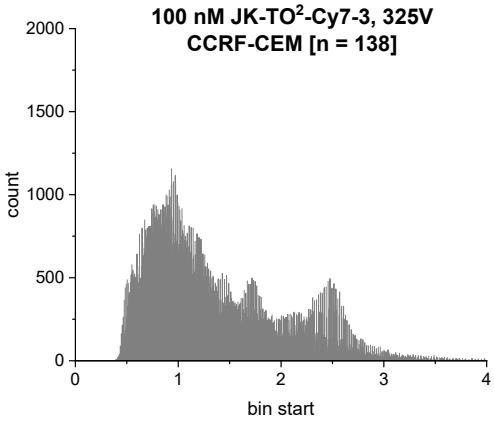
100 nM JK-TO2-Cy7-3, 325V
CCRF-CEM [n = 138]
count
bin start

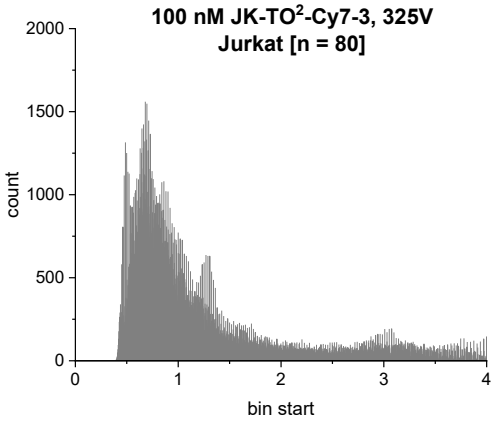
100 nM JK-TO2-Cy7-3, 325V
Jurkat [n = 80]
count
bin start

8.6 Abbreviations

2'-MOE	2'-*O*-methoxyethyl
2'-OMe	2'-*O*-methoxy
A	Adenosine
Ac	Acetyl
aeg	*N*-(2-Aminoethyl)glycine
AU	Arbitrary units
BiFC	Bimolecular fluorescence complementation
BO	Benzothiazole orange
BTT	5-Benzylthio-1*H*-tetrazole
C	Cytidine
CDR3	Complementarity determining region
CPG	Controlled pore glas
CPP	Cell-penetrating peptide
cpPNA	Cyclopentane PNA
CuAAC	Copper-catalysed azide-alkyne cycloaddition
Cy3	Cyanine 3
Cy5	Cyanine 5
Cy7	Cyanine 7
DFHBI	3.5-Difluoro-4-hydroxybenzylidene imidazolinone
DFHO	3.5-Difluoro-4-hydroxybenzylidene-imidazolinone-2-oxime
DMT	4.4'-Dimethoxytrityl
DNA	Deoxyribonucleic acid
ds	Double strand
dsRNA	Double stranded RNA
ECHO	Exciton-controlled hybridization-sensitive oligonucleotide
ED	Edited
eIF4A	Eukaryotic initiation factor 4A
em	Emission
ESI	Electrospray ionization
ETT	5-Ethylthio-1*H*-tetrazole
ex	Excitation
FACS	Fluorescence-activated cell sorting
FISH	Fluorescence *in situ* hybridization
FIT	Forced Intercalation
FRET	Förster resonance energy transfer
G	Guanosine
GFP	Green fluorescent protein
GlyR	Glycine receptor
h	Hours
HPLC	High performance liquid chromatography
IC	Internal conversion
IGF-1	Insulin-like growth factor
ISC	Intersystem crossing
LNA	Locked nucleic acid
lncRNA	Long non-coding RNA
m	Match
MALDI	Matrix-assisted laser desorption
MB	Molecular beacon
MCP	MS2 coat protein
min	Minutes
miRNA	Micro RNA
mm	Mismatch
MPPS	Microporous polystyrene
mRNA	Messenger RNA
MS	Mass spectometry
NADPH	Nicotinamide adenine dinucleotide phosphate
ncRNA	Non-coding RNA
NIR	Near-infrared

NMR	Nuclear magnetic resonance
ODN	Oligodeoxynucleotide
PAGE	Polyacrylamide gel electrophoresis
PBS	Phosphate buffered saline
PCP	PP7 bacteriophage coat protein
PCR	Polymerase chain reaction
PI	Propiodium iodide
PMA	Phorbol 12-myristate 13-acetate
PNA	Peptide nucleic acid
PS	Phosphorothiate
PyBOP	Benzotriazol-1-yloxytripyrrolidinophosphonium hexafluorophosphate
QB	Quinoline blue
qFIT	Quantitative FIT
QV	Quinoline violet
RBMB	Ratiometric bimolecular beacon
RBP	RNA-binding protein
RNA	Ribonucleic acid
RNAi	RNA interference
RP	Reversed phase
rRNA	Ribosomal RNA
s	Seconds
SELEX	Systematic evolution of ligands by exponential enrichment
siRNA	Small interfering RNA
smFISH	Single molecule FISH
SNA	Serinol nucleic acid
snoRNA	Small nucleolar RNA
snRNA	Small nuclear RNA
ss	Single strand
T	Thymidine
tbl	Tablet
TBAF	Tetrabutylammonium fluoride
TBDS	*tert*-Butyldimethylsilyl
TCR	T-cell receptor
TLE	Temporal lobe epilepsy
TO	Thiazole orange
TOF	Time of flight
TR	Thiazole red
tRNA	Transfer RNA
U	Uridine
UE	Unedited
UNA	Unlocked nucleic acid
UPLC	Ultrahigh performance liquid chromatography
UV	Ultraviolet
Vis	Visible
YO	Oxazole Yellow

9 References

1. J. Watson and F. Crick, *Nature*, 1953, **171**, 737.
2. R. T. Batey, R. P. Rambo and J. A. Doudna, *Angew. Chem. Int.*, 1999, **38**, 2326-2343.
3. X.-D. Fu, *Natl. Sci. Rev.*, 2014, **1**, 190-204.
4. T. R. Cech and J. A. Steitz, *Cell*, 2014, **157**, 77-94.
5. J. S. Mattick and I. V. Makunin, *Hum. Mol. Genet.*, 2006, **15**, R17-R29.
6. B. S. Zhao, I. A. Roundtree and C. He, *Nat. Rev. Mol. Cell Biol.*, 2017, **18**, 31-42.
7. H. Lodish, A. Berk, S. L. Zipursky, P. Matsudaira, D. Baltimore and J. Darnell, *Molecular Cell Biology*, W.H. Freeman and Company, New York, 4. Ed., 2000.
8. T. Pan, *Cell Res.*, 2018, **28**, 395-404.
9. T. Suzuki, *Nat. Rev. Mol. Cell Biol.*, 2021, **22**, 375-392.
10. M. C. Wahl, C. L. Will and R. Lührmann, *Cell*, 2009, **136**, 701-718.
11. M. M. Scotti and M. S. Swanson, *Nat. Rev. Genet.*, 2016, **17**, 19-32.
12. T. Samji, *Yale J. Biol. Med.*, 2009, **82**, 153.
13. J. Dubois, O. Terrier and M. Rosa-Calatrava, *mBio*, 2014, **5**, e00070-00014.
14. J. M. Gott and R. B. Emeson, *Annu. Rev. Genet.*, 2000, **34**, 499-531.
15. R. Benne, J. Van Den Burg, J. P. Brakenhoff, P. Sloof, J. H. Van Boom and M. C. Tromp, *Cell*, 1986, **46**, 819-826.
16. W. Tang, Y. Fei and M. Page, *Mol. Biotechnol.*, 2012, **52**, 91-100.
17. L. M. Powell, S. C. Wallis, R. J. Pease, Y. H. Edwards, T. J. Knott and J. Scott, *Cell*, 1987, **50**, 831-840.
18. T. Christofi and A. Zaravinos, *J. Transl. Med.*, 2019, **17**, 1-15.
19. S. Maas, Y. Kawahara, K. M. Tamburro and K. Nishikura, *RNA Biol.*, 2006, **3**, 1-9.
20. J. C. Meier, S. Kankowski, H. Krestel and F. Hetsch, *Front. Mol. Neurosci.*, 2016, **9**, 124.
21. J. C. Meier, M. Semtner, A. Winkelmann and J. Wolfart, *Front. Cell. Neurosci.*, 2014, **8**, 164.
22. T. R. Damase, R. Sukhovershin, C. Boada, F. Taraballi, R. I. Pettigrew and J. P. Cooke, *Front. Bioeng. Biotechnol.*, 2021, **9**.
23. E. Uhlmann and A. Peyman, *Chem. Rev.*, 1990, **90**, 543-584.
24. P. J. Paddison and G. J. Hannon, *Cancer Cell*, 2002, **2**, 17-23.
25. N. Pardi, M. J. Hogan, F. W. Porter and D. Weissman, *Nat. Rev. Drug Discov.*, 2018, **17**, 261-279.
26. J. Zhang, R. E. Campbell, A. Y. Ting and R. Y. Tsien, *Nat. Rev. Mol. Cell Biol.*, 2002, **3**, 906-918.
27. B. N. Giepmans, S. R. Adams, M. H. Ellisman and R. Y. Tsien, *Science*, 2006, **312**, 217-224.
28. J. R. Lakowicz, *Principles of Fluorescence Spectroscopy*, Springer, 2. Ed., 2013.
29. A. Jablonski, *Nature*, 1933, **131**, 839-840.
30. M. Kasha, *Discuss. Faraday Soc.*, 1950, **9**, 14-19.
31. D. F. Swinehart, *J. Chem. Educ.*, 1962, **39**, 333.
32. D. L. Dexter, *J. Chem. Phys.*, 1953, **21**, 836-850.
33. T. Förster, *Ann. Phys.*, 1948, **437**, 55-75.
34. A. Kaur, P. Kaur and S. Ahuja, *Anal. Methods*, 2020, **12**, 5532-5550.
35. L. Ma, F. Yang and J. Zheng, *J. Mol. Struct.*, 2014, **1077**, 87-100.
36. M. J. Lohse, S. Nuber and C. Hoffmann, *Pharmacol. Rev.*, 2012, **64**, 299-336.
37. K. Quan, C. Yi, X. Yang, X. He, J. Huang and K. Wang, *Trends Anal. Chem.*, 2020, **124**, 115784.
38. J. Birks, *Nature*, 1967, **214**, 1187-1190.
39. J. Birks, *Rep. Prog. Phys.*, 1975, **38**, 903.
40. J. Vollbrecht, *New J. Chem.*, 2018, **42**, 11249-11254.
41. M. Sauer, J. Hofkens and J. Enderlein, *Handbook of Fluorescence Spectroscopy and Imaging: From Ensemble to Single Molecules*, Wiley, 1. Ed., 2010.
42. A. Eisfeld and J. Briggs, *Chem. Phys.*, 2006, **324**, 376-384.
43. J. L. Bricks, Y. L. Slominskii, I. D. Panas and A. P. Demchenko, *Method. Appl. Fluoresc.*, 2017, **6**, 012001.

44. F. C. Spano and C. Silva, *Annu. Rev. Phys. Chem.*, 2014, **65**, 477-500.
45. N. C. Maiti, S. Mazumdar and N. Periasamy, *J. Phys. Chem. B*, 1998, **102**, 1528-1538.
46. H. H. Billsten, V. Sundström and T. Polívka, *J. Phys. Chem. A*, 2005, **109**, 1521-1529.
47. S. Sengupta and F. Würthner, *Acc. Chem. Res.*, 2013, **46**, 2498-2512.
48. H. Wang, T. E. Kaiser, S. Uemura and F. Würthner, *Chem. Commun.*, 2008, 1181-1183.
49. M. Kasha, H. Rawls and M. A. El-Bayoumi, *Pure Appl. Chem.*, 1965, **11**, 371-392.
50. M. Kasha, *Radiat. Res.*, 1963, **20**, 55-70.
51. A. S. Davydov, *Sov. Phys. Usp.*, 1964, **7**, 145.
52. E. E. Jelley, *Nature*, 1936, **138**, 1009-1010.
53. G. Sheibe, *Angew. Chem. Int.*, 1936, **49**, 563-564.
54. G. Scheibe and L. Kandler, *Naturwissenschaften*, 1938, **26**, 412-413.
55. P. Borst, *IUBMB Life*, 2005, **57**, 745-747.
56. R. Haugland, *Molecular Probes: Handbook of Fluorescent Probes and Research Chemicals*, Interchim, 1. Ed., 1994.
57. L. G. Lee, C. H. Chen and L. A. Chiu, *Cytometry, Part A*, 1986, **7**, 508-517.
58. L. G. Lee and C.-H. Chen, *US Pat.,* US4883867A, 1989.
59. J. T. Petty, J. A. Bordelon and M. E. Robertson, *J. Phys. Chem. B*, 2000, **104**, 7221-7227.
60. J. Nygren, N. Svanvik and M. Kubista, *Biopolymers*, 1998, **46**, 39-51.
61. J. P. Jacobsen, J. B. Pedersen, L. F. Hansen and D. E. Wemmer, *Nucleic Acids Res.*, 1995, **23**, 753-760.
62. L. F. Hansen, L. K. Jensen and J. P. Jacobsen, *Nucleic Acids Res.*, 1996, **24**, 859-867.
63. H. P. Spielmann, D. E. Wemmer and J. P. Jacobsen, *Biochemistry*, 1995, **34**, 8542-8553.
64. H. S. Rye, S. Yue, D. E. Wemmer, M. A. Quesada, R. P. Haugland, R. A. Mathies and A. N. Glazer, *Nucleic Acids Res.*, 1992, **20**, 2803-2812.
65. S. Olsen and R. H. McKenzie, *J. Chem. Phys.*, 2009, **131**, 234306.
66. A. Yartsev, J.-L. Alvarez, U. Åberg and V. Sundström, *Chem. Phys. Lett.*, 1995, **243**, 281-289.
67. A. Sanchez-Galvez, P. Hunt, M. A. Robb, M. Olivucci, T. Vreven and H. B. Schlegel, *J. Am. Chem. Soc.*, 2000, **122**, 2911-2924.
68. V. Karunakaran, J. L. Pérez Lustres, L. Zhao, N. P. Ernsting and O. Seitz, *J. Am. Chem. Soc.*, 2006, **128**, 2954-2962.
69. T. L. Netzel, K. Nafisi, M. Zhao, J. R. Lenhard and I. Johnson, *J. Phys. Chem.*, 1995, **99**, 17936-17947.
70. O. Suss, L. Motiei and D. Margulies, *Molecules*, 2021, **26**, 2828.
71. C. S. O'Neil, J. L. Beach and T. D. Gruber, *Electrophoresis*, 2018, **39**, 1474-1477.
72. H. S. Rye, J. M. Dabora, M. A. Quesada, R. A. Mathies and A. N. Glazer, *Anal. Biochem.*, 1993, **208**, 144-150.
73. F. Bartolomé and A. Y. Abramov, in *Mitochondrial Medicine*, SpringerEd., 2015, pp. 263-270.
74. R. B. Merrifield, *J. Am. Chem. Soc.*, 1963, **85**, 2149-2154.
75. P. T. Gilham and H. G. Khorana, *J. Am. Chem. Soc.*, 1958, **80**, 6212-6222.
76. H. Khorana, *Science*, 1979, **203**, 614-625.
77. R. L. Letsinger and K. K. Ogilvie, *J. Am. Chem. Soc.*, 1969, **91**, 3350-3355.
78. R. L. Letsinger and V. Mahadevan, *J. Am. Chem. Soc.*, 1966, **88**, 5319-5324.
79. R. Letsinger, *J. Am. Chem. Soc.*, 1965, **87**, 3526-3527.
80. M. H. Caruthers, *Proc. Natl. Acad. Sci. USA*, 2014, **111**, 18098-18099.
81. A. P. Guzaev, *Curr. Protoc. Nucleic Acid Chem.*, 2013, **53**, 3.1. 1-3.1. 60.
82. B. Sproat, F. Colonna, B. Mullah, D. Tsou, A. Andrus, A. Hampel and R. Vinayak, *Nucleosides Nucleotides Nucl. Acids*, 1995, **14**, 255-273.
83. R. Welz and S. Müller, *Tetrahedron Lett.*, 2002, **43**, 795-797.
84. M. Reddy, N. Hanna and F. Farooqui, *Tetrahedron Lett.*, 1994, **35**, 4311-4314.
85. S. Beaucage and M. Caruthers, *Tetrahedron Lett.*, 1981, **22**, 1859-1862.
86. M. H. Caruthers, *Science*, 1985, **230**, 281-285.
87. M. Caruthers, A. Barone, S. Beaucage, D. Dodds, E. Fisher, L. McBride, M. Matteucci, Z. Stabinsky and J.-Y. Tang, *Methods Enzymol.*, 1987, **154**, 287-313.

88. A. Michelson and A. R. Todd, *J. Chem. Soc.*, 1955, 2632-2638.
89. R. Hall, A. Todd and R. Webb, *J. Chem. Soc.*, 1957, 3291-3296.
90. C. B. Reese, *Tetrahedron*, 1978, **34**, 3143-3179.
91. A. T. Yeung and C. G. Miller, *Anal. Biochem.*, 1990, **187**, 66-75.
92. F. Guo, Q. Li and C. Zhou, *Org. Biomol. Chem.*, 2017, **15**, 9552-9565.
93. W. B. Wan and P. P. Seth, *J. Med. Chem.*, 2016, **59**, 9645-9667.
94. K. Duffy, S. Arangundy-Franklin and P. Holliger, *BMC Biol.*, 2020, **18**, 1-14.
95. L. K. McKenzie, R. El-Khoury, J. D. Thorpe, M. J. Damha and M. Hollenstein, *Chem. Soc. Rev.*, 2021, **50**, 5126-5164.
96. H. Inoue, Y. Hayase, A. Imura, S. Iwai, K. Miura and E. Ohtsuka, *Nucleic Acids Res.*, 1987, **15**, 6131-6148.
97. M. Majlessi, N. C. Nelson and M. M. Becker, *Nucleic Acids Res.*, 1998, **26**, 2224-2229.
98. B. P. Monia, E. Lesnik, C. Gonzalez, W. F. Lima, D. McGee, C. J. Guinosso, A. M. Kawasaki, P. D. Cook and S. M. Freier, *J. Biol. Chem.*, 1993, **268**, 14514-14522.
99. S. Obika, D. Nanbu, Y. Hari, K.-i. Morio, Y. In, T. Ishida and T. Imanishi, *Tetrahedron Lett.*, 1997, **38**, 8735-8738.
100. A. A. Koshkin, S. K. Singh, P. Nielsen, V. K. Rajwanshi, R. Kumar, M. Meldgaard, C. E. Olsen and J. Wengel, *Tetrahedron*, 1998, **54**, 3607-3630.
101. G. Wang, E. Gunic, J.-L. Girardet and V. Stoisavljevic, *Bioorg. Med. Chem. Lett.*, 1999, **9**, 1147-1150.
102. A. A. Koshkin, P. Nielsen, M. Meldgaard, V. K. Rajwanshi, S. K. Singh and J. Wengel, *J. Am. Chem. Soc.*, 1998, **120**, 13252-13253.
103. D. A. Braasch and D. R. Corey, *Chem. Biol.*, 2001, **8**, 1-7.
104. Y. You, B. G. Moreira, M. A. Behlke and R. Owczarzy, *Nucleic Acids Res.*, 2006, **34**, e60-e60.
105. N. Langkjær, A. Pasternak and J. Wengel, *Bioorg. Med. Chem.*, 2009, **17**, 5420-5425.
106. M. A. Campbell and J. Wengel, *Chem. Soc. Rev.*, 2011, **40**, 5680-5689.
107. F. Eckstein, *Annu. Rev. Biochem.*, 1985, **54**, 367-402.
108. A. P. Guzaev, *Tetrahedron Lett.*, 2011, **52**, 434-437.
109. R. P. Iyer, W. Egan, J. B. Regan and S. L. Beaucage, *J. Am. Chem. Soc.*, 1990, **112**, 1253-1254.
110. P. E. Nielsen, M. Egholm, R. H. Berg and O. Buchardt, *Science*, 1991, **254**, 1497-1500.
111. M. Egholm, O. Buchardt, P. E. Nielsen and R. H. Berg, *J. Am. Chem. Soc.*, 1992, **114**, 1895-1897.
112. V. V. Demidov, V. N. Potaman, M. Frank-Kamenetskil, M. Egholm, O. Buchard, S. H. Sönnichsen and P. E. Nlelsen, *Biochem. Pharmacol.*, 1994, **48**, 1310-1313.
113. P. E. Nielsen and G. Haaima, *Chem. Soc. Rev.*, 1997, **26**, 73-78.
114. B. Hyrup and P. E. Nielsen, *Bioorg. Med. Chem.*, 1996, **4**, 5-23.
115. J. J. Turner, G. D. Ivanova, B. Verbeure, D. Williams, A. A. Arzumanov, S. Abes, B. Lebleu and M. J. Gait, *Nucleic Acids Res.*, 2005, **33**, 6837-6849.
116. N. Bendifallah, F. W. Rasmussen, V. Zachar, P. Ebbesen, P. E. Nielsen and U. Koppelhus, *Bioconjugate Chem.*, 2006, **17**, 750-758.
117. P. E. Nielsen and T. Shiraishi, *Artif. DNA PNA XNA*, 2011, **2**, 90-99.
118. S. E. Hamilton, C. G. Simmons, I. S. Kathiriya and D. R. Corey, *Chem. Biol.*, 1999, **6**, 343-351.
119. P. Zhou, M. Wang, L. Du, G. W. Fisher, A. Waggoner and D. H. Ly, *J. Am. Chem. Soc.*, 2003, **125**, 6878-6879.
120. U. Koppelhus and P. E. Nielsen, *Adv. Drug Delivery Rev.*, 2003, **55**, 267-280.
121. H. Ikeda, F. Kitagawa and Y. Nakamura, *Tetrahedron*, 2007, **63**, 5677-5689.
122. L. Bethge, D. V. Jarikote and O. Seitz, *Bioorg. Med. Chem.*, 2008, **16**, 114-125.
123. T. Vilaivan, *Beilstein J. Org. Chem.*, 2018, **14**, 253-281.
124. K. S. Ramasamy and W. Seifert, *Bioorg. Med. Chem. Lett.*, 1996, **6**, 1799-1804.
125. B. T. Le, K. Murayama, F. Shabanpoor, H. Asanuma and R. N. Veedu, *RSC Adv.*, 2017, **7**, 34049-34052.
126. K. Murayama, Y. Kamiya, H. Kashida and H. Asanuma, *ChemBioChem*, 2015, **16**, 1298-1301.
127. C. A. Harrington, C. Rosenow and J. Retief, *Curr. Opin. Microbiol.*, 2000, **3**, 285-291.

128. S. Deepak, K. Kottapalli, R. Rakwal, G. Oros, K. Rangappa, H. Iwahashi, Y. Masuo and G. Agrawal, *Curr. Genomics*, 2007, **8**, 234-251.
129. D. Samanta, S. B. Ebrahimi and C. A. Mirkin, *Adv. Mater.*, 2020, **32**, 1901743.
130. S. C. Kim, I. C. Clark, P. Shahi and A. R. Abate, *Anal. Chem.*, 2018, **90**, 1273-1279.
131. M. Toledo-Rodriguez and H. Markram, in *Patch-Clamp Methods and Protocols*, SpringerEd., 2007, pp. 123-139.
132. Y. Ben-Ari, Y. Brody, N. Kinor, A. Mor, T. Tsukamoto, D. L. Spector, R. H. Singer and Y. Shav-Tal, *J. Cell Sci.*, 2010, **123**, 1761-1774.
133. G. Bao, W. J. Rhee and A. Tsourkas, *Annu. Rev. Biomed. Eng.*, 2009, **11**, 25-47.
134. Y. Xia, R. Zhang, Z. Wang, J. Tian and X. Chen, *Chem. Soc. Rev.*, 2017, **46**, 2824-2843.
135. K. Czaplinski, in *Neuroepigenomics in Aging and Disease*, SpringerEd., 2017, pp. 425-441.
136. A. M. Sydor, K. J. Czymmek, E. M. Puchner and V. Mennella, *Trends Cell Biol.*, 2015, **25**, 730-748.
137. M. O. Urbanek, P. Galka-Marciniak, M. Olejniczak and W. J. Krzyzosiak, *RNA Biol.*, 2014, **11**, 1083-1095.
138. E. Bertrand, P. Chartrand, M. Schaefer, S. M. Shenoy, R. H. Singer and R. M. Long, *Mol. Cell*, 1998, **2**, 437-445.
139. A. Bernardi and P.-F. Spahr, *Proc. Natl. Acad. Sci. USA*, 1972, **69**, 3033-3037.
140. H. E. Johansson, L. Liljas and O. C. Uhlenbeck, *Semin. Virol.*, 1997, **8**, 176-185.
141. P. G. Stockley, N. J. Stonehouse, J. B. Murry, S. T. Goodman, S. J. Talbot, C. J. Adams, L. Lilijas and K. Valegå, *Nucleic Acids Res.*, 1995, **23**, 2512-2518.
142. C.-D. Hu and T. K. Kerppola, *Nat. Biotechnol.*, 2003, **21**, 539-545.
143. D. R. Larson, D. Zenklusen, B. Wu, J. A. Chao and R. H. Singer, *Science*, 2011, **332**, 475-478.
144. M. Valencia-Burton, R. M. McCullough, C. R. Cantor and N. E. Broude, *Nat. Methods*, 2007, **4**, 421-427.
145. Y. Kodama and C.-D. Hu, *Biotechniques*, 2012, **53**, 285-298.
146. J. Ouellet, *Front. Chem.*, 2016, **4**, 29.
147. F. Bouhedda, A. Autour and M. Ryckelynck, *Int. J. Mol. Sci.*, 2018, **19**, 44.
148. P. Swetha, Z. Fan, F. Wang and J.-H. Jiang, *Journal of Materials Chemistry B*, 2020, **8**, 3382-3392.
149. J. S. Paige, K. Y. Wu and S. R. Jaffrey, *Science*, 2011, **333**, 642-646.
150. A. D. Ellington and J. W. Szostak, *Nature*, 1990, **346**, 818-822.
151. K. D. Warner, M. C. Chen, W. Song, R. L. Strack, A. Thorn, S. R. Jaffrey and A. R. Ferre-D'Amare, *Nat. Struct. Mol. Biol.*, 2014, **21**, 658-663.
152. M. Ormö, A. B. Cubitt, K. Kallio, L. A. Gross, R. Y. Tsien and S. J. Remington, *Science*, 1996, **273**, 1392-1395.
153. G. S. Filonov, J. D. Moon, N. Svensen and S. R. Jaffrey, *J. Am. Chem. Soc.*, 2014, **136**, 16299-16308.
154. E. V. Dolgosheina, S. C. Jeng, S. S. S. Panchapakesan, R. Cojocaru, P. S. Chen, P. D. Wilson, N. Hawkins, P. A. Wiggins and P. J. Unrau, *ACS Chem. Biol.*, 2014, **9**, 2412-2420.
155. W. Song, G. S. Filonov, H. Kim, M. Hirsch, X. Li, J. D. Moon and S. R. Jaffrey, *Nat. Chem. Biol.*, 2017, **13**, 1187-1194.
156. J. Zhang, L. Wang, A. Jäschke and M. Sunbul, *Angew. Chem.*, 2021, **133**, 21611-21618.
157. L.-Z. Yang, Y. Wang, S.-Q. Li, R.-W. Yao, P.-F. Luan, H. Wu, G. G. Carmichael and L.-L. Chen, *Mol. Cell*, 2019, **76**, 981-997. e987.
158. D. A. Nelles, M. Y. Fang, M. R. O'Connell, J. L. Xu, S. J. Markmiller, J. A. Doudna and G. W. Yeo, *Cell*, 2016, **165**, 488-496.
159. S. Tyagi, *Nat. Methods*, 2009, **6**, 331-338.
160. G. T. Rudkin and B. Stollar, *Nature*, 1977, **265**, 472-473.
161. J. G. Gall and M. L. Pardue, *Proc. Natl. Acad. Sci. USA*, 1969, **63**, 378-383.
162. A. P. Young, D. J. Jackson and R. C. Wyeth, *PeerJ*, 2020, **8**, e8806.
163. A. M. Femino, F. S. Fay, K. Fogarty and R. H. Singer, *Science*, 1998, **280**, 585-590.

164. T. Trcek, J. A. Chao, D. R. Larson, H. Y. Park, D. Zenklusen, S. M. Shenoy and R. H. Singer, *Nat. Protoc.*, 2012, **7**, 408-419.
165. A. N. Player, L.-P. Shen, D. Kenny, V. P. Antao and J. A. Kolberg, *J. Histochem. Cytochem.*, 2001, **49**, 603-611.
166. N. Battich, T. Stoeger and L. Pelkmans, *Cell*, 2015, **163**, 1596-1610.
167. J. M. Levsky, S. M. Shenoy, R. C. Pezo and R. H. Singer, *Science*, 2002, **297**, 836-840.
168. A. Raj, C. S. Peskin, D. Tranchina, D. Y. Vargas and S. Tyagi, *PLoS Biol.*, 2006, **4**, e309.
169. A. Raj, P. van den Bogaard, S. A. Rifkin, A. van Oudenaarden and S. Tyagi, *Nat. Methods*, 2008, **5**, 877-879.
170. Y. Taniguchi, P. J. Choi, G.-W. Li, H. Chen, M. Babu, J. Hearn, A. Emili and X. S. Xie, *Science*, 2010, **329**, 533-538.
171. A. Lyubimova, S. Itzkovitz, J. P. Junker, Z. P. Fan, X. Wu and A. Van Oudenaarden, *Nat. Protoc.*, 2013, **8**, 1743-1758.
172. K. H. Chen, A. N. Boettiger, J. R. Moffitt, S. Wang and X. Zhuang, *Science*, 2015, **348**.
173. A. Orjalo, H. E. Johansson and J. L. Ruth, *Nat. Methods*, 2011, **8**, i-ii.
174. F. Wang, J. Flanagan, N. Su, L.-C. Wang, S. Bui, A. Nielson, X. Wu, H.-T. Vo, X.-J. Ma and Y. Luo, *J. Mol. Diagn.*, 2012, **14**, 22-29.
175. K. E. Brown, S. S. Guest, S. T. Smale, K. Hahm, M. Merkenschlager and A. G. Fisher, *Cell*, 1997, **91**, 845-854.
176. C. Duval, M. de Tayrac, F. Sanschagrin, K. Michaud, P. V. Gould and S. Saikali, *PLoS One*, 2014, **9**, e100342.
177. A. Sepsi, A. Fábián, K. Jäger, J. Heslop-Harrison and T. Schwarzacher, *Front. Plant Sci.*, 2018, **9**, 1193.
178. H. M. Choi, J. Y. Chang, L. A. Trinh, J. E. Padilla, S. E. Fraser and N. A. Pierce, *Nat. Biotechnol.*, 2010, **28**, 1208-1212.
179. R. Deng, L. Tang, Q. Tian, Y. Wang, L. Lin and J. Li, *Angew. Chem. Int.*, 2014, **126**, 2421-2425.
180. J. Ge, L.-L. Zhang, S.-J. Liu, R.-Q. Yu and X. Chu, *Anal. Chem.*, 2014, **86**, 1808-1815.
181. A. N. Silahtaroglu, D. Nolting, L. Dyrskjøt, E. Berezikov, M. Møller, N. Tommerup and S. Kauppinen, *Nat. Protoc.*, 2007, **2**, 2520-2528.
182. J. Lu and A. Tsourkas, *Nucleic Acids Res.*, 2009, **37**, e100-e100.
183. C. Molenaar, S. Marras, J. Slats, J.-C. Truffert, M. Lemaitre, A. Raap, R. Dirks and H. Tanke, *Nucleic Acids Res.*, 2001, **29**, e89-e89.
184. S. Paillasson, M. Van De Corput, R. Dirks, H. Tanke, M. Robert-Nicoud and X. Ronot, *Exp. Cell Res.*, 1997, **231**, 226-233.
185. V. V. Didenko, *Biotechniques*, 2001, **31**, 1106-1121.
186. Y. Okamura, S. Kondo, I. Sase, T. Suga, K. Mise, I. Furusawa, S. Kawakami and Y. Watanabe, *Nucleic Acids Res.*, 2000, **28**, e107-e107.
187. A. Tsuji, H. Koshimoto, Y. Sato, M. Hirano, Y. Sei-Iida, S. Kondo and K. Ishibashi, *Biophys. J.*, 2000, **78**, 3260-3274.
188. S. Sixou, F. Szoka Jr, G. Green, B. Giusti, G. Zon and D. Chin, *Nucleic Acids Res.*, 1994, **22**, 662-668.
189. S. Tyagi and F. R. Kramer, *Nat. Biotechnol.*, 1996, **14**, 303-308.
190. Y. Li, X. Zhou and D. Ye, *Biochem. Biophys. Res. Commun.*, 2008, **373**, 457-461.
191. C. J. Yang, H. Lin and W. Tan, *J. Am. Chem. Soc.*, 2005, **127**, 12772-12773.
192. S. Tyagi, D. P. Bratu and F. R. Kramer, *Nat. Biotechnol.*, 1998, **16**, 49-53.
193. R. Manganelli, S. Tyagi and I. Smith, in *Mycobacterium tuberculosis Protocols*, SpringerEd., 2001, pp. 295-310.
194. S. Mao, Y. Ying, R. Wu and A. K. Chen, *iScience*, 2020, 101801.
195. Z.-Q. Cui, Z.-P. Zhang, X.-E. Zhang, J.-K. Wen, Y.-F. Zhou and W.-H. Xie, *Nucleic Acids Res.*, 2005, **33**, 3245-3252.
196. X.-H. Peng, Z.-H. Cao, J.-T. Xia, G. W. Carlson, M. M. Lewis, W. C. Wood and L. Yang, *Cancer Res.*, 2005, **65**, 1909-1917.

197. W. Wang, Z.-Q. Cui, H. Han, Z.-P. Zhang, H.-P. Wei, Y.-F. Zhou, Z. Chen and X.-E. Zhang, *Nucleic Acids Res.*, 2008, **36**, 4913-4928.
198. W. Chen, G. Martinez and A. Mulchandani, *Anal. Biochem.*, 2000, **280**, 166-172.
199. M. M. Mhlanga and L. Malmberg, *Methods*, 2001, **25**, 463-471.
200. W. Tan, K. Wang and T. J. Drake, *Curr. Opin. Chem. Biol.*, 2004, **8**, 547-553.
201. G. Goel, A. Kumar, A. Puniya, W. Chen and K. Singh, *J. Appl. Microbiol.*, 2005, **99**, 435-442.
202. J. H. Kim, D. Morikis and M. Ozkan, *Sensors Actuators B: Chem.*, 2004, **102**, 315-319.
203. D. Y. Ryazantsev, M. V. Kvach, D. A. Tsybulsky, I. A. Prokhorenko, I. A. Stepanova, Y. V. Martynenko, S. V. Gontarev, V. V. Shmanai, S. K. Zavriev and V. A. Korshun, *Analyst*, 2014, **139**, 2867-2872.
204. J. F. Lovell, J. Chen, E. Huynh, M. T. Jarvi, B. C. Wilson and G. Zheng, *Bioconjugate Chem.*, 2010, **21**, 1023-1025.
205. A. K. Chen, M. A. Behlke and A. Tsourkas, *Nucleic Acids Res.*, 2007, **35**, e105.
206. A. Tsourkas, M. A. Behlke and G. Bao, *Nucleic Acids Res.*, 2002, **30**, 5168-5174.
207. A. K. Chen, M. A. Behlke and A. Tsourkas, *Nucleic Acids Res.*, 2009, **37**, e149-e149.
208. D. Zhao, Y. Yang, N. Qu, M. Chen, Z. Ma, C. J. Krueger, M. A. Behlke and A. K. Chen, *Biomaterials*, 2016, **100**, 172-183.
209. L. Wang, C. J. Yang, C. D. Medley, S. A. Benner and W. Tan, *J. Am. Chem. Soc.*, 2005, **127**, 15664-15665.
210. Y. Wu, C. J. Yang, L. L. Moroz and W. Tan, *Anal. Chem.*, 2008, **80**, 3025-3028.
211. I. E. Catrina, S. A. Marras and D. P. Bratu, *ACS Chem. Biol.*, 2012, **7**, 1586-1595.
212. H. Kuhn, V. V. Demidov, J. M. Coull, M. J. Fiandaca, B. D. Gildea and M. D. Frank-Kamenetskii, *J. Am. Chem. Soc.*, 2002, **124**, 1097-1103.
213. A. A. Martí, S. Jockusch, Z. Li, J. Ju and N. J. Turro, *Nucleic Acids Res.*, 2006, **34**, e50-e50.
214. H. Kashida, T. Osawa, K. Morimoto, Y. Kamiya and H. Asanuma, *Bioorg. Med. Chem.*, 2015, **23**, 1758-1762.
215. H. Kashida, T. Takatsu, T. Fujii, K. Sekiguchi, X. Liang, K. Niwa, T. Takase, Y. Yoshida and H. Asanuma, *Angew. Chem. Int.*, 2009, **121**, 7178-7181.
216. D. M. Kolpashchikov, *J. Am. Chem. Soc.*, 2006, **128**, 10625-10628.
217. P. J. Santangelo, B. Nix, A. Tsourkas and G. Bao, *Nucleic Acids Res.*, 2004, **32**, e57-e57.
218. S. Tyagi, S. A. Marras and F. R. Kramer, *Nat. Biotechnol.*, 2000, **18**, 1191-1196.
219. C. Wang, Z. Zhu, Y. Song, H. Lin, C. J. Yang and W. Tan, *Chem. Commun.*, 2011, **47**, 5708-5710.
220. S. F. Bakshi, N. Guz, A. Zakharchenko, H. Deng, A. V. Tumanov, C. D. Woodworth, S. Minko, D. M. Kolpashchikov and E. Katz, *J. Am. Chem. Soc.*, 2017, **139**, 12117-12120.
221. S. F. Bakshi, N. Guz, A. Zakharchenko, H. Deng, A. V. Tumanov, C. D. Woodworth, S. Minko, D. M. Kolpashchikov and E. Katz, *Nanoscale*, 2018, **10**, 1356-1365.
222. S. Tyagi and O. Alsmadi, *Biophys. J.*, 2004, **87**, 4153-4162.
223. M. M. Mhlanga, D. Y. Vargas, C. W. Fung, F. R. Kramer and S. Tyagi, *Nucleic Acids Res.*, 2005, **33**, 1902-1912.
224. A. K. Chen, O. Davydenko, M. A. Behlke and A. Tsourkas, *Nucleic Acids Res.*, 2010, **38**, e148-e148.
225. A. K. Chen, M. A. Behlke and A. Tsourkas, *Nucleic Acids Res.*, 2008, **36**, e69-e69.
226. X. Huang, J. Song, B. C. Yung, X. Huang, Y. Xiong and X. Chen, *Chem. Soc. Rev.*, 2018, **47**, 2873-2920.
227. X. Zhang, A. L. Zajac, L. Huang, M. A. Behlke and A. Tsourkas, *PLoS One*, 2014, **9**, e85813.
228. N. Svanvik, G. Westman, D. Wang and M. Kubista, *Anal. Biochem.*, 2000, **281**, 26-35.
229. J. Isacsson, H. Cao, L. Ohlsson, S. Nordgren, N. Svanvik, G. Westman, M. Kubista, R. Sjöback and U. Sehlstedt, *Mol. Cell. Probes*, 2000, **14**, 321-328.
230. K. L. Robertson, L. Yu, B. A. Armitage, A. J. Lopez and L. A. Peteanu, *Biochemistry*, 2006, **45**, 6066-6074.
231. M. Tanaka, N. Shigi, J. Sumaoka and M. Komiyama, *RSC Adv.*, 2014, **4**, 63533-63538.
232. R. Lartia and U. Asseline, *Chem. Eur. J.*, 2006, **12**, 2270-2281.
233. N. Svanvik, J. Nygren, G. Westman and M. Kubista, *J. Am. Chem. Soc.*, 2001, **123**, 803-809.

234. E. J. Fechter, B. Olenyuk and P. B. Dervan, *J. Am. Chem. Soc.*, 2005, **127**, 16685-16691.
235. C. Holzhauser and H.-A. Wagenknecht, *J. Org. Chem.*, 2013, **78**, 7373-7379.
236. C. Holzhauser, S. Berndl, F. Menacher, M. Breunig, A. Göpferich and H. A. Wagenknecht, *European Journal of Organic Chemistry*, 2010, 1239-1248.
237. C. Holzhauser, PhD thesis Thesis, Karlsruher Institut für Technology (KIT), 2012.
238. C. Holzhauser and H. A. Wagenknecht, *Angew. Chem. Int.*, 2011, **50**, 7268-7272.
239. C. Holzhauser, R. Liebl, A. Goepferich, H.-A. Wagenknecht and M. Breunig, *ACS Chem. Biol.*, 2013, **8**, 890-894.
240. F. Menacher, M. Rubner, S. Berndl and H.-A. Wagenknecht, *J. Org. Chem.*, 2008, **73**, 4263-4266.
241. S. Berndl and H. A. Wagenknecht, *Angew. Chem. Int.*, 2009, **48**, 2418-2421.
242. C. Holzhauser, M. M. Rubner and H.-A. Wagenknecht, *Photochem. Photobiol. Sci.*, 2013, **12**, 722-724.
243. H.-K. Walter, B. Olshausen, U. Schepers and H.-A. Wagenknecht, *Beilstein J. Org. Chem.*, 2017, **13**, 127-137.
244. C. Holzhauser and H. A. Wagenknecht, *ChemBioChem*, 2012, **13**, 1136-1138.
245. J. Steinmeyer, H.-K. Walter, M. A. Bichelberger, V. Schneider, T. Kubař, F. Rönicke, B. Olshausen, K. Nienhaus, G. U. Nienhaus and U. Schepers, *Org. Biomol. Chem.*, 2018, **16**, 3726-3731.
246. H.-K. Walter, J. Bauer, J. Steinmeyer, A. Kuzuya, C. M. Niemeyer and H.-A. Wagenknecht, *Nano Lett.*, 2017, **17**, 2467-2472.
247. W. West and S. Pearce, *J. Phys. Chem.*, 1965, **69**, 1894-1903.
248. A. Okamoto, *Chem. Soc. Rev.*, 2011, **40**, 5815-5828.
249. D. O. Wang and A. Okamoto, *J. Photochem. Photobiol. C*, 2012, **13**, 112-123.
250. A. Okamoto, *Appl. Microsc.*, 2019, **49**, 1-7.
251. S. Ikeda and A. Okamoto, *Chem. Asian J.*, 2008, **3**, 958-968.
252. S. Ikeda, T. Kubota, K. Kino and A. Okamoto, *Bioconjugate Chem.*, 2008, **19**, 1719-1725.
253. S. Ikeda, T. Kubota, H. Yanagisawa, M. Yuki and A. Okamoto, *Nucleic Acids Symp. Ser.*, 2009, **53**, 155-156.
254. S. Ikeda, M. Yuki, H. Yanagisawa and A. Okamoto, *Tetrahedron Lett.*, 2009, **50**, 7191-7195.
255. T. Kubota, S. Ikeda, H. Yanagisawa, M. Yuki and A. Okamoto, *Bioconjugate Chem.*, 2009, **20**, 1256-1261.
256. T. Kubota, S. Ikeda and A. Okamoto, *Bull. Chem. Soc. Jpn.*, 2009, **82**, 110-117.
257. S. Ikeda, T. Kubota, M. Yuki and A. Okamoto, *Angew. Chem. Int.*, 2009, **121**, 6602-6606.
258. S. Ikeda, H. Yanagisawa, A. Nakamura, D. O. Wang, M. Yuki and A. Okamoto, *Org. Biomol. Chem.*, 2011, **9**, 4199-4204.
259. I. Oomoto, A. Suzuki-Hirano, H. Umeshima, Y.-W. Han, H. Yanagisawa, P. Carlton, Y. Harada, M. Kengaku, A. Okamoto and T. Shimogori, *Nucleic Acids Res.*, 2015, **43**, e126-e126.
260. A. Okamoto, K. Sugizaki, M. Yuki, H. Yanagisawa, S. Ikeda, T. Sueoka, G. Hayashi and D. O. Wang, *Org. Biomol. Chem.*, 2013, **11**, 362-371.
261. S. Ikeda, T. Kubota, D. O. Wang, H. Yanagisawa, T. Umemoto and A. Okamoto, *ChemBioChem*, 2011, **12**, 2871-2880.
262. S. Ikeda, T. Kubota, D. O. Wang, H. Yanagisawa, M. Yuki and A. Okamoto, *Org. Biomol. Chem.*, 2011, **9**, 6598-6603.
263. J. Chen, K. Morihiro, D. Fukui, L. Guo and A. Okamoto, *ChemBioChem*, 2020, **21**, 1022-1027.
264. L. Guo and A. Okamoto, *Chem. Commun.*, 2017, **53**, 9406-9409.
265. S. Ikeda, T. Kubota, M. Yuki, H. Yanagisawa, S. Tsuruma and A. Okamoto, *Org. Biomol. Chem.*, 2010, **8**, 546-551.
266. K. Sugizaki and A. Okamoto, *Bioconjugate Chem.*, 2010, **21**, 2276-2281.
267. O. Seitz, F. Bergmann and D. Heindl, *Angew. Chem. Int.*, 1999, **38**, 2203-2206.
268. O. Köhler and O. Seitz, *Chem. Commun.*, 2003, 2938-2939.
269. O. Köhler, D. V. Jarikote and O. Seitz, *Chem. Commun.*, 2004, 2674-2675.
270. D. V. Jarikote, O. Köhler, E. Socher and O. Seitz, *European Journal of Organic Chemistry*, 2005, 3187-3195.

271. D. V. Jarikote, N. Krebs, S. Tannert, B. Röder and O. Seitz, *Chem. Biol.*, 2007, **13**, 300-310.
272. O. Köhler, D. V. Jarikote and O. Seitz, *ChemBioChem*, 2005, **6**, 69-77.
273. E. Socher, D. V. Jarikote, A. Knoll, L. Röglin, J. Burmeister and O. Seitz, *Anal. Biochem.*, 2008, **375**, 318-330.
274. E. Socher, L. Bethge, A. Knoll, N. Jungnick, A. Herrmann and O. Seitz, *Angew. Chem. Int.*, 2008, **47**, 9555-9559.
275. A. Tonelli, T. Tedeschi, A. Germini, S. Sforza, R. Corradini, M. C. Medici, C. Chezzi and R. Marchelli, *Mol. Biosyst.*, 2011, **7**, 1684-1692.
276. S. Kummer, A. Knoll, E. Socher, L. Bethge, A. Herrmann and O. Seitz, *Bioconjugate Chem.*, 2012, **23**, 2051-2060.
277. S. Kummer, A. Knoll, E. Socher, L. Bethge, A. Herrmann and O. Seitz, *Angew. Chem. Int.*, 2011, **50**, 1931-1934.
278. I. Walev, S. C. Bhakdi, F. Hofmann, N. Djonder, A. Valeva, K. Aktories and S. Bhakdi, *Proc. Natl. Acad. Sci. USA*, 2001, **98**, 3185-3190.
279. Y. Kam, A. Rubinstein, A. Nissan, D. Halle and E. Yavin, *Mol. Pharm.*, 2012, **9**, 685-693.
280. M. V. Sonar, M. E. Wampole, Y.-Y. Jin, C.-P. Chen, M. L. Thakur and E. Wickstrom, *Bioconjugate Chem.*, 2014, **25**, 1697-1708.
281. N. Kolevzon, D. Hashoul, S. Naik, A. Rubinstein and E. Yavin, *Chem. Commun.*, 2016, **52**, 2405-2407.
282. D. Hashoul, R. Shapira, M. Falchenko, O. Tepper, V. Paviov, A. Nissan and E. Yavin, *Biosens. Bioelectron.*, 2019, **137**, 271-278.
283. T. Sato, Y. Sato and S. Nishizawa, *J. Am. Chem. Soc.*, 2016, **138**, 9397-9400.
284. T. Sato, Y. Sato and S. Nishizawa, *Chem. Eur. J.*, 2017, **23**, 4079-4088.
285. A. G. Torres, M. M. Fabani, E. Vigorito, D. Williams, N. Al-Obaidi, F. Wojciechowski, R. H. Hudson, O. Seitz and M. J. Gait, *Nucleic Acids Res.*, 2012, **40**, 2152-2167.
286. N. Loibl, C. Arenz and O. Seitz, *ChemBioChem*, 2020, **21**, 2527.
287. Y. Kam, A. Rubinstein, S. Naik, I. Djavsarov, D. Halle, I. Ariel, A. O. Gure, A. Stojadinovic, H. Pan and V. Tsivin, *Cancer Lett.*, 2014, **352**, 90-96.
288. D. Gahtory, M. Murtola, M. M. Smulders, T. Wennekes, H. Zuilhof, R. Strömberg and B. Albada, *Org. Biomol. Chem.*, 2017, **15**, 6710-6714.
289. L. Bethge, I. Singh and O. Seitz, *Org. Biomol. Chem.*, 2010, **8**, 2439-2448.
290. F. Hövelmann, L. Bethge and O. Seitz, *ChemBioChem*, 2012, **13**, 2072-2081.
291. F. Hövelmann, I. Gaspar, A. Ephrussi and O. Seitz, *J. Am. Chem. Soc.*, 2013, **135**, 19025-19032.
292. F. Hövelmann, I. Gaspar, S. Loibl, E. A. Ermilov, B. Röder, J. Wengel, A. Ephrussi and O. Seitz, *Angew. Chem. Int.*, 2014, **53**, 11370-11375.
293. F. Hövelmann, I. Gaspar, J. Chamiolo, M. Kasper, J. Steffen, A. Ephrussi and O. Seitz, *Chem. Sci.*, 2016, **7**, 128-135.
294. I. Haralampiev, M. Schade, J. Chamiolo, F. Jolmes, S. Prisner, P. T. Witkowski, M. Behrent, F. Hövelmann, T. Wolff and O. Seitz, *ChemBioChem*, 2017, **18**, 1589-1592.
295. I. Gaspar, F. Hövelmann, J. Chamiolo, A. Ephrussi and O. Seitz, *ACS Chem. Biol.*, 2018, **13**, 742-749.
296. A. Knoll, S. Kankowski, S. Schöllkopf, J. C. Meier and O. Seitz, *Chem. Commun.*, 2019, **55**, 14817-14820.
297. J. Chamiolo, G. m. Fang, F. Hövelmann, D. Friedrich, A. Knoll, A. Loewer and O. Seitz, *ChemBioChem*, 2019, **20**, 595-604.
298. P. Klimkowski, S. De Ornellas, D. Singleton, A. H. El-Sagheer and T. Brown, *Org. Biomol. Chem.*, 2019, **17**, 5943-5950.
299. E. Socher, A. Knoll and O. Seitz, *Org. Biomol. Chem.*, 2012, **10**, 7363-7371.
300. G.-m. Fang, J. Chamiolo, S. Kankowski, F. Hövelmann, D. Friedrich, A. Löwer, J. C. Meier and O. Seitz, *Chem. Sci.*, 2018, **9**, 4794-4800.
301. S. Obika, D. Nanbu, Y. Hari, J.-i. Andoh, K.-i. Morio, T. Doi and T. Imanishi, *Tetrahedron Lett.*, 1998, **39**, 5401-5404.
302. K. E. Nielsen, S. K. Singh, J. Wengel and J. P. Jacobsen, *Bioconjugate Chem.*, 2000, **11**, 228-238.

303. A. Ivanova and N. Rösch, *J. Phys. Chem. A*, 2007, **111**, 9307-9319.
304. U. Wenge, J. Wengel and H. A. Wagenknecht, *Angew. Chem. Int.*, 2012, **51**, 10026-10029.
305. J. Chamiolo, PhD thesis, Humboldt Universität zu Berlin, 2019.
306. S. Bartsch, Bachelor thesis, Humboldt Universität zu Berlin, 2016.
307. J. K. Pokorski, M. A. Witschi, B. L. Purnell and D. H. Appella, *J. Am. Chem. Soc.*, 2004, **126**, 15067-15073.
308. J. K. Pokorski, J.-M. Nam, R. A. Vega, C. A. Mirkin and D. H. Appella, *Chem. Commun.*, 2005, 2101-2103.
309. C. M. Micklitsch, B. Y. Oquare, C. Zhao and D. H. Appella, *Anal. Chem.*, 2013, **85**, 251-257.
310. H. Zheng, M. Saha and D. H. Appella, *Org. Lett.*, 2018, **20**, 7637-7640.
311. O. Tepper, H. Zheng, D. H. Appella and E. Yavin, *Chem. Commun.*, 2021, **57**, 540-543.
312. I. Peled and E. Yavin, *ACS Omega*, 2018, **3**, 3813-3818.
313. I. A. Mellis, R. Gupte, A. Raj and S. H. Rouhanifard, *Nat. Methods*, 2017, **14**, 801-804.
314. J. Chamiolo, G. m. Fang, F. Hövelmann, D. Friedrich, A. Knoll, A. Loewer and O. Seitz, *ChemBioChem*, 2018.
315. F. Hövelmann, I. Gaspar, A. Ephrussi and O. Seitz, *J. Am. Chem. Soc.*, 2013, **135**, 19025-19032.
316. A. Knoll, S. Kankowski, S. Schöllkopf, J. C. Meier and O. Seitz, *Chem. Commun.*, 2019, **55**, 14817-14820.
317. O. Köhler, D. V. Jarikote and O. J. C. Seitz, *ChemBioChem*, 2005, **6**, 69-77.
318. O. Köhler and O. Seitz, *Chem. Commun.*, 2003, 2938-2939.
319. O. Seitz and O. Köhler, *Chem. Eur. J.*, 2001, **7**, 3911-3925.
320. E. Socher, D. V. Jarikote, A. Knoll, L. Röglin, J. Burmeister and O. J. A. b. Seitz, *Anal. Biochem.*, 2008, **375**, 318-330.
321. K. Susann, K. Andrea, S. Elke, B. Lucas, H. Andreas and S. Oliver, *Angew. Chem. Int.*, 2011, **50**, 1931-1934.
322. F. Hövelmann and O. Seitz, *Acc. Chem. Res.*, 2016, **49**, 714-723.
323. C. Knopf, Master thesis, Humboldt Universität zu Berlin, 2015.
324. F. Hövelmann, PhD thesis, Humboldt Universität zu Berlin, 2015.
325. B. Lucas, PhD thesis, Humboldt Universität zu Berlin, 2011.
326. A. T. Ansevin, D. L. Vizard, B. W. Brown and J. McConathy, *Biopolymers*, 1976, **15**, 153-174.
327. M. K. Campbell, S. O. Farrell and O. M. McDougal, *Biochemistry*, Cengage Learning, 9. Ed., 2017.
328. R. C. Wade and P. J. Goodford, *Prog. Clin. Biol. Res.*, 1989, **289**, 433-444.
329. M. Spencer, *Acta Crystallogr.*, 1959, **12**, 66-71.
330. B. A. Armitage, *Heterocyclic Polymethine Dyes*, 2008, 11-29.
331. L. Stryer, *Annu. Rev. Biochem.*, 1978, **47**, 819-846.
332. M. C. Wahl and M. Sundaralingam, *Biopolymers*, 1997, **44**, 45-63.
333. J. Choi and T. Majima, *Chem. Soc. Rev.*, 2011, **40**, 5893-5909.
334. A. Eisfeld and J. S. Briggs, *Chem. Phys.*, 2006, **324**, 376-384.
335. R. Khairutdinov and N. Serpone, *J. Phys. Chem. B*, 1997, **101**, 2602-2610.
336. P. J. Sanstead, P. Stevenson and A. Tokmakoff, *J. Am. Chem. Soc.*, 2016, **138**, 11792-11801.
337. A. Uzman, *Biochem. Mol. Biol. Educ.*, 2003, **31**, 212-214.
338. A. E. Zamora, J. C. Crawford and P. G. Thomas, *J. Immunol.*, 2018, **200**, 392-399.
339. A. D. Waldman, J. M. Fritz and M. J. Lenardo, *Nat. Rev. Immunol.*, 2020, **20**, 651-668.
340. H. C. Ertl, J. Zaia, S. A. Rosenberg, C. H. June, G. Dotti, J. Kahn, L. J. Cooper, J. Corrigan-Curay and S. E. Strome, *Cancer Res.*, 2011, **71**, 3175-3181.
341. M. Kalos, B. L. Levine, D. L. Porter, S. Katz, S. A. Grupp, A. Bagg and C. H. June, *Sci. Transl. Med.*, 2011, **3**, 95ra73.
342. C. H. June, R. S. O'Connor, O. U. Kawalekar, S. Ghassemi and M. C. Milone, *Science*, 2018, **359**, 1361-1365.
343. S. L. Maude, N. Frey, P. A. Shaw, R. Aplenc, D. M. Barrett, N. J. Bunin, A. Chew, V. E. Gonzalez, Z. Zheng and S. F. Lacey, *N. Engl. J. Med.*, 2014, **371**, 1507-1517.
344. B. M. Wile, K. Ban, Y.-S. Yoon and G. Bao, *Nat. Protoc.*, 2014, **9**, 2411-2424.

345. C. Yee, J. Thompson, D. Byrd, S. Riddell, P. Roche, E. Celis and P. Greenberg, *Proc. Natl. Acad. Sci. USA*, 2002, **99**, 16168-16173.
346. H. C. Kolb and K. B. Sharpless, *Drug Discov. Today*, 2003, **8**, 1128-1137.
347. F. Abendroth and O. Seitz, *Angew. Chem.*, 2014, **126**, 10672-10677.
348. M. C. Wahl and M. Sundaralingam, *Biopolymers*, 1997, **44 1**, 45-63.
349. ThermoScientific, Maximize Your RNA Yield https://www.thermofisher.com/de/de/home/references/ambion-tech-support/rna-isolation/tech-notes/maximize-your-rna-yield.html, (accessed 21.08.2022).
350. I. Gaspar and A. Ephrussi, *Wiley Interdisciplinary Reviews: Developmental Biology*, 2015, **4**, 135-150.
351. E. T. Jordan, M. Collins, J. Terefe, L. Ugozzoli and T. Rubio, *J. Biomol. Tech.*, 2008, **19**, 328.
352. O. Ebert, S. Finke, A. Salahi, M. Herrmann, B. Trojaneck, P. Lefterova, E. Wagner, R. Kircheis, D. Huhn and F. Schriever, *Gene Ther.*, 1997, **4**, 296.
353. L. Chicaybam, A. L. Sodre, B. A. Curzio and M. H. Bonamino, *PLoS One*, 2013, **8**, e60298.
354. S. I. Sukharev, V. A. Klenchin, S. M. Serov, L. V. Chernomordik and A. Chizmadzhev Yu, *Biophys. J.*, 1992, **63**, 1320-1327.
355. G. Saulis, R. Saulė, A. Bitinaitė, N. Žurauskienė, V. Stankevič and S. Balevičius, *IEEE Trans. Plasma Sci.*, 2013, **41**, 2913-2919.
356. A. Fyrberg and K. Lotfi, *Cytotechnology*, 2010, **62**, 497-507.
357. R. Notman, M. Noro, B. O'Malley and J. Anwar, *J. Am. Chem. Soc.*, 2006, **128**, 13982-13983.
358. H. Melkonyan, C. Sorg and M. Klempt, *Nucleic Acids Res.*, 1996, **24**, 4356-4357.
359. E. Ferret, C. Evrard, A. Foucal and P. Gervais, *Biotechnol. Bioeng.*, 2000, **67**, 520-528.
360. A. Draeger, R. Schoenauer, A. P. Atanassoff, H. Wolfmeier and E. B. Babiychuk, *Biochimie*, 2014, **107**, 66-72.
361. J. Schindelin, I. Arganda-Carreras, E. Frise, V. Kaynig, M. Longair, T. Pietzsch, S. Preibisch, C. Rueden, S. Saalfeld, B. Schmid, J. Y. Tinevez, D. J. White, V. Hartenstein, K. Eliceiri, P. Tomancak and A. Cardona, *Nat. Methods*, 2012, **9**, 676-682.
362. A. Savitzky and M. J. E. Golay, *Anal. Chem.*, 1964, **36**, 1627-1639.

10 Acknowledgements

First of all, I want to thank Prof. Dr. Oliver Seitz for providing an interesting and important research topic and giving me the opportunity to work on it during my PhD. I would also like to thank Prof. Dr. Christian Hackenberger and Prof. Dr. Hans-Achim Wagenknecht for agreeing to review this dissertation, as well as the Deutsche Forschungsgemeinschaft e.V. for funding this work within their priority program 1784 - Cellular Imaging of RNA C-to-U Editing.

I also want to express my gratitude to Andrea Knoll, Jasmine Chamiolo and Christina Kuznia for the great introduction into the topic and helpful discussions. My further thanks go to Peter Bou Dip, Sophie Neuber and Jaqueline Schneider for their support with the biological experiments and preparation of the cell lysate.

To the whole research group Seitz I am grateful for their good companionship, inspiring tea breaks and memorable activities inside and outside the lab. In this context I want to particularly mention my labmates Margherita di Pisa and Gunnar Bachem, but also Georgina Gavins, Tim Bilbrough, Natali Dubel and Pablo Lores Lareo.

Moreover, I thank Sean Yeldell and Yannic Altrichter for their valuable advice during the writing of this dissertation and for proofreading the manuscript.

Finally, I could not have undertaken this journey without my friends and family who always offered moral support and encouragement.

11 Selbstständigkeitserklärung

Ich, Sophie Schöllkopf, erkläre hiermit, dass ich die vorliegende Dissertation selbständig und nur unter Verwendung der von mir gemäß § 7 Abs. 3 der Promotionsordnung der Mathematisch-Naturwissenschaftlichen Fakultät, veröffentlicht im Amtlichen Mitteilungsblatt der Humboldt-Universität zu Berlin Nr. 126/2014 am 18.11.2014, angegebenen Hilfsmittel angefertigt habe.

…… …….

Ort, Datum Unterschrift

12 List of Publications

S. Schöllkopf, A. Knoll, A. Homer, O. Seitz
„Double FIT hybridization probes - towards enhancing brightness, turn-on and specificity of RNA detection"
Chem. Sci., 2023
DOI: 10.1039/D3SC00363A

A. Knoll, S. Kankowski, S. Schöllkopf, J. Meier, O. Seitz
„Chemo-Biological mRNA Imaging with Single Nucleotide Specificity"
Chem. Commun., 2019, **55**, 14817-14820
DOI: 10.1039/C9CC06989E

A.-K. Späte, V. Schart, S. Schöllkopf, A. Niederwieser, V. Wittmann
„Terminal Alkenes as Versatile Chemical Reporter Groups for Metabolic Oligosaccharide Engineering"
Chem. Eur. J., 2014, **20**, 16502-16508
DOI: 10.1002/chem.201404716